

Detection and Analysis of Martian Low-Temperature Geochemistry

Thesis by
Peter Eckels Martin

In Partial Fulfillment of the Requirements for
the degree of
Doctor of Philosophy

The Caltech logo, featuring the word "Caltech" in a bold, orange, sans-serif font, centered within a light orange rectangular background.

CALIFORNIA INSTITUTE OF TECHNOLOGY
Pasadena, California

2020
(Defended December 3, 2019)

© 2019

Peter Eckels Martin
ORCID: 0000-0003-4243-2090

All rights reserved

ACKNOWLEDGEMENTS

Graduate school has been a fantastic experience and one of the happiest times in my life. That's a rather unusual sentence coming from a sixth-year graduate student. That sentiment speaks volumes about, and is in large part thanks to, the long list of wonderful people I've had the good fortune to meet and work with since arriving in Pasadena in 2014. No PhD happens without a very long list of people who contributed somewhere along the line, in both critical and small ways. As a result, these acknowledgements are quite long, and yet there will inevitably be someone who I forget to thank in this section. If you're that person, please accept my apologies and know that I treasure the support you've given me regardless of my forgetfulness here.

The first round of thanks goes to my committee members. John Grotzinger has been a source of inspiration and a fount of geologic knowledge for the entirety of my PhD. It's only been in the last two years that I've gotten a chance to work closely with him; it's been a real treat. John Eiler is another source of seemingly infinite wisdom; the way he intuitively responds to any question about isotopes, science history, or star wars is an inspiration for any aspiring scientist. Bethany Ehlmann has been a fantastic mentor throughout my time here. I'm grateful to have approached her looking for a first-year proposition and to have worked with her since. She's always ready with probing questions, passion for planetary science, and good advice for navigating the world of science careers. Finally, I would like to thank my advisor, Ken Farley. Ken's hands-off approach let me struggle with problems to just the right degree, and he was always there and ready to help out when I got really stuck. He has a good sense of what might be feasible and worth trying, and what's likely to end up getting bogged down in painful, uninteresting details. I'll miss the time spent in Ken's office, brainstorming new and unique ways of approaching data-limited problems and working towards understanding how Mars really works.

There are a number of other people who have been vital to my experience here: Joe Kirschvink and the Ge136 trips he makes happen create a fantastic opportunity for grad students looking to gain some knowledge of California geology; George Rossmann, who I thank for his perennial open door, welcoming smile, and thoughtful input; Paul Asimow for always having an answer ready and for giving me help in my brief foray into experimental petrology; Jonathan Treffkorn, Nathan Dalleska, Jay Dickson, Annie Morodian, Mike Baker, Ma Chi, and Aaron

Celestian for help in getting lab setups done efficiently and correctly; Michele Judd and KISS for introducing me to so many great scientists and engineers and for excellent dinners and discussions; and to Paul Mahaffy, Charles Malespin, and the rest of the SAM team for their collaboration and thought-provoking discussions for the last five and a half years.

I also need to thank the staff at Caltech for helping make the experience here so wonderful. Janice Grancich, Jen Shechet, Liz Boyd, Ulrika Terrones, Mark Garcia and Julie Lee have made all the administrative details of grad school go smoothly in the background, which let me focus exclusively on science. Thanks also to the people I see at the gym nearly every day, especially Lee Olitt, who is always ready with a smile and a first bump. The janitorial staff here are excellent as well. They work hard, are here early in the morning every day, and much like the administrative staff, help make sure that the only thing I need to worry about is science.

I would like to thank some of my mentors and professors at Wesleyan for getting me started on this journey. Brian Northrop was a great academic guide and mentor, and I thank him for his willingness to see me leave organic chemistry behind to find what I care most deeply about. Tim Ku, Joop Varekamp, Peter Patton, and Jim Greenwood all contributed directly to my education and were happy to lend helpful thoughts and opinions while I was working on research problems. Dana Royer let me work in his lab when I was looking for a new home. Marty Gilmore introduced me to planetary geology, and then taught me to do real, proper research.

I've also had to good fortune of making lots of wonderful friends while I've been at Caltech. Without any one of these people, my experience would have been changed for the worse. My thanks go out to:

Alistair Hayden for the support he provides everyone around him,
Austin Chadwick for his sense of humor and for the help with that first social hour,
Cecilia Sanders for being the kind human being we should all aspire to be,
Celeste Labedz for the sheer amount passion with which she approaches everything,
Cody Finke for keeping the stoke high,
Dan Johnson for being such a kind person by nature,
Daven Quinn for being unafraid to tell you what he really thinks,
Elise Cutts for becoming a good friend and running a fantastic DnD campaign on short notice,

Elizabeth Bailey for having a unique perspective on nearly everything,
 Elle Chimiak for being exactly who she wants to be,
 Ellen Leask for her sincerity and for being willing to make a pun even when the time isn't right,
 Eva Scheller for how easy and fun she is to talk to,
 Giuliana Viglione for bringing the party with her,
 Hayden Miller for being a great officemate and a pleasure to hang out with,
 Jake Jencson for everything,
 Jen Buz for having a creative and passionate approach to friendship and science,
 Joe Biasi for always being willing to exchange an exasperated glance,
 John Naviaux for innumerable lunches and shared tents, and close friendship,
 Kyle Metcalf for the unique way he sees the world,
 Leah Sabbeth for bringing a New England sensibility to the West Coast,
 Lee Saper for being more of a mid-20's curmudgeon than I am,
 Maddie Lewis for her passion for the outdoors,
 Madison Douglas for bringing the metal and for sincere friendship when it matters,
 Mathieu Lapôtre for being a good conference roommate and a good gossip partner,
 Matt Liebowitz for talking sports and workouts, and for a great first-year living situation,
 Nancy Thomas for putting up with my pestering questions about LIBS and PCA,
 Nathan Stein for having a wry approach to Mars science,
 Preston Kemeny for always stopping for a word,
 Rachel Theios for throwing the laid-back kind of parties I enjoy,
 Sang Chen for his quiet brilliance,
 Serg Parra for his positive attitude and happy outlook on life,
 Ted Present for having an opinion and making it known,
 Voon Lai for her infectious positivity, and
 Yuanlong Huang for always being ready with a smile and a wave.

There is a long list of friends from before coming to Caltech who, without their influence in my life, I would not be where I am or who I am today. A few people I'd like to thank specifically (listed in chronological order): Nathan Grater, Billy Volante, Cullen Schiele, Paul Decker, Carter McCormick, Lily Zucker, Elle Markell, Eric Stephen, and Ethan Currie.

Loss is inevitable in any five and a half year period, and 2019 has been especially difficult with the death of my grandfather, Nathaniel F.G. Martin, and my grandmother, Patti W. Eckels. With my grandfather's passing, the world lost a uniquely compassionate and analytical mind and we are all poorer without his presence. I know he would be proud of this thesis. My grandmother and I spent a significant amount of time alone together at the cabin on Echo Lake, which I feel very fortunate for. I attribute much of my love of the outdoors to summers spent in northern Vermont with grandma. Despite both of them living long, happy lives, I miss both of my grandparents dearly, and I'm thankful that I had the opportunity to get to know them both so well.

My family gave me the start in life and the love and support that I needed to get through 22 years of high-octane education. Despite my extended family being physically distant, I cherish the times we've managed to get together, especially all in one place at one time. My parents, Jon and Ellen Martin, provided a safe and loving home through childhood and adolescence. From college onwards, they have acted as mentors, friends, and role models through the process of my joining the ranks of geology, and then making the decision to go to grad school. I also thank my brother, Eric, for the friendship we've developed as we've become adults. I hope we stay close for many years to come.

Finally, and most importantly, I want to thank my girlfriend, Ellen. Our relationship forms the foundation for everything I do, and is the reference point I come back to when I'm lost in my work or in my thoughts. I couldn't have done this without your help and encouragement, and I wouldn't have wanted to experience the last six years without you in my life. I love you.

ABSTRACT

The history of Mars is encoded in the geochemistry of ancient sedimentary Martian rocks and secondary phases. Recent landed missions have provided unparalleled datasets with which to investigate this geochemistry. Accordingly, this thesis is concerned primarily with the in-situ analysis of low-temperature Martian geochemical processes by landed missions, and the attendant Earth-based studies which enrich those in-situ investigations. There are five main studies reported here. The first is an analysis of a Mars-analog environment on Earth. Datasets similar to those that will be produced by the upcoming Mars-2020 rover are used to evaluate the ability of the rover to reconstruct a known paleoenvironment, to identify reference datasets that require further development, and to suggest operational modes that most efficiently use the rover's resources. The second study is an in-situ noble gas analysis using the SAM instrument on the Curiosity rover to investigate a jarosite-containing sample using a two-step heating analysis for K-Ar dating. The jarosite likely formed at 2.12 ± 0.36 Ga while plagioclase in the sample formed at 4.07 ± 0.63 Ga, indicating that liquid water interactions continued in Gale crater well past the end of the Hesperian period. The following chapter details another noble gas analysis, focusing on cosmogenic dating of surface exposure. In contrast to <100 Ma exposure ages observed at the floor of Gale crater, exposure ages exceeding 1 Ga are detected on the flanks of Mount Sharp. These ages indicate Mount Sharp formed during the Hesperian and has been largely unchanged in the intervening 3.1 Ga. The next study is a reevaluation of the data used to identify the presence of perchlorate in Gale crater. These data suggest that perchlorate is indeed present, but that it must be Amazonian in age, suggesting that rare surface wetting events have caused leaching of this soluble ion into the bedrock. The final study reports the development of a technique for measuring the isotopes in perchlorate using Orbitrap mass spectrometry on Earth, allowing investigation of the formation processes that impact the chlorine isotope ratio of this molecule on both Earth and Mars.

PUBLISHED CONTENT AND CONTRIBUTIONS

Martin, P. E., K. A. Farley, M. B. Baker, C. A. Malespin, S. P. Schwenzer, B. A. Cohen, P. R. Mahaffy, A. C. McAdam, D. W. Ming, P. M. Vasconcelos, and R. Navarro-González (2017). A Two-Step K-Ar Experiment on Mars: Dating the Diagenetic Formation of Jarosite from Amazonian Groundwaters. *Journal of Geophysical Research: Planets*, 122(12), 2017JE005445. <https://doi.org/10.1002/2017JE005445>

P.E.M. participated in data collection, analyzed the data, and wrote the manuscript.

Martin, P. E., B. L. Ehlmann, N. H. Thomas, R. C. Wiens, J. J. R. Hollis, L. W. Beegle, R. Bhartia, S. M. Clegg, and D. L. Blaney (2019). Studies of a Lacustrine-Volcanic Mars Analog Field Site with Mars-2020-like Instruments. *In Revision*.

P.E.M. participated in data collection, analyzed the data, and wrote the manuscript

Martin, P. E., K. A. Farley, P. D. Archer, Jr., J. V. Hogancamp, K. L. Siebach, J. P. Grotzinger, and S. M. McLennan (2019). Reevaluation of Perchlorate in Gale Crater Rocks Suggests Geologically Recent Perchlorate Addition. *In Revision*.

P.E.M. conceived the study, performed the analyses, and wrote the manuscript

TABLE OF CONTENTS

Acknowledgements	iii
Abstract	vii
Published Content and Contributions.....	viii
Table of Contents.....	ix
List of Illustrations and/or Tables	xi
Abbreviations	xiii
Chapter I: Introduction	1
1.1 Martian geology.....	1
1.2 Exploration of Mars.....	3
1.3 Thesis outline.....	4
Chapter II: Studies of a Lacustrine-Volcanic Mars Analog Field Site With Mars-2020-Like Instruments	6
2.1 Abstract.....	6
2.2 Introduction	7
2.3 Methods	9
2.4 Results of Mars-2020 payload simulation	19
2.5 Discussion.....	38
2.6 Conclusions	48
Chapter III: A Two-Step K-Ar Experiment on Mars: Dating the Diagenetic Formation of Jarosite from Amazonian Groundwaters	52
3.1 Abstract.....	52
3.2 Introduction	53
3.3 Sample and Methodology	54
3.4 Results.....	62
3.5 Discussion.....	71
3.6 Conclusions	77
Chapter IV: Billion-Year Exposure Ages in Gale Crater Indicate a Pre-Amazonian Formation of Mount Sharp.....	79
4.1 Abstract.....	79
4.2 Introduction	79
4.3 Materials and methods	85
4.4 Results.....	88
4.5 Discussion.....	89
4.6 Erosion and exposure history of Mount Sharp.....	91
4.7 Conclusions	98
4.8 Appendix.....	100
Chapter V: Reevaluation of Perchlorate in Gale Crater Rocks Suggests Geologically Recent Perchlorate Addition.....	105
5.1 Abstract.....	105
5.2 Introduction	106
5.3 Perchlorate in Gale crater.....	108
5.4 Alternative explanations for O ₂ release	117

5.5 Modern perchlorate	124
5.6 Conclusions	125
5.7 Appendix.....	126
Chapter VI: A New Method of Isotopic Analysis of Perchlorate Using Electrospray-Orbitrap	
Mass Spectrometry	141
6.1 Abstract.....	141
6.2 Introduction	142
6.3 Methods	143
6.4 Results.....	150
6.5 Discussion.....	152
6.6 Conclusions	165
Bibliography:	167

LIST OF ILLUSTRATIONS AND TABLES

<i>Number</i>	<i>Page</i>
Table 2-1 Instrument capabilities of the Mars-2020 rover	9
Figure 2-1 Geologic map of field site and photo of outcrop	11
Table 2-2 Units defined in this study	15
Figure 2-2 Outcrop-scale unit map.....	15
Table 2-3 Ground Truth XRD	17
Figure 2-3 Simulated Navcam mosaic	19
Figure 2-4 Unit map derived from Mars-like data and decorrelation stretch	20
Figure 2-5 Mars-2020-like data of outcrop.....	21
Figure 2-6 Spectral properties of simulated data	23
Figure 2-7 Supercam-like data of selected samples	24
Figure 2-8 PCA of LIBS-like data and individual spectra	26
Table 2-4 Ground truth lithochemistry	27
Table 2-5 LIBS results.....	29
Figure 2-9 PIXL-like data of mudstone	32
Figure 2-10 PIXL-like data of travertine carbonate.....	33
Figure 2-11 Deep-UV fluorescence spectra chart.....	35
Table 2-6 Literature values for fluorescence attribution	35
Figure 2-12 Deep-UV Raman spectra.....	36
Figure 2-13 Spectral downsampling plot.....	40
Figure 2-14 XRD pattern of samples	50
Figure 3-1 Color MAHLI image of Mojave 2 surface	55
Table 3-1 Mineralogy of geochronology samples.....	56
Table 3-2 APXS results from Mojave 2.....	57
Figure 3-2 Gas traces from Mojave 2 noble gas measurement	61
Figure 3-3 Anorthite content of Martian meteorites.....	65
Table 3-3 Noble gas results from Moajve 2.....	69
Figure 3-4 Modeled ages of Mojave 2	74
Figure 3-5 Distribution of potassium in Mojave 2 and Cumberland	75
Figure 4-1 Conceptual cross-section of Gale crater.....	81
Figure 4-2 Mojave 2 location map and images.....	85
Figure 4-3 Quela location map and images	87
Table 4-1 Mojave 2 and Quela cosmogenic noble gas results	89
Figure 4-4 Sample locations and elevations vs age	95
Figure 4-5 Diagram of potential exposure scenarios.....	96
Figure 4-6 Mass spectra for ^{21}Ne	100
Table 4-2 Mojave 2 expanded cosmogenic noble gas results	101
Table 4-3 Mojave 2 chemistry and mineralogy	102
Table 4-4 Quela chemistry and mineralogy	103
Figure 4-7 m/z 20 vs 21 for Quela and Cumberland.....	104
Table 5-1 Radiolysis calculations for each sample.....	111
Figure 5-1 Gas release temperatures compared to O_2	114

Figure 5-2 Molar HCl vs. CH ₃ Cl for each sample.....	116
Figure 5-3 Lab- and SAM-derived O ₂ traces.....	121
Figure 5-4 Mn vs O ₂ molar amounts.....	122
Table 5-2 List of metal oxide nanopowders	128
Table 5-3 Oxygen release experiment results.....	129
Figure 5-5 Gas traces for each metal oxide heating experiment	130
Figure 5-6 Gas traces for every sample.....	135
Figure 5-7 Additional gas release temperatures compared to O ₂	139
Figure 5-8 Analyses restricted to sediment samples.....	140
Table 6-1 Isotopologues of perchlorate.....	146
Figure 6-1 Time series of total ion current.....	147
Figure 6-2 Perchlorate reduction concentrations	150
Figure 6-3 Isotope and fractionation factor values	151
Figure 6-4 Fractionation factors vs. temperature.....	154
Figure 6-5 Time series of <i>m/z</i> 99 and 102.....	157
Figure 6-6 Mass spectrum with zoom of 101 <i>m/z</i>	158
Figure 6-7 $\delta^{37}\text{Cl}$ data with additional error term.....	159
Figure 6-8 Perchlorate standard values and secular drift.....	160

ABBREVIATIONS

APXS Alpha Particle X-ray Spectrometer

DUV Deep Ultraviolet

EGA Evolved Gas Analysis

GCR Galactic Cosmic Ray

IC Ion Chromatograph

IR Infrared

LIBS Lased-Induced Breakdown Spectroscopy

MAHLI MArS Hand Lens Imager

MEDA Mars Environmental Dynamics Analyzer

MOXIE Mars Oxygen In-Situ Resource Utilization Experiment

MSL Mars Science Laboratory

PIXL Planetary Instrument for X-ray Lithochemistry

RIMFAX Radar Imager for Mars's Subsurface Exploration

RMI Remote Micro-Imager

SAM Sample Analysis at Mars

SHERLOC Scanning for Habitable Environments with Raman and Luminescence for
Organics and Chemistry

SWIR Short Wave Infrared

TOC Total Organic Carbon

UCIS Ultra-Compact Imaging Spectrometer

UV Ultraviolet

VIS Visible

VNIR Visible and Near-Infrared

XRD X-ray Diffraction/X-ray Diffractometer

XRF X-ray Fluorescence

Chapter 1

INTRODUCTION

1.1 Martian geology

Unlike the Earth, which recycles the majority of rocks that make up its crust via plate tectonics, much of Mars's surface is composed of rocks over three billion years old (Tanaka et al., 2014). In this way, the surface of Mars serves as a time capsule that allows us to examine the geology of a rocky planet early in the history of the solar system. Many of the major driving forces on early Mars (bombardment by meteorites as accretion ends, the formation of an early crust, the generation of an atmosphere, etc.) are the same processes that likely took place on early Earth. By studying Mars, we can by proxy study how these processes may have affected the Earth in its earliest stages. The drastic environmental change which transformed Mars from a relatively wet and clement planet to the cold and dry planet we observe today also offers an opportunity to understand the mechanisms behind such catastrophic, planet-wide climate change. Furthermore, to the extent that Mars functions as a proxy for the history of the Earth, it also permits interrogation of the history of life. By investigating whether life ever arose on Mars, we can seek to understand the reasons that life arose on Earth. Depending on the answer to whether life ever existed on Mars, either the similarities or the differences between these planets may emerge as key factors in determining whether abiogenesis occurs on a given world.

In order to begin to address the major topics mentioned above, and for the purposes of building a framework in which to place the findings of this thesis, it is first necessary to convey a general summary of the current state of knowledge about Mars's geologic history. The history of Mars is divided into four major periods: the pre-Noachian (4.5-4.1 Ga), the Noachian (4.1-3.7 Ga), the Hesperian (3.7-3.1 Ga), and the Amazonian (3.1 Ga-present; Hartmann & Neukum, 2001; Nimmo & Tanaka, 2005). The pre-Noachian era has no surviving rock record, and has therefore received little scientific study (Carr & Head, 2010). The Noachian is characterized by abundant surface water, expressed in geomorphology by lake deposits and high-density drainage networks (e.g., Fassett & Head, 2008; Malin & Edgett, 2003; Mangold et al., 2004) and in geochemistry by

the presence of abundant phyllosilicate and other alteration minerals associated with the most ancient crust on Mars (Bibring et al., 2006; Ehlmann et al., 2011; Ehlmann & Edwards, 2014; Poulet et al., 2005). The end of the Noachian corresponds with a general decrease in the amount of liquid water at the surface, appearing as a decrease in the prevalence of valley networks. In their place, large outflow channels appear. These massive channels are thought to have resulted from the release of entire aquifers after the pore pressure within the aquifers exceeded the lithostatic pressure which retained them (Fassett & Head, 2008; Squyres, 1984). The mineralogy associated with this reduction in water correspondingly shifts from phyllosilicate- to sulfate-dominated (Bibring et al., 2006; Chevrier et al., 2007; Squyres et al., 2004). Finally, in the Amazonian no major water-associated features are observed. Instead, the dominant surface features are carved by wind (Arvidson et al., 1979; Day & Kocurek, 2016; Golombek et al., 2014), and the changing mineralogy is primarily characterized by the formation of iron oxides (Bibring et al., 2006).

The primary goal of this thesis is to understand more deeply this history of the surface and near-surface environments on Mars. Water (or the lack thereof) plays a dominant role in shaping the morphology and mineralogy of planetary surfaces at the temperatures found on Earth and Mars, and is therefore critical to the major transitions in Mars's geologic past. In its liquid form, water allows the leaching and alteration of the primary minerals that make up Mars's crust, and it has enormous erosive power to shape the landforms at the surface. Reduced availability of water, in this case due to both loss to space and sequestration in polar ice caps and subsurface ice (e.g., Squyres, 1984), results in the landforms and mineralogy observed in Hesperian-aged portions of the surface. Eventually a complete lack of water culminates in the dusty, oxidizing modern environment. This thesis is therefore concerned with tracing the effects of water and reconstructing environments where water was once more abundant (Chapters 1 & 2), understanding the extent to which the conventional paradigm of a completely dry Mars is accurate (Chapters 2 & 4), and observing the results of this lack of water, evidenced by modern geomorphic changes and the chemistry of highly soluble ions such as perchlorate (Chapters 4-6).

Integral to the science of these investigations are the mechanisms by which they are carried out. The study of Mars by necessity involves remote analyses and data collection. Understanding how these measurements are made and how to interpret the data returned from missions to Mars is

as critical to developing an accurate and integrated model of Martian history as is the science itself. This theme is woven throughout this thesis, and discussed explicitly in the next section.

1.2 Exploration of Mars

The most recent 30 years in particular have been a very active period of Mars exploration; 17 of the 27 successful missions to Mars have taken place in this time. Not only has the number of ongoing missions to Mars increased dramatically since the mid-1990s, but the capability of those missions to detect crucial information about Mars's past has also increased dramatically. The resolution (both spatial and spectral) of orbiting instruments has steadily improved over this period. The high-level history presented in section 1.1 is told primarily through data collecting by orbiting missions, which can provide planet-scale observations and contribute, in a sense, statistical significance to findings, e.g., the distribution of alteration phases across Mars's entire surface (Ehlmann & Edwards, 2014). Landed missions, on the other hand, offer a something akin to a case study at a given site. These missions, while spatially restricted, allow unparalleled detail and enhanced analytical capabilities for understanding a specific location. Much like orbiting spacecraft, the capabilities of these landed missions have also steadily increased through time.

The Mars Science Laboratory (MSL)-class rovers are the current generation of Mars rovers, which provide unprecedented capabilities for in-situ analysis of extraterrestrial bodies. The first of these, Curiosity, landed in Gale crater in 2012. A second rover, the as-yet unnamed Mars-2020 mission, will launch in July of 2020 with a planned landing date in February of 2021. Each of these rovers brings new techniques to the field of in-situ planetary exploration. The suite of instruments onboard the Mars-2020 rover includes two Raman spectrometers, a technique which has never been employed in a planetary setting. One of the powerful new tools carried by the Curiosity rover is the Sample Analysis at Mars (SAM) instrument, which (among other capabilities) permits volatile extraction from drilled or scooped samples and analysis of these volatiles using a quadrupole mass spectrometer (Mahaffy et al., 2012). This instrument provides the data for much of the analysis presented in this thesis. The data collected by SAM would convey far less information without a complete prior knowledge of the sample being measured, and so is supported by analyses of mineralogy as measured by an X-ray diffractometer (CheMin) and elemental chemistry, measured by an Alpha Particle X-ray Spectrometer (APXS).

1.3 Thesis outline

For mission success, scientific support of landed missions must range from the ability to understand the data returned, to analysis of the data itself, to Earth-based analyses which can inform the decision making and data collected on Mars. These basic tenets inform the structure of this thesis; there are accordingly three parts:

Chapter 2 describes pre-launch science support for the Mars-2020 mission. This study focuses on a lacustrine deposit on Earth in the Mojave Desert analogous to the anticipated sedimentary sequence at the Mars-2020 landing site, Jezero crater. Analyses similar to those that will be possible using the Mars-2020 rover instrument payload are employed to understand the geochemistry and depositional environment of a lacustrine sedimentary sequence broadly similar to what will be encountered by the Mars-2020 mission. This chapter identifies synergies between instruments in the Mars-2020 instrument suite, areas where further development of databases for reference during the mission are necessary, and suggests modes of analysis that allow efficient data collection without the loss of critical information.

The following three chapters (**Chapters 3-5**) utilize data collected by the Curiosity rover on Mars, focusing on data produced by the SAM instrument. These chapters are organized chronologically by the process they investigate. Chapter 3 involves K-Ar dating of the potassium-bearing mineral jarosite, which precipitated from liquid water in the shallow subsurface as recently as 2 Ga. This result confirms the presence of liquid water at the near-surface of Mars past the end of the Hesperian. The following chapter (Chapter 4) focuses again on noble gas analyses using SAM, but instead of age dating the formation of minerals in samples collected by Curiosity, this research focuses on the cosmic-ray produced nuclides ^3He , ^{21}Ne , and ^{36}Ar to investigate the length of time the rocks in Gale crater have been at the surface. This cosmogenic dating allows determination of the rates and styles of modern erosion, which are produced strictly by wind. Chapter 5 is a comprehensive analysis of the suggestion in the literature that the molecule perchlorate exists in Gale crater. In particular, this study examines the likely age of such perchlorate, and determines that any perchlorate in Gale crater, even that observed in the rocks deposited at ~ 3.6 Ga, must be Amazonian in age. The fact that this perchlorate must be young most likely indicates that thin films of water

periodically carry perchlorate deposited at the surface of Mars into the shallow subsurface, probably transported along microscopic cracks and fissures in the rock.

Finally, **Chapter 6** is a study which utilizes the more complex technical abilities of Earth-based instrumentation to inform the data collected on Mars. Spurred by the perchlorate analysis in Chapter 5 and an analysis of chlorine isotope signatures in HCl extracted from rocks in Gale crater (not included in this thesis; Farley et al., 2016), this chapter details the development of a new technique for the isotopic analysis of perchlorate. This technique is applied to a potentially Mars-relevant reaction (the reduction of perchlorate by iron) to determine whether the chlorine isotope signatures observed on Mars are partially or entirely the result of such a reaction.

Chapter 2

STUDIES OF A LACUSTRINE-VOLCANIC MARS ANALOG FIELD SITE WITH MARS-2020-LIKE INSTRUMENTS

The content of this chapter has been submitted for publication as:

Martin, P. E., B. L. Ehlmann, N. H. Thomas, R. C. Wiens, J. J. R. Hollis, L. W. Beegle, R. Bhartia, S. M. Clegg, and D. L. Blaney (2019). Studies of a Lacustrine-Volcanic Mars Analog Field Site with Mars-2020-like Instruments. *In Revision*.

2.1 Abstract

On the upcoming Mars-2020 rover two remote sensing instruments, Mastcam-Z and SuperCam, and two microscopic proximity science instruments, SHERLOC and PIXL, will collect compositional (mineralogy, chemistry, and organics) data essential for paleoenvironmental reconstruction. The synergies between and limitations of these instruments were evaluated via study of a Mars analog field site in the Mojave Desert, using instruments approximating the data that will be returned by Mars-2020. A ground truth dataset was generated for comparison to validate the results. The site consists of a succession of clay-rich mudstones of lacustrine origin, interbedded tuffs, a carbonate-silica travertine deposit, and gypsiferous mudstone strata. The major geological units were mapped successfully using simulated Mars-2020 data. Simulated Mastcam-Z data identified unit boundaries and Fe-bearing weathering products. Simulated SuperCam passive shortwave infrared and green Raman data were essential in identifying major mineralogical composition and changes in lacustrine facies at distance; this was possible even with spectrally downsampled passive IR data. LIBS and simulated PIXL data discriminated and mapped major element chemistry. Simulated PIXL revealed mm-scale zones enriched in zirconium, of interest for age dating. SHERLOC-like data mapped sulfate and carbonate at sub-mm scale; silicates were identified with increased laser pulses/spot or by averaging of hundreds of spectra. Fluorescence scans detected and mapped varied classes of organics in all samples, characterized further with follow-on spatially targeted deep-UV Raman spectra. Development of dedicated organics spectral libraries is needed to aid interpretation. Given these observations, the important units in the outcrop would be sampled and cached for sample return.

2.2 Introduction

The Mars-2020 rover is an upcoming Mars Science Laboratory (MSL)-class rover with a similar design to the current Curiosity rover operating on the surface of Mars. The 2020 rover will have a new instrument payload designed to address four main objectives: A) Explore and decipher the geological processes, history, and past habitability of an astrobiologically relevant site on Mars; B) search for potential biosignatures; C) gather a cache of samples for return to Earth; and D) prepare for human exploration of Mars (Mustard et al., 2013; Williford et al., 2018). Seven instruments were selected for the Mars-2020 mission to address these objectives: Mastcam-Z, a stereo multispectral imager; the Mars Environmental Dynamics Analyzer (MEDA), a weather station; the Mars Oxygen ISRU Experiment (MOXIE), an in-situ oxygen production experiment; the Planetary Instrument for X-ray Lithochemistry (PIXL), a microfocus X-ray fluorescence spectrometer; the Radar Imager for Mars's Subsurface Experiment (RIMFAX), a ground-penetrating radar; the Scanning for Habitable Environments with Raman and Luminescence for Organics and Chemicals (SHERLOC), an autofocusing context imager and microfocus deep-UV Raman and fluorescence spectrometer; and SuperCam, a set of spectrometers capable of remote laser induced breakdown, Raman, and reflectance spectroscopies, along with a remote micro-imager. Four of these instruments (Mastcam-Z, SuperCam, SHERLOC, and PIXL) enable detailed imaging at multiple scales and spectroscopic measurements that provide information on mineralogy, chemistry, and organics at meter-scale to micrometer-scale. Such compositional data are essential to determining the geologic history of the landing site, assessing its paleohabitability, and searching for biosignatures. In addition to the measurements enabled by these instruments, the Mars-2020 rover will be capable of abrading potential targets to achieve a flat surface, removing dust from potential targets, and sampling targets by taking a core approximately one centimeter across and 5 cm long (Farley, 2017). The samples with the most potential for new discoveries will be cached for sample return, allowing thorough investigations to be conducted in laboratories on Earth.

As with other rovers, after landing, the Mars-2020 rover will explore regions of interest, the locations of which will be partially predetermined using orbital data. The general structure of a science campaign will begin with remote imaging from a distance of hundreds of meters, as the site of interest comes into view. This distant imaging will be followed up with imaging and spectroscopy of increasingly high resolution as the rover approaches the outcrop, allowing determination of some

aspects of the composition of the units within a given outcrop and preliminary mapping of these units from a distance. Upon the rover's close approach to the outcrop, continued remote sensing will guide selection of targets for proximity science, i.e., microscopic analyses using the instruments PIXL and SHERLOC. The full suite of contextual data collected by all of the instruments will then allow determination of the geologic and environmental history of the outcrop, which will guide the decision whether to sample a core from the near surface, and then which samples to add to the sample cache for possible return to Earth.

Each rover mission to Mars has so far carried a different instrument suite with distinct capabilities and modes of synergistic use as well as some limitations in measurement abilities. In this study, we examine how the Mars-2020 rover will detect composition (mineralogy, chemistry, and organics) and stratigraphic and petrographic relationships at a given outcrop to determine environmental history and habitability/habitation. Using an analog field site in the Mojave Desert and a suite of field portable and laboratory instruments, we simulate the data that would be generated from the instruments most directly capable of measuring composition: Mastcam-Z multispectral, SuperCam, SHERLOC, and PIXL. A number of previous studies have undertaken similar Mars-like field studies using analog data (Arvidson et al., 2010; Johnson et al., 2001). The two remote instruments (Mastcam-Z and SuperCam) have heritage with instruments on the currently operating Curiosity rover (Malin et al., 2017; Maurice et al., 2012; Wiens et al., 2012), though both will have updated capabilities on Mars-2020. The other two instruments, SHERLOC and PIXL, will be used for proximity science; their microscale compositional mapping techniques have not yet been utilized in a planetary setting. The datasets produced by this instrument suite will therefore be novel in the context of Mars, and a full understanding of the synergies between and limitations of these instruments will be crucial to the success of the mission as a whole. Our study addresses stratigraphy at a local scale only insofar as is needed for environmental reconstructions by basic imaging. On Mars, RIMFAX may show radar reflections indicative of deep structural geology but such data are not collected here. We compare our Mars-2020-analog data and interpretations with the known composition and environmental history of the Mojave outcrop based on prior work (e.g., Hillhouse, 1987; Mason, 1948) and our field verification. This comparison allows us to reveal the synergies between the Mars-2020 instruments in terms of building an environmental history from an outcrop and discern which aspects of a given site can be easily determined and which aspects will be more

difficult to address. Using these lessons, we suggest operating modes for the instruments, data collection, and analysis protocols that maximize efficient use of the capabilities and limited resources available to the Mars-2020 rover, e.g., time, power, and data volume.

2.3 Methods

Table 2-1. Instrument capabilities and simulated datasets for assessing Mars-2020 instrument performance.

Instrument	Data to be Generated	Simulated Data	Data Used
Navcam	RGB image 0.35 mrad/pixel 103°x77° FOV	Color image at 135 m	False color UCIS image (R: 622 G: 552 B: 462)
Mastcam-Z	13-color image (incl. RGB) 55 μ rad/pixel at best zoom 18°x23° FOV at lowest zoom	Zoomed color image at 200 m	RGB iPhone image mosaic
		Multispectral image at 190 m	Spectrally downsampled UCIS image
		VNIR spectra	Spectrally downsampled ASD spectra
Supercam	0.7 mrad/spot 7 m distance limit	LIBS	LANL ChemCam-like instrument
	0.7 mrad/spot 12 m distance limit 532 nm excitation laser	Green Raman	Renishaw M-1000 microRaman spectrometer
	0.7 mrad/spot 10 cm^{-1} resolution 400-850 nm wavelength range	VIS passive	ASD spectra
	1.15 mrad/spot 30 cm^{-1} resolution 1300-2600 nm wavelength range	IR passive	Spectrally downsampled ASD spectra
	RBG image 40 μ rad/pixel 20 mrad FOV	RMI	RGB iPhone images
	Sound	microphone	Not simulated
PIXL	120 μ m spot size 25 mm^2 scan area 28 kV X-ray energy	Micro-XRF	LA NHM Horiba XGT- 7200 micro-XRF
SHERLOC	100 μ m spot size 7x7 mm scan area 248.6 nm excitation laser	Deep-UV Raman	JPL breadboard instrument (MOBIUS)
		Deep-UV fluorescence	JPL breadboard instrument (MOBIUS)
WATSON	0.30 mrad/pixel	High-resolution color imaging	iPhone 4s camera photos

The Mars-2020 instruments for compositional analysis and image-based contextualization were simulated using laboratory, field and camera instruments (Table 2-1).

2.3.1 Imaging simulation: Navcam and Mastcam-Z

Mars-2020's engineering reconnaissance capability consists of stereo navigation cameras (Navcam) on the mast, which provide 20 megapixel, 3-color images at a resolution of 0.35 mrad/pixel with a 103°x77° field of view (Maki et al., 2016). The science imaging instrument is Mastcam-Z, a mast-mounted, adjustable zoom, stereoscopic multispectral imager with heritage from the Mastcam instrument onboard the Curiosity rover (Bell et al., 2016), Pancam on the Mars Exploration Rovers (Bell et al., 2003), and the Imager for Mars on Pathfinder (Smith et al., 1997). It acquires RGB images with a multiple lens optical assembly and Bayer-patterned microfilters on a CCD detector over focus distances from 1-2 m to infinity at a resolution of up to 55-200 μ rad/pixel (highest to lowest zoom) (Bell et al., 2014). Images in 15 discrete visible/near-infrared (VNIR) channels from 440-1013 nm are acquired using a filter wheel assembly (Bell et al., 2014; Buz et al., 2019). Mastcam-Z can characterize geomorphology, stratigraphy, and texture and is sensitive to variations in mineralogy, particularly for Fe-bearing minerals, which have distinctive absorptions in the VNIR wavelength range. It can also be used to aid in the operation, navigation, and target selection for the rover and other instruments.

Images collected using an iPhone 4s in standard photo mode were used to simulate basic color imaging capabilities of both Navcam and Mastcam-Z to provide context for the composition-focused study. A mosaic of these images was constructed using Adobe Photoshop CS 5.1 (Figure 2-1b). We do not simulate the stereo processing ability in this study. The resolution of the iPhone camera is 320 μ rad/pixel (determined empirically using a photograph of a measuring tape; a formal assessment to determine Nyquist sampling was not performed). Thus, from distances of 35m and 2m, respectively, the 11mm/pixel and 64 μ m/pixel resolution of the iPhone images acquired are similar to that of Mastcam-Z from 45 m and 2.6 m and Navcam from 32 m and 1.8 m.

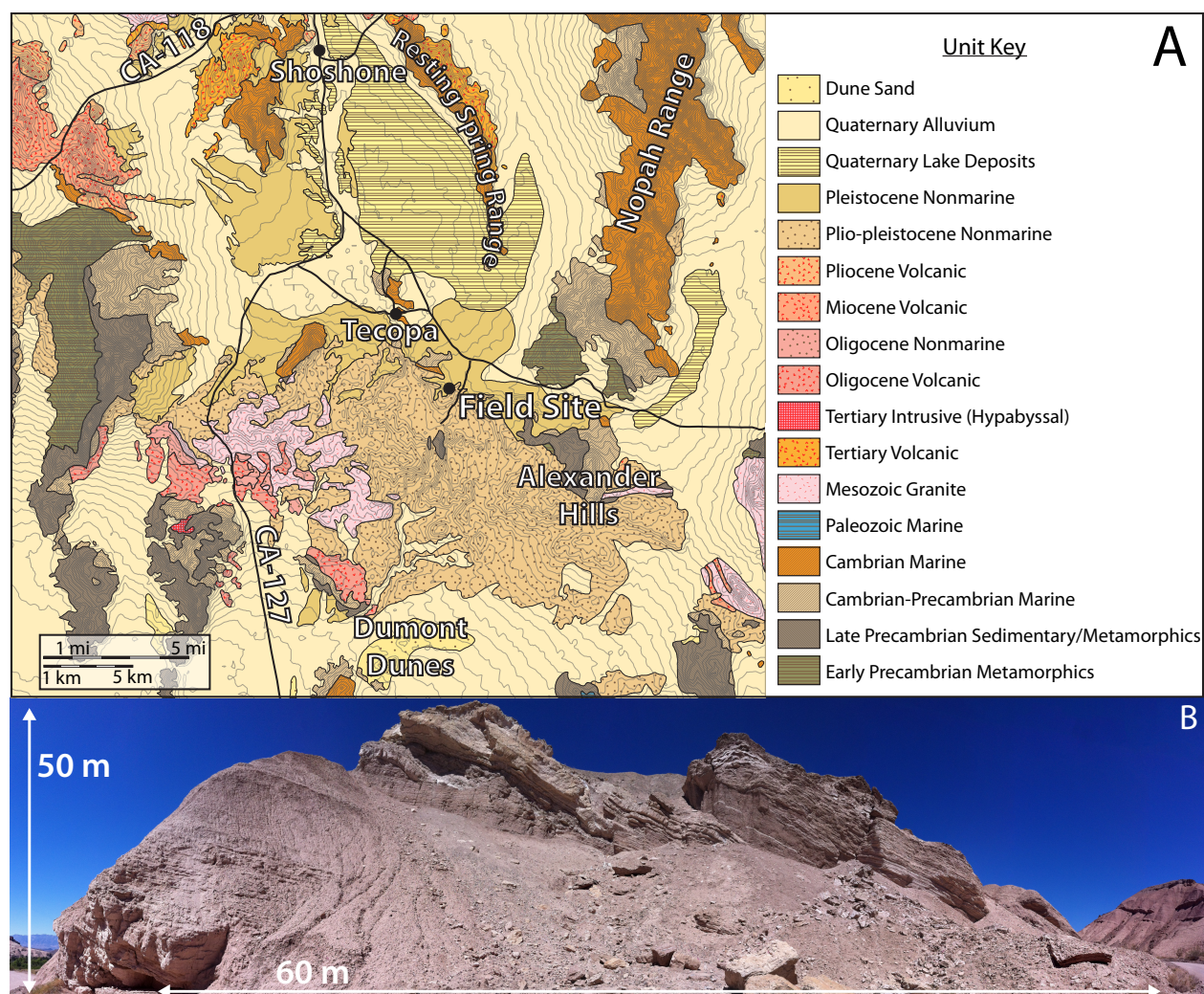


Figure 2-1. (A) A geologic map of the field site with 25-m contour intervals, modified from Jennings et al. (1962). (B) photomosaic of the field site outcrop located at $35^{\circ}48'25.5''\text{N}$ $116^{\circ}11'24.9''\text{W}$.

The Ultra Compact Imaging Spectrometer (UCIS; Van Gorp et al., 2014) was used to collect a spectral image cube of the outcrop over wavelengths of 400-2500nm and a resolution of 1.4 mrad/pixel from a distance of 35 m. This spectral image was then subset and resampled to the Mastcam-Z detector and band pass filters using the spectral resampling tool in ENVI to simulate Mastcam-Z multispectral imaging at an approximate distance of 193 m. These were used to create images of multispectral VNIR color variability of the outcrop, similar to what will be collected by Mastcam-Z. VNIR color differences were accentuated by using decorrelation stretches as is typical in analysis of Mars data (e.g. Farrand et al., 2006). Mastcam-Z spectra were simulated with data acquired by an ASD Fieldspec3 in the lab due to terrestrial atmospheric influences in the UCIS field data (e.g., a water vapor band at 940 nm) that will not be present on Mars. Representative individual

bulk spectra of rock hand samples with a spot size of ~1 cm were acquired over the wavelength range 350-2500 nm and subset and resampled to Mastcam-Z filter bandpasses.

2.3.2 SuperCam simulation

SuperCam is a Mars-2020 mast instrument which will provide laser-induced breakdown spectroscopy (LIBS), remote pulsed green Raman spectroscopy (532 nm excitation), passive Visible (VIS; 400-850 nm) and Infrared (IR; 1300-2600 nm) spectroscopy, color remote micro-imaging (RMI), and a microphone to record sound (Wiens et al., 2017). This suite of capabilities allows SuperCam to detect mineralogy (VIS, IR, and Raman spectroscopy), chemistry (LIBS), and textures/morphology (RMI) without sample preparation. LIBS and Raman acquisition are active techniques, utilizing pulsed lasers, and can be acquired at distances up to 7 m and 12 m, respectively, both at a spatial resolution of 0.7 mrad/spot. All other capabilities have no distance limitations other than atmospheric opacity. Passive VIS and passive IR have spatial resolutions of 0.7 mrad/spot and 1.15 mrad/spot and spectral resolutions of $\leq 12 \text{ cm}^{-1}$ and 30 cm^{-1} , respectively (Wiens et al., 2017). The RMI uses a Bayer-patterned CMOS detector to acquire color images with a field of view of 20 mrad and a resolution of 40 $\mu\text{rad/pixel}$ (Gasnault et al., 2015; Wiens et al., 2017).

RMI images were simulated using iPhone images taken from a simulated distance of 24 m from the outcrop (a simulated distance of 192 m). Passive spectroscopy from SuperCam was simulated using UCIS image-derived field spectra resampled to the wavelength range, spectral, and spatial resolution of the SuperCam VIS and IR spectroscopies. As with simulation of Mastcam-Z data, ASD spectra were used for detailed spectral analysis to avoid complicating terrestrial atmospheric effects. The SuperCam VIS spectral sampling of $<1 \text{ nm}$ is smaller than either UCIS (10 nm) or the ASD (1 nm), though known passive spectral absorptions are generally broader than 10 nm (Clark et al., 1990), and so we do not anticipate missing spectral features due to this difference. The SuperCam IR passive range of 1300-2600 nm extends slightly beyond the maximum range of UCIS and the ASD spectrometer, meaning that carbonate minerals, which have absorption bands centered from 2500-2600 nm, would be better characterized by SuperCam than the simulation instruments.

SuperCam LIBS data were simulated by data collected using the ChemCam testbed instrument at the Los Alamos National Laboratory (Clegg et al., 2017), and data reduction was completed using a simple model in an open-source, multivariate data reduction program termed PySAT (Anderson et al., 2017). Green Raman was simulated using a green Raman instrument at Caltech, a Renishaw M-1000 microRaman spectrometer. This Raman spectrometer is not a remote instrument, and so offers significantly higher detail and sensitivity than will be present on Mars-2020. The green Raman spectra were resampled to the SuperCam resolution of 10 cm^{-1} (Wiens et al., 2017). The Raman used at Caltech has a spatial resolution of $3\text{ }\mu\text{m}$ and, therefore, is able to target individual grains in a way that the SuperCam Raman instrument will not with its minimum spot size of approximately 1.5 mm at the $\sim 2\text{ m}$ mast height. Due to the active nature of Raman spectroscopy, downsampling the spatial resolution of the Renishaw M-1000 measurement is not possible. We do not anticipate significant spectral changes as a result of these differing resolutions, simply increased spatial resolution and decreased spatial footprint. A fluorescence background was subtracted from the green Raman data using a built-in cubic spline background removal tool in the WiRE program.

2.3.3 SHERLOC simulation

The Scanning for Habitable Environments with Raman and Luminescence for Organics and Chemicals (SHERLOC) instrument is an arm-mounted deep-UV (DUV) fluorescence and pre-resonance/resonance Raman spectrometer, which is co-boresighted to a $10\text{ }\mu\text{m}/\text{pixel}$ greyscale autofocus and context imager (Beegle et al., 2015). Additionally, a built-to-print copy of the Mars Hand Lens Imager (MAHLI, $0.30\text{ mrad}/\text{pixel}$; Edgett et al., 2009) has been added to the instrument (termed WATSON), allowing color imaging of samples (Beegle et al., 2017). A deep-UV laser with a spot size of $100\text{ }\mu\text{m}$ is scanned systematically across a $7\times 7\text{ mm}$ area to induce fluorescence, generating a compositional map of Raman and fluorescence spectroscopy, allowing the fine scale and bulk detection of organic compounds in a bulk material. This technique is typically able to detect $<10^{-6}$ weight fraction (w/w) concentrations of aromatics and $<10^{-4}$ w/w concentrations of aliphatics with a spatial resolution of $100\text{ }\mu\text{m}/\text{pixel}$ (Beegle et al., 2017). The deep-UV laser excitation wavelength of 248.6 nm was chosen to avoid mineral fluorescence, which occurs at wavelengths longer than 360 nm (Beegle et al., 2016). SHERLOC's capabilities allow characterization of the organic content and some mineral contents of a given sample, rastered and mapped spatially to reveal

textures and patterns that can indicate the presence of potential biosignatures in the rock (Abbey et al., 2017).

SHERLOC-like spectra were acquired using a JPL prototype breadboard instrument named MOBIUS. Both instruments use pulsed 248.6 nm NeCu lasers (Photon Systems Inc.) as their excitation sources, but differ in their spectral resolution and optical focusing. With SHERLOC, DUV Raman and Fluorescence spectra are collected simultaneously using a 1200 lines/mm grating (resolution: 0.05 nm or 8 cm⁻¹), while MOBIUS collects Raman and Fluorescence spectra separately, using 1800 and 300 lines/mm gratings respectively (resolutions: 3.5 cm⁻¹ and 0.16 nm). MOBIUS lacks the autofocus feature that provides SHERLOC a ± 8 mm tolerance to surface roughness (Beegle et al., 2017) and instead has a depth of focus of ± 500 μ m. Therefore, the samples used in the laboratory were cut using an MK Diamond Products MK-100 Tile Saw to produce a flat face or carefully selected for a smooth surface. These sample preparation procedures will not be necessary during the Mars-2020 mission, though an abrasion tool is included on Mars-2020 for analysis of particularly weathered or rough surfaces. A commercially available DSLR camera was used to take context images of samples before measurement with MOBIUS, providing context images akin to those that will be acquired by WATSON of targets on Mars and used for inter-instrumental comparisons. Other WATSON images (0.30 mrad/pixel) are replicated using an iPhone 4s (0.32 mrad/pixel) to image individual samples in a laboratory setting at high-resolution.

2.3.4 PIXL simulation

The Planetary Instrument for X-Ray Lithochemistry (PIXL) is an arm-mounted micro-focus X-ray fluorescence spectrometer. PIXL directs a beam of 28 kV energy X-rays onto a sample and then examines a spectrum of intensity as a function of energy (Allwood et al., 2015). PIXL will be capable of rastering across a 25 mm² area at 120 μ m/spot resolution to determine elemental abundance and distribution, correlated to visible textures in the rock imaged with a 50 μ m/pixel micro-context camera with a field of view of 29 mm x 36 mm and illumination provided by an LED array (Allwood et al., 2015, 2016). The geometry of the PIXL instrument also allows rudimentary X-ray diffraction patterns to be collected; this capability is still under development (Schofield et al., 2017) and is not simulated in this study. The XRF measurements will allow determination of relative

and absolute elemental abundances on small spatial scales, which will enable detection of past conditions that affect habitability and potential biosignature preservation.

Simulated PIXL data were acquired using a commercially available Horiba XGT-7200 micro-XRF at the Natural History Museum of Los Angeles, which was adjusted to acquire data at conditions similar to the specifications of PIXL (e.g., similar spot size, X-ray energy). Both instruments use a rhodium anode. While PIXL will have the ability to detect absolute abundances by applying a ground-based calibration for quantitative analysis of the measured spectra (Allwood et al., 2015), the data collected with the Horiba only provides relative abundances.

2.3.5 Field site and ground truth data acquisition

Table 2-2. Unit names from mapping using both ground truth data (Figure 2-2) and Mars-like data (Figure 2-4). The first letter of each name refers to texture. Names from ground truth mapping use a lower case second letter and refer to a geologic description, while the Mars-mapped units use an upper-case second letter and refer to the coloration of the unit

Ground Truth Mapping Unit Name	Mars-like Mapping Unit Name	Figures with Additional Mars-like Data
Qa (Quaternary Alluvium)	SS (Scree Slope)	Figure 2-6
Lm1 (Layered Mudstone 1)	LB (Layered Brown)	Figure 2-5c Figures 2-5b, 2-6, 2-7, 2-10 Figures 2-5a, 2-6, 2-7, 2-9 Figures 2-5b, 2-6, 2-7
Lm2 (Layered Mudstone 1)	TL1 & TL2 (Thick Light)	
Mc (Massive Carbonate)	ML (Massive Light-toned)	
Lm3 (Layered Mudstone 1)	MD/LD (Massive/Layered Dark)	
Lg (Layered Gypsum)	LL (Layered Light-toned)	

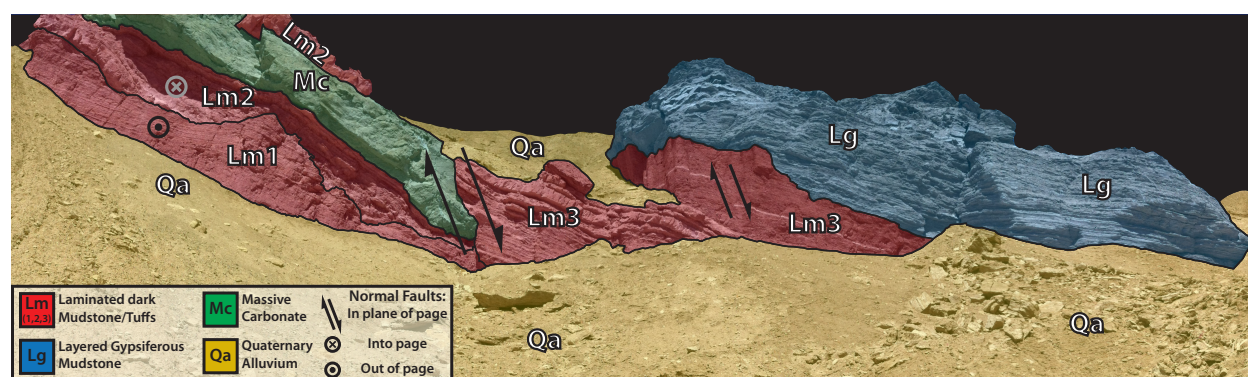


Figure 2-2. A unit map of the outcrop used in this study. See text for a detailed description of the geology of the site.

A field site in the Tecopa Basin near the China Ranch oasis, located at 35°48'25.5"N 116°11'24.9"W, was selected as the Mars-analog site (Figure 2-1). This locality is a Tertiary

paleolake deposit (Hillhouse, 1987) with interbedded volcanic ashes and travertines. The mineralogy includes primary phases of quartz, feldspars, and pyroxenes, and secondary phases and chemical sediments that include phyllosilicates, sulfates, carbonates, chalcedony, and iron oxides. Several samples contained a significant percentage of less crystalline materials, which include smectite clays and/or x-ray amorphous components (Table 2-3). The strong 001 peaks and lack of a broad amorphous peak as observed in glasses and nanocrystalline alteration phases lead us to interpret that most of these materials are smectite clays. This mineralogical assemblage and especially the paleolacustrine environmental setting is relevant to anticipated geological observations at the Jezero landing site selected for Mars-2020 (Ehlmann et al., 2008; Fassett & Head, 2005; Goudge et al., 2015). The site was chosen over other nearby sites with basaltic lavas that are more directly mineralogically analogous because of the record of multiple environmental processes presented in multiple units with various mineralogies at a single outcrop. We discuss the implications of instrument suite capabilities for more basalt-rich lithologic units in section 2.5.2.1.

In order to compare the data and resulting geologic history generated from the simulated Mars-2020 instruments to the “true” geologic history of the field site, a ground truth dataset was generated and used to construct a geologic history for this specific outcrop. The ground truth data set includes 1) background literature on the field site and the surrounding geology from prior researchers (e.g., Hillhouse, 1987; Jennings et al., 1962; Mason, 1948) 2) spectral analyses using the full resolution of UCIS, 3) field observations and geologic mapping (Figure 2-2) combined with extensive sampling guided by UCIS spectral analyses, 4) high resolution spectral analyses using spectra generated from an ASD Fieldspec3, and 5) X-ray diffraction patterns and derived mineralogy and flux fusion lithochemistry provided by Actlabs analytical services (Table 2-3 and 2-4).

High-resolution ASD spectra were acquired using a contact probe with a built-in lightsource. White reference calibrations were performed after every five analyses. The assignments of spectral features in both the Mars-like data and ground-truth data were made by comparison to spectral libraries and by direct expert analysis of specific spectral features in reference to the primary literature. The libraries used in this study include the RRUFF database for Raman spectroscopy and the JPL VNIR spectroscopy library (Grove, 1992). These libraries will be used during the Mars-

2020 mission for the same purpose. Standard reference libraries for fluorescence spectroscopy are not available, as discussed below.

Table 2-3. Ground-truth XRD results on select samples (all measurements in weight %). Relative accuracies are approximately $\pm 3\%$ (Hillier, 2016). Individual XRD patterns are available in the supplemental data.

Sample Number	CR002	CR003	CR008	CR012	CR018	CR019	CR025	CR026	CR028	CR029	TM	MB
Source Unit (simulated Mars mapping)	MD/LD	Unmapped highlands	TL1	LL	LL	Unmapped highlands	ML	ML	SS	MD /LD		SS
Source Unit (ground truth mapping)	ML3 Light layer	Lag Deposit	ML2	GM	GM	Nearby highlands	MC	MC	Qa1	ML 3		Loose Cobbles
Quartz	0.9	53.2	1.6	0.6	0.3	16.3	27		1.5	7.6	100	2
Tridymite							2.7					
Plagioclase	32.1	20.1	4.7			5.8			6.6	6.5		25
K feldspar						3.9				17.4		3.2
Diopside												3.7
Orthopyroxene										3.9		
Muscovite		21.2	3.1			7.6			4.3	8.1		6.6
Chlorite		5.5				0.8						11.2
Amphibole												23.7
Clinozoisite												9.6
Clinoptilolite	2.6											
Calcite			63.7			43.5	57.8	100	67.8	13.2		
Dolomite						12.3						
Gypsum				87.2	86.4							
Anhydrite					6.5							
Celestine	2.8											
Smectite and Amorphous	61.6		26.9	12.3	6.8	9.8	12.5		19.7	43.2		15.1
Total	100	100	100	100.1	100	100	100	100	99.9	99.9	100	100.1

Based on the ground-truth observations, the geologic history of the outcrop involves the deposition in a lacustrine environment of flat-lying clay-rich mudstones, which are finely laminated to massive and contain ~50 wt% smectite clays (mapped as units Lm1-3 in Figure 2-2). These mudstones are interspersed with felsic tuffs, which are weathered to have approximately 60 wt% smectite and 5 wt% zeolite. The smectite abundances described here are based on the abundance of smectite/amorphous reported in Table 2-3, the presence of a 001 peak, and the lack of an amorphous hump in the individual XRD patterns (Figure 2-14). These tuffs are of varying thicknesses and grainsizes, indicating different volcanic sources at different distances. The ash beds appear to have been deposited subaqueously in sequence with the mudstones. Bedding of larger grainsize up to pebble conglomerates exist throughout the sequence and likely indicate major storm events. Extensive faulting has resulted in tilting, offset, and obscuration of the exact stratigraphic relationships between many of these strata, though a distal lacustrine environmental history appears to have been the dominant setting throughout deposition. A normal fault with a sense of motion into the plane of the page separates mudstone units Lm1 and Lm2. A massive travertine carbonate (unit Mc in Figure 2-2) with associated chalcedony exists as a lens within Lm2. The fenestral textures within the carbonate likely record microbial mat formation (Gandin & Capezzuoli, 2014). A large normal fault with an offset greater than the total exposed stratigraphic height within the outcrop has displaced upward the entire left-hand portion of the outcrop (units Lm1-2 and Mc) to a higher apparent stratigraphic height (i.e., the continuing strata cannot be traced in the outcrop; offset is perhaps hundreds of meters; Hillhouse, 1987). To the right of this fault mudstone/tuff laminae continue, mapped as Lm3. A disconformity exists at the top of the mudstone unit Lm3, above which interbedded mudstone and gypsum with fewer tuff beds was deposited (unit Lg in Figure 2-2), likely indicating a more saline lake environment with episodic drying. The mudstone strata within unit Lg either lack laminations or they exist at such a fine scale that the mudstone beds appear massive. Extensive dissolution and recrystallization has in many beds re-precipitated the gypsum into pure sparry selenite within unit Lg which exhibits little evidence of faulting.

2.4 Results of Mars-2020 payload simulation

2.4.1 Remote sensing

2.4.1.1 Image-based remote analysis

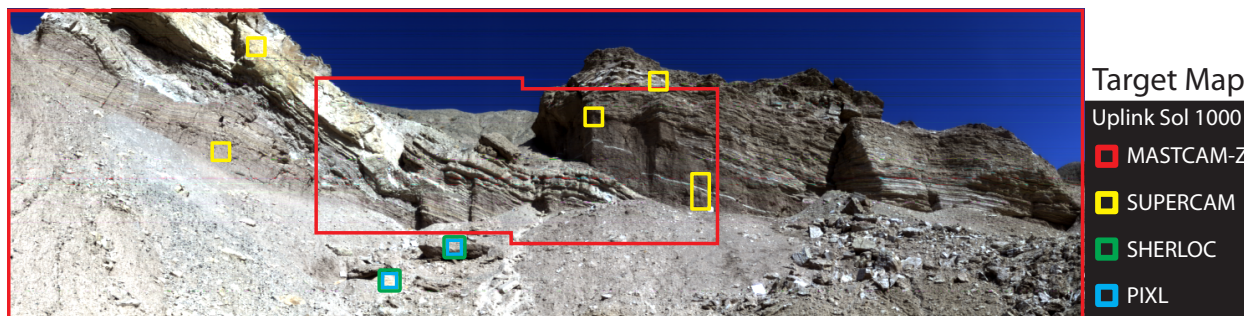


Figure 2-3. Simulated Navcam drive direction mosaic from a distance of 140 m. Examples of targets used in simulated remote sensing and proximity science are shown.

The simulated Navcam drive direction mosaic from a distance of 140 m (Figure 2-3) shows an outcrop composed of a number of intriguing units based on the textural and color differences present in the image. The mineralogical interpretations of the units in Figure 2-4a are described in section 2.4.1.2. All units dip towards the right of the image. A scree slope (SS) covers the lowest stratigraphic units and portions higher on the outcrop. The left-hand side of the outcrop has at least three units and the right-hand side has two stratigraphically higher units. The lowermost unit on the left-hand side is a layered brown (LB, all unit labels designated by Texture and Color) unit with layers a few centimeters in thickness. An apparent disconformity, possibly indicating subaerial erosion, separates this lower unit from a more thickly and irregularly bedded and folded light-toned (thickly-bedded light, TL1) unit. A massive light-toned unit with color variation between white, yellow, and orange tones (massive light-toned unit, ML) lies above TL1. A second thickly-bedded light unit (TL2) is stratigraphically at the top of the left side of the image. To the right of the image, there is a massive dark brown (massive dark, MD) unit containing a single thin, light-toned bed which runs parallel to the large-scale layering, suggesting that the MD unit may be laminated at a scale too fine to observe at the resolution of the simulated Navcam image (Figure 2-3). A unit with variable dark and light coloration (light-toned layered unit, LL) overlies the MD unit, with beds a few cm in thickness, slightly thicker than the beds in the LB unit. The LL unit exhibits alternating recessed bedding, possibly due to differential weathering, which could indicate that the unit has been

exposed to weathering processes for a longer period than the other units. However, the recent scree below this unit is composed of larger blocks of a similar color, which may instead indicate that the LL unit is compositionally distinct from the lower units and contains more fissile material.

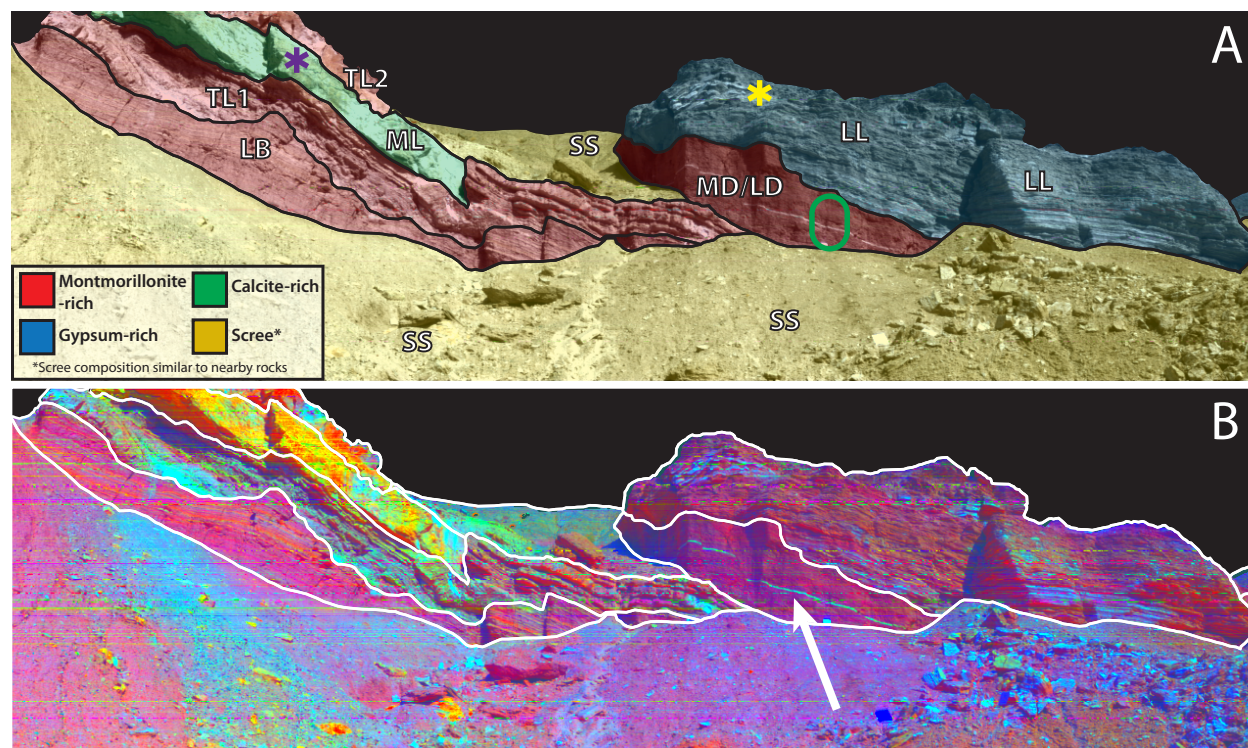


Figure 2-4. A) A unit map derived from the remote sensing data acquired while approaching the outcrop (i.e. before proximity science and drilling). The inferred mineralogy is from the data shown in Figure 2-5. Unit abbreviations: LB = layered brown, TL1 & TL2 = thickly-bedded light, ML = massive light, LD = laminated dark, LL = layered light-toned, SS = scree slope. Green oval, purple asterisk, and yellow asterisk denote location of data shown in Figure 2-5. B) Mastcam-Z-like DCS from UCIS data with bands at 676, 527, and 445 nm (RGB), showing variability in Fe-related phases in the outcrop. Unit outlines are delineated from a combination of color, texture, and DCS data as described in the text. A white arrow notes the location of a layer of ash (See section 2.5.1).

Based on the information available in the Navcam image, a Mastcam-Z color drive direction mosaic and zoomed Mastcam-Z color image would most likely be acquired over the area covered by the Navcam image to allow selection of remote sensing targets for more detailed mineral and chemical compositional investigations and vet areas accessible for future in-situ science. This study does not attempt to replicate traversability challenges for the Mars-2020 rover, so all desired targets and samples were considered “accessible” for the purposes of data collection (see section 2.5.3 for operational considerations). A Mastcam-Z multispectral image would also be acquired over a subset of the drive direction, and Mastcam-Z’s zoom capability would be applied in areas where the textural

and stratigraphic relationships in the image are not clearly visible in the unzoomed imaging (Figure 2-3). SuperCam would likely target all of the major units described above to determine composition using the passive techniques (i.e., VIS, IR, and RMI) from this long distance. Preliminary proximity science targets could also be selected using the Mastcam-Z drive direction.

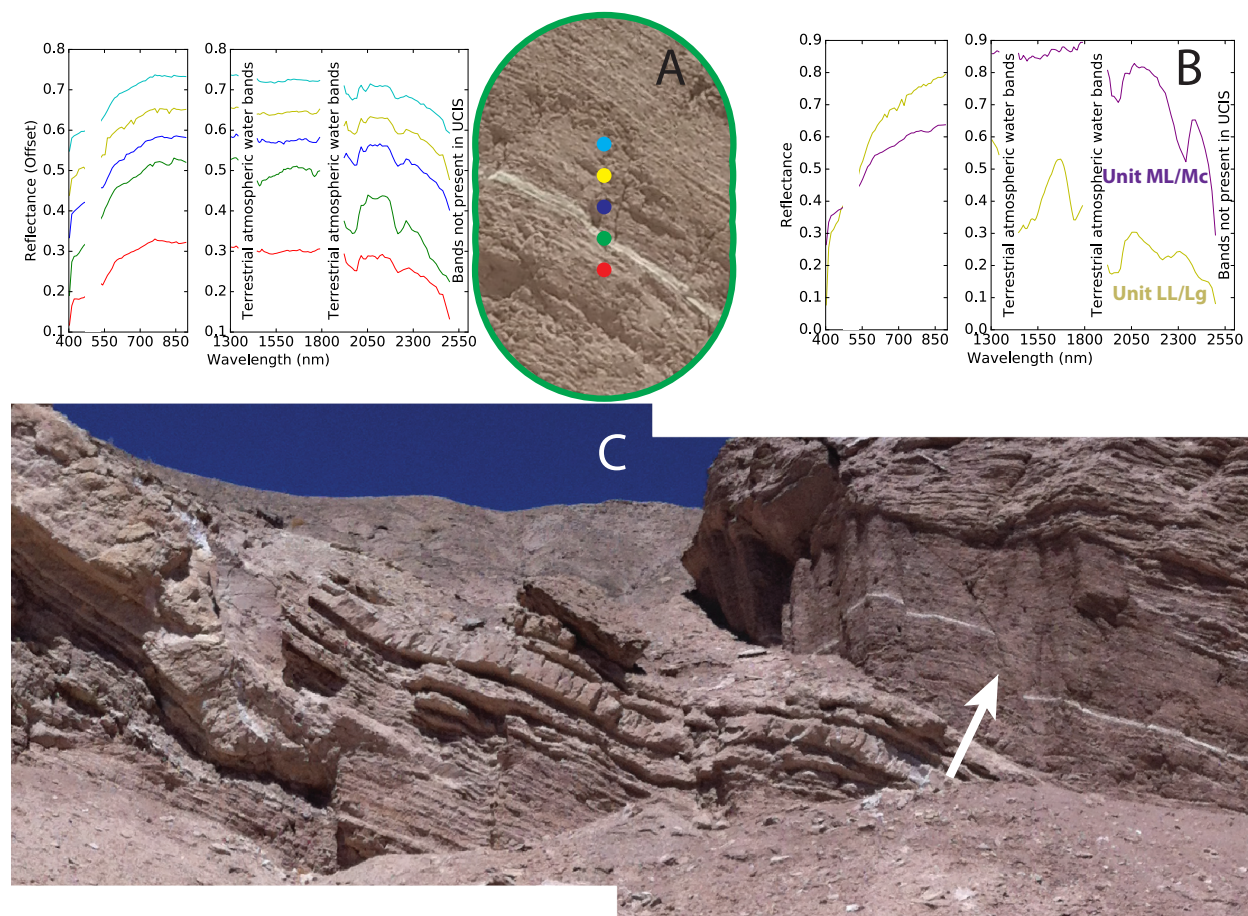


Figure 2-5. Select data from locations shown targeted in Figure 2-4. A) SuperCam transect through unit MD/LD/Lm3, showing a discrete layer with an increased 2200-nm Al-OH absorption from montmorillonite. While SuperCam does not cover much of the 530 nm region, the shallow spectral slope of the passive spectrum from this layer from 535-600 nm seen in the Mastcam-Z simulated data in Figure 2-4 suggests a decreased ~535 nm absorption from iron oxides. The simulated RMI resolution is approximately half that of the true RMI. The color of the spectra correspond with the color of the circles in the RMI, which are accurate to the spot size of a SuperCam passive measurement. B) Example reconnaissance spectra identifying the presence of carbonate (purple from unit ML/Mc, upper left SuperCam target in Figure 2-4) and gypsum (yellow from unit LL/Lg, upper right SuperCam target in Figure 2-4) in units ML and LL, respectively. SuperCam does not have spectral coverage 475-535 nm. This wavelength range is therefore not depicted in (A) or (B). C) Mastcam-Z zoomed image of a fault (shown with white arrow) and laminations in unit MD/LD.

A simulated Mastcam-Z multispectral image is shown in Figure 2-4b, which depicts a decorrelation stretch (DCS) of bands 676, 527, and 445 nm (RGB; Farrand et al., 2006). In this color combination, rocks with spectral features indicative of iron oxides appear red due to a strong absorption near 535 nm (Morris et al., 1985). Cyan colors indicate fewer iron oxides or those of different mineralogy, i.e., the TL1 unit and the thin light bed in the MD unit. The spectral differences mapped through this DCS suggest compositional differences between the thickly and finely bedded units and the existence of discrete iron oxide-bearing zones of MD and LL (Figure 2-4b). The ML unit on the left near the top of the section is unique in this color combination and stands out as having no iron-oxide related features. The zoomed Mastcam-Z images (Figure 2-5c) indicate that the MD unit, which was apparently massive, actually has visible fine-scale lamination in the zoomed image at the sub-centimeter scale, and should be re-termed the laminated dark (LD) unit.

2.4.1.2 Spectra-based remote analysis

Selected single spectra from outcrop units, resampled to Mastcam-Z multispectral resolution, show variations in iron oxidation, mineralogy, and crystallinity (Figure 2-6). Fe oxides are present in multiple units, e.g. LD mudstone laminae and the scree slope, based on absorptions near 535 nm (Morris et al., 1985). Other units (or portions of units) are notable for their lack of Fe oxides, e.g. the bright bed in LD, select beds in LL, and most of ML. The LL unit spectra occasionally displays a downturn in the last Mastcam-Z filter band, indicative of hydration (Rice et al., 2010). Outside of these specific spectra, differences generally involve subtle shifts in the 535 nm band position and are difficult to detect by eye, especially given the relative weakness of Fe-related absorptions in the scene. The DCS enhances these spectral differences in a spatial context, allowing these slight differences to inform the delineation of putative units within the scene.

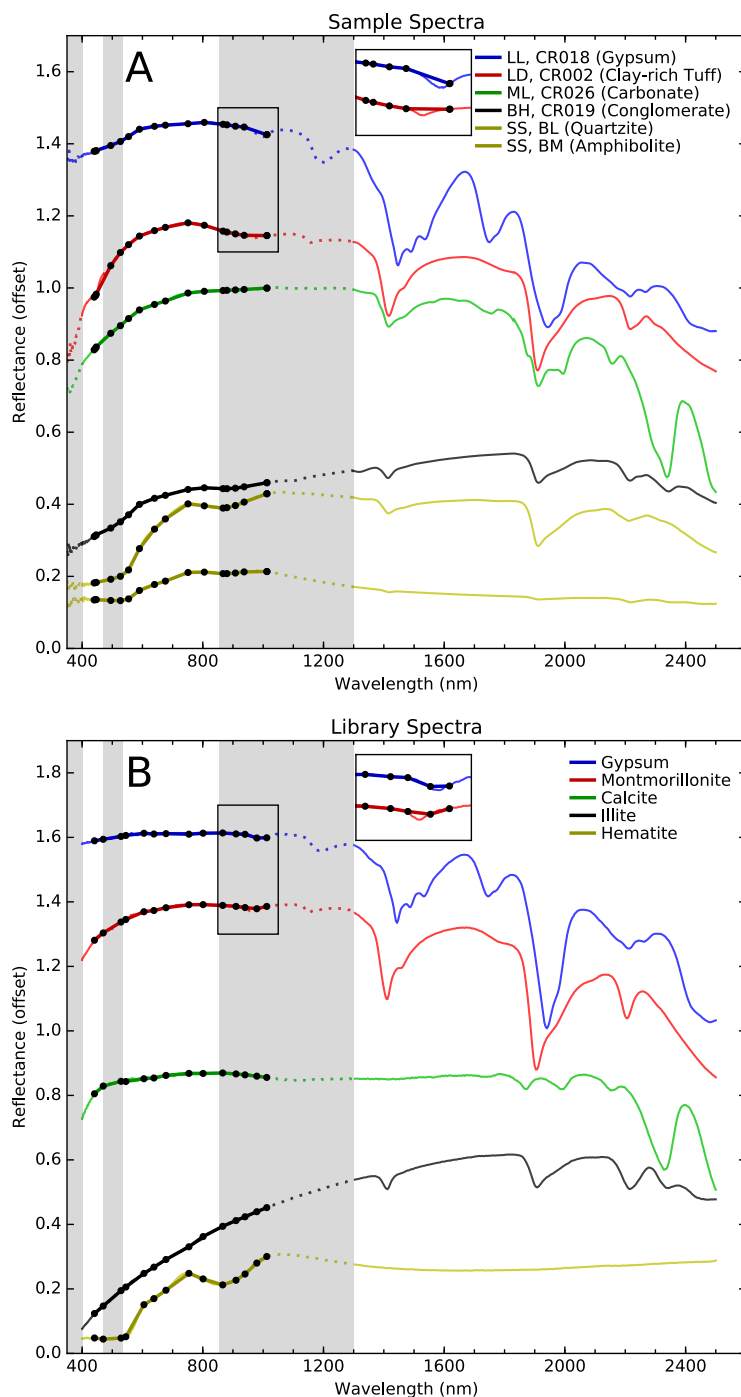


Figure 2-6. (A) Simulated Mars-2020 passive spectroscopy data acquired with an ASD spectrometer. Chemistry, mineralogy, and source units for all samples are given in Table 2-2. Mastcam-Z multispectral data are shown overplotted with black dots indicating filter locations. Light gray regions with dotted spectra indicate a lack of SuperCam passive coverage. The ASD spectra extend to 2600 nm, while SuperCam passive IR will extend to 2600 nm. Detail of the resolution of the hydration feature near 1000 nm for gypsum- and montmorillonite-bearing rocks is shown in the blow-up box. (B) Library spectra corresponding to the mineral components in (A). Spectra are from the JPL spectral library (Grove et al., 1992).

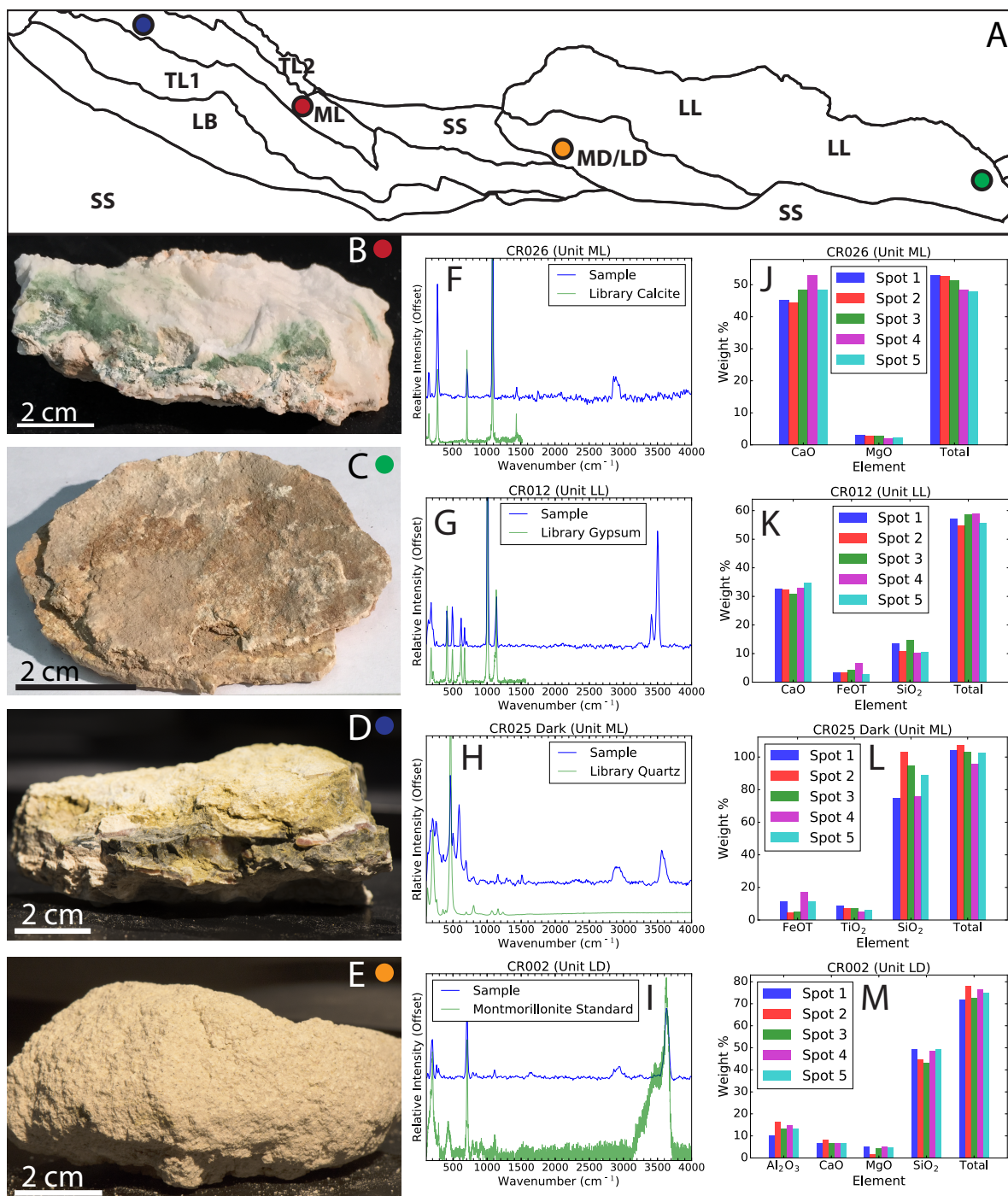


Figure 2-7. Close-approach data of the outcrop locations in (A) collected by simulated SuperCam, showing (B-E) RMI images for texture; images are representative and exact location of spectra are not shown (visible green areas in panel B are chlorophyll-bearing and were avoided in all analyses), (F-I) green Raman spectra for mineralogy, and (J-M) LIBS chemistry. Except for sample CR002, Raman library spectra (F-H) are taken from the RRUFF database and therefore extend only to 1500 cm^{-1} . CR025 Dark (H) contains peaks that could not be matched with library spectra. Broad peaks near 3500 cm^{-1} are related to OH/H₂O. LIBS oxide abundance data not shown are indistinguishable from 0 wt. % within uncertainty; see Anderson et al. (2011) for a detailed discussion of LIBS uncertainties.

Passive IR spectra simulating SuperCam indicate the presence of phyllosilicates in each of the brown layered (LB), thickly bedded (TL1&2), and layered dark (LD) units based on the presence of a metal-OH ~2200 nm vibrational absorption (e.g. Figure 2-5a). The band center location of 2210 nm is diagnostic of Al-OH, indicating the presence of montmorillonite (Clark et al., 1990). These units all have weak hematite-like 535 nm features in the VIS range (Morris et al., 1985), which are strongest in the LD unit. The ML unit has a strong 2340 nm absorption and downturn toward 2500 nm with no other diagnostic features (Figure 2-5b), suggesting that this unit is calcite-bearing (Hunt & Salisbury, 1971). The light-toned thin bed in the LD unit has similar spectral properties to the rest of the unit, though band depth trends indicate relative enhancement of montmorillonite compared to iron oxide (Figure 2-5a). The LL unit above the LD unit shows a mix of gypsum and montmorillonite spectral features (Figure 2-5b); lower in the unit, the montmorillonite-like spectral features dominate, which grades to progressively more gypsum-like spectra in the higher, lighter-toned units. Gypsum is detected by the diagnostic sharp triplet at 1400 nm and absorptions at 1700 nm and 2200 nm (Hunt et al., 1971).

Upon arrival within a few meters of the outcrop, SuperCam's active techniques (Raman and LIBS) can be employed to further understand the mineralogy and determine the chemistry of the targets. Peaks in green Raman spectra confirm the presence of large amounts of calcite and gypsum in the ML and LL units (Figure 2-7). Montmorillonite was not detected in comparison with available spectral libraries; however, hydration-related features in literature spectra of clay minerals (Wang et al., 2015) are apparent. A montmorillonite standard analyzed on the same Raman instrument resulted in a good match to spectra from the clay-rich units (Figure 2-7i), indicating that clays are detectable with green Raman (at least with the in-situ unit for this test), given adequate spectral libraries for comparison.

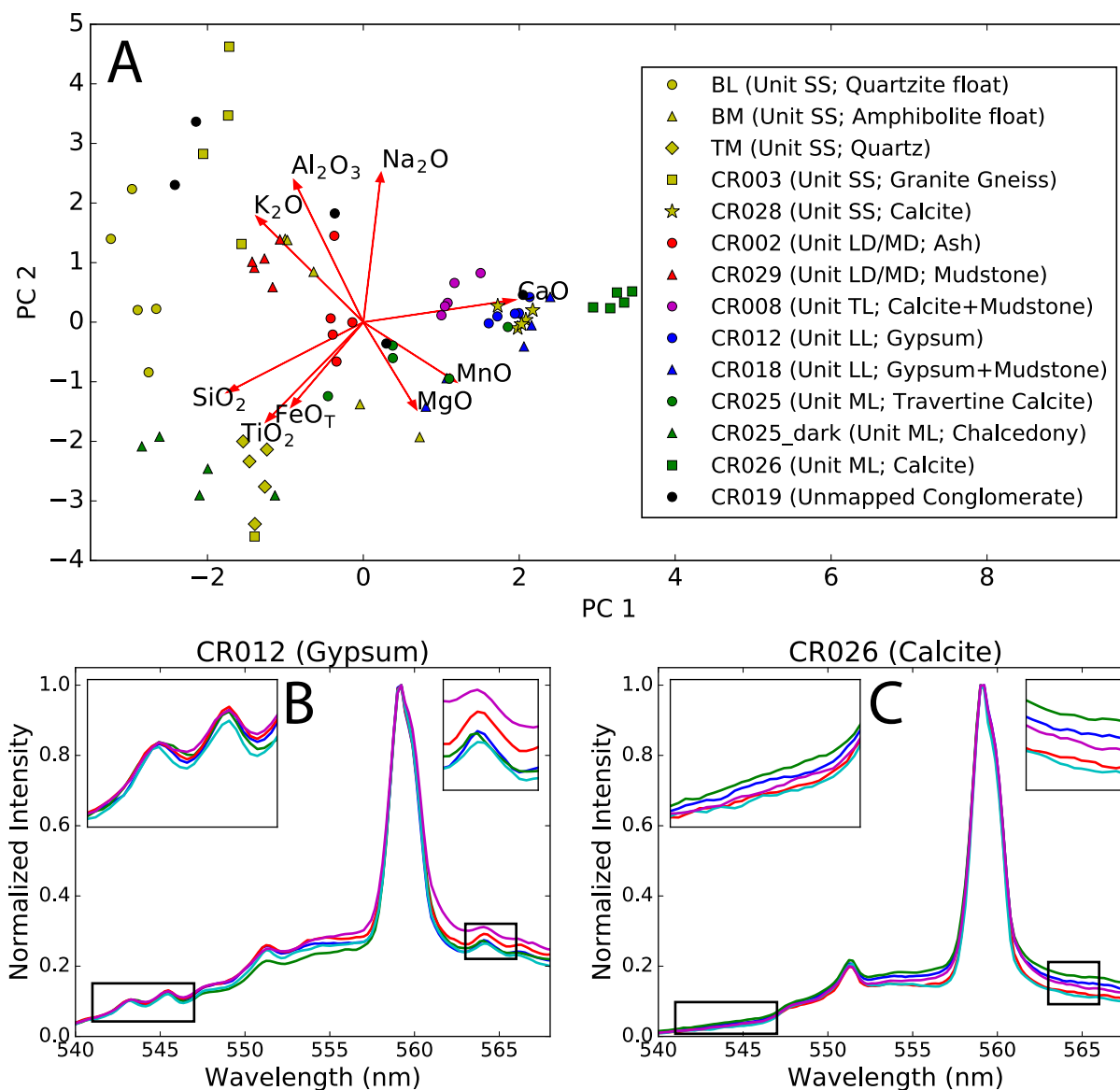


Figure 2-8. (A) principal component analysis-based grouping of LIBS data. Individual LIBS spectra demonstrate the differentiation of (B) gypsum and (C) calcite using the small S peaks at 543, 545, and 563 nm. Calcite and gypsum are otherwise indistinguishable given just their bulk Ca-rich composition. The large peak at ~559nm is calcium.

Table 2-4. Ground-truth TOC and lithochemistry results on select samples (measurements in wt%). Detection limits 0.01 wt% for all except MnO₂ and TiO₂, which have detection limits of 0.001 wt%

	CR002	CR003	CR008	CR012	CR018	CR019	CR025
TOC	0.59	0.56	0.83	0.70	1.63	1.46	0.92
TOC ±	0.15	0.15	0.19	0.16	0.10	0.12	0.13
SiO ₂	52.5	74.2	16.6	6.2	2.6	30.7	43.5
Al ₂ O ₃	16.7	11.1	4.3	1.7	0.6	4.7	0.3
FeO _T	4.02	4.32	1.88	0.83	0.22	1.65	1.01
MnO	0.07	0.07	0.22	0.02	0.01	0.03	0.03
MgO	3.21	1.29	1.33	0.56	0.31	2.83	0.35
CaO	3.86	0.79	39.87	29.10	31.84	30.42	29.94
Na ₂ O	2.69	1.92	0.56	0.13	0.07	0.58	0.06
K ₂ O	0.92	2.26	1.05	0.38	0.11	1.50	0.14
TiO ₂	0.59	0.47	0.18	0.07	0.03	0.21	0.01
P ₂ O ₅	0.19	0.11	0.09	0.03	0.03	0.08	0
C	0.03	0.12	8.08	0.19	0.02	7.03	6.48
S	0.48	0.01	0.04	16.10	18.20	0.03	0.03
Cl	0.04	0.02	0.06	0.02	0.01	0.02	0.01
LOI	14.5	2.1	32.8	25.4	20.9	26.8	24.7
Total	99.3	98.7	98.9	64.4	56.8	99.4	100.0
	CR025	CR026	CR028	CR029	TM	BM	
TOC	0.92	3.53	0.65	0.74	0.54	0.55	
TOC ±	0.13	0.33	0.16	0.15	0.15	0.14	
SiO ₂	43.5	1.0	16.8	47.5	96.1	48.2	
Al ₂ O ₃	0.3	0.2	3.7	12.6	1.0	14.9	
FeO _T	1.01	0.09	2.29	4.54	2.14	14.00	
MnO	0.03	0.00	0.46	0.13	0.01	0.21	
MgO	0.35	0.51	2.21	2.55	0.08	5.58	
CaO	29.94	54.51	37.86	9.49	0.19	8.58	
Na ₂ O	0.06	0.03	0.38	1.31	0.02	2.66	
K ₂ O	0.14	0.02	0.33	3.97	0.11	1.62	
TiO ₂	0.01	0.01	0.14	0.58	0.08	1.83	
P ₂ O ₅	0	0.04	0.05	0.23	0.03	0.24	
C	6.48	11.40	8.08	1.82	0.03	0.03	
S	0.03	0.09	0.04	0.29	0.04	0.04	
Cl	0.01	0.04	0.10	0.06	0.01	0.07	
LOI	24.7	43.0	34.1	15.5	0.6	2.7	
Total	100.0	99.4	98.4	98.4	100.4	100.4	

Principal components analysis of the reduced LIBS elemental chemistry data (Figure 2-8) clearly differentiates the gypsum and calcite samples from the silicates, while the silicates are distributed according to their major chemical constituents (e.g. limbs with increasing K_2O and Al_2O_3 suggest the presence of K-feldspar or micas). LIBS data show elemental compositions consistent with the evaporite minerals detected via VIS/IR and Raman spectroscopy: CaO present at ~30 wt% (gypsum, unit LL) and ~50 wt% (calcite, unit ML) level with no other major elements detected above ~5 wt% and major-element (oxides of Si, Ti, Al, Fe, Mg, Ca, Na, K) totals below 55 wt% (Figure 2-7). Gypsum and calcite can be distinguished by the presence or lack of relatively weak sulfur peaks at ~545, ~547, and ~563 nm to differentiate these two CaO-dominated minerals (Figure 2-8). The gypsum sample (unit LL) has slightly higher than expected FeO_T and SiO_2 , which are likely a result of clastic silicate and oxide minerals trapped in a primarily gypsum matrix, or could be a result of the relatively simple data reduction model used for LIBS in this study (discussed in section 2.5.2.2 below). LIBS analysis of the clay-rich detrital sediments (sample CR002, unit LD) reveals aluminum-rich compositions with some additional potassium and calcium beyond what would be expected for pure montmorillonite, likely indicating the presence of minor gypsum, plagioclase and K-feldspars, illite, or muscovite (Table 2-5). The total elemental wt% measured in the typical mudstone is around 85%, potentially low due to the water of hydration present in the clay minerals or other volatile species, not quantified by this LIBS analysis. The loss-on-ignition for typical mudstone samples was ~15 wt% in ground-truth lithochemistry analyses, well in line with this hypothesis (samples CR002 and CR029 in Table 2-4). Point-to-point variability within the rasters is low in individual beds of the mudstone LIBS data (generally within 5%, and almost always within 10%; Table 2-5, Figure 2-7j-m), indicating relatively homogenous composition.

Table 2-5 (continues next page). Complete LIBS results (wt%); 5 points taken on each sample.

Unit	Sample	Al ₂ O ₃	CaO	FeOT	K ₂ O	MgO	MnO	Na ₂ O	SiO ₂	TiO ₂	Total
SS	BL	10.8	1.1	1.2	7.8	-0.5	-4.6	1.9	69.6	9.7	97.1
SS	BL	14.7	-0.8	2.3	8.8	0.4	-4.8	1.7	77.3	4.1	103.9
SS	BL	6.8	0.2	-0.8	5.8	0.7	-3.5	0.5	81.4	9.7	100.7
SS	BL	6.5	0.7	1.8	6.0	0.5	-4.3	0.6	76.9	9.8	98.6
SS	BL	7.7	1.7	21.3	3.2	0.5	-3.9	1.2	49.0	8.2	88.9
SS	BM	4.6	14.5	6.0	2.8	10.0	-5.5	-0.8	40.0	4.7	76.4
SS	BM	8.9	13.2	7.9	-0.4	9.9	-2.5	-0.5	35.6	4.8	77.0
SS	BM	17.9	6.5	5.3	2.7	3.7	-5.2	2.3	44.8	2.9	80.9
SS	BM	17.1	8.9	4.0	3.7	4.0	-5.3	1.4	44.9	2.7	81.2
SS	BM	16.7	8.3	6.1	1.7	4.4	-4.8	1.7	42.6	2.9	79.6
MD/LD	CR002	10.3	6.9	-1.4	0.5	5.0	-4.1	-1.2	49.4	6.3	71.8
MD/LD	CR002	16.3	8.4	3.5	1.2	1.8	-3.2	2.8	44.6	2.7	78.1
MD/LD	CR002	13.4	6.9	1.4	0.9	4.5	-2.8	0.3	43.4	4.6	72.5
MD/LD	CR002	15.1	6.8	0.2	1.3	5.1	-4.1	-0.6	48.5	4.4	76.7
BL	CR002	13.4	6.6	0.0	0.8	5.0	-4.1	-0.8	49.3	4.9	75.0
SS	CR003	28.9	1.7	5.0	5.2	1.4	-4.1	4.4	48.8	1.3	92.6
SS	CR003	22.8	3.6	3.6	7.7	1.8	-5.2	1.5	40.9	2.4	79.2
SS	CR003	33.9	2.7	2.6	5.6	1.0	-5.1	5.2	52.6	-0.9	97.6
SS	CR003	20.9	4.1	5.5	5.0	2.8	-2.4	1.9	35.6	6.5	79.9
SS	CR003	-3.2	-1.1	7.1	0.4	4.8	-1.0	-3.4	103.3	7.9	114.7
TL1	CR008	7.4	23.6	1.1	2.1	5.2	-3.0	0.1	32.9	1.3	71.0
TL1	CR008	5.6	29.5	0.8	2.4	4.4	-2.7	1.1	26.2	0.5	67.9
TL1	CR008	6.8	24.5	2.4	2.0	4.6	-2.7	0.5	29.1	2.1	69.3
TL1	CR008	7.2	26.5	1.5	2.4	4.5	-2.9	0.7	29.4	1.1	70.6
TL1	CR008	5.8	26.8	2.7	1.8	4.3	-2.9	0.3	26.8	2.9	68.3
LL	CR012	4.1	32.7	3.3	0.3	3.2	-2.5	0.3	13.6	2.2	57.2
LL	CR012	3.8	32.3	3.6	0.1	2.8	-1.3	0.7	10.9	1.9	54.8
LL	CR012	4.6	30.9	4.2	0.4	3.3	-2.2	0.2	14.9	2.3	58.7
LL	CR012	3.8	32.9	6.8	-0.5	2.5	-1.0	2.0	10.2	2.3	59.0
LL	CR012	3.1	34.8	2.9	0.7	2.9	-1.5	0.9	10.7	1.1	55.6
LL	CR018	1.9	39.5	0.4	0.1	1.9	-1.3	1.1	3.5	2.8	49.9
LL	CR018	2.5	16.6	9.5	2.3	5.2	3.5	2.5	21.0	8.4	71.4
LL	CR018	3.1	19.9	9.9	2.2	4.6	3.7	3.5	17.6	7.6	72.0
LL	CR018	3.7	31.3	-0.1	0.9	5.7	-1.8	-0.8	16.3	2.3	57.4
LL	CR018	2.5	32.8	5.5	0.4	2.8	2.1	3.4	6.5	4.9	60.8
SS	CR019	19.7	0.1	4.8	6.5	1.5	-4.3	6.9	66.3	2.8	104.4
SS	CR019	10.3	22.7	1.3	5.2	1.3	-5.5	0.3	27.2	2.2	65.0

Unit	Sample	Al ₂ O ₃	CaO	FeOT	K ₂ O	MgO	MnO	Na ₂ O	SiO ₂	TiO ₂	Total
SS	CR019	1.1	24.6	0.6	2.1	3.0	-4.6	-1.5	42.9	3.9	71.9
SS	CR019	17.5	2.3	5.8	6.2	0.8	-5.3	3.6	52.5	5.1	88.5
SS	CR019	1.0	40.0	-0.6	1.1	3.2	-3.8	0.1	10.3	1.9	53.3
ML	CR025	1.8	34.3	3.9	0.9	3.6	-1.5	0.5	19.4	1.9	64.8
ML	CR025	3.7	9.7	5.1	0.8	3.1	-3.3	-2.1	59.1	4.3	80.4
ML	CR025	6.0	18.7	4.4	2.0	4.2	-2.3	-0.6	42.0	3.1	77.5
ML	CR025	1.1	27.6	3.3	0.1	3.7	-1.9	-0.5	40.7	4.0	78.2
ML	CR025	5.7	19.4	5.3	0.9	4.3	-3.5	-0.8	40.8	3.1	75.1
ML	CR025 dark	0.1	2.3	11.3	2.6	5.1	1.2	-1.4	74.6	8.5	104.2
ML	CR025 dark	-2.3	-1.6	4.7	2.1	3.0	-3.6	-5.2	103.0	7.1	107.2
ML	CR025 dark	-1.2	-0.7	5.0	2.8	2.9	-3.3	-4.4	94.8	6.9	102.8
ML	CR025 dark	0.9	0.2	16.8	3.1	2.4	-5.9	-2.9	75.5	5.2	95.4
ML	CR025 dark	-0.2	-0.8	11.3	4.3	3.3	-6.4	-4.2	89.1	5.9	102.2
ML	CR026	-0.7	45.2	0.6	0.0	3.0	0.0	1.5	1.5	1.7	52.8
ML	CR026	-0.9	44.4	0.8	0.2	2.9	-0.4	1.7	1.8	2.4	52.7
ML	CR026	-1.5	48.4	-0.7	0.1	2.8	-0.3	1.3	-0.2	1.6	51.4
ML	CR026	-3.0	52.9	-1.7	0.3	2.1	-0.8	1.2	-4.3	1.8	48.3
ML	CR026	-1.8	48.4	-1.0	0.2	2.2	-1.0	0.9	-1.4	1.1	47.7
ML	CR028	2.0	35.9	-0.1	0.4	3.9	-3.3	-0.8	17.8	1.9	57.8
ML	CR028	2.6	36.1	-0.4	0.6	4.8	-3.3	-0.3	16.4	1.7	58.2
ML	CR028	2.1	36.0	-0.7	0.6	4.7	-3.4	-0.4	18.4	1.9	59.4
ML	CR028	3.5	33.4	-0.1	1.0	3.9	-3.4	-0.1	21.5	1.6	61.4
ML	CR028	2.6	36.6	-0.2	0.7	4.6	-3.2	0.0	15.9	1.2	58.2
MD/LD	CR029	14.2	8.0	2.0	4.4	2.6	-4.7	0.9	49.5	3.0	79.9
MD/LD	CR029	13.9	5.4	1.7	4.5	3.2	-4.7	0.3	51.9	4.7	80.9
MD/LD	CR029	13.2	7.8	2.2	4.6	2.8	-4.7	0.7	49.0	4.4	79.9
MD/LD	CR029	13.7	6.1	1.6	4.6	3.1	-5.0	0.5	51.9	4.7	81.1
MD/LD	CR029	13.7	5.7	2.1	3.8	3.5	-4.1	0.2	51.1	4.8	80.7
SS	TM	3.0	1.1	16.6	-0.9	2.3	-3.2	-1.5	69.6	5.6	92.6
SS	TM	3.9	0.1	8.4	0.4	4.0	-2.1	-1.6	83.0	6.1	102.1
SS	TM	-4.4	-1.8	6.8	-0.6	4.4	-2.4	-2.6	102.5	7.8	109.7
SS	TM	0.3	1.5	9.5	0.3	2.8	-4.1	-1.7	85.6	5.5	99.6
SS	TM	-1.9	-0.4	7.9	-0.1	4.0	-2.6	-2.2	94.2	6.2	105.1

Based on the remote sensing data presented above, a holistic picture of the geology of the outcrop with 5 major units begins to emerge (Figure 2-4a). Lowest in stratigraphic order are two distinct bedded montmorillonite-bearing units (LB and TL1) with minor iron oxide spectral features and bedding on the scale of a few cm (LB) and tens of cm (TL1), respectively. LB and TL1 are separated by a disconformity. The massive carbonate (ML) unit is potentially conformable with the TL1 and TL2 units, which are found both above and below. To the right of the scene, and not clearly related to the three units on the left, is a finely laminated unit composed of montmorillonite and iron oxide (LD), containing a light-toned bed having a stronger spectral detection of montmorillonite and a weaker iron oxide signature. Finally, an upper finely bedded (cm scale) unit of intermixed gypsum and montmorillonite (LL), with strong detections of gypsum in the upper beds tops the stratigraphic section, separated from LD by a disconformity. This disconformity between LD and LL appears to be an erosional contact based on the truncation of strata in the LD unit. Collectively, these units suggest a lacustrine environment with varying water chemistry which contains several unconformities indicating possible pauses in deposition. The float rocks, scree, and regolith at the base of the outcrop generally have the same spectral properties as the rock units above with a few outlier clasts, perhaps indicating longer distance transport. Based on this synthesis of information, the massive carbonate, sedimentary rocks with gypsum, and finely-laminated, clay-bearing sedimentary units would likely be prioritized for proximity science.

2.4.2 Proximity science

Proximity science data collection by SHERLOC/WATSON and PIXL typically would occur after the rover's arrival at select outcrop locations, guided by the remote sensing data described above. The reverse will also likely occur: unexpected findings from the proximity instruments will be followed up with further investigation using the remote sensing techniques in cases where those techniques (e.g., VIS/IR spectroscopy, LIBS, green Raman) may be informative.

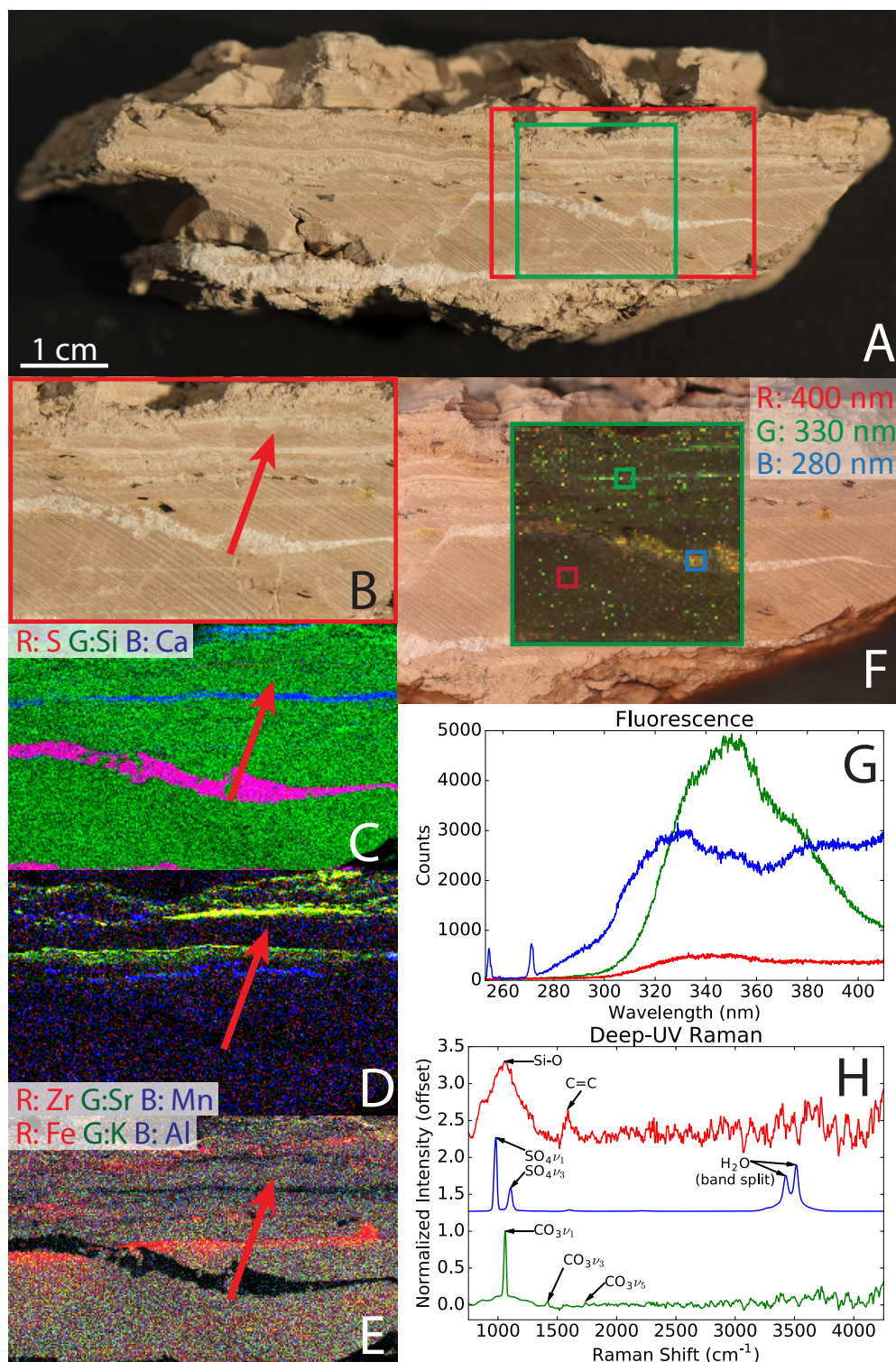


Figure 2-9. Proximity science results on phyllosilicate with gypsum and calcite bands (sample CR002, clay-rich unit LD). A) color image with the simulated PIXL area shown in red and the simulated SHERLOC area shown in green. B-E) PIXL-like results for CR002. A red arrow notes the location of a spatially coherent band of Zr and Sr, which appears yellow in (D). F) Low-resolution UV-fluorescence scan map, with (G) averaged fluorescence and (H) Raman spectra shown in the same color as the highlighted areas in (F).

WATSON-like microscopic imaging of units LB, LD, and LL indicates grain sizes smaller than the resolution of the imager (see color image of sample CR002 in Figure 2-9b), meaning that the individual grains are silt-sized or smaller. In combination with the fine lamination, this small grain size suggests a lacustrine origin, as was inferred by remote sensing data. The laminated fenestral texture of irregularly curled and wavy laminations in the carbonate indicates it likely formed as a travertine deposit, possibly associated with microbial mats (see CR025 image in Figure 2-10a; as also interpreted by Gandin & Capezzuoli, 2014). The calcite is associated with a green and red solid, which forms botryoidal textures on the exterior of the rock (Figure 2-7d), and appears to alternate with the calcite in laminae. Green Raman demonstrates that this material is quartz (Figure 2-7h). LIBS observed relatively pure SiO_2 in these quartz veins with minor Fe and Ti (Figure 2-7i).

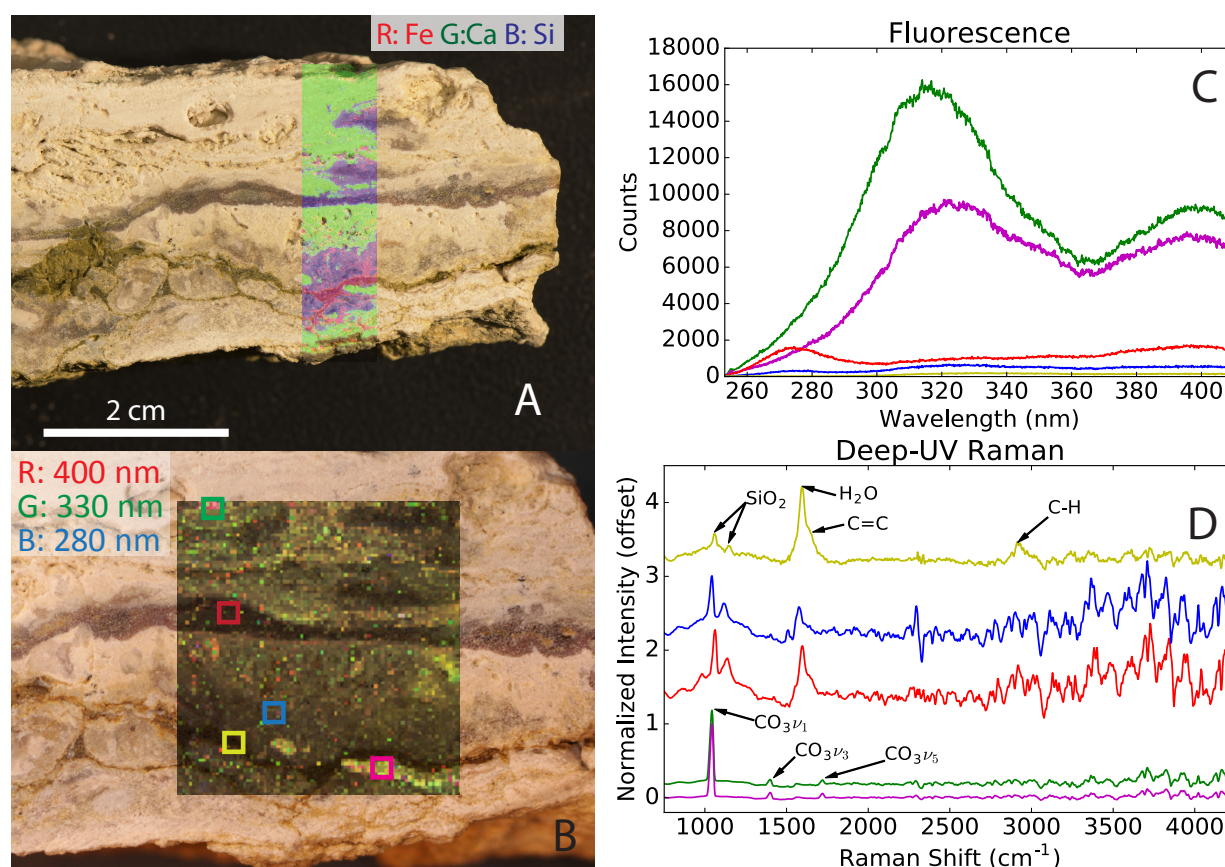


Figure 2-10. Proximity science results on calcite-bearing sample CR025 (carbonate-rich unit ML) with bands of chalcedony and an Fe-bearing silicate. A) PIXL-like image with overlay of elemental abundance for CR025. B) Low-resolution fluorescence scan map, with averaged (C) UV-fluorescence and (D) Raman spectra from the highlighted areas shown below.

Simulated PIXL results demonstrate the ability to detect spatial patterns of major, minor, and trace chemistry. On a cut face of mudstone sample CR002 from unit LD (analogous to an abraded

surface prepared by the Mars-2020 system), the spatial distribution of S, Si, and Ca reveals mm-scale layers of gypsum and a new detection of calcium carbonate (not observed by the remote sensing instruments) within the phyllosilicate (Figure 2-9c-e). The spatial distribution of Al and K suggests that Al-phyllosilicates and/or K-feldspar are present throughout the rock, and a band with Fe enrichment is also visible. Trace elements show coherent patterns, including spatially correlated Zr and Sr enrichments and laminae with Mn enrichment. Analysis of the carbonate sample CR025 from unit ML shows Ca with Si banding interpreted as laminae of quartz in a primarily calcite sample (Figure 2-10a). Based on WATSON-like imaging of texture, the quartz lacks visible structure and is likely a cryptocrystalline polymorph of quartz such as chalcedony. A lighter green lamination in this sample shows the presence of both Si and Fe, potentially indicating the presence of a secondary Fe-bearing phyllosilicate phase (Figure 2-10a). Samples that appeared spectrally to be pure gypsum (not shown) demonstrate the expected combination of Ca and S.

Fluorescence signals from organics were observed in all sample spectra ($n=387$) and in three example low-resolution scan maps, utilizing 200- μm spacing and 25 laser pulses per point, replicating the quick scans likely to be done in an initial search for organics with Mars-2020 (Figures 2-9 & 2-10). The interior and exterior fluorescence spectra from the same rock typically exhibit similar maxima, suggesting that the fluorescence observed is originating from organics held within the rocks, and not simply from airfall organic contamination common on the Earth. The wavelength of fluorescence maxima indicates the class of organic molecule observed (Berlman, 1971). The fluorescence spectra of the carbonate (unit ML, Figure 2-10c) have a peak near 325 nm, suggesting the presence of organic material related to bacterial flora (Figure 2-11; Table 2-6). Some fluorescence peaks appear to correlate with rock type; carbonates tend to have peaks at 310-320 nm and exotic metamorphic clasts from the scree slope (SS) have peaks at 260 and 340 nm (Figure 2-11). Statistically representative sampling was not done on a sample-by-sample basis, so these correlations are purely qualitative. Differing rock types from the other units have more scattered peak wavelengths, varying significantly by sample (Figure 2-11). The quick scan results guided follow-up targeting with higher resolution, 100 μm spacing and 1200 laser pulses per point, deep-UV Raman to search for more specific organic signatures.

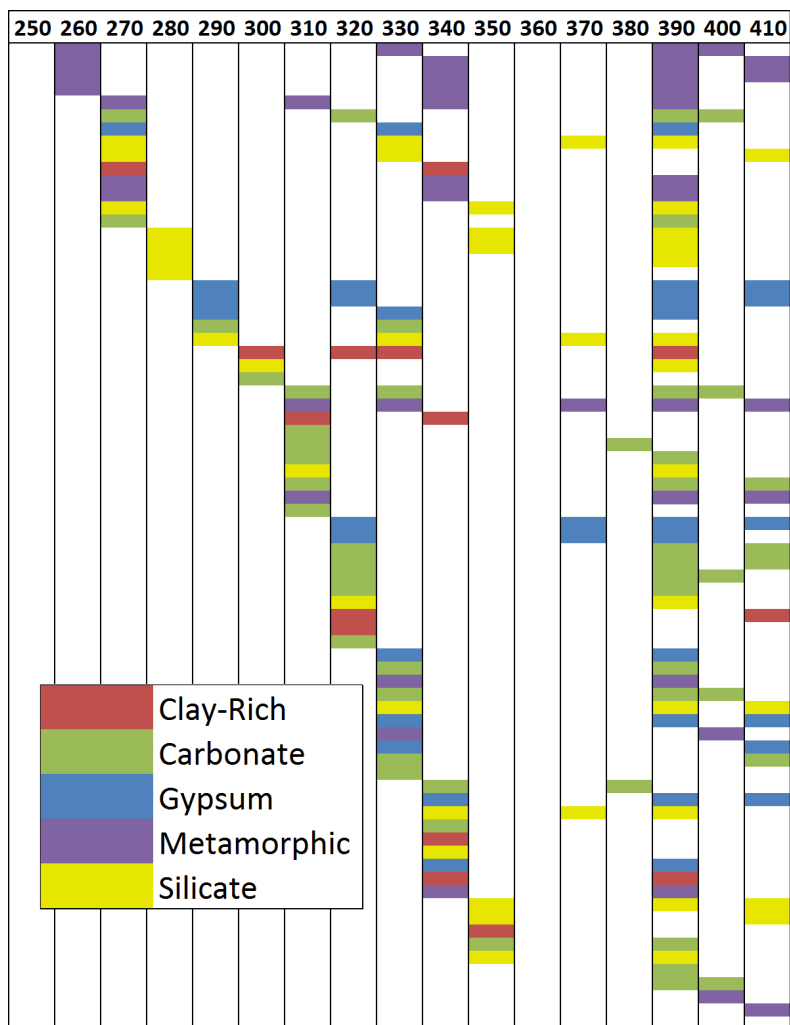


Figure 2-11. Fluorescence spectral classes observed in targets, classified by the dominant type of material in the sample. Each peak observed in a given spectrum was placed within a 10-nm wavelength bin and targets are classified by type. Spectra in a single sample with the same peak locations are not repeated on the chart. See Table 2-4 for potential fluorescence spectral classification.

Table 2-6. Literature data on attributions for individual fluorescence peaks.

Fluorescence peak (nm)	Molecular Attribution	Reference
280	1-ring aromatics	Bhartia et al., 2008
290	Bacterial Spores	Bhartia et al., 2008
326	Bacterial vegetative cells	Bhartia et al., 2008
330	2-ring aromatics	Bhartia et al., 2008
350	Indoles	Bhartia et al., 2008
350	Proteins	Beegle et al., 2015
364	Bent 3-ring aromatics	Bhartia et al., 2008
374	Linear 3-/bent 4-ring aromatics	Bhartia et al., 2008
458	Humic substances	Yamashita et al., 2008
464	Linear 4-/bent 5-ring aromatics	Bhartia et al., 2008

Single point SHERLOC deep-UV Raman spectra show peaks due to sulfate and carbonate anions (Figure 2-12a), as expected given the information from the other datasets. Conversely, the Raman signal from silicate minerals appears to be weak or nonexistent (depending on the mineral) in simulated SHERLOC point spectra. SHERLOC Raman data $<800\text{ cm}^{-1}$ are not collected due to a filter designed to avoid Rayleigh scattering from the sample. The major peaks in silicate Raman spectra tend to be $<800\text{ cm}^{-1}$; however, a phyllosilicate-related broad feature at $\sim 1100\text{ cm}^{-1}$ and a quartz doublet feature at ~ 1050 and 1120 cm^{-1} are apparent in these spectra when averaging ~ 100 spectra (Figures 2-9h & 2-10d; Nakamoto, 2008). Multi-point averaging also revealed a weak OH-related feature in a ground truth-confirmed sample of montmorillonite (Figure 2-12b).

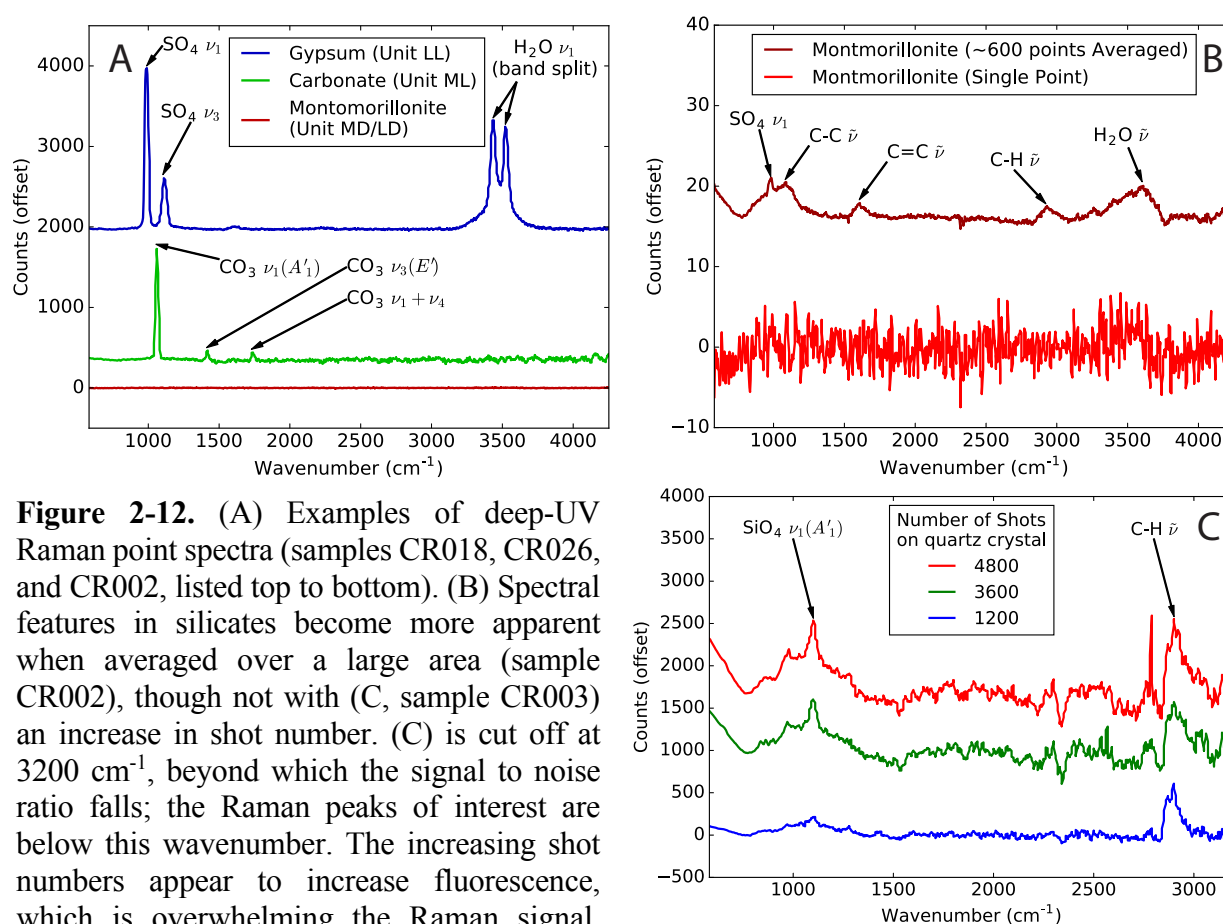


Figure 2-12. (A) Examples of deep-UV Raman point spectra (samples CR018, CR026, and CR002, listed top to bottom). (B) Spectral features in silicates become more apparent when averaged over a large area (sample CR002), though not with (C, sample CR003) an increase in shot number. (C) is cut off at 3200 cm^{-1} , beyond which the signal to noise ratio falls; the Raman peaks of interest are below this wavenumber. The increasing shot numbers appear to increase fluorescence, which is overwhelming the Raman signal. Inorganic Raman peak designations from Nakamoto (2008).

In Deep-UV Raman data, the appearance of a broad, asymmetric peak at 1600 cm^{-1} is the primary indicator of carbon-rich material (Figures 2-9h & 2-10d), which is caused by an in-plane

C=C stretching mode of polyaromatic carbonaceous material (Socrates, 2004). Its broadening may be due to high defect density, which could signify the material is relatively pristine (i.e., has not been significantly graphitized; Beyssac et al., 2004). Low signal-to-noise ratio makes detection of other organic peaks difficult, with one exception: the chalcedony in sample CR025 (unit ML/Mc, Figure 2-10d) exhibits sufficiently intense signal that a $\sim 2900\text{ cm}^{-1}$ peak from C-H stretching modes (Socrates, 2004) can clearly be identified. This association between strong Raman signal of unaltered organics and directly precipitated silica deposits would be highly intriguing in a Mars context.

2.4.3 Sampling decisions

SHERLOC Raman and fluorescence spectra, along with PIXL data, will allow determination of petrology of a given unit and detection of the organics within the rock. This information is vital in determining whether to take a sample from a specific locality, and, once the decision has been made to sample, which section of the rock to sample from. In the case of this outcrop, at least 3 samples would likely be considered for caching (not counting duplicates or blanks). The calcite-bearing (ML) unit would be intriguing from a geological perspective immediately upon its detection due to the scarcity of carbonate detections (especially Ca-carbonates) on Mars and their relevance to the climatic history of the planet (Ehlmann & Edwards, 2014; Hu et al., 2015). The determination that the calcite represents a travertine deposit, and especially with the presence of associated silica and organics, make it a high priority target for both understanding Martian climate/geological history and seeking biosignatures of past life on Mars. A travertine sample would be important because one of the key factors in biosignature preservation is rapid entrapment, including in fine grained chemical precipitates (Farmer & Des Marais, 1999). Gypsum has also been noted as a potential preserver of microfossils on Mars (Schopf et al., 2012). On Earth, it is largely disfavored due to its solubility (and consequently rare preservation without recrystallization in ancient deposits), though this is less of a problem in Mars exploration due to the paucity of water after the Hesperian period (Bibring et al., 2006). Finally, low-energy environments with sedimentation of clay-rich mudstones concentrate organics on Earth (Kennedy et al., 2002) and are considered a promising location for preservation of organic molecules on Mars (Summons et al., 2008). Therefore, a sample from the base of the laminated mudstone (LB) unit would likely be considered for potential caching.

2.5 Discussion

2.5.1 “Rover” vs. ground truth data environmental interpretation

The map composed using data from simulated Mars-2020 remote sensing instruments is largely consistent with the ground truth map of the outcrop, at least from a mineralogical standpoint (Figures 2-2 & 2-4). The success of the mineralogical and compositional characterization of the scene primarily with simulated SuperCam data, in combination with the high-resolution color simulated Mastcam-Z and Navcam images, allowed identification of multiple sedimentary deposits, correctly interpreted as primarily lacustrine in origin. Mars-2020 simulated datasets also suggested a lake dominated by subaqueous deposition of clay minerals progressing to a more ephemeral lake system higher in the stratigraphic section, with potential local groundwater/hydrothermal activity resulting in deposition of the carbonate unit. These Mars-2020-like paleoenvironmental interpretations closely match the high-level paleoenvironmental interpretations based on ground-truth data and prior literature.

One important aspect of the geology that was not readily recognized from simulated rover remote sensing data is the presence of numerous beds of volcanic ash interbedded with mudstones of purely lacustrine origin. The most likely immediate interpretation of these lighter-toned beds could simply be erosion of alternating source regions, without specific attributions as to the nature of those regions. Even in terrestrial settings, recognition of ash beds can be difficult, especially in cross section, and SEM imaging to reveal highly angular glassy components at a nano-scale is considered diagnostic. The lack of uniquely distinguishing features in ash deposits at a micro- to macro-scale in rover remote sensing and proximity data must, therefore, be appreciated and care must be taken to positively identify any such potential deposit. There is no single dataset in this study which conclusively could be used to determine the presence of ash in the outcrop. A plausible strategy for consistent recognition of tephra relies on multiple steps of increasing scrutiny to determine a given sedimentary layer's origin: 1) recognition of an abrupt change in color or texture as in the decorrelation stretch shown in Figure 2-4b, 2) micro-imaging to probe for a fine and well sorted grain size and/or accretionary lapilli, and 3) analysis with the spectral and chemical instruments to confirm glassiness, bulk chemical changes (e.g. increases in alkali elements), and/or slight changes in the incompatible element composition of the layer. In this case, ash collection

would not calibrate Martian crater-density based ages (i.e., the exposure is not a surface), but rather establish the absolute timing and deposition rate of sediments at this site. Top surfaces of the underlying sedimentary units would then be bounded by a minimum age, while overlying sediments would be bounded by a maximum age. The ability to derive an absolute age of deposition would be useful for interpretation of the climatic history of Mars and the timing of active lake systems.

2.5.2 Instrument synergies and limitations

2.5.2.1 Mineralogy

All four of the instruments simulated in this study determine mineralogy to varied extents and with different sensitivities. Coarse unit discrimination was possible using Mastcam-Z from a simulated distance of approximately 200 m based on their color, texture, and spectral properties. The distance for initial Mastcam-Z is likely to be smaller than 200 m in practice, lending confidence to the ability of Mastcam-Z to provide effective reconnaissance data. A gypsum-associated 995 nm hydration feature was observed in Mastcam-Z spectra. However, the weak reflectance minimum due to H₂O in phyllosilicates is at 960 nm, where the 1013 nm filter did not detect it (Figure 2-6). Thus, on Mars-2020, SuperCam IR point spectra from a distance will be essential for the recognition of hydrated/hydroxylated minerals by features at 1400 and 1900 nm and metal OH absorptions from 2200-2400 nm (Clark et al., 1990). Mineralogy of the mapped units was constrained by analysis of several point spectra from SuperCam.

Calibration of passive spectroscopy (from either Mastcam-Z or SuperCam) may be complicated when performed over a relatively long distance. The longer path length to a given target relative to calibration standards on the rover may introduce uncertainty to the measurement, particularly when atmospheric opacity is high such as during a dust storm. These uncertainties may be somewhat mitigated by performing long-distance spectroscopy close to midday for relatively consistent phase angles.

Iron-related electronic absorptions occur primarily at the wavelengths covered by Mastcam-Z and the SuperCam passive spectral range. This capability will be effective in the context of the more mafic surface mineralogy on Mars. At the outcrop used in this study, variations in iron-related absorptions were in several cases a result of surface weathering rather than being characteristic of

the bulk rock. Coverage gaps between 470-535nm and beyond 855 nm in SuperCam's VIS spectra, due to the green Raman laser, may complicate the detection of hematite, which has strong absorptions at ~535 nm and ~860 nm (Morris et al., 1985). These gaps are covered by the Mastcam-Z filters, meaning that the payload instruments together will acquire the needed information. A more substantive spectral coverage gap occurs between 1013-1300 nm (Figure 2-6), which neither Mastcam-Z nor SuperCam has the ability to measure. Pyroxene, olivine, and Fe-bearing feldspars, glasses, and alteration phases have important absorption bands in this wavelength range (Horgan et al., 2014). Variations in pyroxene crystal chemistry, which indicate changing properties of the parent magma, are tracked by examining band shifts between 900-1200 nm (e.g. Klima et al., 2011). Diagnostic band minima will sometimes not be captured in the Mars-2020 dataset. To compensate, cross-calibration of passive spectral data in overlapping ranges and synergistic use of SuperCam passive data, the Mastcam-Z longest wavelength channels 975 nm and 1013 nm (Bell et al., 2014), and remote elemental composition are likely needed for identifying variations in mafic mineralogy, and PIXL chemistry data or Raman spectroscopy of mineral grains will be used for mafic mineral crystal chemistry as required.

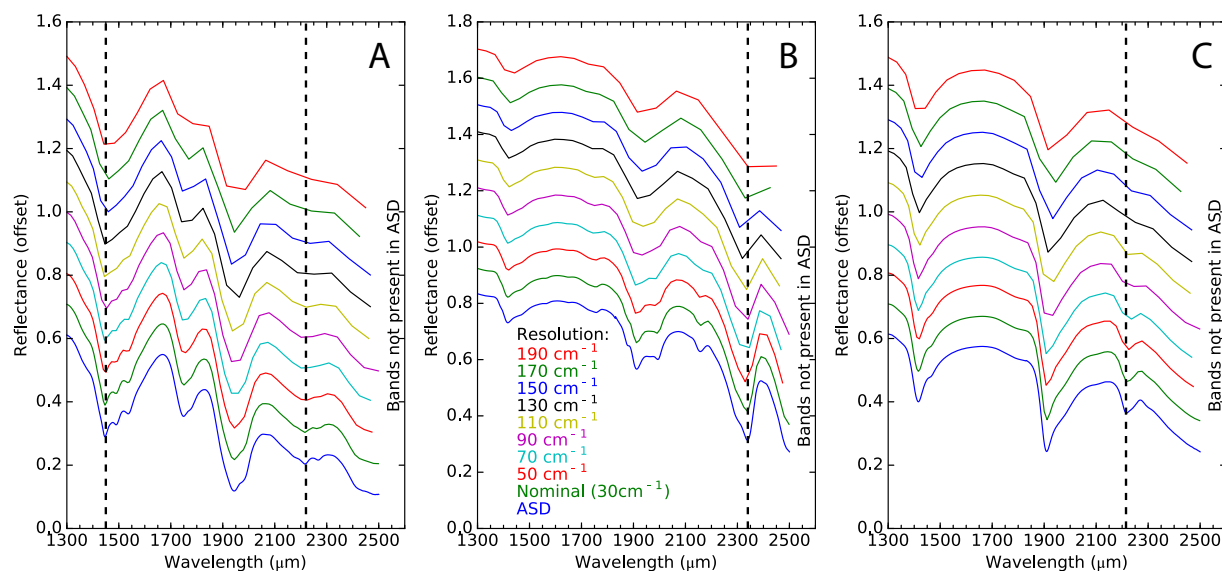


Figure 2-13. The result of down sampling the resolution of SuperCam passive IR spectra at even spectral sampling to decrease time of acquisition required. It will also be possible to selectively sample portions of the spectrum most diagnostic of minerals of interest. Examples are shown of (A) gypsum-bearing sample CR018 (unit LL), (B) calcite-bearing sample CR026 (unit ML), and (C) montmorillonite-bearing sample CR002 (unit LD).

No anticipated vibrational absorptions were missed in the simulated SuperCam IR dataset, validating SuperCam's effectiveness in this wavelength range at full resolution and even when spectrally downsampled to $\sim 100 \text{ cm}^{-1}$ (Figure 2-13). The ability to observe VIS and IR absorption features of phyllosilicates, carbonates, sulfates, and iron oxides at a small scale will allow mapping of major alteration mineralogy at a range of distances (see section 2.5.2.3. below). Due to spectral overlap with CRISM, large-scale mapping may also be confirmed using SuperCam's IR capability, giving the Mars-2020 team the ability to perform strategic route planning based on the confirmation or rejection of CRISM-mapped locations of various mineral deposits with SuperCam passive data. One potential challenge for both Mastcam-Z and SuperCam remote ($>7 \text{ m}$ distance) observations is the obscuration of target mineralogy by surface dust, which is not simulated in this study. SuperCam can partially avoid this issue within 7 m , as the shock wave from LIBS partially clears the surface. Of course, the DRT can remove dust completely for targets within the arm work zone.

Based on these results, the judicious and frequent selection of SuperCam passive VIS and IR targets using imaging as a guide to delineate the boundaries between suspected lithological/mineralogical units or variations in mineral composition within a distinct unit will be crucial to the effective determination of mineralogy via remote sensing. A potential standard campaign once color Navcam data are acquired could involve: 1) full filter set multispectral imaging using Mastcam-Z (downsampled spectrally or spatially if dictated by data volume restrictions, as is common) with SuperCam of each color unit, 2) further SuperCam VIS and IR passive measurements of areas highlighted by Mastcam-Z (perhaps with downsampling for greater time and data volume operational efficiency; see 4.3), and 3) Mastcam-Z zoom images of areas that potentially exhibit small-scale variability or structure. Follow-up SuperCam spectral transects and Mastcam-Z zoomed full filter set high resolution images can then be used to elucidate any remaining outstanding ambiguities upon close approach.

The results from the green Raman analog for the SuperCam Raman capability are only partially similar due to the lab instrument's much higher spatial resolution and greater sensitivity compared to SuperCam. However, information about green Raman's relative sensitivities to different minerals is still valuable. The confirmation of minerals detected via passive remote sensing techniques (e.g. gypsum and calcite) and positive identification of quartz (otherwise undetectable to the instruments on Mars-2020) is accomplished with the analog instrument and anticipated for the

SuperCam instrument. Montmorillonite was also observed via Raman, although some reference spectra show no major peaks, possibly due to weak Raman scattering cross-sections or orientation effects of the grains during generation of the library spectra (Frost & Shurvell, 1997), suggesting that special care should be taken in searching for clay minerals on Mars and in developing appropriate clay reference libraries. The ability to detect minerals with green Raman that cannot be observed by reflectance spectroscopy (and vice-versa) make this suite complementary.

SHERLOC detects salt mineral-associated CO_3 (1050 cm^{-1}), SO_4 (950 and 1100 cm^{-1}), and H_2O (3500 cm^{-1}) in single point spectra collected in milliseconds. The identification of silicates, especially clays, proved more difficult and in our study required the additional collection of hundreds of data points as the dominant SiO_2 Raman feature ($\sim 465\text{ cm}^{-1}$) is cut off by the instrumental notch filter that removes unwanted Rayleigh scattering at Raman shifts $< 800\text{ cm}^{-1}$. The relative weakness of spectral features of silicate minerals in the SHERLOC-observable range is likely a result of the smaller interrogation area probed due to the relative opacity of silicates to the UV laser compared with sulfates and carbonates and a lack of resonance effects due to the excitation wavelength of 248.6 nm . By increasing the number of laser shots in a single quartz crystal, the $\sim 1100\text{ cm}^{-1}$ SiO_4 -related feature was observed (Figure 2-12c). However, at higher wavenumbers the signal-to-noise ratio falls due to fluorescence, making this technique less effective in the higher wavenumber range for these samples. By averaging several individual spectra taken over a small area, hydration features of montmorillonite from unit LD (XRD confirmed to contain abundant smectites; sample CR002 in Table 2-3) were detected, suggesting multi-point averaging as a potential method of silicate mineral detection by deep-UV Raman if other methods are not available. Quartz was also detected in this way in sample CR025 (Figure 2-10d), confirming multi-point averaging as a reliable technique for teasing weak (but present) mineral features from the spectra. Given the importance of identifying and interpreting silica and clay minerals to understanding the nature and extent of interactions of water with Martian materials, cross-instrument strategies for their analysis by other methods (e.g., IR spectroscopy, PIXL crystal chemistry estimates from elemental composition) are necessary and should be incorporated in the routine workflow during outcrop examination.

2.5.2.2 Chemistry

Major-element abundances determined using LIBS compare favorably with the bulk chemistry measured as part of the ground truth data (see Table 2-4 and Figure 2-7). The simple model used provided data with sufficient accuracy for the purposes of this study although, as expected, it resulted in larger uncertainties and deviations from the true chemistry than LIBS is capable of achieving using the more sophisticated submodel approaches available (Anderson et al., 2017). The absolute uncertainties in this analysis were not constrained, but are likely to be $\leq \pm 5$ wt%; see Anderson et al. (2011) for a detailed discussion of LIBS uncertainties. This simplified model is likely partially responsible for small variations from a one-to-one correlation between LIBS and bulk lithochemistry as is the fact that LIBS has a small spot size, leading to large (real) variations between grain-scale vs. bulk lithochemistry data. Very large differences in chemistry between mudstone, tuff, carbonates, and sulfates meant mapping and characterization of the different units could be done on the basis of just a few elements. Though we did not simulate it here, quantification of H, Li, B, F, Cr, Mn, Cl, Ni, Rb, Sr, and Ba, will also be possible on Mars-2020 as with MSL (e.g., Gasda et al., 2017; Lanza et al., 2014; Payré et al., 2017; Rapin et al., 2017; Thomas et al., 2018, 2019). In addition to providing routine chemical analysis, LIBS data from SuperCam will function in a reconnaissance capacity, searching for chemically unusual targets to be more closely investigated by the other instruments in the Mars-2020 suite.

Simulated PIXL demonstrated the ability to observe sub-mm spatial patterns in chemistry (e.g., Figures 2-9 & 2-10). This ability will be revealing for the characterization of the geological history of a given rock, the targeting of potential biosignatures for further analysis by SHERLOC, and sampling target downselection. For example, targets high in zirconium such as found here would be prioritized for geochronology, and samples with clear growth texture relationships allowing straightforward interpretation of the time relationships between sample components would be desirable. PIXL's ability to detect trace elements at small spatial scale may give insight to the redox, pH, and weathering history of the rock, which can inform our understanding of the geological and diagenetic history of a rock at that small scale, as well as suggest the presence of potential biosignatures (Mustard et al., 2013). Both SuperCam LIBS and PIXL provided additional evidence to support mineralogy determinations that were made by the other techniques. PIXL's capabilities on Mars-2020 will be greater than simulated here because of the ability to quantify as well as map

the spatial distribution of elements. PIXL can also be used both to determine grain-scale chemistry for coarse rocks or sediments and establish the quantitative bulk chemistry of a given target by averaging across a full-sized map.

In the case of analyses of fine-grained rocks such as a mudstone, neither SuperCam LIBS nor PIXL has the spatial resolution to determine the chemistry of individual grains. This challenge of small grain sizes may be solved by statistical unmixing to find mineral/chemical endmembers within a given target or group of targets. With both instruments, bulk chemistry can always be observed by multi-point averaging, yielding data similar to APXS measurements familiar from past rover missions (Gellert et al., 2013; Golombek, 1997; Rieder et al., 2003). Additionally, a method has been developed for estimating relative grain size from the compositional spread of the observation points within a ChemCam raster (Rivera-Hernández et al., 2018). At large grain size, individual grains will dominate the chemistry as measured at one point, thus increasing the variability between points, while a grain size much smaller than the laser spot size will yield more consistent chemistry between points (Rivera-Hernández et al., 2018). This technique requires that samples with large grainsize exhibit chemical variability and that diagenetic cements not dominate at large grain size, as cement may cause the sample's chemistry to appear more homogenous than its true bulk chemistry. Presumably PIXL could use this method for individual pixels, with much greater accuracy for small grain sizes.

2.5.2.3 Organics

The Deep-UV fluorescence results simulating SHERLOC data demonstrated that organics were present throughout all collected samples. Raman detection limits are $\sim 10^{-6}$ w/w for aromatics and $\sim 10^{-4}$ w/w for aliphatics, and fluorescence is generally several orders of magnitude more sensitive depending on the specific molecule (Beegle et al., 2017), so detection is fully expected given >0.5 wt% total organic carbon (TOC) in all samples. Different classes of organic molecules have characteristic maxima (Berlman, 1971), and indeed the samples showed a variety of fluorescence spectra (Figure 2-11). That the fluorescence peak locations and rock types shown in Figure 2-11 correlate poorly suggests that either the organic compounds held within the rocks are relatively uniform (and therefore likely sourced from endolithic microbes) or that this technique is not capable of detecting the differing organics present in the strata despite their differing formation

environments. Further work characterizing the fluorescence spectra of organic molecules known to have been preserved in rock would clarify this question. Simulated low-resolution quick scans of three samples spatially mapped organics successfully, giving locations for follow-up targeting with deep-UV Raman (Figures 2-9 & 2-10). However, using existing published attributions of fluorescence peak positions (summarized in Table 2-6), we were not able to constrain the types of organics in the samples. Fluorescence spectroscopy of organics in geological samples is a relatively new, underexplored field. As a result, extensive digitized fluorescence libraries like those used for VNIR, VIS, IR, or green Raman spectral analysis simply do not exist. In order to maximize the effectiveness of SHERLOC's fluorescence capabilities, an effort to construct such libraries for high-resolution fluorescence data is warranted prior to the landing of Mars-2020 in order to be able to interpret organics detections.

Prior work indicates SHERLOC Deep-UV Raman is capable of detection and identification of organic compounds at thresholds of ~ 0.1 -1 wt% (Abbey et al., 2017). Here, all samples have >0.5 wt% TOC. Broad peaks at $\sim 1600\text{ cm}^{-1}$ and $\sim 2900\text{ cm}^{-1}$ indicate the presence of C=C bonds and C-H bonds in the organic compounds contained in several samples (Figure 2-9h & 2-10d). An H₂O bend also generates a Raman peak at $\sim 1600\text{ cm}^{-1}$ in hydrated samples; these overlapping features may be distinguished by width as mineralogical features tend to be sharper. The observation with the best signal-to-noise ratio is in sample CR025, which includes a strong 1600 cm^{-1} band in a chalcedony matrix (this sample includes quartz SiO₂ Raman bands, Figure 2-10d; Nakamoto, 2008), demonstrating that samples with a strong biosignature preservation potential are effectively probed by SHERLOC. These 1600 cm^{-1} signals have a shoulder, suggesting that they may be a mixture of two peaks: one sharp peak (likely H₂O bending), and one broader peak (likely organic). The 2900 cm^{-1} peak attributed to C-H is observed only in areas of relatively low fluorescence as the increase in noise due to higher amounts of fluorescence obscure this peak (Figure 2-10d). Intriguingly, the areas highlighted by fluorescence in the quick scans appear to have generally weaker organic Raman peaks, while the areas with less fluorescence often have the strongest organic Raman peaks (Figures 2-9 & 2-10). These results suggest that fluorescence and deep-UV Raman may be complementary to one another, although the more limited areal coverage of the Deep-UV Raman means care must be taken to investigate all spectral components of a sample, including fluorescence-dark areas to ensure strong Raman signals are not missed.

Some organic components (especially at 2900 cm^{-1}) are visible in the green Raman data as well as the Deep-UV data (Figure 2-7f-i). In both Raman datasets, it is not possible to identify or classify the organics present in detail due to the broadness of the observed peaks, which likely indicate a wide variety of organics with distinctive molecular structures and chemical environments. The lack of a “D”-band (at 1400 cm^{-1} , Socrates, 2004), the relative intensity of the 2900 cm^{-1} band, and the broadness of the C=C band at 1600 cm^{-1} in these samples indicates almost no graphitization of these organics, suggesting that they are rich in aliphatics and may be considered “fresh” organics which are entirely thermally immature. The origin of these fresh organics is ambiguous from these data and could result from entombment at the time of deposition or from modern endolithic microorganisms. On Mars, such pristine organic molecules are unlikely to be observed after ~ 3 Gyr of preservation due to radiolytic decomposition (Pavlov et al., 2012). The intensity of the organic signals observed here appear to be dependent on the mineral matrix as a result of the integrated volume of the minerals probed by the laser, which suggests that the true detection limit of SHERLOC may depend on the mineral substrate. This possibility should be explored further but is beyond the scope of this work.

2.5.3 Operational considerations

In this study, traversability and reachability considerations were ignored and the entire outcrop was treated as though it were accessible. Of course, ancillary remote sensing data will be required for reconnaissance of these parameters for actual Mars-2020 operations. This study also assumes that optimal illumination angles can be achieved for imaging and remote spectral observations of the outcrop, which may not be the case for all outcrop exposures.

As with prior rover missions, day-to-day operations of Mars-2020 will be limited by time, power, and data downlink volume available. Another limitation in an operational setting is the overall complexity of a given plan. In practice, this means that the full range of rover instrumentation presented here for most targets is unlikely to be deployed unless particularly interesting results are obtained from that target. However, selection of sample locations and complete documentation of drill samples is of high importance, meaning that the data crucial to the interpretations provided in this study would likely have been collected.

Our analog study points to a few measurement modes that may minimize resource use without compromising scientific requirements. Mastcam-Z will be capable of providing data compression and transmitting only sections of images to limit the overall data transmission necessary for a given measurement. In addition, by using only a subset of Mastcam-Z filters, both time and data will be saved.

SuperCam uses an acousto-optical tunable filter rather than a diffraction grating to generate high-resolution spectra in the IR range, acquiring data of each wavenumber step independently (Wiens et al., 2017). Downsampling passive reflectance spectra from the optimal over-sampled 15 cm^{-1} or the nominal 30 cm^{-1} resolution (Fouchet et al., 2015) can provide time savings without compromising needed data for initial reconnaissance. For example, three spectra downsampled from the nominal resolution to 190 cm^{-1} show that as low as $\sim 100 \text{ cm}^{-1}$, the mineral class is discernable, depending on the exact mineral in question (Figure 2-13). It will also be possible to selectively sample portions of the spectral range most diagnostic of mineral classes of interest at the nominal resolution, while lowering the spectral sampling at other wavelengths. Because the SuperCam IR passive data are the only Mars-2020 data suited for detection and distinguishing hydrated/hydroxylated mineral-bearing outcrops in the far field, these lower spectral resolution measurement modes may be highly useful for reconnaissance of potential campaign locations while allowing more efficient rover operations. Of course, follow-on high-resolution spectra are required to move from mineral class to identification of specific minerals (e.g. clay vs. montmorillonite or carbonate vs. calcite). The ability to select a specific wavelength of measurement in the IR range also allows SuperCam to make rudimentary band depth maps at the outcrop scale by rastering across the outcrop with three specific wavelengths selected to give a band depth at each point, again reducing data needs while permitting large-scale reconnaissance.

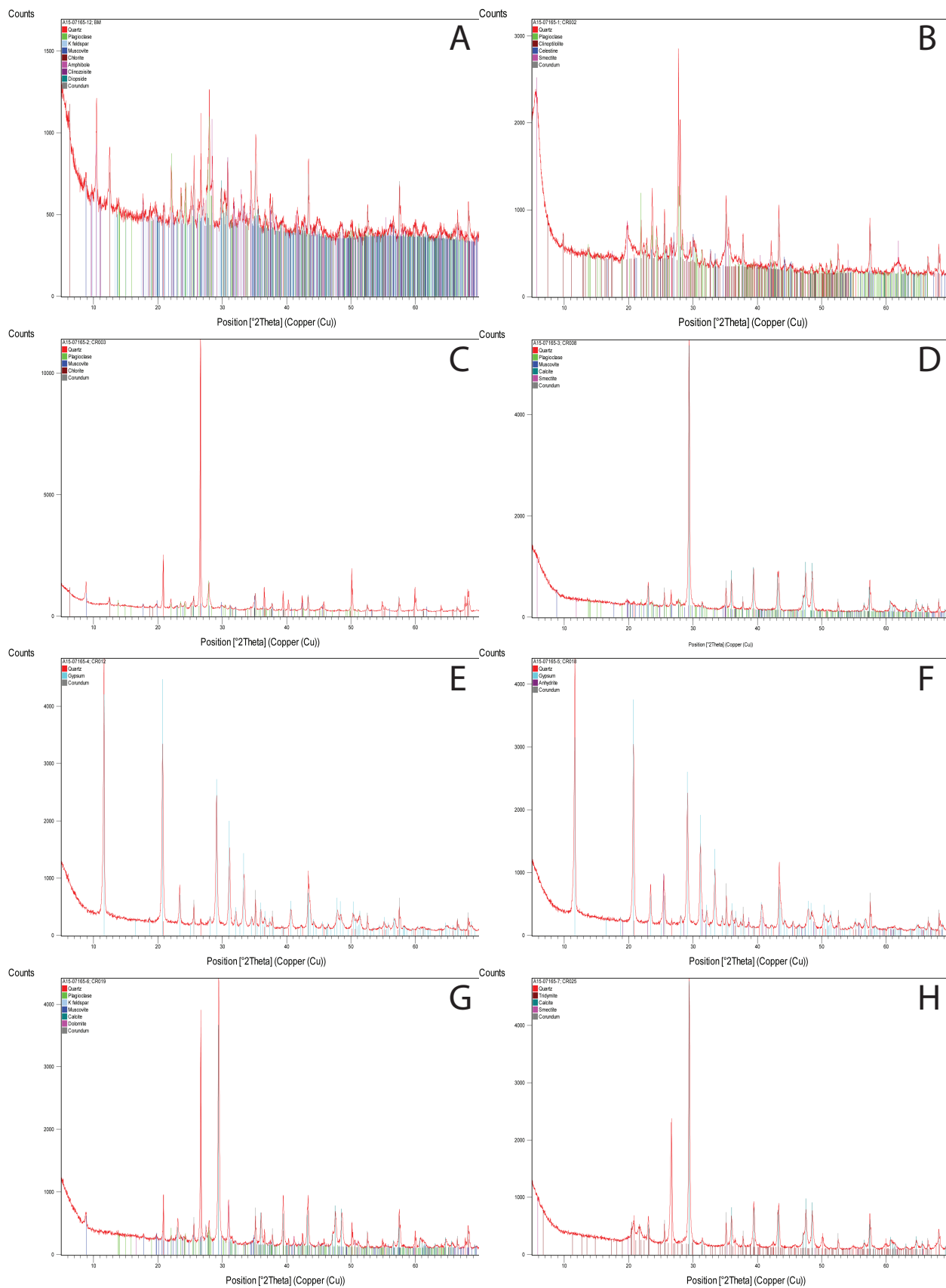
Similarly, spatial downsampling of SHERLOC and PIXL may be used to acquire “quick-look” or lower data volume reconnaissance data that remote sensing instruments are unable to easily provide, e.g. searching for the presence of organics with SHERLOC or an element like zirconium with PIXL. These modes may also be used for selection of targets for higher resolution analysis by the same instruments in a given workspace, especially for eventual drill target selection, where comprehensive but low-resolution data will ensure no important potential drill sites are left uninvestigated.

2.6 Conclusions

Using data simulating the Mars-2020 instrument suite, an outcrop near China Ranch in the Mojave Desert was analyzed in a similar fashion to the likely analytical procedures to be followed in the upcoming mission. Overall, we find that the Mars 2020 instruments are well suited and complement each other to provide rapid reconnaissance for selection of samples to cache. Coarse unit discrimination and target selection was made using the simulated Mastcam-Z color filters, and was further aided by full Mastcam-Z multispectral data, enhanced by the use of decorrelation stretches. SuperCam VIS/IR point spectra were critical to identifying unit composition and compositional variability remotely. Carefully selected transects identified montmorillonite, carbonate, and gypsum-montmorillonite mixtures for each of the units delineated using Mastcam-Z. Together, the Mastcam-Z and SuperCam passive VIS/IR and Raman data allowed mapping of the general mineralogy of units present in the outcrop. LIBS gave reconnaissance-level major element chemistry that allowed further identification of targets for proximity science. The proximity science instruments confirmed expected mineralogy based on chemistry from PIXL; PIXL also identified previously unrecognized trace element patterns that would prompt further investigation and sampling for geochronology. Salts were readily identified and mapped with SHERLOC deep UV spectra. Organics were identified in all collected samples with fluorescence data from SHERLOC with more detailed information provided by Deep-UV Raman in some cases. Materials from the carbonate, finely laminated clay mudstones, and gypsiferous mudstones with organics would likely be considered for sampling and caching. Successful collection and caching of these samples would fulfill the Mars-2020 requirements to examine a site for Mars's geologic/climate history, search for signs of life, and collect and cache samples at this site alone. These results indicate that the instrument suite as simulated in this study is capable of exploration, identification of units of interest, and sampling and caching to support the high-level goals of the Mars-2020 mission.

The study further revealed approaches that could improve science return and operational efficiency and thus warrant further development. First, frequent long distance scans (from tens of meters) using SuperCam's IR passive capability will be important to discriminate compositional changes in outcrops with otherwise similar colors to avoid missing important mineralogical features during the Mars-2020 mission. As an example, coupling remote sensing with proximity data will be essential for identification of potential glassy ash units useful for age dating. Second, cross-

calibration of Mastcam-Z and SuperCam passive data will be required to best recognize and map variation in mafic mineralogy (olivine, pyroxenes, and volcanic glasses), which is most distinct near 1000-1300 nm where there is a gap in spectral coverage between the instruments. Third, further investigation should be made of deep UV Raman spectra of silicate (especially phyllosilicate) minerals to understand what operational modes are optimal for their detection, and both green and deep UV Raman spectral libraries of phyllosilicates are needed. Fourth, libraries of specific organic compounds with the potential to be encountered on Mars should be measured with high spectral resolution fluorescence and Raman spectroscopies to equip the rover with a centralized, comprehensive spectral library from which to interpret mission data.



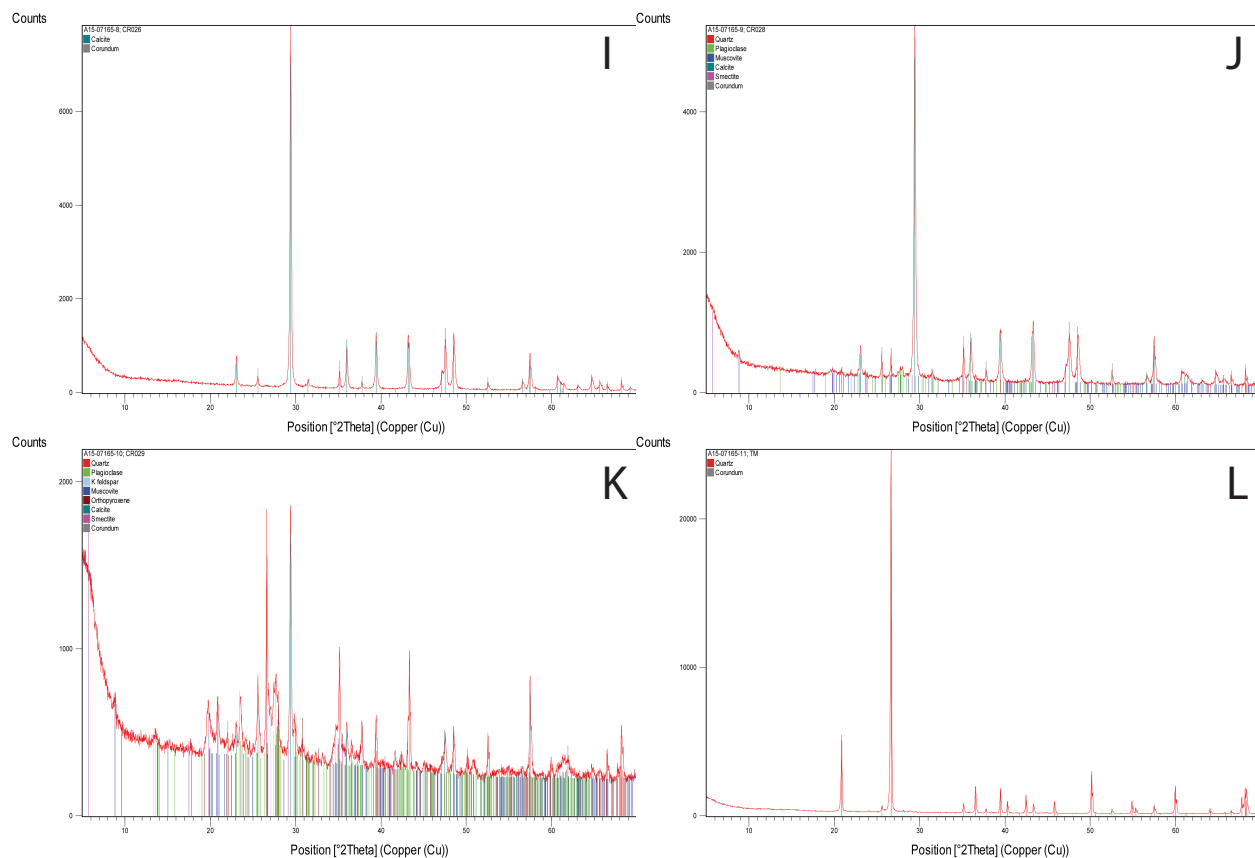


Figure 2-14. XRD spectra for each sample reported in Table 2-3. A) BM, B) CR002, C) CR003, D) CR008, E) CR012, F) CR018, G) CR019, H) CR025, I) CR026, J) CR028, K) CR029, L) TM

A TWO-STEP K-AR EXPERIMENT ON MARS: DATING THE DIAGENETIC FORMATION OF JAROSITE FROM AMAZONIAN GROUNDWATERS

The content of this chapter has been published with the following citation:

Martin, P. E., K. A. Farley, M. B. Baker, C. A. Malespin, S. P. Schwenzer, B. A. Cohen, P. R. Mahaffy, A. C. McAdam, D. W. Ming, P. M. Vasconcelos, and R. Navarro-González (2017). A Two-Step K-Ar Experiment on Mars: Dating the Diagenetic Formation of Jarosite from Amazonian Groundwaters. *Journal of Geophysical Research: Planets*, 122(12), 2017JE005445. <https://doi.org/10.1002/2017JE005445>

3.1 Abstract

Following K-Ar dating of a mudstone and a sandstone, a third sample has been dated by the Curiosity rover exploring Gale crater. The Mojave 2 mudstone, which contains relatively abundant jarosite, yielded a young K-Ar bulk age of 2.57 ± 0.39 Ga (1σ precision). A two-step heating experiment was implemented in an effort to resolve the K-Ar ages of primary and secondary mineralogical components within the sample. This technique involves measurement of ^{40}Ar released in low (500°C) and high (930°C) temperature steps, and a model of the potassium distribution within the mineralogical components of the sample. Using this method, the high-temperature step yields a K-Ar model age of 4.07 ± 0.63 Ga associated with detrital plagioclase, compatible with the age obtained on the Cumberland mudstone by Curiosity. The low-temperature step, associated with jarosite mixed with K-bearing evaporites and/or phyllosilicates, gave a youthful K-Ar model age of 2.12 ± 0.36 Ga. The interpretation of this result is complicated by the potential for argon loss after mineral formation. Comparison with the results on Cumberland and previously published constraints on argon retentivity of the individual phases likely to be present suggests that the formation age of the secondary materials, correcting for plausible extents of argon loss, is still less than 3 Ga, suggesting post-3 Ga aqueous processes occurred in the sediments in Gale crater. Such a result is inconsistent with K-bearing mineral formation in Gale Lake, and instead suggests post-depositional fluid flow at a time after surface fluvial activity on Mars is thought to have largely ceased.

3.2 Introduction

The surface regions of Mars and their associated geologic features are divided into three major epochs: the Noachian (4.1–3.7 Ga), the Hesperian (3.7–3.1 Ga), and the Amazonian (3.1–present) (Hartmann and Neukum, 2001; Nimmo and Tanaka, 2005). The Noachian is characterized by abundant surface water, illustrated by the presence of phyllosilicates and high-drainage-density valley networks (e.g., Ehlmann et al., 2011; Fassett and Head, 2008). A relative increase in the proportions of sulfates and other evaporite minerals, along with the lack of highly dissected drainage networks, in Hesperian-aged terranes suggest a large-scale desiccation of Mars (Bibring et al., 2006). This overall drying trend continued in the Amazonian, with liquid water playing no apparent major role in generating or altering large-scale features of the Martian surface during this time period. Understanding the absolute and relative timing of these geomorphic and mineralogical features is critical to a complete understanding of the planet’s evolution. However, the ages of Mars’s epochs are based on cratering chronology and are accordingly subject to limitations and uncertainties inherent to that technique (e.g., Hartmann and Daubar, 2017; Hartmann, 2005; Hartmann and Neukum, 2001; McEwen et al., 2005; Robbins et al., 2014).

Although the Curiosity rover was not designed to implement the K-Ar method, by combining the capabilities of the Alpha Particle X-ray Spectrometer (APXS), CheMin, and Sample Analysis at Mars (SAM) instruments onboard the rover, in situ radiometric dating of Martian materials by the K-Ar method is possible (Farley et al., 2014), albeit with analytical uncertainties far larger than those routinely obtained in terrestrial labs. The results of Farley et al. (2014) and Vasconcelos et al. (2016) represent the first attempts at off-planet radiometric geochronology. A K-Ar bulk age of 4.21 ± 0.35 Ga (1σ) was obtained from the Cumberland sample (Farley et al., 2014), drilled from the Sheepbed lacustrine mudstone in Gale crater. This age is consistent with crater-counting results from nearby terranes (Le Deit et al., 2012) and the expected ancient age of igneous materials on Mars, suggesting that the technique successfully retrieved the formation age of minerals in the sample. A second geochronology experiment was undertaken on the Windjana sandstone in the Kimberly formation; this experiment was clearly unsuccessful because it resulted in extremely variable and young K-Ar ages of 627 ± 50 Ma and 1710 ± 110 Ma on separate aliquots of the same sample (Vasconcelos et al., 2016). The failure of this second experiment has been attributed to incomplete argon extraction due to a combination of the larger grain size of the material sampled at Windjana compared to that

of Cumberland, as well as the extraordinary abundance of the highly argon-retentive mineral sanidine (~20 wt%) in the Windjana sample.

The mudstone sample Mojave 2, drilled later in the mission in the Pahrump Hills, was found to contain several weight percent jarosite [$\text{KFe}_3(\text{SO}_4)_2(\text{OH})_6$], making it the most jarosite-rich sample yet discovered by Curiosity (Rampe et al., 2017). Like many other samples measured by CheMin, Mojave 2 also contains phyllosilicates and an amorphous component (Rampe et al., 2017). As jarosite is formed by interaction with water (as are the phyllosilicates and possibly the amorphous materials), the Mojave 2 sample potentially offers an opportunity to investigate the timing of aqueous interaction with the sediments in Gale crater relative to the formation of the potassium-containing detrital igneous grains (i.e., feldspar and any glass present) in those sediments. A unique aspect of the current work is an attempt to separate the ages of these two components. Jarosite has been shown to be suitable for K-Ar dating (Vasconcelos et al., 1994), and releases argon at temperatures below 500°C (Kula and Baldwin, 2011). In contrast, plagioclase retains the vast majority of its argon to above 500°C (e.g., Bogard et al., 1979; Cassata et al., 2009). To take advantage of this differential Ar release, a two-step heating methodology was devised and applied to Mojave 2; stepped heating experiments are a standard technique in noble gas geochronology used to resolve ages of various components in single samples. Such a two-step measurement was not attempted for the Cumberland sample to allow method development with a simpler analytical protocol; two-step heating for the Windjana sample was not attempted due to the small amount of potassium inferred to be held in its secondary phases. The phases present in Mojave 2 cluster conveniently by formation mechanism and argon release temperature: the low-temperature step should yield information about the formation and preservation of minerals associated with water in the sample (i.e., secondary components), while the high-temperature step should date detrital components only.

3.3 Sample and methodology

3.3.1 Sample description

The Mojave 2 drill hole is located stratigraphically low in the Pahrump Hills locality, which is in the Murray mudstone formation, at the base of Mount Sharp. The Pahrump Hills are ~13 m thick, representing the lowermost 10% of the Murray formation (Grotzinger et al., 2015). The

Murray is a deposit of mudstone and fine-grained sandstone with mm-scale lamination interpreted to represent the distal lacustrine sediment deposited in the lake once contained in Gale crater. Mojave 2 is located within a finely-laminated mudstone in the Pahrump Hills, with a grain size too small to be resolved by MAHLI ($<60\text{ }\mu\text{m}$; Grotzinger et al., 2015). These fine-grained sediments interfinger with the coarser-grained deltaic sediments which comprise the lower Bradbury group (Grotzinger et al., 2015). The coarsening-upwards nature of the Pahrump Hills sequence indicates fluvio-deltaic progradation over the older lacustrine mudstone deposits (Grotzinger et al., 2015).

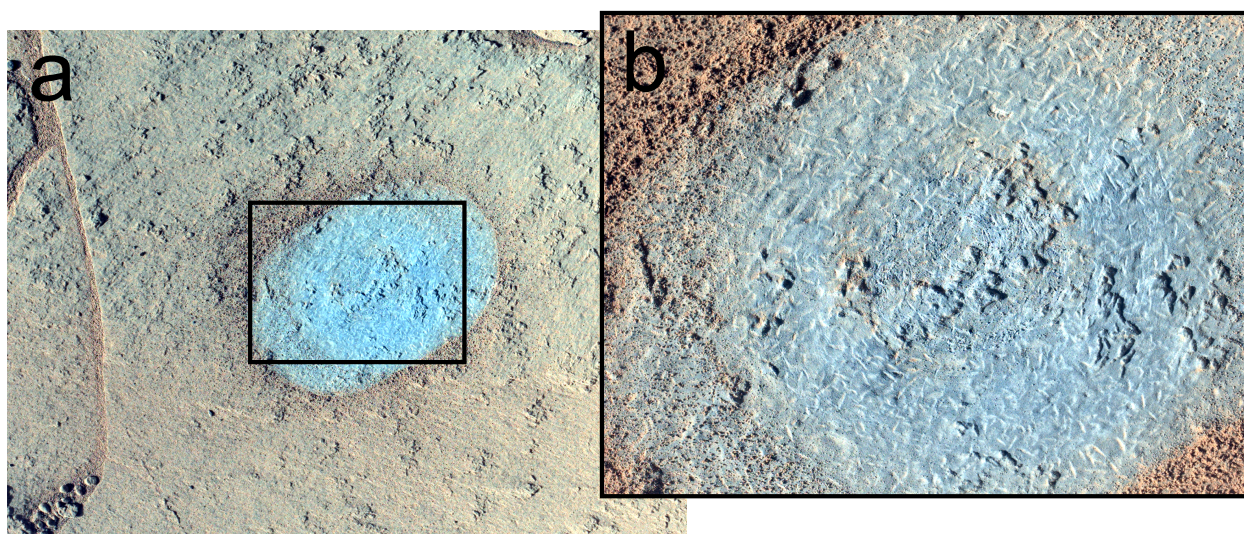


Figure 3-1. MAHLI images of (A) the brushed Mojave 2 surface, showing pronounced crystal laths, and (B) a magnification of image (A) in the area denoted by the black rectangle. The brushed area is approximately 4 cm across along the short axis. The color has been stretched to increase contrast.

Diagenetic features have been observed in the Pahrump Hills and in association with the Mojave 2 target specifically (Gellert et al., 2015; Grotzinger et al., 2015; McBride et al., 2015; Nachon et al., 2017; Schieber et al., 2015). Lenticular crystal laths, lighter in color than the host rock, comprise ~30% of the substrate in the brushed Mojave 2 target (Figure 3-1; McBride et al., 2015; Schieber et al., 2015). Their presence in broken pieces of outcrop show that these features extend vertically into the bedrock, implying they are not simply a surface feature (Grotzinger et al., 2015). On the basis of morphology, these lenticular forms have been suggested to be gypsum crystals which, in terrestrial environments, form in saline mudflats and ephemeral lakes (Mees et al., 2012; Schieber et al., 2015). Given the lack of mineralogical (CheMin) or chemical (APXS) evidence for calcium sulfates in the Mojave 2 sample, it is possible that these crystal laths formed syndepositionally with

the Murray mudstone, and were later redissolved by post-depositional fluid flow, forming pseudomorphs of unknown composition (L. Kah, personal communication, 2017).

Drilling followed standard MSL procedures: a 5 cm deep hole was drilled, and rock from below 1.5–2 cm depth was delivered to the CHIMRA unit on board Curiosity (Sunshine, 2010). The rock cuttings were sieved to <150 μm for delivery to the SAM and CheMin (Anderson et al., 2012; Mahaffy et al., 2012).

3.3.2 Sample chemistry and mineralogy

Table 3-1. Mineralogy of samples used for geochronology by Curiosity^a

Mineral	Mojave 2 ^b	Windjana ^c	Cumberland ^d
Plagioclase	23.5 \pm 1.6	3.0 \pm 0.3	22.2 \pm 1.3
Sanidine	-	21.0 \pm 3.0	1.6 \pm 0.8
Forsterite	0.2 \pm 0.8	4.7 \pm 1.0 (olivine)	0.9 \pm 0.45
Augite	2.2 \pm 1.1	20 \pm 0.3	4.1 \pm 1.0
Pigeonite	4.6 \pm 0.7	11 \pm 0.2	8.0 \pm 2.0
Orthopyroxene	-	-	4.1 \pm 1.0
Magnetite	3.0 \pm 0.6	12 \pm 0.2	4.4 \pm 1.1
Hematite	3.0 \pm 0.6	0.6 \pm 0.4	0.7 \pm 0.35
Anhydrite	-	0.4 \pm 0.3	0.8 \pm 0.4
Bassanite	-	0.5 \pm 0.4	0.7 \pm 0.35
Quartz	0.8 \pm 0.3	-	0.1 \pm 0.1
Jarosite	3.1 \pm 1.6	-	-
Fluorapatite	1.8 \pm 1.0	0.8 \pm 0.8	-
Ilmenite	-	0.8 \pm 0.5	0.5 \pm 0.5
Akaganeite	-	0.2 \pm 0.2	1.7 \pm 0.85
Halite	-	-	0.1 \pm 0.1
Pyrrhotite	-	0.3 \pm 0.3	1.0 \pm 0.5
Phyllosilicate	4.7 \pm 2.4	10 \pm 0.2	18 \pm 9
Amorphous	53 \pm 15	15 \pm 0.3	31 \pm 19

^a Phases potentially containing significant potassium are in bold. See references for discussions of reported uncertainties.

^b(Rampe et al., 2017)

^c(Treiman et al., 2016)

^d(Vaniman et al., 2014)

The mineralogy of Mojave 2 includes plagioclase and jarosite, and no detectable sanidine (~1 wt% detection limit (Vaniman et al., 2014); the full mineralogy is listed in Table 3-1). This

mineral assemblage paradoxically suggests both oxidizing (hematite) and reducing (magnetite) environments, as well as acidic (jarosite) and neutral (apatite) conditions. This juxtaposition could imply a post-depositional acidic, oxidizing fluid flowed through the Pahrump Hills area, possibly forming the jarosite (Rampe et al., 2017). Mojave 2 also contains an amorphous phase making up over 50 wt% of the total sample (Rampe et al., 2017). A comparison to the apparently successful geochronology experiment on Cumberland reveals that the only major difference in mineralogy between the two samples is the presence of jarosite in Mojave 2, which is known to be amenable to argon extraction at relatively low temperatures. In contrast with the failed run at Windjana on the other hand, the lack of coarse-grained sanidine in Mojave 2 eliminates this potential difficulty with argon extraction.

Table 3-2. APXS results from Mojave 2^a

Chemistry (wt%)	
SiO ₂	49.48
TiO ₂	1.19
Al ₂ O ₃	11.43
FeO	16.11
MnO	0.40
MgO	4.55
CaO	4.33
Na ₂ O	3.01
K ₂ O	0.73
P ₂ O ₅	1.29
Cr ₂ O ₃	0.37
Cl	0.43
SO ₃	6.27
Ni (ppm)	1032
Zn (ppm)	2204
Br (ppm)	65

^aMeasured on the post-sieve dump pile. Accuracy relative to calibration is 15% of the absolute value (R. Gellert, personal communication, 2017).

The chemical composition of Mojave 2 was measured several times by the APXS instrument: the surface of Mojave 2 after the dust removal tool (DRT) was applied to the surface, tailings from a preliminary “mini-drill” of the Mojave 2 outcrop, the drill tailings from the full drill, the dump pile from before sieving was completed (unsieved), and the dump pile discarded after sieving (sieved to <150 µm) and delivery to the SAM and CheMin instruments; these measurements yielded K₂O contents of 0.69, 0.74, 0.63, 0.73, and 0.73 wt%, respectively. Of the available measurements, the

pre-sieve and post-sieve dump piles are the most closely related to the K₂O content of the Mojave 2 sample measured by SAM, because they consist of the same material taken from below the 1.5-2 cm depth during drilling, while the other measurements targeted materials which were not ingested by the rover. The fact that the K₂O measurements of the pre- and post-sieve sample are identical adds confidence in this measured value. The full chemistry of the post-sieve dump pile is shown in Table 3-2.

3.3.3 Release temperatures

To correlate the ⁴⁰Ar releases in each temperature step (<500°C and 500–930°C) with the component of the sample containing the associated parent ⁴⁰K, the temperature step in which each potassium-bearing material releases Ar must be established. Of the minerals in Mojave 2, plagioclase, jarosite, phyllosilicates (e.g., illite), the amorphous phase(s) and possibly pyroxene are the only components likely to contain significant proportions of the total potassium. Pyroxenes release argon at very high temperatures (Cassata et al., 2011). However, the median K₂O content of over a thousand microprobe analyses of pyroxenes in Martian meteorites with non-zero K₂O values is ~0.02 wt% (references given in Supplement A), indicating that the ~6.8 wt% of pyroxene in Mojave 2 plays no role in the K-Ar characteristics of this bulk-rock analysis. Plagioclase hosts potassium (see section 3.4.1 below) and is known to release the vast majority of its argon in excess of 500°C (Bogard et al., 1979; Cassata et al., 2009), so it will degas almost entirely in the high-temperature step. Indeed, complete Ar degassing from plagioclase might be expected to require temperatures higher than the 930°C achieved in the SAM oven. Based on the very old age of 4.21±0.35 Ga measured on the Cumberland mudstone, complete (or near-complete) extraction of Ar from feldspar was apparently achieved (Farley et al., 2014). It is possible that the small grain size of the mudstone and/or flux melting associated with volatile-bearing minerals in the rock aid in the release of Ar. The similarities in grain size and mineralogy between Mojave 2 and Cumberland suggest that near complete Ar release from plagioclase in Mojave 2 might be expected as well. Jarosite begins to break down structurally at ~300°C, implying that Ar release occurs via disruption of the mineral lattice (as opposed to diffusion) well below the first temperature step cutoff of 500°C (Kula and Baldwin, 2011). In Ar-Ar dating experiments, illite and other clays have been shown to release >95% of their total Ar content below 500°C (Evernden et al., 1960; Hassanipak and

Wampler, 1996). Illite argon release may also proceed by structural changes during dehydroxylation (Halliday, 1978), suggesting that behavior similar to jarosite might be expected.

Characterizing the expected Ar release temperatures for the amorphous fraction is more complex, since the phase or phases that host potassium in this material are uncertain, even though the amorphous fraction contains a non-trivial fraction of the potassium in Mojave 2 (see section 3.4.1. for discussion). Likely constituents of the amorphous fraction such as nanophase iron oxide, hissingite, and allophane are devoid of potassium. Glass is unlikely to be present in Mojave 2 (see section 3.4.1.1), but would, if present, likely contain at least some potassium and release its argon mostly in the high-temperature step (Gombosi et al., 2015). More speculatively, potassium in the amorphous fraction may be carried by X-ray amorphous salts that would likely release Ar in the low-temperature step. As an example, the common K-bearing salt KCl (sylvite) releases Ar at temperatures $<500^{\circ}\text{C}$ (Amirkhanoff et al., 1961). Similarly, if any potassium-containing salts in Mojave 2 are hydrated, they could potentially behave in a similar manner to jarosite, breaking down via dehydration and releasing argon due to crystallographic shifts at $<500^{\circ}\text{C}$ (e.g., $\sim 255^{\circ}\text{C}$ for the common K-bearing sulfate polyhalite $[\text{K}_2\text{Ca}_2\text{Mg}(\text{SO}_4)_4 \cdot 2\text{H}_2\text{O}]$; Leitner et al., 2014). The assumption that any salts present would likely release Ar in the low-temperature step is also supported by the fact that they must be amorphous or nanocrystalline ($\lesssim 500$ unit cells) to avoid detection by CheMin. The tiny grain size and/or lack of large-scale crystalline order might further decrease the argon release temperatures of these materials.

To summarize, Ar in the high-temperature step will be strongly dominated by plagioclase, a detrital igneous mineral. In contrast, the low-temperature step will carry Ar from jarosite and possibly from nanocrystalline salts and clays. Jarosite and any salts in Mojave 2 are almost certainly diagenetic and/or authigenic (Rampe et al., 2017) and clays measured in earlier samples at Gale crater appear to be authigenic (Bristow et al., 2015). Thus the two-step experiment may isolate the K-Ar age of the detrital igneous components from the K-Ar age of fluid-associated low-temperature diagenetic/authigenic phases.

3.3.4 Noble gas extraction

Samples were delivered to preconditioned quartz cups in the SAM instrument prepared by the same method described by Ming et al. (2014). A portioning tube of known volume (76 mm³) was used to pour sample into a funnel that delivered the powder to the SAM instrument. The exact amount of sample delivered is not directly measured. Rather, a model is used to describe the most likely amount transferred (Farley et al., 2014). Three separate aliquots of Mojave 2 were delivered to the SAM instrument to facilitate multiple independent measurements: two triple-portion aliquots (135±18 mg each, all reported uncertainties are 1σ) were used for noble gas geochronology experiments, and one single-portion aliquot (45±6 mg) was used in an evolved gas analysis (EGA; Sutter et al., 2017). While the first triple-portion aliquot was deposited in a pristine quartz cup, the second was deposited on top of the residue of the single-portion aliquot (i.e., into the same sample cup already used for EGA). It is possible that some ⁴⁰Ar could be retained by this single portion through the EGA heating process and then released during the high-temperature step of the noble gas experiment. Because the aliquot previously analyzed during EGA is one third of the mass of the aliquot used for noble gas measurement, and because EGA reaches temperatures similar to those achieved in noble gas extraction, we consider the total effect of this potential extraneous argon release to be negligible.

After delivery, each sample was prepared for noble gas measurements by conducting a “boil-off” stage, where the sample was heated gradually over 26 minutes to a maximum target temperature of ~150°C under He flow to drive off adsorbed volatiles, which are mostly composed of residual derivatizing agent in the SAM vacuum system or adsorbed on the sample (Freissinet et al., 2015; Glavin et al., 2013). After “boil-off”, the first step was performed by heating the sample monotonically to ~500°C over approximately one hour, targeting phases that release argon at low temperatures. We use the term “low-temperature phases” for these materials in reference to the temperature of argon release (as opposed to their formation temperature). Unlike a typical EGA, the released gases were exposed to the Linde 13x zeolite scrubber and an SAES ST175 sintered titanium and molybdenum getter (heated to approximately 300°C) within SAM to purify the noble gases of reactive species (Mahaffy et al., 2012). After the gases were purified, they were first measured by the quadrupole mass spectrometer (QMS) in a low-sensitivity dynamic mode (Farley et al., 2014), similar to a conventional EGA analysis (Sutter et al., 2017) but without the He carrier gas. Upon

completion of the dynamic mode measurements, a semi-static mode was initiated wherein a valve pumping the QMS was almost entirely closed to allow a buildup of pressure, increasing sensitivity (Farley et al., 2014). At the end of the semi-static measurement, all gas was pumped out of the manifold while leaving the QMS in scanning mode to enable a determination of the background present in semi-static mode (Vasconcelos et al., 2016). The following sol, an identical procedure was followed with the second heating step, which reached a peak temperature of around 930°C, releasing radiogenic argon from the phases with high release temperatures (“high-temperature phases”). This two-step heating procedure was validated using the SAM testbed instrument on Earth prior to its execution on Mars.

3.3.5 Quantification of ^{40}Ar

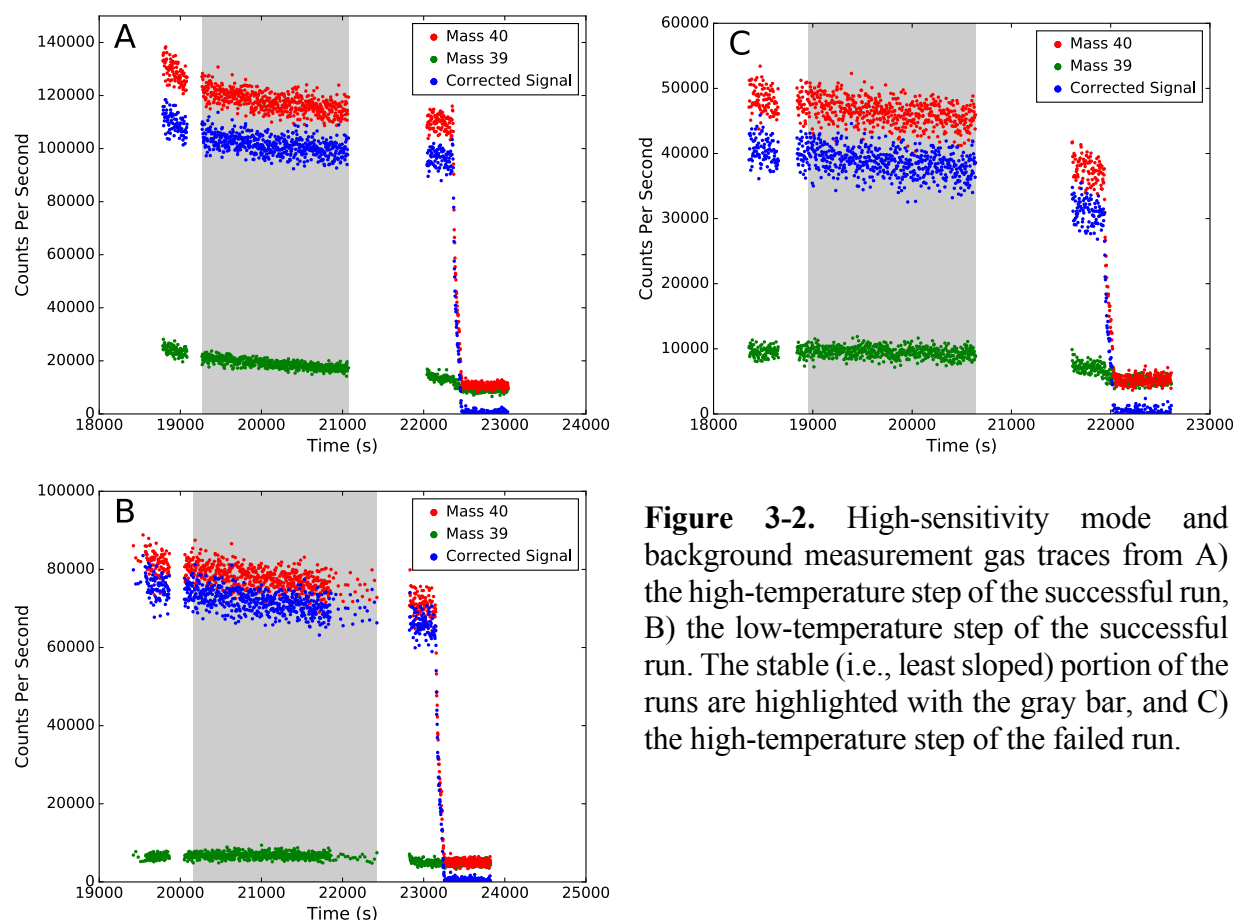


Figure 3-2. High-sensitivity mode and background measurement gas traces from A) the high-temperature step of the successful run, B) the low-temperature step of the successful run. The stable (i.e., least sloped) portion of the runs are highlighted with the gray bar, and C) the high-temperature step of the failed run.

The mass 40 peak in the mass spectrum (M40) is corrected for a small isobaric contribution from the hydrocarbon C₃H₄ using mass 39 (C₃H₃) as a tracer (Figure 3-2). The ratio of C₃H₄/C₃H₃ was measured to be 0.56±0.02 earlier in the mission during a previous SAM run containing little to no ⁴⁰Ar. The ⁴⁰Ar contribution to the mass 40 signal can then be calculated as follows:

$$^{40}\text{Ar} = \text{M40} - \text{M39} \times 0.56 \quad (3-1)$$

After hydrocarbon isobaric interferences are corrected, the background measured at the end of the run is subtracted from the mass spectrum, yielding what we infer to be the ⁴⁰Ar peak. In the absence of additional data we cannot correct for Martian atmosphere-derived ⁴⁰Ar or any other non-radiogenic sources of ⁴⁰Ar. As previously discussed by Farley et al. (2014), non-radiogenic ⁴⁰Ar is unlikely to be significant in these ancient K-rich rocks.

3.4 Results

Here we develop a model for the potassium content of each phase in Mojave 2, and then calculate the K-Ar age of the bulk sample and each step separately using the model. Unless otherwise specified, the word age herein refers to the K-Ar age (i.e., the output of the age equation). Therefore, the terms “bulk age”, “model age”, “mixed age”, and “K-weighted average age” mean the K-Ar age of the entire sample, the K-Ar age of one or more specific components of the sample, the K-Ar age of multiple components of the sample, and the K-Ar age resulting from multiple combined components with differing potassium contents, respectively. The one exception is the phrase “formation age”, which refers to the time at which a component physically formed.

3.4.1 Potassium partitioning

A model of the K₂O content of each phase in Mojave 2 is vital for assigning ages to the diagenetic and detrital components based on ⁴⁰Ar release from the low- and high-temperature steps. This problem may be modeled by a simple mass-balance equation:

$$K_T = K_2 + K_1 = K_{\text{plag}} + K_{\text{K-spar}}^* + K_{\text{jar}} + K_{\text{phyllo}} + K_{\text{amorph}} \quad (3-2)$$

$$K_2 = K_{\text{plag}} + K_{\text{K-spar}}^* \quad (3-3)$$

$$K_1 = K_{\text{jar}} + K_{\text{phyllo}} + K_{\text{amorph}} \text{ or } K_1 = K_T - K_2 \quad (3-4)$$

Where K_T is the total potassium in the sample, K_2 and K_1 are the total potassium contents of the phases releasing argon in high- (step 2) and low-temperature (step 1) steps, and K_{plag} , $K_{\text{K-spar}^*}$, K_{jar} , K_{phyllo} , and K_{amorph} are the potassium contents of each individual component (plag = plagioclase, K-spar* = potassium feldspar, jar = jarosite, phyllo = phyllosilicate, amorph = amorphous) weighted by their abundances as determined by CheMin (Table 3-1). $K_{\text{K-spar}^*}$ is noted with an asterisk because although potassium feldspar was not detected in the Mojave 2 sample, it has been detected in eight of the eleven samples drilled thus far in the mission and thus we cannot, a priori, rule out the presence of potassium feldspar in Mojave 2 at concentrations below the CheMin detection limit (~1 wt%; Vaniman et al., 2014). The effect that <1 wt% potassium feldspar might have on the step 1 and step 2 model ages is included in the discussion below. The two forms of Equation 3-4 reflect that $K_{\text{phyllo}} + K_{\text{amorph}}$ are not well constrained by CheMin and thus K_1 is better estimated by difference. Given the bulk K_2O content of the sample and the total amount of ^{40}Ar released during heating ($^{40}\text{Ar}_T$), the bulk K-Ar age of the sample is calculated from the ratio:

$$^{40}\text{Ar}_T/K_T \quad (3-5)$$

Since the total ^{40}Ar release is simply the sum of ^{40}Ar released in each heating step,

$$^{40}\text{Ar}_T = ^{40}\text{Ar}_1 + ^{40}\text{Ar}_2 \quad (3-6)$$

the model age associated with each step is calculated by

$$^{40}\text{Ar}_2/K_2 \quad (\text{high-T step}) \quad (3-7)$$

and

$$^{40}\text{Ar}_1/K_1 \text{ or alternatively } ^{40}\text{Ar}_1/(K_T - K_2) \quad (\text{low-T step}), \quad (3-8)$$

which is then used to solve the K-Ar age equation, after converting K to ^{40}K :

$$t = \frac{1}{\lambda} \ln \left[\frac{^{40}\text{Ar}}{^{40}\text{K}} \left(\frac{\lambda}{\lambda_e} \right) + 1 \right] \quad (3-9)$$

where t is time since formation, λ is the ^{40}K decay constant ($5.5492 \pm 0.0093 \times 10^{-10} \text{ a}^{-1}$; Renne et al., 2010), and λ_e is the electron capture decay constant ($5.755 \pm 0.016 \times 10^{-11} \text{ a}^{-1}$; Renne et al., 2010). It is apparent from Equations 3-7 and 3-8 that estimating the fraction of the bulk K_2O content measured by APXS that is contained in phases that degas in each of the steps is critical to determining the model step ages, and that assumptions made about the potassium contents of these phases will affect the model ages of both steps.

The K_2O content of the plagioclase cannot be directly measured by any instrument onboard Curiosity but it can be estimated from published analyses of plagioclase in Martian meteorites. The average anorthite content (An , defined as $100 \times \text{Ca}/(\text{Ca} + \text{Na})$, molar) of Mojave 2 was calculated using plagioclase unit-cell parameters that are based on a Rietveld refinement; the resulting value is $\text{An}_{41 \pm 6}$ (Rampe et al., 2017). The calculated plagioclase composition for Mojave 2 reported more recently by Morrison et al. (2017) are identical: An_{41} . In both terrestrial plagioclases (e.g., Deer et al., 1997) and Martian meteorite “plagioclases” (e.g., Papike et al., 2009), there is a broad inverse correlation between Ca\# ($100 \times \text{Ca}/(\text{Ca} + \text{Na})$, molar) and the K_2O content of the plagioclase, i.e., more Na-rich plagioclases have higher K_2O contents. Note that An number mentioned above is equivalent to Ca\# and the vast majority of Martian “plagioclases” are actually maskelynite (e.g., McSween and Treiman, 1998). Based on 1,442 “plagioclase” analyses from Martian meteorites with $100 \times \text{K}/(\text{Ca} + \text{Na} + \text{K}) < 10$ (molar; a commonly used dividing line between plagioclase and alkali feldspar; Deer et al., 1997), we fit a third-order polynomial to the K_2O content (in wt%) as a function of Ca\# (Figure 3-3). Fitting was done by minimizing the sum of absolute deviations and all plotted “plagioclase” compositions satisfy the stoichiometric constraints discussed in Papike et al. (2009). Our data set includes analyses from both the polymict breccia NWA 7034/7533/7475 (of Noachian age; Humayun et al., 2013) and SNCs (plus the orthopyroxenite ALH 84001). All together, these samples span nearly the entire geologic history of Mars and, more importantly, calculated K_2O contents at An_{41} based on fits using just the polymict breccia data or the SNC plus orthopyroxenite data overlap at 1σ . Given the functional relationship shown in Figure 3-3, the average An content of Mojave 2 translates into a K_2O content of $0.45 \pm 0.11 \text{ wt\%}$ (see section 3.4.3 for a discussion of uncertainty estimations). Based on this estimate, plagioclase contains around 15% of the total K_2O in Mojave 2, implying that K_{plag} (Equations 3-2 and 3-3) is $0.11 \pm 0.02 \text{ wt\% K}_2\text{O}$.

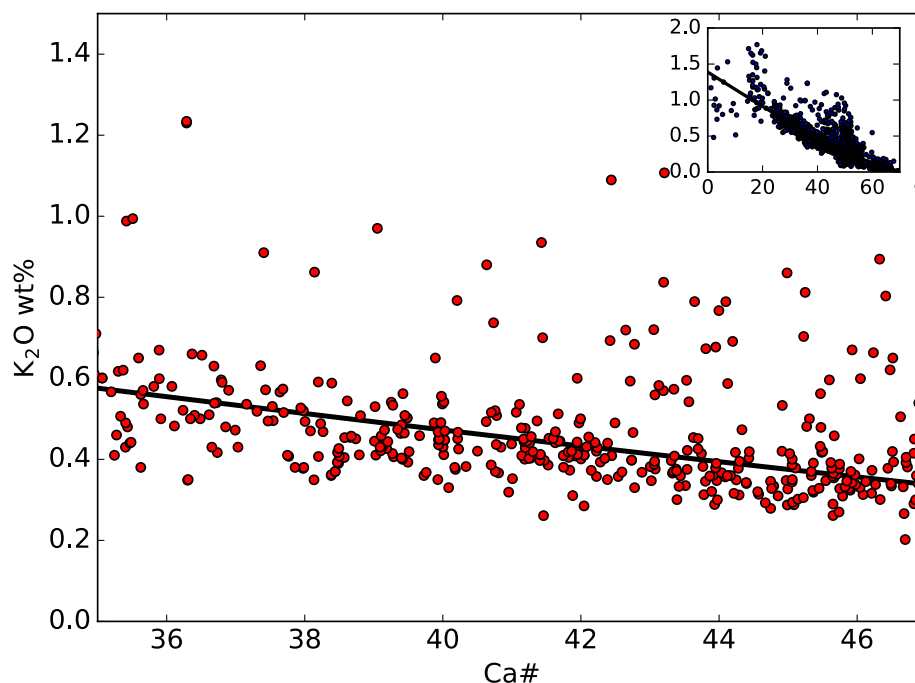


Figure 3-3. Ca# (or An# as defined in Rampe et al., 2017) vs. K₂O content for Martian meteorite plagioclase microprobe analyses (i.e., analyses with molar Or < 10%). For the main panel, the data shown are restricted to plagioclase analyses with Ca#s in the range given by Rampe et al. (2017). The inset shows all plagioclase measurements.

Jarosite forms a solid-solution series with natrojarosite [NaFe₃(SO₄)₂(OH)] in nature (e.g., Brophy and Sheridan, 1965; Dutrizac, 1983; 2008), so K_{jar} will vary depending on the amount of sodium that has substituted for potassium in the jarosite structure. The formation of synthetic jarosite with K/(K+Na)<0.5 requires that the K/(K+Na) of the precipitating solution be <0.1 (Brophy and Sheridan, 1965; Dutrizac, 1983), suggesting that natural jarosites should generally be relatively K-rich; this preference is also observed in analyses of natural samples (Dutrizac, 2008). This preference for K over Na is enhanced at low temperatures (Brophy and Sheridan, 1965), and such low temperatures are believed to have been prevalent throughout Gale crater's history (Vaniman et al., 2014). Based on these considerations of jarosite geochemistry and because the Murray formation does not show strong sodium enrichments (Siebach et al., 2017), we assume limits between pure K-endmember and 1:1 K:Na jarosite. As jarosite makes up 3.1 wt% of Mojave 2, this range in K-content implies that 40–20% of the potassium in the sample is carried by jarosite, placing K_{jar} in the range 0.29±0.10 to 0.15±0.05 wt% K₂O.

The remaining 45–65% of the K_2O in Mojave 2 must reside in the amorphous and/or phyllosilicate fractions. Amorphous material is common in samples at Gale crater, and has also been measured elsewhere on Mars, by both landed missions and orbiters (Bish et al., 2013; Blake et al., 2013; Morris et al., 2000; Singer, 1985; Vaniman et al., 2014). The likely components of the amorphous phases in Gale crater, deduced by examining the differences between expected chemistry based on CheMin results and the APXS measurements, include volcanic or impact glass, hisingerite, amorphous sulfate salts, and nanophase iron oxides (Dehouck et al., 2014). Of these phases, the glasses and sulfates are possible hosts of potassium. Below, we examine the likelihood that potassium is held in glass, salts, or phyllosilicates. Determination of which phase(s) contain potassium is central to the geologic interpretation of the K-Ar age measured. For example, salts, being authigenic and releasing argon at low temperatures, might yield information about when liquid water was most recently present in Gale crater, while a glass, of either igneous or impact origin, would release argon at high temperature and reflect information about the detrital grains in the sample.

3.4.1.1 Glass

Putative glass has been observed on Mars from orbit and in aeolian deposits in Gale crater (Cannon and Mustard, 2015; Minitti et al., 2013), though not in the Gale crater bedrock. The K_2O contents of Martian glasses can potentially vary from values <0.5 wt%, assuming glasses exist that have bulk compositions similar to those of basaltic shergottites (Treiman and Filiberto, 2015) or the basaltic clasts in NWA 7533 (Humayun et al., 2013) to ~ 7 wt% if the glasses are either similar in composition to the most silica-rich breccia clast in NWA 7533 or to the compositions of some melt inclusions in Nakhla (e.g., Lee and Chatzitheodoridis, 2016). Given this large range in potassium concentrations, all of the K_2O in the amorphous fraction could hypothetically be accommodated by the presence of a glass with ~ 2 wt% K_2O (assuming half of the total amorphous content of the sample is glass). However, glass devitrifies to plagioclase and other minerals or dissolves rapidly under most geologic conditions, especially in the presence of water, and even more so in high-ionic strength water (Lofgren, 1970; Wolff-Boenisch et al., 2004). For example, a 1 mm basaltic glass sphere at $25^\circ C$ will survive only 500 years in moderately acidic conditions (~ 4000 years for a glass of rhyolitic composition; Wolff-Boenisch et al., 2004). The Mojave 2 sample, the Pahrump Hills area, and Gale crater more broadly, exhibit abundant evidence for the presence of liquid water at the time of

deposition, post-deposition, and during diagenesis (e.g., Gellert et al., 2015; Grotzinger et al., 2014; Nachon et al., 2014; Schieber et al., 2015; Stack et al., 2014). Additionally, modeling efforts suggest that any glass present at the Yellowknife Bay locality has dissolved preferentially (Bridges et al., 2015). We therefore find it unlikely that Mojave 2 contains significant amounts of K₂O in glass.

3.4.1.2 Salts

Mojave 2 contains 6.19 wt% SO₃, of which only ~1 wt% is held in jarosite, indicating that ~5 wt% SO₃ in Mojave 2 is held in the amorphous phases. Alternatively, the remaining unassigned SO₃ could be present in individual phases at abundances below the ~1 wt% CheMin detection limit, though the lack of any observed evaporites throughout the mission and the large amount of SO₃ that would need to be contained in these minor mineral phases make this possibility unlikely. Additionally, though no Cl-bearing species are present in the crystalline fraction, Mojave 2 contains 0.42 wt% Cl (Rampe et al., 2017). Fluorapatite is present at 1.8 wt% and could host some chlorine, though even if it is pure chlorapatite, it would carry only 0.12 wt% Cl. This relatively high concentration of anions that cannot be linked (via the CheMin analysis; Table 3-1) to specific minerals containing structural sulfur or chlorine argues for the presence of X-ray amorphous salts in Mojave 2. X-ray amorphous K-bearing sulfate salts have been shown to precipitate from acid sulfate analog brines by cryoprecipitation (Morris et al., 2015). Such amorphous salts are the most likely carriers of a large fraction of the S and Cl in Mojave 2. As potassium is a common cation in salts, X-ray amorphous salts are also likely hosts of potassium in Mojave 2.

3.4.1.3 Phyllosilicates

Potassium in Mojave 2 could also be held in the phyllosilicate fraction, though the exact amount of K-bearing phyllosilicates in Mojave 2 is difficult to constrain. Illite is the most common phyllosilicate containing potassium. Although K-bearing smectite has been observed terrestrially, these occurrences are rare and require formation conditions not thought to have been present in Gale crater (e.g., Bischoff, 1972; Dekov et al., 2007). Due to the combination of the relatively subtle peak position shifts between differing phyllosilicate species and the broadness of those peaks, their characterization is difficult using the XRD pattern generated by the CheMin instrument (Vaniman et al., 2014). However, the 001 spacing of phyllosilicates, a feature that distinguishes illites from

smectites, can be deduced from CheMin data (Bristow et al., 2015). The dehydrating conditions within the measurement chamber can cause smectite to collapse, reducing its 001 spacing to approximately that of illite, making the two phases nearly indistinguishable with respect to CheMin (e.g., Bristow et al., 2015; Treiman et al., 2016; Vaniman et al., 2014). Optimization of the Mojave 2 XRD pattern fit suggests that if illite is present, it does not make up a significant portion of the phyllosilicates (T. Bristow, personal communication, 2017). If nanocrystalline or disordered illitic clays are present, they would not appear as distinct peaks, but would contribute to the broad “hump” in the XRD pattern that is associated with the amorphous component and thus would be included with that component.

The water peak attributed to dehydroxylation in SAM EGA can also provide partial constraints on the nature of the phyllosilicate phases in Mojave 2. There are two dehydroxylation peaks in the Mojave 2 EGA pattern. One occurs at $>800^{\circ}\text{C}$, and is more consistent with smectite clay minerals (e.g., saponite) than illite (McAdam et al., 2017). The amount of water released at this high temperature and measured by SAM EGA is consistent with the wt% of phyllosilicates calculated from the XRD pattern if the clay minerals are entirely smectite (McAdam et al., 2017). The other dehydroxylation peak occurs at a lower temperature of $\sim 450^{\circ}\text{C}$, is attributed to jarosite, and the water abundance is within error of the expected amount based on the CheMin estimate of the mass fraction of jarosite in Mojave 2 (McAdam et al., 2017).

Overall, there is no data precluding K-bearing phyllosilicates in Mojave 2, but nor is there any evidence to support their presence, especially at a high abundance. The exact distribution of K_2O between putative K-phyllosilicate and salt components is unknown and cannot be quantitatively constrained based on the available data, but it appears likely that most or all of the K_2O associated with the low-temperature release of argon not attributable to jarosite is held in X-ray amorphous salt species.

3.4.2 ^{40}Ar results

Table 3-3 shows the ^{40}Ar results obtained from the two heating steps of Mojave 2 (aliquot 2, see paragraph below). In the first step, 3590 ± 480 pmol/g of ^{40}Ar were measured, while 2330 ± 320 pmol were measured in the second step. For both steps the hydrocarbon correction was small, $\sim 10\%$

of the mass 40 signal on step 1 and ~5% on step 2. The correction associated with background measured at the end of the runs was similarly small, a 5% correction to step 1 and a 3% correction to step 2. These corrections are slightly higher than those applied to the Cumberland (Farley et al., 2014) and Windjana (Vasconcelos et al., 2016) samples, mainly because the ^{40}Ar yields were lower during the two individual Mojave 2 heating steps and the amount of hydrocarbons measured in the SAM instrument was somewhat higher.

Table 3-3. Noble Gas Results from Mojave 2

	K_2O (wt%)	^{40}Ar (pmol/g)	K-Ar age (Ga)
Bulk (aliquot 2)	$K_T = 0.73 \pm 0.11$	5920 ± 800	2.57 ± 0.40
Low-Temperature Step (aliquot 2)	$K_1 = 0.62 \pm 0.11$ (model)	3590 ± 480	2.12 ± 0.36 (model)
High-Temperature Step (aliquot 2)	$K_2 = 0.11 \pm 0.02$ (model)	2330 ± 320	4.07 ± 0.63^c (model)
High-Temperature Step (aliquot 1) ^b	$K_2 = 0.11 \pm 0.02$ (model)	1640 ± 220	3.51 ± 0.61^c (model)

^aUncertainties are reported at the 1σ level

^bData only collected for step 2 of the failed run on aliquot 1

^cNote that the model ages of the two high-temperature steps are within uncertainty of one another due to uncertainty introduced from the potassium measurement

An initial attempt at noble gas analysis on Mojave 2 ("aliquot 1") was not successfully completed. Upon inlet of the gas released during the first heating step into the quadrupole mass spectrometer during the high-sensitivity semi-static mode, an overpressure condition was generated that caused the experiment to be aborted and the gas to be vented (i.e., the run terminated at the start of the semi-static analysis). Therefore, data were only collected during the low-sensitivity portion of the run. This overpressure condition was possibly due to a buildup of organics in SAM which had not been fully released during the boil-off stage. The second heating step was conducted as planned. Unexpectedly, the ^{40}Ar yield from step 2 of aliquot 1 (1640 ± 220 pmol) was ~30% lower than the same step from aliquot 2 (2330 ± 320 pmol). Using the available low sensitivity portion of the high-temperature step of aliquot 1, we find that it too was ~30% lower than measured in aliquot 2. This proportional decrease in ^{40}Ar retrieved from aliquot 1 relative to aliquot 2 is most readily attributed to incomplete sample delivery of aliquot 1, possibly due to loss via a wind gust as the sample was transferred from CHIMRA into SAM.

3.4.3 Age calculations and uncertainties

Combining the total ^{40}Ar release from Mojave 2 (aliquot 2; Table 3-3) with the APXS K_2O measurement and the modeled sample mass, a bulk K-Ar age of 2.57 ± 0.39 Ga is obtained using Equations 3-6 and 3-9. Based on the potassium partitioning model, the ^{40}Ar in step 2 is associated with potassium in detrital feldspar, and yields a model age of 4.07 ± 0.63 Ga via Equations 3-7 and 3-9. The jarosite, phyllosilicates, and/or salts in step 1 combined with the potassium partitioning model indicate a model age of 2.12 ± 0.36 Ga from Equations 3-8 and 3-9.

Several individual sources of error were combined to quantify the uncertainties on the reported K-Ar ages including: the sample mass transfer model (Farley et al., 2014), the APXS measurement of the bulk potassium in the sample, the SAM measurement of ^{40}Ar , and, for the model ages, the mineralogy as measured by CheMin, and the estimates of the potassium contents of the minerals within Mojave 2. The reported uncertainties do not include any potential systematic errors which cannot be quantified. All uncertainties are reported here at the 1σ uncertainty level. The uncertainty associated with sample delivery is derived from modeling efforts performed at JPL (Farley et al., 2014), and has a relative uncertainty of approximately 13%. The bulk potassium content has an accuracy of 15% of the measured value (R. Gellert, personal communication, 2017). Except where noted, uncertainty associated with the CheMin estimates of the weight fractions of mineral and amorphous phases are taken from the original references (e.g., Rampe et al., 2017; Treiman et al., 2016; Vaniman et al., 2014).

The uncertainty associated with the measurement of ^{40}Ar is calculated for each sweep of the mass spectrum according to the equation:

$$\sigma_{\text{Ar}} = [\sigma_{40}^2 + (\text{K}_{\text{HC}} \times \text{M39})^2 \times ((\sigma_{\text{HC}}/\text{K}_{\text{HC}})^2 + (\sigma_{39}/\text{M39})^2) + \sigma_{\text{bkgrd}}^2]^{1/2} \quad (3-10)$$

where σ indicates the absolute uncertainty of the component in subscript (e.g., σ_{Ar} is the overall ^{40}Ar measurement uncertainty, σ_{HC} is the uncertainty in the hydrocarbon correction, and σ_{bkgrd} is the uncertainty on the background correction). The uncertainty associated with the background correction is taken as the standard error of the mean of the measurements taken after pumpdown (see Figure 3-2).

The estimated potassium content of the plagioclase in the sample has an uncertainty of 20%, reflecting the stated uncertainty of the An# estimated for the average plagioclase in Mojave 2 by CheMin (Rampe et al., 2017) combined with the standard deviation of the data from the best-fit regression line (Figure 3-3).

The dominant sources of uncertainty in this study are the sample transfer model and the estimates of potassium contents of the various phases. The low abundance of jarosite measured by CheMin has an uncertainty large enough to impact the final age calculations on the model age of the first step.

3.5 Discussion

Here we discuss the implications of the bulk K-Ar age measured on the Mojave 2 sample, followed by discussion of the model ages for the two temperature steps. We also consider the assumptions regarding the argon retention characteristics of the various phases within the sample and their potential impact on the model ages. Finally, we put these results into the context of the broader geological history of Mars.

3.5.1 Bulk age

The bulk age of 2.57 ± 0.39 Ga determined for Mojave 2 is lower than the previous result of 4.21 ± 0.35 Ga from the Cumberland sample (Farley et al., 2014), suggesting that one or more of the potassium-bearing components in Mojave 2 has a formation age younger than the K-Ar age measured at Cumberland. As the sediment source for both samples is thought to be the crater rim and walls (Grotzinger et al., 2015), the detrital plagioclase is unlikely to have a formation age billions of years younger than that measured in Cumberland, implying that the young component in the sample is the jarosite, phyllosilicates, and/or amorphous materials.

3.5.2 Ages of the two steps

3.5.2.1 High-T step

The high-temperature step is modeled to record the age of the detrital plagioclase feldspar in Mojave 2. A detrital component model age of 4.07 ± 0.63 Ga is consistent with the previous in-situ

geochronology experiment at Cumberland (Farley et al., 2014). This model age is sensitive to the mineralogy reported by CheMin, especially whether sanidine was present at low concentrations in the sample. Sanidine was not detected by CheMin in Mojave 2, but many of the rocks analyzed at Gale crater do carry sanidine (Rampe et al., 2017; Treiman et al., 2016; Vaniman et al., 2014). If sanidine was in fact present in Mojave 2 but below the detection limit of CheMin (~ 1 wt%), its ^{40}Ar would be released either completely or partially during the high-temperature step. By analogy with the Cumberland sample (also a mudstone) that contained 1.6 wt% K-feldspar and completely (or almost completely) degassed (Farley et al., 2014), we assume that any sanidine in the Mojave 2 sample would also have degassed thoroughly during the high-temperature step. However, its potassium content would have been incorrectly assigned to the low-temperature step rather than the high-temperature step. This would have implications for the model ages of both steps (Equations 3-7 and 3-8), with the age of step 2 needing to be revised downward and the age of step 1 revised upward.

A limit to how large this effect could be is obtained by considering the plausible formation ages of the Gale crater feldspars. Detrital minerals in Mojave 2 are most likely older than the crater, being sourced from the crater target rocks, making their plausible formation age >3.6 Ga (Le Deit et al., 2012; Thomson et al., 2011). If more than 0.25 wt% endmember sanidine was present in the sample, the model age for step 2 would fall below 3.6 Ga. This is a reasonable upper limit on the amount of undetected sanidine in Mojave 2. By mass balance, the increase in the low-temperature step model age due to <0.25 wt% sanidine is $<4\%$ of the age (well within the stated uncertainty). Thus the step 1 model age is robust to the presence of plausible amounts of sanidine.

3.5.2.2 Low-T step

The model age of 2.12 ± 0.36 Ga measured in step 1 is a mixed age involving jarosite and amorphous/phylosilicate fractions (Table 3-3). We cannot specifically disentangle the ages of these individual components, resulting in two possibilities: 1) the jarosite and amorphous/phylosilicate components have the same K-Ar age, or 2) the step 1 model age is a mixture of two or more different K-Ar ages. In the first scenario, assuming complete argon retention, the model age of 2.12 ± 0.36 Ga represents the formation age of both of these components and most likely reflects a single fluid flow event which formed or recrystallized the secondary phases in Mojave 2 at that time, consistent with

the interpretations of Rampe et al. (2017). In the second scenario, the step 1 model age is a K-weighted average age of the jarosite and other low-temperature K-bearing components in the sample, meaning at least one phase has a K-Ar age of $\lesssim 2$ Ga. The only potential scenario in which both phases have a formation age older than the model age is in the case of argon loss, which is explored in the following section.

3.5.3 Argon loss from phases in the low-temperature step

A K-Ar age is only equivalent to a mineral formation age in the case of a closed system. Thus we must consider that a potential reason for the observation of a young K-Ar age at Mojave 2 is the loss of radiogenic argon from one or more of the low-temperature phases at any time prior to those phases being analyzed in SAM. This loss could have occurred via solution-reprecipitation (i.e., as a result of fluid migration events), by diffusion over geologic time, during sample drilling and handling, or as a result of the brief low temperature ($<150^{\circ}\text{C}$) boil-off step applied to the sample to release adsorbed volatiles. If radiogenic ^{40}Ar was lost before being measured by SAM, the K-Ar age of the low-temperature components would be younger than their formation age or ages. Jarosite is known to retain ^{40}Ar over geologic time at temperatures up to $\sim 150^{\circ}\text{C}$ (Kula and Baldwin, 2011; Vasconcelos et al., 1994). Therefore, if one of the components in Mojave 2 has lost significant argon, it is unlikely to be the jarosite.

We next assess the K-weighted average age of step 1 based on a full range (0–100%) of Ar retention in the low-temperature phases excluding jarosite (Figure 3-4). If all of these phases are fully retentive with respect to argon, then the K-weighted average formation age of step 1 is 2.12 ± 0.36 Ga, as calculated, suggesting a single age resetting event occurred at this time (see section 3.5.4 below for discussion of this possibility). If the amorphous/phylosilicate fraction has lost all of its argon (making that component's K-Ar age zero), the model age of the jarosite alone would be 3.17 ± 0.60 Ga, placing a firm upper limit on its formation age if it were endmember jarosite [i.e., $\text{KFe}_3(\text{SO}_4)_2(\text{OH})_6$]. Decreasing the K content of the jarosite increases its model age in this scenario. However, as described above, K-rich jarosite is geochemically likely (Dutrizac, 2008). For a reasonable lower compositional limit of 1:1 K:Na, the model age of the jarosite alone is 4.25 ± 0.66 Ga.

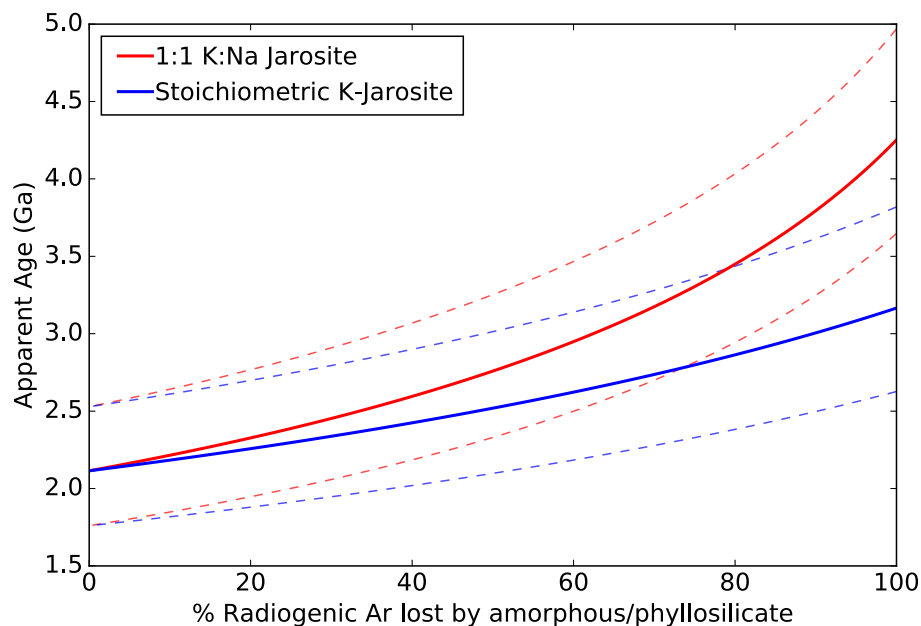


Figure 3-4. Potential ages of the low-temperature materials given varied argon retention in the amorphous/phyllsilicate fraction. The most likely values are shown with solid lines, 1σ uncertainties are shown with dashed lines. Endmember cases of jarosite composition (stoichiometric K-jarosite and 1:1 K:Na jarosite) are shown in blue and red, respectively.

Without strong constraints on the actual phases making up the amorphous/phyllsilicate fraction, it is difficult to constrain the extent to which this fraction has lost argon by natural processes. Illite has an argon closure temperature of around 100°C on timescales of millions of years (e.g., Evernden et al., 1960; Hamilton et al., 1989); mineral assemblages present in the drilled Cumberland and John Klein samples suggest burial temperatures $<80^{\circ}\text{C}$ (Vaniman et al., 2014), arguing against potential ^{40}Ar loss from putative illite in Mojave 2. Possible potassium-containing salts in Mojave 2 likely also retain radiogenic argon over geologic time against diffusive loss. Several sulfate and chloride salts have been determined to be useful for Ar dating (e.g., Leitner et al., 2014; Renne et al., 2001; Smits and Gentner, 1950), although there are no data on Ar closure temperatures for these phases. It has been suggested that liquid brines in the near subsurface may occur in Gale crater from deliquescing of perchlorate in the soil (Martín-Torres et al., 2015). The possibility exists that these brines have reprecipitated salts within Mojave 2, resetting their ages. However, jarosite is dissolved relatively rapidly in the presence of circum-neutral water (Madden et al., 2004); jarosite's presence in the sample argues against resetting of any salts in Mojave 2 by the presence of liquid water after their initial deposition. The presence of a brine would be unlikely to affect the argon retention of phyllosilicates.

Crystalline hydrated salts have been observed to lose their water under the extremely dry conditions inside CheMin, causing salts that were crystalline to appear X-ray amorphous (Vaniman et al., 2014). This process could have occurred with K-bearing hydrated salts in Mojave 2. If a similar phenomenon occurs within SAM during sample processing before analysis, most likely as a result of the boil-off stage (150°C maximum), the change in mineral structure could cause the loss of significant amounts of argon from these phases. However, the evolved water trace in the Mojave EGA below 150°C is minimal and mostly attributed to the release of adsorbed water (Sutter et al., 2017), suggesting that argon loss coincident with dehydration during the boil-off stage is unlikely. Phyllosilicate phases would also be unlikely to lose significant amounts of argon at 150°C (Evernden et al., 1960).

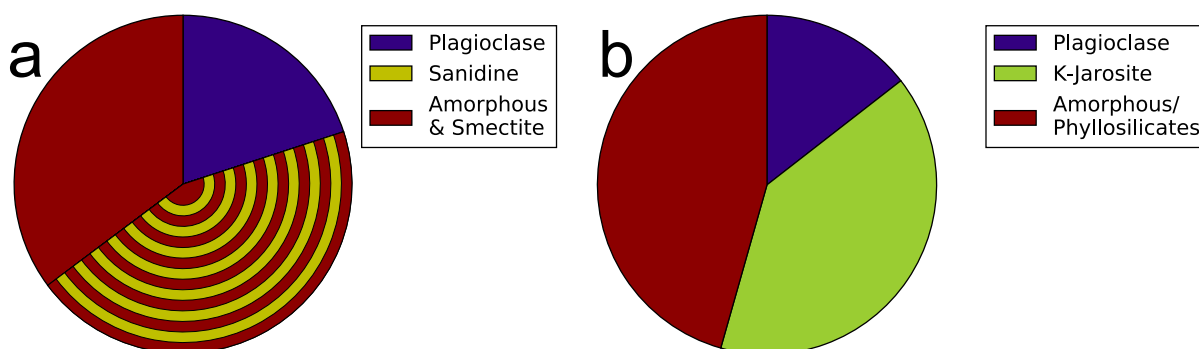


Figure 3-5. Comparison of the distribution of potassium between minerals in (a) Cumberland and (b) Mojave 2. The sanidine in Cumberland is at the detection limit; stripes indicate that the K_2O held in sanidine will trade off against the amorphous and phyllosilicate fraction depending on the true amount of sanidine in the sample.

The K-Ar geochronology result on the Cumberland sample (Farley et al., 2014) provides additional insight into the issue of Ar retention. Like Mojave 2, the amorphous and/or phyllosilicate components in Cumberland were a significant host of potassium (Figure 3-5). Cumberland's bulk K-Ar age was measured to be 4.21 ± 0.35 Ga (Farley et al., 2014); if greater than 25% of the argon contained in the amorphous/phyllosilicate fraction was lost prior to analysis, the K-Ar age of the sample corrected for Ar loss would exceed the age of Mars. By analogy between Cumberland and Mojave 2, more than 25% Ar loss in the amorphous and/or phyllosilicate fractions of Mojave 2 seem unlikely. To put this degree of loss in perspective, more than 90% Ar loss from these phases would be required to cause the loss-corrected model age of the low-T phases in Mojave 2 to exceed 3.0 Ga (60% if the jarosite in the sample has 1:1 K:Na rather than pure K-jarosite). Therefore, it appears

that the K-weighted average formation age of the low-T components in Mojave 2 is <3.0 Ga, indicating that at least one major phase in Mojave 2 was formed or recrystallized well after the Hesperian period on Mars. Given that the only major mineralogical difference between Cumberland and Mojave 2 is the presence of jarosite, if the jarosite and evaporite/phylllosilicate phases have different formation ages (i.e., Mojave 2 reflects the second scenario described above in section 3.5.2.2), jarosite appears most likely to be this young component.

3.5.4 Implications of young components in Mojave 2

The most noteworthy result from the low-temperature step is the young model age attributable to the phase or phases in Mojave 2 whose genesis reflects an interaction with water, indicating a likely formation age of the jarosite and potentially the K-bearing salts and/or phylllosilicates of less than three billion years. This young age is potentially an indication of the most recent aqueous activity at Mojave 2. It is possible that this last aqueous activity occurred in the final stages of the drying of the lake in Gale crater, implying that the lake (and therefore the presence of large perennial bodies of water on Mars) was much longer-lived than previously thought (Bristow et al., 2015; Grotzinger et al., 2015). However, the presence of such a long-lived lake would contravene the generally understood geologic history of water on Mars (Bibring et al., 2006). It is more likely that the formation age (or ages) of these diagenetic materials is related to post-depositional subsurface fluid flow. There are a number of diagenetic features in Mojave 2 and in the surrounding bedrock that are indicative of water/rock interaction and post-depositional fluids (Gellert et al., 2015; Grotzinger et al., 2015; McBride et al., 2015; Nachon et al., 2017; Schieber et al., 2015). We postulate that the crystal laths observed in Mojave 2 (Figure 3-1; McBride et al., 2015; Schieber et al., 2015) could have been redissolved by such a fluid during precipitation of the jarosite. Specifically, Rampe et al. (2017) suggest that after mudstone deposition in a circumneutral, relatively reducing lake environment, one or more influxes of oxidizing acidic fluids could have produced the jarosite in Mojave 2. Additionally, young alluvial fans and chloride deposits hint at minor fluvial activity extending well into the Amazonian in the vicinity of Gale crater (Ehlmann and Buz, 2015; Grant et al., 2014). These late fluvial features reinforce the prospect of relatively young water-lain minerals inside Gale crater.

Evidence of relatively recent water activity in Gale crater is paralleled by alteration features in the Nakhilite Martian meteorites (Changela and Bridges, 2010; Hicks et al., 2014) that substantially post-date the meteorites' crystallization ages. These alteration features (small veinlets of carbonate, ferric saponite, serpentine, and amorphous gel), historically described as “iddingsite” (see Treiman (2005) for an overview), have been dated to the Amazonian period with a maximum age of 670 Ma by the K-Ar method (Swindle et al., 2000). This alteration age is much younger than the crystallization age of ~ 1.3 Ga determined for the nakhilite host rocks (Nyquist et al., 2001), and is attributed to impact-generated hydrothermal activity (Changela and Bridges, 2010; Schwenzer et al., 2012).

Recurring slope lineae are contemporary slope-darkening streaks observed on Mars (e.g., McEwen et al., 2014; McEwen et al., 2011). These transient features occur on sun-facing slopes during the warmest period of the year and are suggested to be associated with hydrated salts such as perchlorates (Ojha et al., 2014; Ojha et al., 2015), potentially indicating that they are formed via liquid brine flows. These modern observations, taken in combination with the young alteration features in the nakhilite meteorites and the young K-Ar age observed at Mojave 2 associated with water-lain features, suggest that liquid water at or near the surface of Mars has been at least episodically (though perhaps only locally) available since the Hesperian-Amazonian transition and likely throughout the planet's geologic history.

3.6 Conclusions

A third radiometric dating experiment has been conducted on Mars using the SAM instrument on the Curiosity rover, yielding a bulk K-Ar age of 2.57 ± 0.39 Ga on the Mojave 2 mudstone. A new two-step heating methodology resulted in separate model ages of what we infer to be detrital feldspar and diagenetic components of the Mojave 2 sample of 4.07 ± 0.63 Ga and 2.12 ± 0.36 Ga, respectively. The ancient age of the detrital component is consistent with previous results and the expected age of igneous material in Gale crater. The young K-Ar age of the diagenetic component could reflect a formation age, or could result from ^{40}Ar loss from the amorphous/phyllosilicate component before measurement, either in nature or in the SAM instrument. Given a full range of argon retention in the amorphous/phyllosilicate component, the model K-weighted average age of the low-temperature phases extends from 2.12 ± 0.36 Ga if argon

is quantitatively retained in all phases to a jarosite model age of 3.17 ± 0.60 Ga if argon is completely lost from the amorphous/phyllosilicate portion (4.25 ± 0.66 Ga in the case of more K-poor 1:1 K:Na jarosite). By analysis of the likely sample components and by comparison to Cumberland, the argon loss from the phyllosilicate/amorphous phase(s) appears unlikely to be substantial, making the likely K-weighted average age of the low-temperature materials <3.0 Ga, corrected for any minor argon loss. This age indicates that at least one of these components was formed well into the Amazonian, after aqueous activity on Mars is thought to have largely stopped, and is inconsistent with precipitation from the desiccation of the lake in Gale crater. The prevalent diagenetic features in Mojave 2 and the surrounding bedrock suggestive of post-depositional fluid flow may be associated with this relatively young age, which is potentially indicative of the most recent liquid water activity at the Mojave 2 drill site. In concert with alteration patterns in meteorites and modern observations of liquid surface water, these results suggest that liquid water has potentially been available at or near the surface of Mars throughout its history.

BILLION-YEAR EXPOSURE AGES IN GALE CRATER INDICATE A PRE-AMAZONIAN FORMATION OF MOUNT SHARP

4.1 Abstract

The erosion rates and mechanisms operating on Mount Sharp may be assessed via experiments performed by the SAM instrument to determine the cosmogenic noble gas content of the new samples Mojave 2 and Quela. Past measurements of samples from the plains at the base of Mount Sharp indicate scarp retreat-generated surfaces have formed within the last 100 Ma. In contrast, Mojave 2 yielded ages of $1,320 \pm 240$ (^3He), 910 ± 420 (^{21}Ne), and 310 ± 60 Ma (^{36}Ar). Quela gave a ^3He age of $1,460 \pm 200$ Ma; ^{21}Ne and ^{36}Ar from this sample could not be quantified due to large isobaric interferences. The discordant and young ^{36}Ar exposure age in Mojave 2 is most likely attributable to resetting via interaction with water due to the solubility of the chlorine-bearing host phases for this nuclide. The most probable exposure scenario is that both Mojave 2 and Quela have been at the surface for the most recent ~ 1 Ga. Based on local geomorphology, scarp retreat is the most likely mechanism of exposure; this may be the dominant form of landscape evolution in Gale crater. The exposure ages measured throughout Curiosity's traverse indicate that the net removal of rock is proceeding more rapidly in the moat between Mount Sharp and the rim of Gale crater than on Mount Sharp itself. The implied differential erosion rate is insufficient to explain the formation of Mount Sharp. Instead, given that the surfaces on Mount Sharp have existed for much of Mars's history, the mound must have been formed early, likely during the Hesperian.

4.2 Introduction

The rates and dominant mechanisms of erosion on modern Mars are of great interest to applications in crater dating (Hartmann & Neukum, 2001; Malin et al., 2006), constraining climate change (Golombek et al., 2006), the geomorphic evolution of Mars's surface features (Arvidson et al., 1979; Carr & Head, 2010), and the search for pristine organic biosignatures (Dartnell et al., 2007; Oró & Holzer, 1979; Pavlov et al., 2012). Modern-day erosion is dominated by eolian processes

(Golombek et al., 2014), evidenced by the prevalence of features such as ventifacts (Bridges et al., 1999, 2014; Greeley et al., 2006) and large-scale yardangs (Ward, 1979). Eolian erosion has widely been thought to proceed on a slow timescale, leaving some landforms largely unchanged for as long as billions of years (Arvidson et al., 1979; Carr & Head, 2010; Golombek et al., 2006, 2014; Golombek & Bridges, 2000). Based on crater counts of landslide deposits (Grindrod & Warner, 2014), other locations have apparently undergone more rapid eolian erosion in the recent past, generating relatively young geomorphic features.

Two previous noble gas-derived cosmic ray exposure ages measured by the Sample Analysis at Mars (SAM) instrument on the Curiosity rover confirmed the existence of young surfaces in Gale crater, where exposure ages of <100 Ma were detected (Farley et al., 2014; Vasconcelos et al., 2016). Both studies were performed early in the Curiosity rover's traverse, at low elevation in Gale crater before reaching Mount Sharp. Here we analyze the cosmogenic noble gases in two Mount Sharp samples, called Mojave 2 and Quela, to inform the likely erosive rate and mechanisms operating at higher elevations in Gale crater, and to evaluate the models and timing of Mount Sharp's formation.

4.2.1 Mount Sharp

Gale crater is a 150 km diameter complex crater formed approximately 3.6 Ga (Le Deit et al., 2012). Gale contains a large sedimentary sequence including a 5.2 km-high sedimentary mound termed Mount Sharp, which surrounds the crater uplift peak, and is similar to other mounds observed in craters across Mars (Thomson et al., 2011). Figure 4-1 shows a cross-sectional view of the major stratigraphic units in Gale crater. The Gale sedimentary sequence broadly consists of a flat plain termed Aeolis Palus, which includes both relatively modern superposed alluvial fans (Grant et al., 2014) and the most ancient rocks explored by Curiosity, referred to as the Bradbury group (Grotzinger et al., 2015). The Bradbury group contains the Yellowknife Bay and Kimberly formations, which are the source of the previously dated Cumberland and Windjana samples, respectively. The Bradbury consists mostly of fluvial sandstones and lacustrine mudstones, interpreted as a fluviodeltaic deposit (Grotzinger et al., 2015). Stratigraphically above the Bradbury group is the Mount Sharp group (Grotzinger et al., 2015). Lower Mount Sharp is composed of the Murray formation, which interfingers and is thought to be the lacustrine counterpart to the primarily fluviodeltaic sediments of the Bradbury group (Grotzinger et al., 2015; Stack et al., 2016). Above

the Murray, a layered sulfate-bearing unit forms the upper portion of the Mount Sharp group (Fraeman et al., 2016; Milliken et al., 2010). The Mount Sharp group is capped by probable eolian upper strata forming the top portion of the sedimentary mound (Grotzinger et al., 2015; Milliken et al., 2010). The Siccar Point group unconformably overlies the Mount Sharp group and includes the eolian Stimson formation, which has an unconformable contact with the Murray formation (Fraeman et al., 2016). The time interval between the formation of Mount Sharp and the deposition of the Stimson formation is currently unconstrained; the samples analyzed for this study exist near this contact and may allow investigation of the depositional and erosional history of the Murray-Stimson contact.

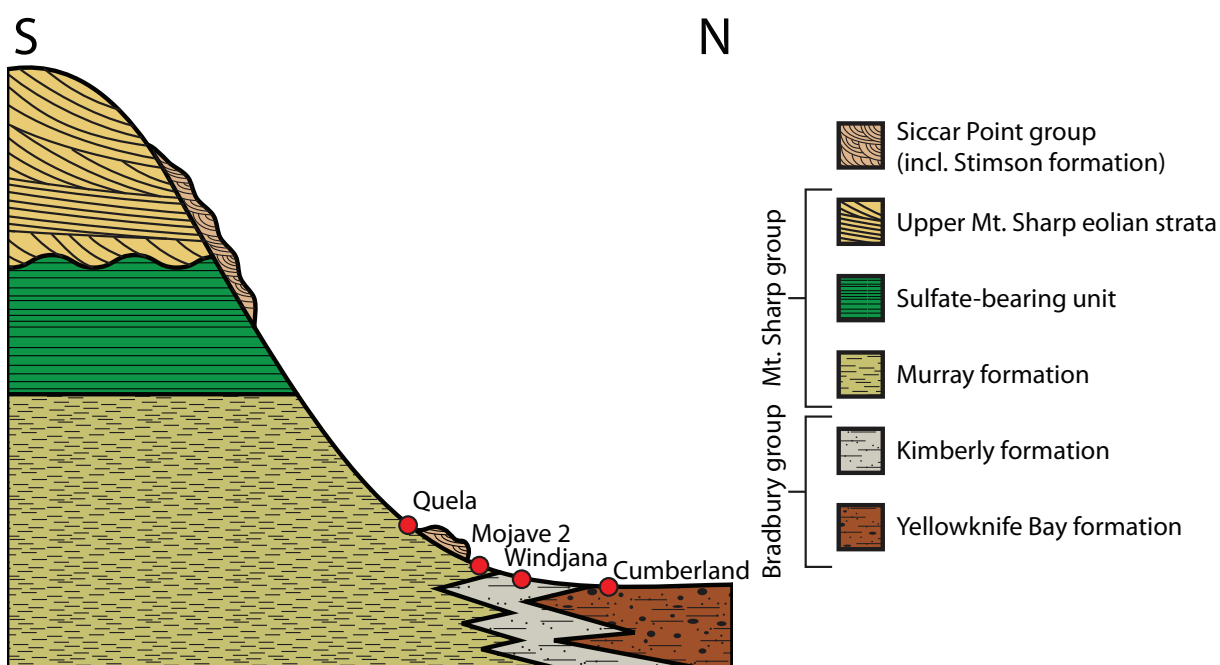


Figure 4-1. Conceptual cross-sectional view of the Gale sedimentary sequence with sample locations noted. Diagram is meant only to illustrate the relative stratigraphic position of each unit and is not to scale. See Grotzinger et al. (2015) for a complete description and to-scale diagram of all Gale crater units.

The formation of Mount Sharp is thought to have proceeded by fluviolacustrine sedimentation, followed by the deposition of windblown eolian sediment which filled and overtopped the rim of the crater and built a mound of positive topographic relief (Grotzinger et al., 2015). After this episode of deposition (and lithification of the lower sediments resulting from compaction; Caswell and Milliken, 2017), eolian erosion lowered the surface to near the modern exposure (Grotzinger et al., 2015), with the preferential northern winds scouring around the central

mound to create the moat observed today (Day & Kocurek, 2016). After Mount Sharp eroded to nearly its current shape, the Siccar Point group was deposited as an eolian draping unit unconformably overlying the rocks in Mount Sharp (Fraeman et al., 2016).

4.2.2 Cosmic Ray Exposure Dating

Cosmogenic nuclides are produced in the upper ~2-3 m of Mars's surface by nuclear interactions of galactic cosmic rays (GCRs) with the atoms in rocks. Below this depth cosmogenic production is negligible (Lal, 1988). In this study, we measured nuclides generated by two mechanisms: ^3He and ^{21}Ne are produced primarily from spallation of Mg, Al, Si, and for just ^3He , O. In Gale crater rocks, the mass balance of these elements is dominated by primary silicate phases such as pyroxene and feldspar. The production of ^{36}Ar occurs via capture of cosmogenic thermal neutrons by ^{35}Cl , forming ^{36}Cl , which undergoes beta decay to ^{36}Ar on a short timescale (~300 kyr) relative to the ages reported here. The majority of Cl (and therefore ^{36}Ar) in the samples is likely present in the form of chloride and perchlorate salts, though minor amounts of detrital chlorapatite may also be present (Rampe et al., 2017; Sutter et al., 2017).

Interpretation of cosmogenic nuclide concentrations in the deep past relies on the assumption of an invariant flux of GCRs through time. Analysis of radioactive cosmogenic nuclides with varying half-lives suggests that on timescales ranging from a few million up to a billion years, the GCR flux is stable within a factor of two (Wieler et al., 2013). In the present study, we make the usual assumption that GCR flux is invariant through time, while recognizing that this has not been established with certainty. The long integration times required for the cosmogenic nuclide concentrations observed in this study further suggest that the impact of any short-term fluctuations will be minimized as these data are an integration of all such fluctuations.

Cosmogenic isotope concentrations can be interpreted via two endmember exposure scenarios: instantaneous exposure followed by negligible erosion, or steady state denudation (Lal, 1991). In the first model, exposure to cosmic rays begins when previously unexposed rock is instantaneously exposed at the surface, for example by the lateral migration of a several meter high scarp. In this case the cosmogenic isotope concentration at the surface (C_0) is equal to the product of

the surface production rate (P_o) and the surface exposure age (τ), where the surface exposure age is the length of time elapsed since the scarp retreated to expose the surface.

$$C_o = P_o \times \tau \quad (4-1)$$

In the second model, vertical denudation removes rock at a steady rate and the cosmogenic nuclide concentration at the surface represents the integration of nuclide production throughout the passage of the rock upward towards the surface. Eventually this leads to a steady state concentration profile in which C_o is a function of mean denudation rate (D , in cm/yr) and the attenuation lengthscale of cosmogenic nuclide production (z^* , typically ~ 70 cm in low-density rocks sedimentary rocks similar to those at Gale crater):

$$C_o = \frac{P_o \times z^*}{D} \quad (4-2)$$

These equations can be related to one another as

$$D = \frac{z^*}{\tau} \quad (4-3)$$

meaning that for a given surface cosmogenic isotope concentration, the implied steady-state denudation rate is related to the implied surface exposure age by the e-folding depth of cosmogenic nuclide production. An exposure age therefore functions as a lower limit on the length of time since exposure to cosmic ray irradiation began for a given sample. Here we discuss the results from the new noble gas measurements as endmember exposure ages, recognizing that this is a shorthand which may not fully capture the history of the samples.

Both vertical denudation and lateral scarp retreat have the net result of erosion, defined broadly as the net removal of rock. We use the term “denudation” throughout this manuscript to refer specifically to vertical surface lowering, and use the term “erosion” as an all-encompassing term to describe the net removal of rock from Gale crater which includes both vertical denudation and lateral scarp retreat. Scarp retreat, integrated over multiple events, can lead to significant downward erosion. Based on the difference in average exposure age of two relatively large areas vertically offset by

scarp retreat, an apparent erosion rate may be derived. For instance, the average exposure age of the surface at the top of a set of scarps will exceed that of the bottom. This may be converted to an apparent erosion rate (E_{geo}) based on the difference in elevation (ΔZ) given two ages from those elevations (τ_1 and τ_2)

$$E_{geo} = \frac{\Delta Z}{\tau_2 - \tau_1} \quad (4-4)$$

Because spallogenic and neutron-capture isotopes have different production profiles with depth, their concentration ratio offers a clue as to which of the above endmember models, if either, has been active (Farley et al., 2014). Specifically, if the surface exposure ages of the spallogenic isotopes (^3He , ^{21}Ne), and the neutron capture isotope (^{36}Ar) are observed to be within error of one another, an instantaneous exposure scenario is supported (i.e., scarp retreat). If the ^{36}Ar surface exposure age exceeds that calculated for the ^3He and ^{21}Ne , the relative cosmogenic nuclide abundances may be consistent with steady-state erosion, or (depending on the exact concentration of each nuclide) may document a more complex erosion scenario.

The Cumberland and Windjana samples were obtained from the Yellowknife Bay and the Kimberly formations within the Bradbury group, respectively, yielding internally consistent exposure ages for all three isotopes. The Cumberland sample returned ^3He , ^{21}Ne , and ^{36}Ar surface exposure ages of 72 ± 15 , 84 ± 28 , and 79 ± 24 Ma, respectively (Farley et al., 2014). Two aliquots of the Windjana sample gave error-weighted mean ^3He , ^{21}Ne , and ^{36}Ar ages of 30 ± 27 , 54 ± 19 , and 63 ± 84 Ma (Vasconcelos et al., 2016). The good agreement between the surface exposure ages for each of these rocks was taken as evidence that the landscape at both of these sample sites has evolved recently via scarp retreat. This model is consistent with local geomorphology: the Cumberland sample was drilled from a wide flat basin surrounded by scarps, at the base of which erosional undercutting was prominent. The closest downwind scarp of several meters relief was observed approximately 60 m from the sample location, suggesting a mean scarp retreat rate of $\sim 0.75 \text{ m Ma}^{-1}$ (Farley et al., 2014). The Windjana cosmogenic isotope concentrations have sufficiently large uncertainties that similar calculations for its sampling location are under-constrained, but the overall similarity between Windjana and Cumberland cosmogenic isotopes was used to infer a similar erosion rate and style at the two sites (Vasconcelos et al., 2016).

4.3 Materials and methods

4.3.1 Sample descriptions

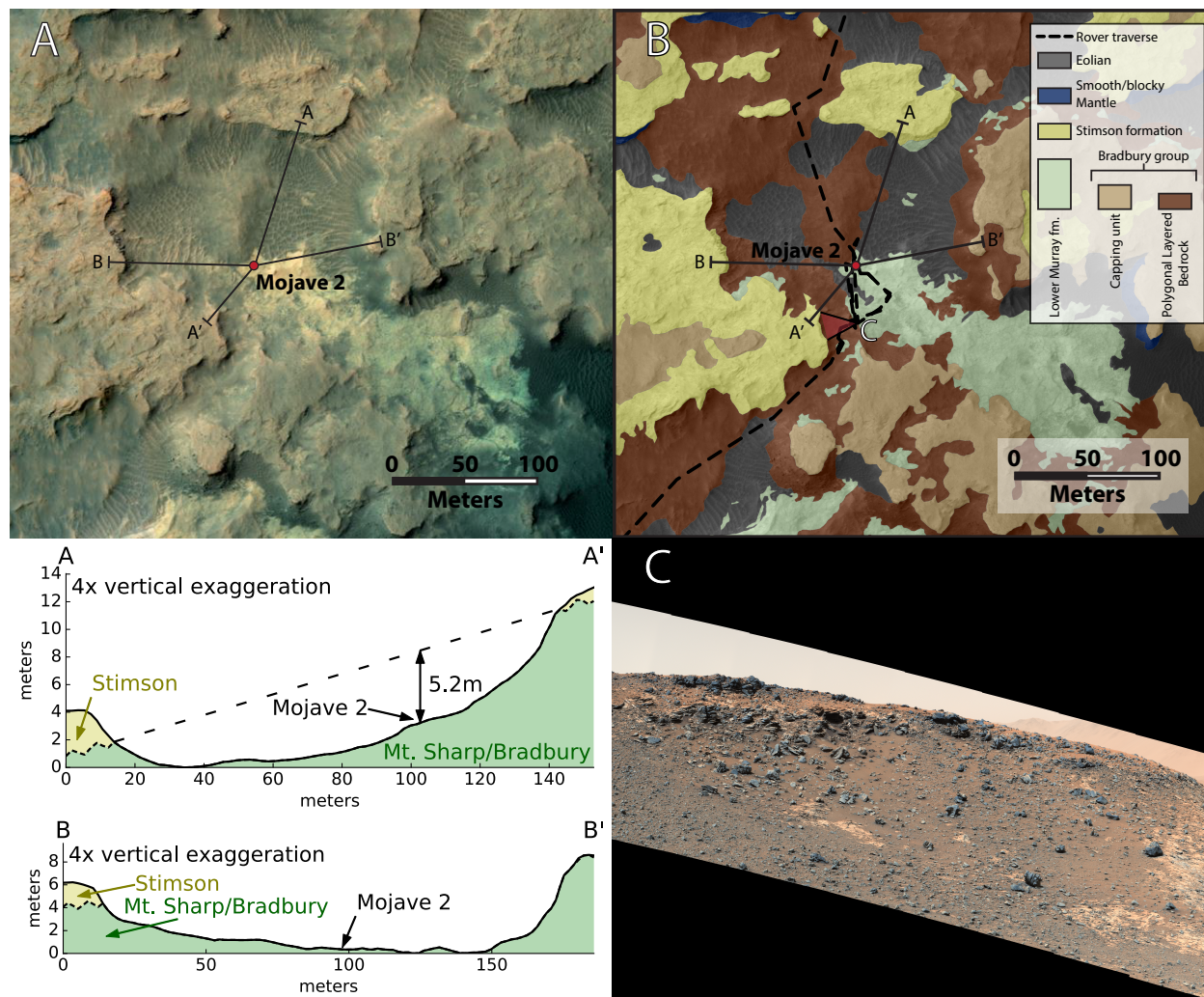


Figure 4-2. A) Color image of Mojave 2's sample location, with cross sections showing the topographic profile of the area and the location of the nearest Murray-Stimson contacts. B) Geologic map of the Pahrump hills with the part (C) image location shown as a red triangle. C) Mastcam mosaic of the Murray-Stimson contact at the southwest portion of the Pahrump Hills.

The Mojave 2 sample was collected from the lower portion of the Murray formation in the Pahrump Hills. As the bedding in Gale crater does not display significant dips, elevation may be used as a proxy for stratigraphic height: Mojave 2 is approximately 60 m stratigraphically above the Cumberland sample and 20 m above the Windjana sample. Its chemistry and mineralogy have been described previously (Table 4-3 in the appendix; Martin et al., 2017; Rampe et al., 2017). K-Ar results from Mojave 2 revealed that the sample contains young (2.12 ± 0.36 Ga) jarosite and

4.07±0.63 Ga plagioclase (Martin et al., 2017), consistent with an extended history of fluid flow and a detrital component concordant with the ancient age of material in Gale measured at Cumberland (Farley et al., 2014). Mojave 2 is situated in a topographic low, 40 m from the nearest scarp, which is ~4.5 m tall with relatively gently sloping sides, and capped by the Stimson formation (Figure 4-2). Based on planar projection from limited visual exposures ~40-90 meters distant, Mojave 2 would be inferred to lie about five meters below the Murray-Stimson contact. However, this contact undulates by as much as 10 vertical meters over distances <200 m (Watkins et al., 2016). Mojave 2 could therefore derive from the unconformity itself, or it could have been buried up to ~15 m below it when Stimson deposition began.

The sample Quela was also collected from the Murray formation, in an area known as the Murray buttes, approximately 80 m stratigraphically above Mojave 2 (again using topographic elevation as a proxy for stratigraphic position; 100 m above Windjana and 140 m above Cumberland). Quela's mineralogy and chemistry are shown in Table 4-4 in the appendix. Given that this sample contains 2.3 wt% sanidine (Bristow et al., 2018), and previous work has demonstrated that sanidine-bearing samples are not amenable to ⁴⁰Ar extraction using SAM (Vasconcelos et al., 2016), we do not report the K-Ar results for this sample. Much like the Pahrump Hills, the Murray buttes are erosional remnants (here approximately eight meters tall), capped by the Stimson formation. Due to a covered interval of talus at the base of each butte, the Stimson makes up an unknown (but most likely large; Figure 4-3) proportion of the stratigraphy of each butte. Quela was collected approximately five meters from the base of a butte, and 1.3 m below the base of this talus-covered layer. Close examination of the north side of the butte nearest Quela reveals that Stimson-style crossbedding can be seen protruding through the talus (Figure 4-3c). We interpret this observation as evidence that the entirety of the covered interval is composed of Stimson. Mapping the edge of the covered interval as the Murray-Stimson contact reveals a contact surface which is slightly dipping to the north. Taking an upper limit of a planar projection of this surface and a lower limit of a horizontal projection from the edge of the talus covered slope as the location of the contact, Quela lies between 1.8 m and 1.3 m below the Murray-Stimson contact.

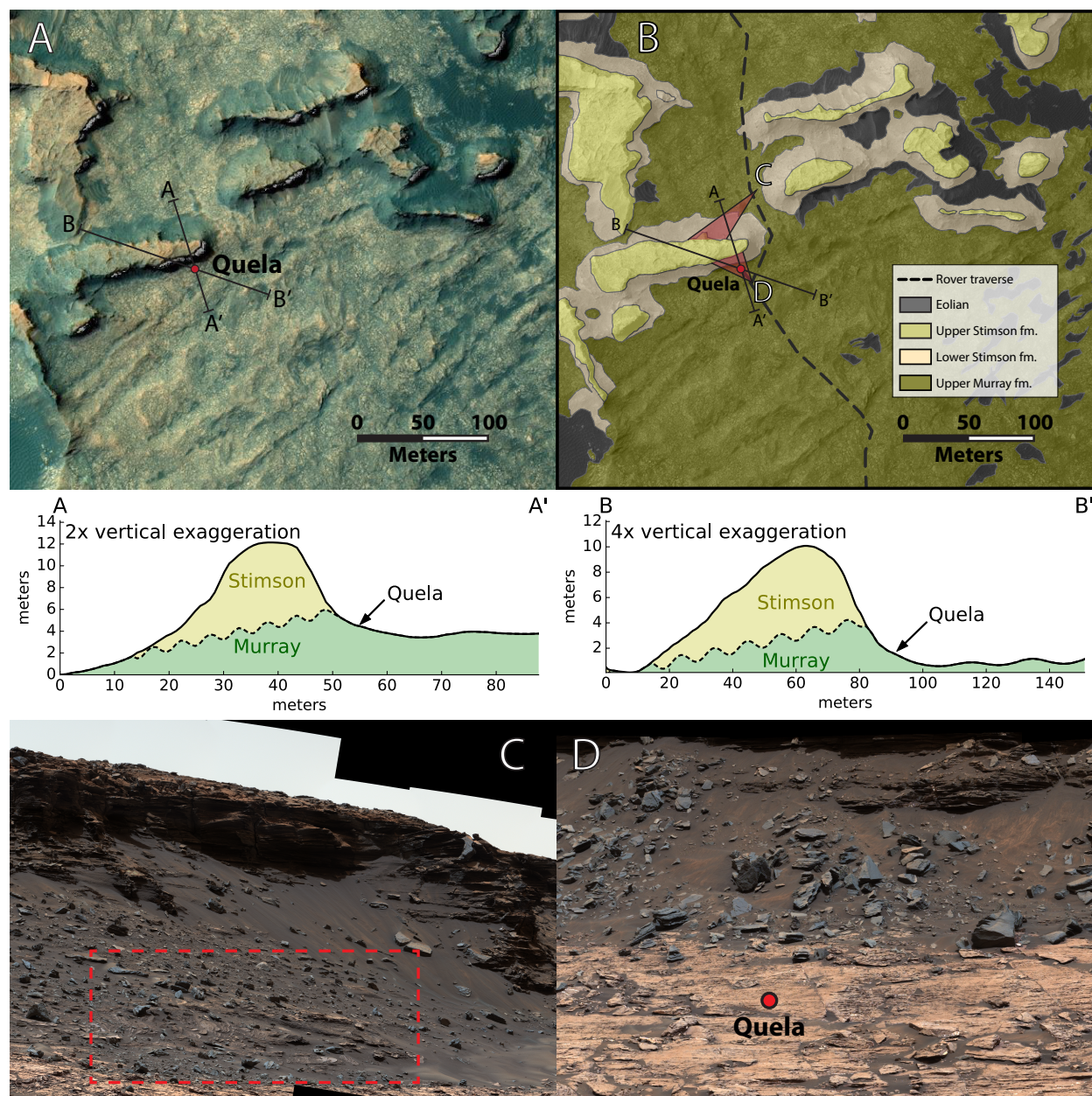


Figure 4-3. A) Color image of Quela's sample location. Cross sections show the approximate location of the Murray-Stimson contact. B) Geologic map of the southern Murray buttes; Mastcam mosaic locations are shown with red triangles. C) Mastcam image taken from the North side of the Butte where Quela was sampled. Cross-strata are shown in the red highlight box indicating that the Murray-Stimson contact extends to the bottom of the Murray Buttes. D) Quela's drill location on the south side of the butte shown in (C).

4.3.2 Methods

The SAM analysis procedures used in this study for the Quela measurement followed those developed by Farley et al. (2014). For Mojave 2, the updated procedures described by Martin et al. (2017) were used. Briefly, $\sim 135 \pm 18$ mg aliquots of drilled samples are heated to $\sim 930^\circ\text{C}$, releasing the volatiles held within the samples. A semi-static measurement mode allows buildup of noble gases while reactive species are drawn down on a scrubber and getter within the gas handling line. The masses of interest (m/z 3, ^3He ; m/z 21, ^{21}Ne ; m/z 36, ^{36}Ar) are corrected for isobaric interferences and for background measured after the mass spectrometer is evacuated. Raw counts are then averaged over the stable portion of the semi-static measurement and converted to molar amounts using a known basic sensitivity, accounting for the enhancement in signal in “semi-static” mode relative to “dynamic” mode (Farley et al., 2014). This sensitivity was calibrated prior to launch and has been monitored for change by periodic atmospheric measurements of ^{40}Ar , which has a largely invariant partial pressure in the Martian atmosphere (VanBommel et al., 2018). No calibration gas standard is carried on the instrument. Cosmogenic isotope production rate calculations for each isotope is dependent on the chemical composition of the samples (Tables 4-3 & 4-5 in the appendix), as described by Farley et al. (2014). A detailed description of the noble gas quantification for each sample is given in the supplement.

The uncertainty associated with each cosmogenic isotope concentration incorporates uncertainties associated with signal and isobar peak heights, regressions for isobar correction, background subtraction, and mass delivery. Uncertainties were computed using a Monte Carlo model. All uncertainties reported here are at the 1σ level.

4.4 Results

Table 4-1 gives the cosmogenic nuclide concentrations of each sample and converts them to both surface exposure age and steady-state mean erosion rate. The Mojave 2 ^3He and ^{21}Ne exposure ages ($1,320 \pm 240$ and 910 ± 420 Ma respectively) agree within uncertainty, giving an error-weighted mean exposure age of $1,060 \pm 330$ Ma. The ^{36}Ar released from Mojave 2 gives a surface exposure age of about 310 ± 60 Ma, significantly younger than either ^{21}Ne or ^3He . The ^3He exposure age measured on Quela of $1,460 \pm 200$ Ma is concordant with the ^3He and ^{21}Ne exposure ages on Mojave

2. The ^{21}Ne and ^{36}Ar measurements from Quela had extremely large uncertainties which preclude their use in this study (see section 4.8.1.3 for discussion).

Table 4-1. Results of the noble gas experiment on Mojave 2, with production rates and calculated ages. ^{21}Ne and ^{36}Ar could not be determined for Quela.

	Mojave 2			Quela
	^3He	^{21}Ne	^{36}Ar	^3He
Gas amount (pmol g $^{-1}$)	620 \pm 110	47 \pm 21	90 \pm 20	670 \pm 90
Surface production rate (pmol g $^{-1}$ Ma $^{-1}$)	0.4653	0.0523	0.2892	0.4566
Exposure Age (Ma)	1,320 \pm 240	910 \pm 420	310 \pm 60	1,460 \pm 200
Mean Denudation Rate (μm Ma $^{-1}$)	780 \pm 140	520 \pm 230	-	470 \pm 60

4.5 Discussion

Mojave 2 and Quela have far higher concentrations of cosmogenic nuclides than those observed in previous studies (Farley et al., 2014; Vasconcelos et al., 2016), and unlike these previous studies have discordant ^3He and ^{21}Ne compared to ^{36}Ar . These discrepancies raises the possibility that non-cosmogenic noble gases have been included in the samples. Here we explore alternative potential sources of these noble gases, and discuss the likely causes of the discordancy in ^{36}Ar .

4.5.1 Potential non-cosmogenic sources of ^3He and ^{21}Ne

Interplanetary dust particles (IDPs) have extremely high concentrations of implanted solar wind ^3He (Ozima et al., 1984) and could potentially contribute to the high ^3He concentrations measured in Mojave 2 and Quela. However, the $^3\text{He}/^{21}\text{Ne}$ ratio of 13 ± 6 in Mojave 2 is consistent with the predicted spallogenic production ratio of 9, and is orders of magnitude lower than the $^3\text{He}/^{21}\text{Ne}$ ratio of $\sim 10^5$ found in IDPs (Pepin et al., 2000). If all of the ^3He in Mojave 2 is derived from IDPs, only 0.01% of the ^{21}Ne could derive from this source. Though the ^{21}Ne for Quela is unavailable for comparison, by analogy to Mojave 2 (and both CB and WJ) we argue that Quela is also unlikely to host significant quantities of IDPs as its lithology, mineralogy, and chemistry are not dramatically different from these other samples.

Another potential source of noncosmogenic He and Ne in these samples is meteoritic material carrying cosmogenic noble gases (Wieler, 2002) but without the surface layer of implanted solar wind noble gases. Iron meteorites have been observed directly on Mars (Meslin et al., 2017). Iron meteorites, devoid of a productive target for ^{21}Ne production, would carry a $^3\text{He}/^{21}\text{Ne}$ ratio of approximately 85, again inconsistent with the observed ratio of 13 ± 6 in Mojave 2. Furthermore, because neither Mojave 2 nor Quela has anomalously high Fe, the inclusion of iron meteorite material in either of these samples is unlikely. Cosmogenic noble gases in silicate meteorite material would likely be isotopically indistinguishable from such gases formed in-situ on the Martian surface, meaning that the inclusion of such material would not be obvious from noble gas data. Because impacts and collisions rapidly erode stony meteorites in space, their surface exposure ages are almost always <100 Ma (Wieler, 2002), with the oldest known being 120 Ma (Eugster et al., 2006). Thus even inclusion of an unreasonably high proportion (tens of %) of meteoritic material cannot explain the high ^3He concentrations in Quela or Mojave 2. Furthermore, the depositional age of Gale sediments is thought to be only ~ 1 Gyr after solar system formation (Grotzinger et al., 2015), setting a firm upper limit on the potential exposure age of infalling meteoritic material that could be present.

Like previous workers (Farley et al., 2014; Vasconcelos et al., 2016), we assume that atmospheric noble gases are negligible in these analyses. Coupled with the above considerations, we conclude that ^3He and ^{21}Ne are cosmogenic in origin, and that they reflect the integrated exposure history of the analyzed sedimentary rock and/or its constituent detrital mineral grains.

4.5.2 Resetting of ^{36}Ar

Because it is formed from Cl and therefore in our samples is held mostly in soluble phases like halite and perchlorate salts (Rampe et al., 2017; Sutter et al., 2017), cosmogenic ^{36}Ar can potentially be released during interaction with even minor amounts of liquid water. This would decouple cosmogenic ^{36}Ar from the cosmogenic ^3He and ^{21}Ne dominantly carried in silicate grains. Such decoupling was not observed in Cumberland or Windjana, as demonstrated by the exposure age agreement among all three cosmogenic isotopes in that sample (Farley et al., 2014; Vasconcelos et al., 2016). There is no erosion scenario which permits the low ratio of ^{36}Ar to ^3He and ^{21}Ne observed in Mojave 2, tentatively suggesting that it reflects either total aqueous resetting or more likely partial resetting at some unknown time or times in the past. Previous work has suggested

transient liquid water at and near the surface of Mars which postdates the original deposition of the sedimentary sequences where these features are observed (Arvidson et al., 2010; Cull et al., 2010; Knoll et al., 2008), including in Gale crater (Thomas et al., 2019; Chapter 5, this thesis), and the Mojave 2 sample (Martin et al., 2017). The observation of ^{36}Ar resetting is consistent with these previous studies. Recent work has also shown that the perchlorate in Gale crater rocks is most likely post-depositional, added during the Amazonian (Chapter 5, this thesis). If this perchlorate was added in the last 300 Ma, the young ^{36}Ar age could in part be due to the young formation age of some of the salts containing ^{36}Ar . We therefore interpret ^{36}Ar independently from that of ^3He and ^{21}Ne .

The likely resetting of ^{36}Ar precludes the direct inference of erosional style responsible for exposure of the new samples presented here. Unlike the case for Cumberland and Windjana (Farley et al., 2014; Vasconcelos et al., 2016), there is thus no geochemical reason to favor a scarp retreat model over a vertical denudation model. A vertical denudation model is therefore a viable alternative for these two samples based on the noble gas data; when cast as a steady-state denudation rate, the Quela and Mojave 2 spallation isotopes indicate a rate of around $500 \mu\text{m Ma}^{-1}$ (Table 4-1). We continue to use the term “exposure age” in the following sections as a shorthand for the overall concentration of cosmogenic noble gas in each sample, which serves as a minimum time a sample may have been exposed to cosmic rays.

4.6 Erosion and exposure history of Mount Sharp

In this section we discuss the possible implications of these cosmogenic isotope data for the history of Mount Sharp. As the total cosmogenic nuclide concentration in each grain represents the integrated exposure history of that grain, these interpretations represent endmember cases. We discuss each scenario by considering the likelihood that the bulk of the cosmogenic nuclide burden was imparted in that scenario, recognizing that the true history is most likely some combination of these endmembers.

4.6.1 Pre-depositional exposure

One potential explanation for the high concentration of cosmogenic noble gases from Mount Sharp relative to Aeolis Palus is pre-depositional exposure. In this scenario, the detrital components in Mojave 2 and Quela were exposed to cosmic irradiation for an extended period of time, in an

outcrop in the source terranes of Gale crater and/or as loose sediment in transport. After deposition in the Gale crater lake, these grains would have been rapidly shielded from continuing buildup of cosmogenic noble gases initially by the water column, and soon afterwards by more layers of sediment. After burial and lithification, the samples would have remained shielded from cosmic ray exposure until being exposed at the surface in the relatively recent past. This model could have a relatively young modern exposure age.

The samples Cumberland and Windjana showed no evidence for long prior exposure (Farley et al., 2014; Vasconcelos et al., 2016). If Mojave 2 and Quela have similar sediment source histories as Cumberland and Windjana, an upper limit of <100 Ma prior exposure is obtained. This upper limit is well within the uncertainty on the Mojave 2 and Quela measurements, and would have a minimal impact on the measured ~1 Ga exposure histories of these samples.

Even assuming differing sediment histories between Cumberland/Windjana and Mojave 2/Quela, such long exposure for grains that were eventually eroded into a basin implies that they must have been entirely eroded from the near surface (to allow for high rates of nuclide production) and either exposed in primary outcrop for ~1 Ga, or their transport as sediment lasted a similar amount of time. This length of exposure requires that the detrital components of the sediments were exposed for the first billion years of Mars's history before being delivered to Gale crater, soon after Mars formed and during a period of heavy bombardment. Such a history is implausible, especially compared with the possibility of extended exposure during the more inactive Amazonian period. The thicker atmosphere and possibility of a magnetic field during Mars's ancient history further suggests that the overall production rate of cosmogenic nuclides was lower in the ancient past. Pre-depositional exposure is therefore an unlikely explanation for the high abundance of the cosmogenic noble gases.

4.6.2 Murray-Stimson paleosurface exposure

The presence of an erosional unconformity between the Murray and Stimson formations indicates that the deposition of the Stimson formation postdates the deposition, lithification, and erosion of the Murray formation (Banham et al., 2018; Fraeman et al., 2016; Watkins et al., 2016). The length of time between initial Murray erosion and Stimson deposition is currently unconstrained

(Banham et al., 2018). As both the Mojave 2 and Quela are relatively close to this contact, these samples may shed light on the length of the interval between erosion in the ancient past and the deposition of the Stimson. In the paleosurface exposure endmember case, both Quela and Mojave 2 were exposed for ~ 1 Ga between the time of Murray erosion and Stimson deposition, which would indicate that there was a long hiatus in Mount Sharp's geomorphic evolution before the Stimson was deposited.

As the e-folding depth of cosmogenic nuclide production is 70 cm and because the nuclear cascade is generated in the top ~ 30 cm of rock, such a possibility requires that Mojave 2 and Quela are both located within ~ 1 m of this paleosurface, where cosmogenic nuclide production would not be significantly inhibited (Farley et al., 2014; Wieler, 2002). Even in the shallow subsurface with reduced shielding from cosmic rays (i.e. depths < 1 m), cosmogenic nuclide production rates are inhibited, lengthening the required exposure to account for the concentration of observed cosmogenic nuclides observed. For Quela, such shielding is likely prohibitive. As discussed in section 4.3.1, Quela is most likely situated 1.3-1.8 meters below the contact (Figure 4-3). The exact placement of Mojave 2 relative to this paleosurface is more uncertain. Based on nearby exposures of the Murray-Stimson contact, Mojave 2 also appears to be well beneath the paleosurface (Figure 4-2). While both Mojave 2 and Quela appear to be deeply buried based on these projections, the Murray-Stimson contact has local topographic relief which could potentially permit both samples to exist at the paleosurface (Watkins et al., 2016). In such a scenario, a hiatus of ~ 1 Ga prior to the deposition of the Stimson would be supported.

While paleosurface exposure cannot be directly eliminated, there is no independent reason to expect a long hiatus prior to Stimson deposition. No paleosol, ferrizone, or silcrete is observed at the Murray-Stimson contact, and there is no evidence for a regolith formed by impact gardening. As an angular unconformity, there cannot be a uniquely indurated layer of the Murray just below the Murray-Stimson contact which would indicate a reason to expect the formation of a paleosurface. In the absence of direct evidence in favor of the observation of paleoexposure at either Quela or Mojave 2, the simplest explanation is that a paleoexposure endmember is not the best interpretation for these data.

4.6.3 Modern exposure

As paleoexposure appears unlikely, the most straightforward explanation for the exposure age results obtained from Mojave 2 and Quela is that both have been exposed to cosmic ray irradiation for the most recent ~ 1 Ga. Given that cosmic ray exposure of these samples appears to be a modern phenomenon, the geomorphology of the sample sites can yield insight to the mechanisms responsible for the generation of fresh surfaces at these locations. In the following section, we discuss the likely style of landscape change. We then describe the implications for ongoing geomorphic change in Gale crater, and conclude with a larger discussion of the long-term evolution of Mount Sharp.

4.6.3.1 Modern erosional style

While erosional style cannot be ascertained from the noble gas data (i.e., scarp retreat vs. vertical denudation, as discussed in section 4.5.2), the geomorphology present at the Quela drill site strongly suggests that scarp retreat is responsible for the exposure of this sample. A scarp eight meters tall exists approximately five meters from Quela's location (Figure 4-3), a geometry that is very unlikely to have arisen purely by vertical denudation. At Mojave 2, the presence of scarps bounding the bowl-shaped depression at Pahrump Hills also strongly implies that the dominant mechanism of landscape change at this locality is also scarp retreat. The gentle slopes in the minor topography surrounding the Mojave 2 sample imply that denudation may have played an additional minor role in the exposure of this sample at the surface (Figure 4-2).

At each of the sites measured for cosmogenic exposure, scarp retreat appears to be the main mechanism of geomorphic change based on their geomorphologies (and noble gas data at Cumberland and Windjana). Scarp retreat is therefore potentially the major mode of landscape change in modern-day Gale crater, with minor contributions from vertical denudation as observed at Mojave 2. We therefore use the term “exposure age” here onwards specifically to refer to the age since a surface formed via scarp retreat, while acknowledging that some small amount of denudation may have occurred.

4.6.3.2 Ongoing landscape evolution in Gale crater

Of the samples measured, two pairs of concordant exposure ages are observed: Cumberland and Windjana, which have been exposed for <100 Ma, and Mojave 2 and Quela, which have been exposed for ~ 1 Ga (Figure 4-4). There are four scenarios which could account for these observations (Figure 4-5): 1) vertical denudation, 2) steady scarp retreat, 3) episodic rapid scarp retreat, or 4) spatially differing steady-state scarp retreat. Of these, vertical denudation is eliminated based on the inferred exposure mechanism of scarp retreat discussed above.

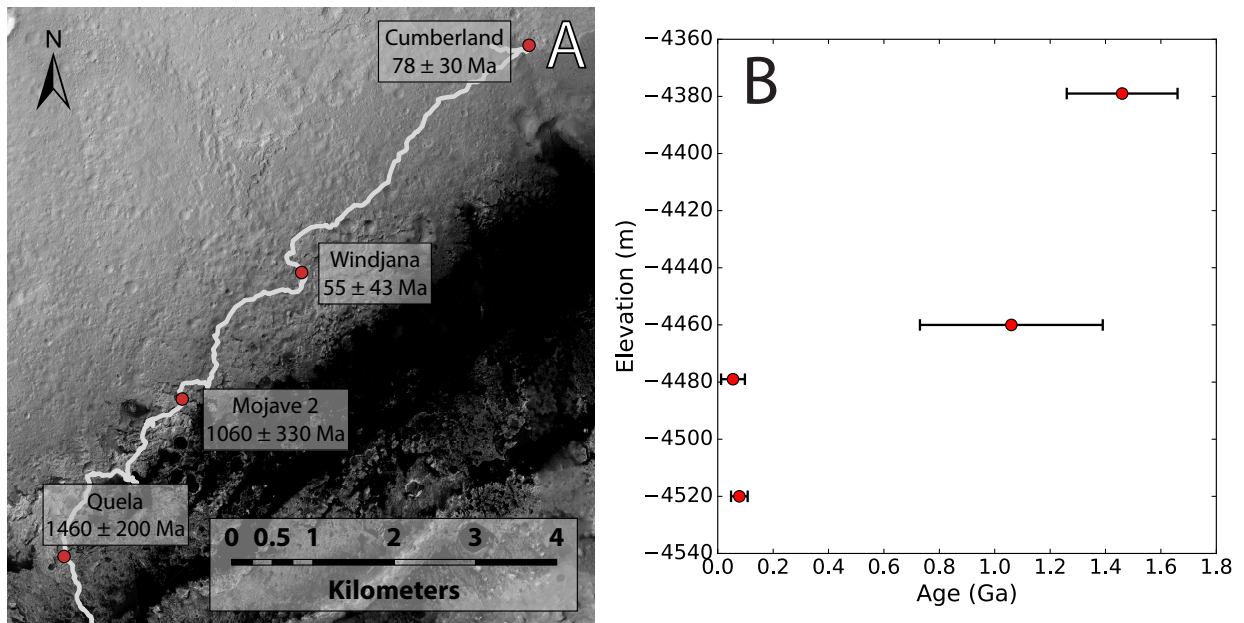


Figure 4-4. A) Map of sample locations with error-weighted mean exposure age of each sample shown. B) Error-weighted mean ages of each exposure age measured by SAM plotted against elevation below the Mars geoid.

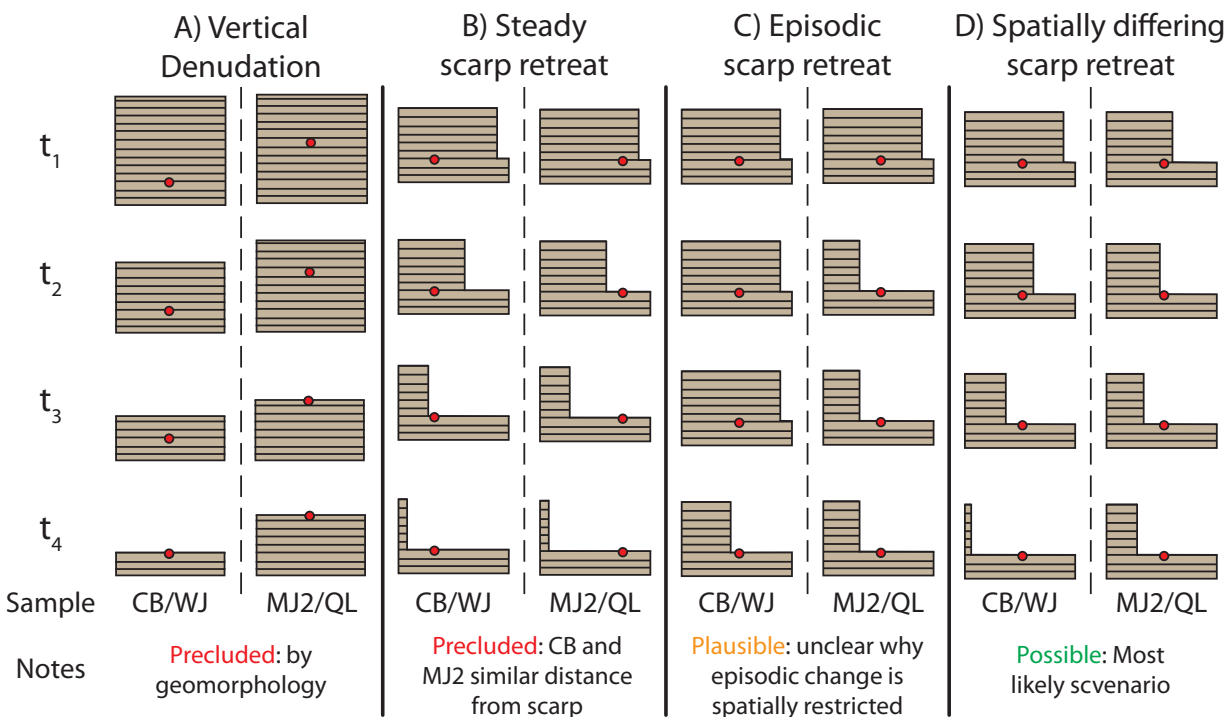


Figure 4-5. Diagram of potential exposure scenarios. CB/WJ stands for Cumberland/Windjana; MJ2/WL stands for Mojave 2/Quela.

Steady scarp retreat refers to a scenario in which scarp retreat happens at a constant rate throughout Gale crater (Figure 4-5b). This model makes the prediction that a sample's horizontal distance to a scarp will directly correlate with exposure age, meaning that a sample exposed for a longer period of time (e.g., Mojave 2 or Quela) should be located farther from the scarp which retreated to expose it relative to a sample with a younger exposure age. While it is not straightforward to determine which nearby scarp exposed a given surface (Williams et al., 2020), Mojave 2 and Cumberland were both sampled in local depressions (Pahrump Hills and Yellowknife Bay, respectively), both 50-100 m from a ring of nearby scarps (Figure 4-2 & Farley et al., 2014). The contrast in age between these samples eliminates the possibility of steady scarp retreat as the cause.

The exposure age groupings (Cumberland/Windjana and Mojave 2/Quela) could indicate that significant geomorphic change is highly episodic (Figure 4-5c). Such a scenario might imply that the majority of modern landscape change on Mars happens during periods of unusual obliquity and/or during uniquely strong windstorm events, reoccurring on timescales of hundreds of millions of years. The possibility of large temporal variations in integrated erosion rate as an explanation for the two clusters of ages is complicated by the fact that the more ancient surfaces at Mojave 2 and

Quela would have been preserved during a period of high erosion recorded by Cumberland and Windjana. There is no a priori reason to expect a large event capable of significant erosion to selectively generate fresh surfaces (for instance, at Cumberland) but leave other areas (e.g., Quela) unaffected. Such an episodic scarp retreat scenario is plausible, but the high variability in exposure age between different areas argues against it.

Another possibility is that landscape change is ongoing at generally steady rates across Gale crater, but that these rates are spatially distinct and laterally highly variable. In this model, some areas have relatively high rates of scarp retreat, while others are mostly quiescent (Figure 4-5d). In other words, given sufficient data, it would be possible to generate a heat map of exposure age, with short exposure ages (high rates of erosion) in areas like Yellowknife Bay and longer exposure ages (low rates of erosion) in Pahrump Hills and the Murray Buttes. Such a model suggests that a sample's location within the crater is the determining factor in its exposure age and, by proxy, the scarp retreat rate of that locality. Given the large lateral separation between samples measured for their noble gas content (average 2.8 km each; Figure 4-4a) and the fact that the exposure ages roughly correlate with this change in location, we consider this scenario the most likely of those listed above. Such spatially distinct scarp retreat rates are most likely determined by regional-scale winds and the large-scale features present in Gale as opposed to the rover-scale features observed during Curiosity's traverse (Day & Kocurek, 2016).

4.6.3.3 Formation of Mount Sharp and history of Gale crater

The longer exposure ages on Mount Sharp proper (Mojave 2 and Quela) relative to those on Aeolis Palus (Cumberland and Windjana) may indicate a differential rate of rock removal, which we calculate as an effective erosion rate using Equation 4-4. Based on such a calculation, the effective modern erosion rate due to vertical relief changes from scarp movement is insufficient to explain the formation of Mount Sharp which requires the removal of at least 1 km of overburden (Grotzinger et al., 2015). The 140 m vertical distance and 1405 ± 205 Ma exposure age difference between Cumberland and Quela suggests a moat-deepening rate of 100 ± 15 m Ga⁻¹; a more conservative estimate using the 20 m vertically separated samples Windjana and Mojave 2 and their age difference of 980 ± 330 Ma gives a rate of 20 ± 7 m Ga⁻¹. With these rates, at most 360 ± 54 m of incision could have occurred in the last 3.6 Ga, clearly far too little to explain the formation of the 5.2 km high

mount sharp, or even the ~1 km high portion of the mound comprised of fluviolacustrine and sulfate-bearing layers (Grotzinger et al., 2015). This insufficient rate could be explained by slowing erosion with time due to atmospheric loss (Armstrong & Leovy, 2005; Grotzinger et al., 2015; Jakosky et al., 1994), if only the rate, and not the style or location, of erosion has changed.

The modern erosion rate of 20-100 m Ga⁻¹ derived above matches an estimate of surface-lowering rate using small-crater degradation by Kite & Mayer (2017). Other estimated rates of erosion on Mars vary depending on geologic context between as high as 2300 m Ga⁻¹ in interior layered deposits (Grindrod & Warner, 2014), to as low as 0.01 m Ga⁻¹ at the Pathfinder landing site (Golombek & Bridges, 2000). Regardless of the formation mechanism of Mount Sharp, these modern erosion rates imply that for the observed landforms in Gale crater (including Mount Sharp itself) to have emerged, the rate of landscape change must have been far greater in the ancient past, in agreement with the conclusions of Grotzinger et al. (2015). This conclusion suggests that Mount Sharp had largely or entirely formed by the start of the Amazonian, consistent with crater counting by (Palucis et al., 2014). In addition, crater morphologies on Aeolis Palus indicate only 20-40 m of post-Hesperian erosion (Grant et al., 2014), reasonably consistent with the 20-100 m Ga⁻¹ derived erosion rate calculated above. Given these extremely slow rates of landscape change, the scarp retreat observed at the sample sites discussed here is most likely only a minor second-order effect on the first-order topography of Mount Sharp and the mantling units that cover it. Mount Sharp therefore likely formed early in Mars's history and has existed in its current form since the Hesperian.

4.7 Conclusions

The first samples from the Mount Sharp stratigraphy in Gale crater yielded exposure ages far older than those from the surrounding plains of Aeolis Palus. Mojave 2 gave a ³He age of 1,320 ± 240 Ma, ²¹Ne of 910 ± 420 Ma, and ³⁶Ar of 310 ± 60 Ma. A cosmogenic ³He age of 1,460 ± 200 Ma was observed in the sample Quela; ²¹Ne and ³⁶Ar could not be quantified due to uncorrectable isobaric interference. The relative youth of the calculated ³⁶Ar age in Mojave 2 may be due to resetting (or partial resetting) during a transient wetting event, consistent with previous results from this sample. The spallation nuclides ³He and ²¹Ne are held mostly in insoluble silicate grains and likely reflect the total accumulated exposure history of the two samples.

Neither pre-depositional exposure nor paleoexposure appear to be plausible scenarios to explain the high concentration of cosmogenic noble gases in these samples. Instead, the most straightforward interpretation of the data is that both Mojave 2 and Quela have been exposed for the most recent ~ 1 Ga. While the lack of geologically meaningful ^{36}Ar data precludes the direct determination of scarp retreat vs. vertical denudation as endmember models of erosion mechanism, the geometry at Quela seems to demand scarp retreat as the major mode of landscape change. Mojave 2 is more likely to have had minor contributions of denudation, but also seems likely to have been largely exposed by scarp retreat. Taken together with the data from Cumberland and Windjana, scarp retreat appears to be the dominant mode of modern landscape evolution in Gale crater.

The contrast between the ~ 1 Ga exposure age of Quela and Mojave 2 and the <100 Ma exposure ages obtained from samples from Aeolis Palus suggests that either geomorphic change occurs only in short bursts during climactically unusual periods, or that erosion is occurring steadily throughout Gale crater, but that the rate of this erosion is dependent on location and highly variable between different areas. Of these options, the lateral variability case is more likely, due to the large horizontal distance between the samples, and because there is no reason to expect any given surface (i.e., Quela and/or Mojave 2) to be preserved through a high-erosion period. In either case, the apparent erosion rate determined by integrating the exposure age difference over the vertical distance between the samples yields an overall erosion rate far too small to account for the formation of Mount Sharp. It is therefore likely that Mount Sharp had been exhumed to nearly its current form early in Mars's history and has since undergone relatively minor geomorphic change.

4.8 Appendix

4.8.1 Data Analysis

In this section, we describe the details of the results for each sample which are not germane to the determination of exposure history as discussed in the main text.

4.8.1.1 ^{21}Ne measurement

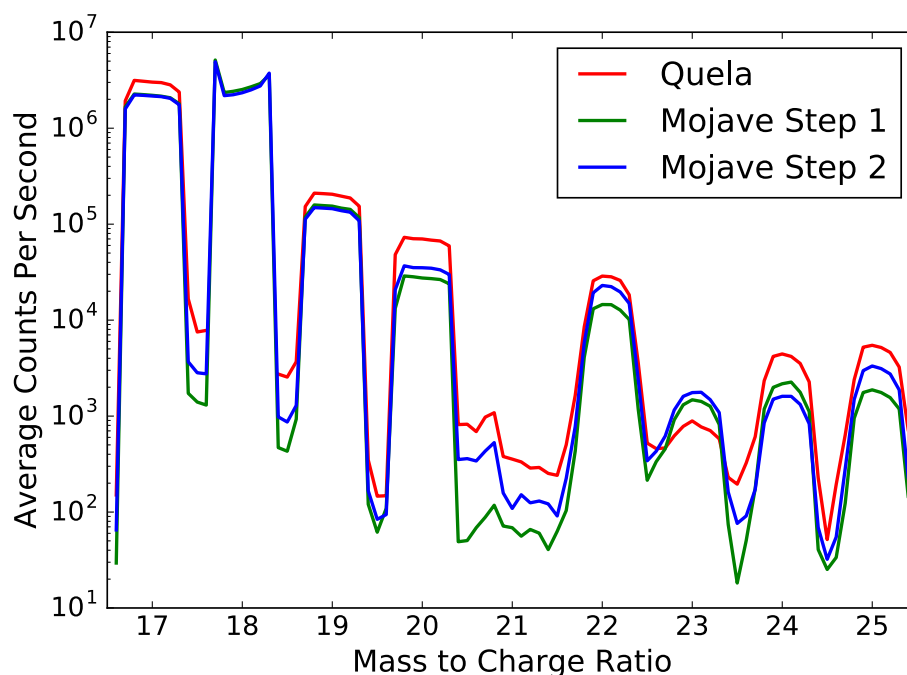


Figure 4-6. Mass spectra for Quela and Mojave 2, demonstrating squared-off peakshapes and the impact of the radiofrequency shift at m/z 20.9 on measurements at m/z 21.0. Counts shown are the average of the complete time series from each run. The dip in the peak at m/z 18 is a result of detector saturation due to H_2O .

A shift in the radiofrequency (RF) for the QMS occurs at m/z 20.9 to allow for measurements at higher masses. This shift briefly disturbs the stability of the ion path through the quadrupole mass analyzer, negatively impacting the measurement of ^{21}Ne using m/z 21.0. To avoid this issue, the off-integer mass spectrum at m/z 20.8 was used as a proxy for measurement of 21.0 in Mojave 2. Due to the nearly flat-topped peak shape of the QMS measurements (Figure 4-6), this selection of m/z to characterize ^{21}Ne abundance does not vary substantially from the “true” value that would be measured at m/z 21.0. This substitution was validated using the noble gas measurement of Quela,

where a mass spectrum was collected across the m/z 21.0-21.5 range without a RF shift. The reduced data using m/z 21.0 and m/z 20.8 are indistinguishable from one another; we therefore conclude that use of m/z 20.8 as a proxy for m/z 21.0 is appropriate for Mojave 2.

Background measurements are not made for non-integer masses after the system is pumped down. This lack of data is a minor complication in using m/z 20.8 for ^{21}Ne quantification in Mojave 2 as it precludes direct measurement of a background to subtract from the isobar-corrected ^{21}Ne signal. The same assumption that m/z 20.8 and m/z 21.0 are equivalent was made, and the ratio of semi-static to background measurements at m/z 21.0 was applied to the uncorrected semi-static measurement of m/z 20.8 to derive an estimated background.

4.8.1.2 Mojave 2

Table 4-2. Results of the noble gas experiment on Mojave 2, with production rates and calculated ages.

Mojave 2	^3He	^{21}Ne	^{36}Ar
High-T step aliquot 1 ^a (pmol g ⁻¹)	200±50	13±9	310±50
Low-T step aliquot 2 (pmol g ⁻¹)	620±110	32±15	90±20
High-T step aliquot 2 (pmol g ⁻¹)	-10±30	15±7	-30±20
Total aliquot 2 ^b (pmol g ⁻¹)	620±110	47±21	90±20
Surface production rate (pmol g ⁻¹ Ma ⁻¹)	0.4653	0.0523	0.2892
Age (Ma)	1,320±240	910±420	310±60

^aThe high temperature step of aliquot 1 is highlighted in red to indicate that we do not consider the data from this run valid.

^bAliquot 2 is highlighted in green as the numbers used for age calculations.

Two heating steps were used for the Mojave 2 sample to separate the K-Ar ages of detrital and secondary components (Martin et al., 2017). This temperature resolution has no advantage in the analysis of cosmogenic nuclides as the major cosmogenic noble gas-bearing minerals in a sample likely share an exposure history and would therefore have the same calculated exposure age (subject to the caveats regarding ^{36}Ar discussed in section 4.5.2). As no additional information would be

obtained by isolating the exposure ages of a few mineral components, the two steps are simply summed for this study.

For unknown reasons, an internal alarm was triggered during the low temperature step of the noble gas experiment on Mojave 2, causing no data to be collected; the high-T step ran successfully (Martin et al., 2017). A second aliquot of Mojave 2 was run successfully and all data was returned. Discrepancies between the successful second heating steps in the first and second aliquots of Mojave 2 have been ascribed to the loss of material during sample transfer (Martin et al., 2017). The measured ^3He and ^{21}Ne are lower in the high-temperature step of aliquot 1 (the failed run) than in aliquot 2, supporting this hypothesis. However, ^{36}Ar decreases between aliquot 1 and aliquot 2, suggesting that lost sample may not be the cause of these discrepancies. As the exact reason for the alarm and aborted noble gas run is unknown and data from half of the heating schedule was not collected, a complete understanding of the data returned from the first aliquot is likely to be elusive. Based on the reasonable K-Ar results from aliquot 2 (Martin et al., 2017), we adopt the interpretation that those data are more reliable and therefore utilize the data from aliquot 2 in forming interpretations for this study.

Table 4-3. APXS and CheMin results from Mojave 2 as reported in Martin et al. (2017) and Rampe et al. (2017). Uncertainty on chemistry measurements is 15% relative.

Chemistry (wt%)		Mineralogy (wt %)	
SiO ₂	49.48	Plagioclase	23.5 ± 1.6
TiO ₂	1.19	Forsterite	0.2 ± 0.8
Al ₂ O ₃	11.43	Augite	2.2 ± 1.1
FeO	16.11	Pigeonite	4.6 ± 0.7
MnO	0.40	Magnetite	3.0 ± 0.6
MgO	4.55	Hematite	3.0 ± 0.6
CaO	4.33	Quartz	0.8 ± 0.3
Na ₂ O	3.01	Jarosite	3.1 ± 1.6
K ₂ O	0.73	Fluorapatite	1.8 ± 1.0
P ₂ O ₅	1.29	Phyllosilicate	4.7 ± 2.4
Cr ₂ O ₃	0.37	Amorphous	53 ± 15
Cl	0.43		
SO ₃	6.27		
Ni (ppm)	1032		
Zn (ppm)	2204		
Br (ppm)	65		

No ^3He was measured in the high-T step of aliquot 2. The negative calculated amount of ^3He is well within uncertainty of zero, and so the high-T step is not included in age calculations. The calculated ^{36}Ar in the high-T step is also below zero, albeit outside of uncertainty. This is a result of the H^{35}Cl isobar correction, which dominates the uncertainty for the ^{36}Ar calculation (Farley et al., 2014). If the input $\delta^{37}\text{Cl}$ value is incorrect, the calculated ^{36}Ar concentration varies by about 3.9 pmol/g for each change of 1‰ in $\delta^{37}\text{Cl}$. The $\delta^{37}\text{Cl}$ cannot be measured directly in semi-static mode, so the value from the Mojave 2 evolved gas analysis, run 543 sols earlier, was used in this case. There are several potential explanations for a change in the $\delta^{37}\text{Cl}$ in this time: the uncertainty of the $\delta^{37}\text{Cl}$ given in Farley et al. (2016) could have been underestimated, resulting in a ^{36}Ar value below 0 outside uncertainty; the $\delta^{37}\text{Cl}$ may be slightly different between aliquots of Mojave 2 due to differing concentrations of Cl-rich phases; or HCl memory built up in SAM could have a heavier isotope value than the true value of Mojave 2, changing the required H^{35}Cl correction factor. A $\delta^{37}\text{Cl}$ value of $-41 \pm 5\text{‰}$ was used in this calculation (Farley et al., 2016); a change in either the value or the uncertainty by 3‰ results in a calculated ^{36}Ar of zero within uncertainty. Therefore, as with ^3He , the high-T step for ^{36}Ar is not included in age calculations.

4.8.1.3 Quela

Table 4-4. APXS and CheMin results from Quela, available on the NASA PDS and in Bristow et al. (2018). Uncertainty on chemistry measurements is 15% relative.

Chemistry (wt%)		Mineralogy (wt %)	
SiO_2	44.81	Andesine	13.5 ± 0.7
TiO_2	1.05	Hematite	7.1 ± 0.4
Al_2O_3	8.48	Ca-Sulfate	5.5 ± 0.4
FeO	18.93	Sanidine	2.3 ± 0.5
MnO	0.22	Pyroxene	2.7 ± 0.7
MgO	4.10	Jarosite	≤ 0.5
CaO	7.48	Quartz	≤ 0.5
Na_2O	2.19	Clay minerals	16 ± 3
K_2O	0.77	Amorphous	52 ± 25
P_2O_5	1.10		
Cr_2O_3	0.29		
Cl	1.01		
SO_3	9.30		
Ni (ppm)	999		
Zn (ppm)	826		
Br (ppm)	42		

Neither ^{21}Ne nor ^{36}Ar were successfully measured for Quela, due to large uncertainties associated with both measurements. For ^{21}Ne , this uncertainty was generated by a lack of spread in m/z 20 for isobaric correction, which resulted in a poor regression and large uncertainty (Figure 4-7; Farley et al., 2014).

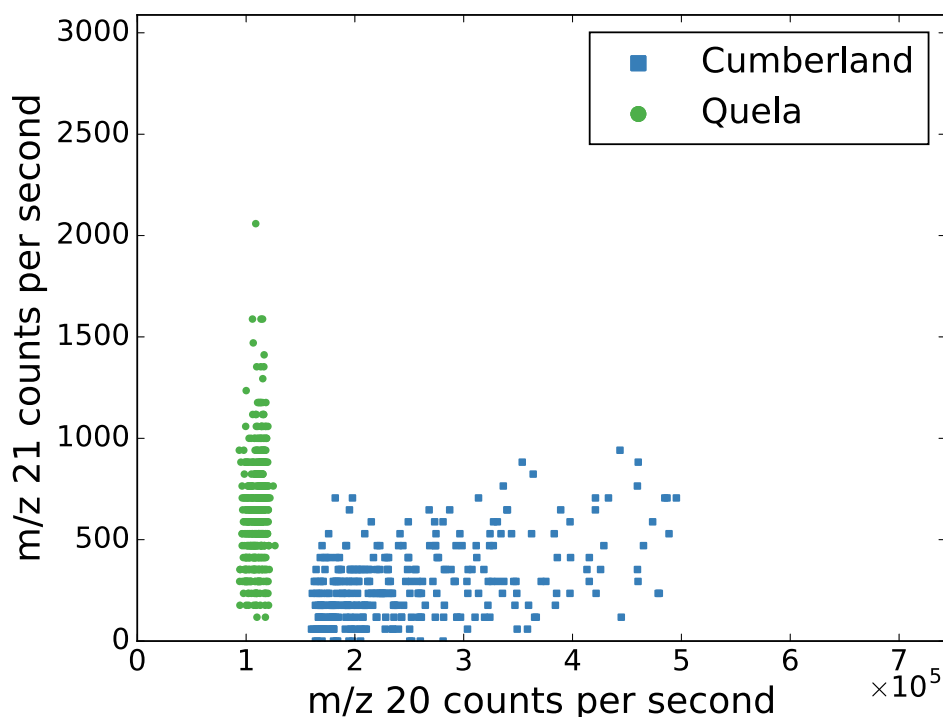


Figure 4-7. Quela m/z 21.0 plotted against m/z 20.0, which is used to correct for interference from H_2^{18}O . The lack of spread in m/z 20.0 precludes valid regression to allow conversion of m/z 21.0 to a ^{21}Ne signal. See Farley et al. (2014) for a detailed description of isobar correction methods.

Measurement of ^{36}Ar was unsuccessful because Quela has an anomalously large release of HCl (both in this analysis and evolved gas analysis; Sutter et al., 2017), resulting in an H^{35}Cl isobar correction much larger than any other sample yet measured by SAM. Additionally, this correction relies on accurate evaluation of the chlorine isotope ratio in Quela, but the $\delta^{37}\text{Cl}$ cannot be accurately calculated as a result of detector saturation at the peak of this large release. If chlorine isotope values typical of the Murray from Pahrump are used and the largest uncertainty measured by Farley et al. (2016) is imposed on this value, the uncertainty on the calculated age is approximately four billion years, making this measurement uninterpretable.

REEVALUATION OF PERCHLORATE IN GALE CRATER ROCKS SUGGESTS GEOLOGICALLY RECENT PERCHLORATE ADDITION

The content of this chapter has been submitted for publication as:

Martin, P. E., Farley, K. A., P. D. Archer, Jr., J. V. Hogancamp, K. L. Siebach, J. P. Grotzinger, and S. M. McLennan (2019). Reevaluation of Perchlorate in Gale Crater Rocks Suggests Geologically Recent Perchlorate Addition. *In Revision*.

5.1 Abstract

Perchlorate (ClO_4^-) was discovered in Martian soil by the Phoenix lander, with important implications for potential Martian biology, photochemistry, aqueous chemistry, and the chlorine cycle on Mars. Perchlorate was subsequently reported in both loose sediment and bedrock samples analyzed by the Sample Analysis at Mars (SAM) instrument onboard the Curiosity rover in Gale crater based on a release of O_2 at 200-500°C. However, the continually wet paleoenvironment recorded by the sedimentary rocks in Gale crater was not conducive to the deposition of highly soluble salts. Furthermore, the preservation of ancient perchlorate to the modern day is unexpected due to its low thermodynamic stability and radiolytic decomposition associated with its long exposure to radioactivity and cosmic radiation. We therefore investigate alternative sources of O_2 in SAM analyses including superoxides, sulfates, nitrate, and nanophase iron and manganese oxides. Geochemical evidence and oxygen release patterns observed by Curiosity are inconsistent with each of these alternatives. We conclude that perchlorate is indeed the most likely source of the detected O_2 release at 200-500°C, but contend that it is unlikely to be ancient. Rather than being associated with the lacustrine or early diagenetic environment, the most likely origin of perchlorate in the bedrock is late stage addition by downward percolation of water through rock pore space during transient wetting events in the Amazonian. The conclusion that the observed perchlorate in Gale crater (and possibly Mars generally) is most likely Amazonian means that its effects need not extend into the early history of Mars.

5.2 Introduction

Perchlorate anion (ClO_4^-) was discovered in Martian soil in 2009 by the Phoenix Lander (Hecht et al., 2009), spurring discussion of the implications for potential Martian biology, photochemistry, aqueous chemistry, and the chlorine cycle on Mars. Central to perchlorate's importance is its exceptional solubility, which allows freezing point depression in saturated fluids of up to -75°C (Marion et al., 2010; Toner et al., 2014, 2015). Perchlorate salts are also highly hygroscopic, deliquescing at the low temperatures and relative humidities of 243 K and $<40\%$, respectively (Gough et al., 2014). These combined traits allow the spontaneous formation of liquid perchlorate brines, even at Mars surface conditions. As a result, perchlorate has been invoked to explain observations such as recurring slope lineae (e.g., Chevrier & Rivera-Valentin, 2012; McEwen et al., 2011) and putative sub-polar cap liquid water (Orosei et al., 2018). Perchlorate may act as an electron acceptor for microbes (McKay et al., 2013; Oren et al., 2014), and may destroy organic molecules via interaction with intermediate oxidation steps during perchlorate formation (Carrier & Kounaves, 2015), interaction with ionizing radiation (Quinn et al., 2013), or during analytical heating of a sample (ten Kate, 2010; Lasne et al., 2016), impacting the search for potential biosignatures.

The discovery of perchlorate by Phoenix was compellingly made using three lines of evidence: (1) an ion-selective electrode with a high perchlorate sensitivity indicated the presence of perchlorate, (2) an electrode designed for Ca^{2+} measurement fell, consistent with a known interference from perchlorate, and (3) a release of oxygen was detected during heating of soil samples, interpreted as a result of perchlorate breakdown (Hecht et al., 2009).

The Tissint Mars meteorite formed (574 ± 20 Ma; Brennecka et al., 2014) has been observed to contain ppb levels of perchlorate along with other oxychlorine phases, which are likely Martian in origin (Jaramillo et al., 2019). Additional detections of perchlorate on Mars have been equivocal. The Shergottite EETA79001 (formed 173 ± 3 Ma; Nyquist et al., 2001) contains perchlorate and nitrate, which isotopically contrasts with the surrounding ice and rock, but matches the isotopic composition of nitrate in the Atacama (Kounaves et al., 2014), leaving its origin ambiguous. The putative in-situ detection of perchlorate based on orbital spectroscopy (Ojha et al., 2015) was shown to be the result of a spectral artifact (Leask et al., 2018; Vincendon et al., 2019). Viking data was

reinterpreted as consistent with perchlorate based on the presence of chloromethane (Navarro-González et al., 2010), though this interpretation has been challenged (Biemann & Bada, 2011).

The first evolved gas analysis (EGA) of a scooped soil sample by the Sample Analysis at Mars (SAM) instrument on the Curiosity rover yielded temporally correlated detections of O₂ and chlorinated hydrocarbons, interpreted as evidence of an oxychlorine phase such as perchlorate in the soil at Gale crater (Glavin et al., 2013; Leshin et al., 2013). Later analysis of a sample of ancient lacustrine bedrock produced similar results (Ming et al., 2014). Perchlorate has since been suggested to be present in additional samples of ancient Gale crater rocks (Sutter et al., 2017) as an original component of those samples (Archer et al., 2016). We use the term “indigenous perchlorate” to refer to putative perchlorate deposited as a lacustrine material in the Gale crater lake or by early diagenetic fluids. We refer to perchlorate rather than oxychlorine or (per)chlorate (as chlorate may explain these observations; Hogancamp et al., 2018a; Sutter et al., 2017); the arguments throughout apply to both chlorate and perchlorate with the caveat that chlorate is far less kinetically stable (section 5.3.1.2).

Another line of evidence supporting perchlorate in Gale crater is the presence of highly unusual chlorine isotope compositions. While the vast bulk of chlorine reservoirs on Earth vary within $\pm 3\text{‰}$ $\delta^{37}\text{Cl}$ (Eggenkamp, 2014), chlorine isotope ratios in Gale crater measured on HCl are strongly depleted in ^{37}Cl and highly variable: -50 to -15‰ $\delta^{37}\text{Cl}$ (Farley et al., 2016). Either direct measurement of oxychlorine phases or cycling of chlorine through oxychlorine phases was the preferred interpretation of Farley et al. (2016). This interpretation was based heavily on analogy with the findings of extremely isotopically ^{37}Cl -depleted perchlorate in the Atacama, fractionated via an unknown mechanism (Böhlke et al., 2005).

The presence of indigenous perchlorate would have significant implications for early Mars and thus warrants critical appraisal. We present evidence that the depositional and early diagenetic paleoenvironments of the bedrock in Gale crater were not conducive to perchlorate deposition/preservation, and that perchlorate deposited at that time is expected to have decomposed in the billions of years after deposition. We therefore consider two alternative explanations to indigenous perchlorate for the oxygen release observed in samples from Gale crater: the oxygen is produced by a substance other than perchlorate, or it is produced by perchlorate that is not indigenous. Our assessment shows that perchlorate remains the most consistent explanation for SAM

EGA observations, and that the simplest solution to the paradox of perchlorate in the ancient sedimentary rocks in Gale crater is that the perchlorate was introduced long after rock deposition. It is possible that perchlorate on Mars is geologically young, and we hypothesize that it has been introduced by percolation of water into the pore spaces of the bedrock in Gale crater during infrequent wetting events.

5.3 Perchlorate in Gale crater

In this section we describe challenges to the deposition of perchlorate during bedrock formation in Gale crater and its subsequent preservation. We then consider the evidence offered in support of perchlorate as measured by the SAM instrument. We show that the presence of a large release of O₂ at 200-500°C is the only line of evidence that cannot be explained by compounds independently confirmed to be present by other instruments.

5.3.1 Evidence against ancient perchlorate based on geologic interpretation

5.3.1.1 Geologic evidence

The geologic setting of bedrock deposition in Gale crater was not likely conducive to perchlorate precipitation. The stratigraphy observed in Gale crater includes mostly fluvial and deltaic sandstones and lacustrine mudstones, the latter of which indicate fresh to mildly saline lake waters (e.g., Grotzinger et al., 2015, 2014; Stack et al., 2019). This setting differs from where perchlorate salts are found on Earth, in arid environments such as the Antarctic Dry Valleys and the Atacama (Ericksen, 1981; Kounaves et al., 2010). Perchlorate salts form via extremely concentrated brines, and are highly vulnerable to dissolution and consequently unlikely to be incorporated into the rock record. On Earth, the perchlorate ion is only ever found as a minor (≤ 0.1 wt%) constituent in soils, caliches, and surficial evaporites (Jackson et al., 2015). In order to be included in the rock record, a perchlorate deposit would need to precipitate as a salt from solution, and subsequently have extremely limited open-system interactions with liquid water during and after lithification (and avoid reduction via biotic interactions; Coates and Achenbach, 2004). Such a scenario is conceivable on Mars, but the rocks so far explored in Gale crater are conformable lacustrine deposits that document a continually wet environment, rather than evaporite beds (Grotzinger et al., 2015).

Other less soluble salt species such as Ca-, Mg-, and Fe-sulfate and various chloride salts (e.g., Hardie et al., 1978; Tosca et al., 2005) would be expected at high abundance in the bulk rock in concert with the perchlorate salts or in discrete highly concentrated layers if more soluble ions were ever precipitated. Calcium sulfate minerals are common, but in late fractures that cross-cut bedding as well as major unconformities (Caswell & Milliken, 2017; Grotzinger et al., 2014; Kronyak et al., 2019; Vaniman et al., 2014, 2018). Abundant bedded evaporite deposits have not been observed, though small amounts of highly soluble Fe- and MgSO_4 (Rapin et al., 2019; Sutter et al., 2017) and chloride salts (Thomas et al., 2018) have been observed in the rock matrix. The possibility therefore exists that other highly soluble salts (including perchlorate) were also included via an unknown mechanism.

Common indicators of aridity such as convolute bedding, enterolithic folding, tepee structures, and displacive/massive evaporite mineral growth are not observed. In only one location have desiccation cracks been confidently observed (Stein et al., 2018). On the other hand, numerous indications of later diagenetic processes extending as much as ~ 1.5 Ga after the original deposition of the lacustrine rocks have been noted (e.g., Grotzinger et al., 2015; Martin et al., 2017a; Nachon et al., 2014), lengthening the timeline of aqueous interaction within this rock sequence. If any perchlorate had precipitated in the early environment, these later fluids could have dissolved and removed it. This idea was suggested by Archer et al. (2016) based on the smaller amount of O_2 released from the vein-rich sample John Klein relative to the nearby, more pristine Cumberland sample. This contrast between Cumberland and John Klein also suggests that a late addition of perchlorate by diagenetic fluids is unlikely (Archer et al., 2016).

5.3.1.2 Thermodynamics and Radiolysis

The thermodynamic instability of perchlorate lowers the likelihood of its long-term survival in Martian bedrock. While perchlorate ion has a high thermodynamic oxidative potential (Urbansky, 2002), it is kinetically stable, impeding reduction in most settings (Brown & Gu, 2006). However, decomposition of perchlorate occurs under exposure to ionizing radiation (Prince & Johnson, 1965a; Quinn et al., 2013; Turner et al., 2016). While ionizing radiation interaction has also been proposed as a formation mechanism for perchlorate (e.g., Carrier & Kounaves, 2015; Wilson et al., 2016), this thermodynamically unfavorable process occurs only when a local energy minimum is encountered.

The radiolysis breakdown described above allows the kinetic barrier to be broken so that thermodynamically favorable decomposition can occur. This decomposition results in the formation of chlorate (ClO_3^-), chlorite (ClO_2^-), chlorine dioxide (ClO_2), hypochlorite (ClO^-), and chloride (Cl^-), though the final product of decomposition is most likely chloride (see the discussion of chlorate below and Prince and Johnson, 1965a). Martian rocks are exposed to ionizing radiation from the radioactive decay of ^{40}K and U- and Th-series isotopes, and from galactic cosmic rays (GCRs) in the uppermost few meters of the surface.

The dose of ionizing radiation from radioactive decay experienced by a rock can be computed from the depositional age of the rock and its radioelement content. On Curiosity, K is measured by both ChemCam and APXS. Although no instruments currently deployed on the surface of Mars can measure U or Th, these three elements do not greatly fractionate from one another in igneous processes. Based on orbital gamma ray spectral mapping of K and Th abundances in the near-surface, the best estimate for the average Martian K/Th ratio is 5,330 (Taylor et al., 2007), which is also consistent with Martian meteorite data that further indicate a K/U ratio of about 20,000 (e.g., Taylor, 2013; Taylor and McLennan, 2009; Wänke et al., 1994). Using measurements of K_2O content (Bristow et al., 2018; Morrison et al., 2018), these assumed elemental ratios, the isotopic heat production values from Van Schmus (1995), and a depositional age of 3.6 Ga (Le Deit et al., 2012), we calculate that the total accumulated radiogenic radiation dose of the samples analyzed by SAM ranges from 6.7 ± 0.9 to 71.3 ± 9.4 MGy (all uncertainties at the 1- σ level, see section 5.7.2 for detailed description of uncertainty derivation; Table 5-1).

The exposure of Gale crater rocks to radiation from GCRs is less well known, but can be estimated from reported cosmic ray exposure ages (Farley et al., 2014; Martin et al., 2017b; Vasconcelos et al., 2016) and modeled GCR dose rates (Pavlov et al., 2012). For samples with no measured exposure age, we take the well-constrained exposure ages measured at Cumberland and Mojave 2 as lower and upper bounds of GCR radiation dose. Table 5-1 shows the results of these calculations, and demonstrates that the average minimum total dose of ionizing radiation experienced at the surface in Gale crater is ~ 30 MGy, mostly coming from radioactive decay rather than from GCRs.

Table 5-1. Radiolysis calculations for each sample. Bold numbers indicate that no extrapolation from other samples has been performed. Radiogenic dose is inferred from K₂O measurements, and exposure ages are directly measured. Samples are shown in stratigraphic order (lowest=lowest in the section). Rows shaded in blue are scooped sediment samples. Rows shaded in red do not have a measured O₂ release. Perchlorate content is calculated based on the work of Archer et al. (2014). All uncertainties are at the 1- σ level. GCR = “galactic cosmic ray”, CB = Cumberland, JK = John Klein, WJ = Windjana, CH = Confidence Hills, MJ = Mojave, TP = Telegraph Peak, BK = Buckskin, OU = Oudam, GH = Greenhorn, BY = Big Sky, MB = Marimba, QL = Quela, DU = Duluth, ST = Stoer, HF = Highfield, RH = Rock Hall (*sample mass unconstrained; large O₂ release observed, but concentration has not been quantified), OG = Ogunquit Beach, GB = Gobabeb, RN = Rocknest

Sample	Perchlorate Content (wt%)	K ₂ O (wt %)	Radiogenic Dose (MGy)	Measured Exposure Age (Ma)	Min Max GCR (MGy)		Min Max Total (MGy)		Min Max % Destroyed	
OG	0.17±0.03	0.59±0.07	13.6±1.8	-	4.4±1.9	69.4±18.6	18.0±2.6	83.1±18.7	60.0±9.2	98.6±22.7
GB1	0.23±0.05	0.49±0.06	11.3±1.5	-	4.4±1.9	69.4±18.6	15.7±2.4	80.7±18.6	55.1±8.9	98.4±23.2
GB2	0.52±0.10	0.40±0.05	9.2±1.2	-	4.4±1.9	69.4±18.6	13.6±2.3	78.7±18.6	50.0±8.7	98.2±23.7
RN	4e-4±2e-4	1.86±0.22	42.9±5.7	-	4.4±1.9	69.4±18.6	47.3±6.0	112.3±19.4	91.0±12.4	99.7±18.0
RH	*	0.58±0.07	13.4±1.8	-	4.4±1.9	69.4±18.6	17.7±2.6	82.8±18.7	59.6±9.1	98.5±22.7
HF	0	0.9±0.11	20.8±2.7	-	4.4±1.9	69.4±18.6	25.1±3.3	90.2±18.8	72.3±10.2	99.0±21.2
ST	0	0.91±0.11	21.0±2.8	-	4.4±1.9	69.4±18.6	25.4±3.4	90.4±18.8	72.6±10.3	99.0±21.1
DU	0	0.94±0.11	21.7±2.9	-	4.4±1.9	69.4±18.6	26.0±3.3	91.1±18.8	73.5±10.4	99.0±21.0
QL	0	0.77±0.09	17.8±2.3	-	4.4±1.9	69.4±18.6	22.1±3.0	87.2±18.7	67.7±9.8	98.8±21.8
MB	0	0.83±0.10	19.1±2.5	-	4.4±1.9	69.4±18.6	23.5±3.2	88.6±18.7	69.9±10.0	98.9±21.5
BY	0.13±0.03	0.49±0.06	11.3±1.5	-	4.4±1.9	69.4±18.6	15.7±2.4	80.7±18.6	55.1±8.9	98.4±23.2
GH	0.11±0.02	0.29±0.03	6.7±0.9	-	4.4±1.9	69.4±18.6	11.1±2.1	76.1±18.6	43.1±8.4	98.0±24.4
OU	0	0.81±0.10	18.7±2.5	-	4.4±1.9	69.4±18.6	23.1±3.1	88.1±18.7	69.2±9.9	98.9±21.6
BK	0.17±0.03	1.00±0.12	23.0±3.0	-	4.4±1.9	69.4±18.6	27.4±3.6	92.5±18.8	75.3±10.5	99.1±20.8
TP	0.09±0.02	0.98±0.12	22.6±3.0	-	4.4±1.9	69.4±18.6	27.0±3.5	92.0±18.8	74.8±10.5	99.1±20.8
MJ	0.11±0.02	0.63±0.08	14.5±1.9	1240±220	69.4±18.6		84.0±18.7		98.6±22.5	
CH	0.06±0.01	0.98±0.12	22.6±3.0	-	4.4±1.9	69.4±18.6	27.0±3.5	92.0±18.8	74.8±10.5	99.0±20.8
WJ	0.23±0.04	3.09±0.37	71.3±9.4	55±43	3.1±2.5		74.3±9.7		97.8±13.7	
JK	0.10±0.02	0.54±0.06	12.5±1.6	-	4.4±1.9	69.4±18.6	16.8±2.5	81.9±18.6	57.6±9.1	98.5±22.9
CB	1.09±0.20	0.62±0.07	14.3±1.9	78±30	4.4±1.9		18.7±2.7		61.4±9.3	

Given these ionizing radiation doses, the fraction of indigenous 3.6 Ga perchlorate destroyed since deposition may be calculated (Table 5-1). We adopt the radiolysis rate reported by Prince and Johnson (1965a) for KClO_4 as this yields the lowest breakdown rate and thus provides a conservative estimate of perchlorate radiolysis. Prince and Johnson (1965a, 1965b) studied the destruction of the perchlorate ion and the ingrowth of breakdown products for multiple perchlorate salts with carefully monitored dose rates and at a sufficiently high radiation dose (~ 5 MGy) that the radiolytic decomposition rate was well defined. Other studies investigated the products of radiolytic perchlorate decomposition but did not report perchlorate radiolysis constants (Quinn et al., 2013; Turner et al., 2016). For these studies we computed radiolysis constants from reported results and found that they agree with the precise estimates of Prince and Johnson (1965a) to within about a factor of two. Radiolysis is essentially independent of temperature, pressure, and cation of the perchlorate salt (Prince & Johnson, 1965b), suggesting that laboratory rates are applicable to the Martian surface throughout Martian history. However, as no study has evaluated perchlorate radiolysis on a geologically relevant matrix, further experiments could be undertaken to refine radiolysis constants for perchlorate.

For some of the analyzed rocks the estimated fraction of surviving putative indigenous perchlorate is prohibitive. The sample Windjana is the most potassic yet analyzed by SAM, providing an endmember for the radiogenic component of the ionizing radiation dose. The radiation dose for Windjana is 74.3 ± 9.7 MGy, which would destroy $97.8 \pm 13.7\%$ of any indigenous perchlorate (Table 5-1). Given Windjana's perchlorate content of 0.23 ± 0.06 wt%, the original perchlorate content would have to have been 10.2 ± 3.0 wt%, two orders of magnitude higher than the maximum concentration observed on Earth (Jackson et al., 2015) and ~ 20 times that inferred at the Phoenix landing site (Hecht et al., 2009). Additionally, if nearly 10 wt% of the original rock were destroyed, collapse structures and/or void space would be expected, but are not observed. This conclusion is further strengthened by considering the Cl budget of the rock. Given Windjana's APXS-measured Cl content of 0.57 ± 0.09 wt% and its putative perchlorate content of 0.23 ± 0.06 wt% (0.082 ± 0.02 wt% as Cl) (Sutter et al., 2017), $14.4 \pm 4.3\%$ of the total Cl in Windjana is presently in the form of perchlorate. If $97.8 \pm 13.7\%$ of indigenous perchlorate has decomposed to chloride, then at most $2.3 \pm 0.3\%$ of the chlorine in Windjana could be in the form of perchlorate if all chlorine in the sample was originally perchlorate, clearly inconsistent with the current amount of perchlorate.

These calculations may not be prohibitive if perchlorate is reduced only to chlorate rather than to chloride. SAM data cannot distinguish among oxychlorine compounds, so either chlorate or perchlorate could explain the SAM data (Hogancamp et al., 2018a). Chlorate is thermodynamically unstable (e.g., Brown and Gu, 2006; Srinivasan et al., 2009), likely suffering the same radiolysis fate as perchlorate. Chlorate is an initial product of perchlorate decomposition in radiolysis experiments (Prince & Johnson, 1965a; Turner et al., 2016), but it is not necessarily the stable end product of radiolysis. Unlike perchlorate, chlorate is kinetically unstable (e.g., Brown, 1986; Cao et al., 2005; Gu et al., 2003) and is reduced to chloride by Fe^{2+} on a timescale of hours to days (Gu et al., 2003; Mitra & Catalano, in press), suggesting that it may not survive long enough to be destroyed by radiation due to (electro)chemical reduction. It appears most likely that chlorate reduction quickly follows radiolysis and perchlorate is rapidly reduced to Cl^- in a stepwise fashion, as observed in numerous instances on Earth (e.g., Cao et al., 2005; Gu et al., 2003; Urbansky, 2002). Thus indigenous chlorate no better accounts for these observations than perchlorate.

5.3.2 Putative perchlorate detection by SAM

No corroborating evidence for the presence of perchlorate has been obtained from any other instrument on *Curiosity* (e.g., ChemCam or CheMin; Gasnault et al., 2012), which is expected because, even at the highest reported levels, the perchlorate is at or below the detection limits of these instruments. In light of the geologic observations that make deposition and survival of perchlorate in ancient Gale crater rocks highly unlikely, and in the absence of corroborating data, it is important to reexamine the varied lines of evidence from SAM that have been offered in favor of its presence.

Rock and regolith samples are delivered to SAM after scooping sediment from the surface or drilling to collect bedrock 1.5-5 cm below the surface (Anderson et al., 2012). A mass of sample between 45 ± 6 and 135 ± 18 mg is gradually heated to $\sim 900^\circ\text{C}$, releasing volatile species (e.g., Sutter et al., 2017). A helium stream acts as a carrier gas, sweeping evolved volatiles into a quadrupole mass spectrometer (Mahaffy et al., 2012), allowing temperature-resolved evolved gas analysis (EGA). For rare isotopologues or uncommon gas species, careful correction for isobaric interferences must be made (e.g., Archer et al., 2014; Eigenbrode et al., 2018; Sutter et al., 2017).

However, the gases analyzed here are sufficiently abundant that the raw signal of m/z corrected only for detector deadtime is used as a proxy for the gas of interest (i.e., $O_2 = m/z\ 32$; $HCl = m/z\ 36$).

The first SAM EGA run on a solid sample was a scooped sand shadow deposit called Rocknest. A large release of O_2 ($m/z\ 32$) was observed with chloromethane (CH_3Cl , $m/z\ 50$ and 52) released at the onset of O_2 evolution (Figure 5-6 in the appendix; Leshin et al., 2013), interpreted as evidence for perchlorate (Glavin et al., 2013; Leshin et al., 2013). A similar correlation was noted in the first drilled bedrock samples, although a temporal connection with HCl ($m/z\ 36$ and 38) was invoked as well (Ming et al., 2014). Samples collected later in the mission also produced large O_2 releases attributed to perchlorate (Sutter et al., 2017), though this O_2 release was not observed in a number of samples high in the stratigraphic section so far explored (Archer et al., 2019).

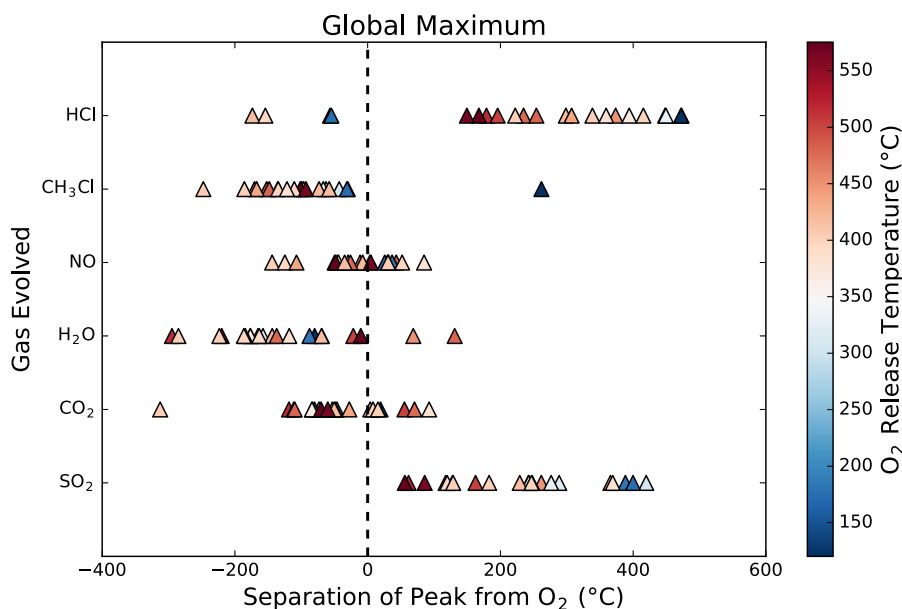


Figure 5-1. The global maximum gas release temperatures for a variety of gases relative to the maximum gas release temperature of O_2 . The color bar shows the absolute temperature of maximum O_2 release. No strong correlation exists between the release temperature of O_2 and HCl and CH_3Cl . However, NO is released near or simultaneously to O_2 , regardless of the absolute temperature of O_2 release.

Figure 5-1 shows that the temporal correlations among O_2 , HCl , and CH_3Cl are not especially strong relative to other abundant gases released during EGA with no known association to perchlorate. This conclusion holds regardless of exactly how the timing is established (e.g., initial onset of release, peak release, or any combination of these; Figure 5-7 in the appendix). Similarly,

the detailed temporal relationships among O₂, HCl and chloromethane are inconsistent among samples (Figure 5-6).

This lack of temporal correlation between HCl and O₂ is not surprising. While Fe- and Mg-perchlorate salts are thought to release HCl and O₂ simultaneously, for other cations perchlorate breakdown proceeds by release of O₂ and formation of chloride salts which then release HCl only when sufficient water is available for protonation (Hogancamp et al., 2017; Sutter et al., 2017). This decoupling between HCl and perchlorate-generated O₂ means that it is impossible to know whether HCl is a product of perchlorate breakdown or was released from chloride salts originally in the sample. If an alternative source of O₂ is present, no perchlorate is required by these observations and all HCl detected by SAM could be sourced from chloride (Hogancamp et al., 2017; Sutter et al., 2017). On the other hand, since a temporal correlation between O₂ and HCl is not expected in the decomposition of all perchlorate salts, the absence of such a correlation is not evidence against the presence of perchlorate.

In many samples, the main release of CH₃Cl occurs as the release of O₂ is beginning (Figure 5-7b; Glavin et al., 2013; Leshin et al., 2013). This ordering is likely not evidence for perchlorate in the sample; its tetrahedral structure presumably prevents interaction of organics with the central chlorine atom until *after* the perchlorate anion has broken down and released O₂. Furthermore, chlorinated hydrocarbons have been produced via heating of chloride salts (Keppler et al., 2014), signifying that the chlorinated hydrocarbons in EGA could be explained by either perchlorate or chloride salts.

Independent of release temperature correlations, consistent molar ratios between O₂ and CH₃Cl or HCl might indicate the presence of perchlorate. No such correlation is evident however (Figure 5-2). Numerous and complex reactions likely occur between the gases released during EGA, between these gases and the rock sample, and potentially within the SAM transfer lines. A lack of correlation in measured abundance therefore does not preclude a correlation in abundance of gases released from the sample, but there is no evidence to support the presence of perchlorate based on measured abundances.

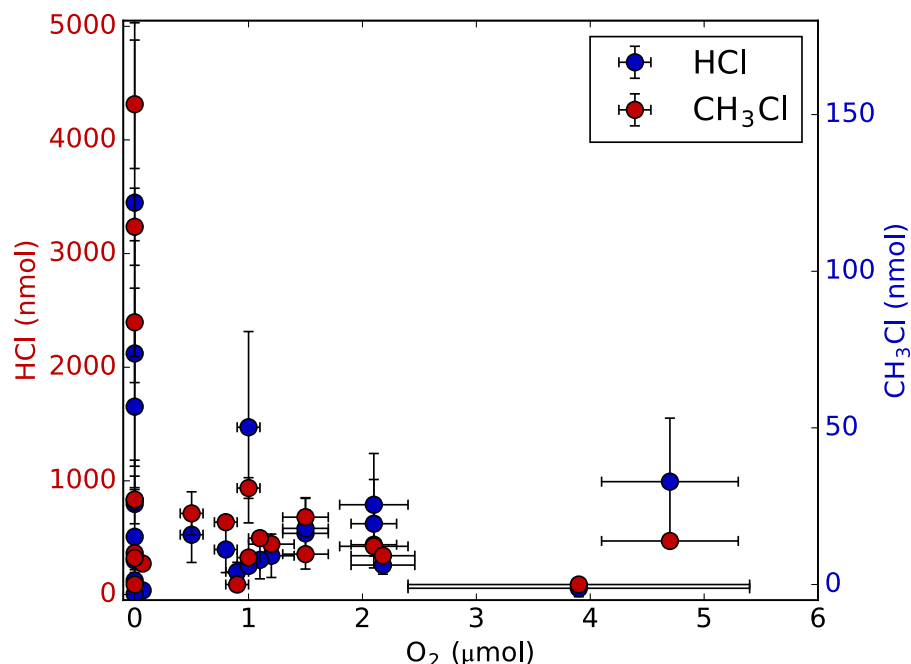


Figure 5-2. The molar amount of HCl and CH₃Cl measured in each sample plotted against the amount of O₂ observed. No correlation between these gases is observed.

In the samples Oudam, Marimba, Quela, Duluth, and Stoer, no evolved O₂ was detected (Table 5-1; Figure 5-2), an observation attributed to the absence of >0.06 wt% perchlorate (the estimated detection limit) in these rocks (Archer et al., 2019). These samples were not included in the temporal correlation assessments described above to avoid potential sampling bias against perchlorate. However, the release patterns of HCl and CH₃Cl in these runs are indistinguishable from the patterns observed in O₂-bearing samples (Figure 5-6), and in fact *more* HCl and CH₃Cl are present (Figure 5-2). These observations compellingly argue that the HCl and CH₃Cl peaks in EGA runs are agnostic as to whether perchlorate is present.

5.3.3 Is perchlorate present in modern Gale crater sediment deposits?

The above discussion centers on the improbability of finding perchlorate indigenous to the ancient sedimentary rocks found in Gale crater. By analogy to the Phoenix perchlorate detection in modern Martian soil (Hecht et al., 2009), perchlorate may have been deposited on and mixed into modern eolian materials in Gale crater. The assessments performed in section 5.3.2 were repeated using only scooped sediment/regolith samples (Figure 5-8 in the appendix); in these modern eolian samples there is no correlation between O₂ and HCl or CH₃Cl. As the drilled bedrock samples and

scooped samples are not distinguishable in these analyses, there are two straightforward possibilities: either perchlorate is present in both, evidenced only by the release of O₂, or perchlorate is not present in either sample set and another compound is responsible for the observed O₂ release.

There is also no apparent enrichment in O₂ release in these samples (Figure 5-8), suggesting that perchlorate is no more abundant in surface materials than near-surface materials. The perchlorate formation mechanism on Mars is debated and may involve irradiation of the surface (Carrier & Kounaves, 2015; Wilson et al., 2016; Zhao et al., 2018), atmospheric interactions (Catling et al., 2010; Smith et al., 2014), or electrochemical processes (Steele et al., 2018). Each of these mechanisms would likely result in enrichment of perchlorate at the surface. This lack of additional O₂ in these surface samples relative to drilled bedrock suggests perchlorate is not enriched in surface materials relative to the shallow subsurface of the rock (1.5-5 cm depth), which may indicate perchlorate equilibration between these locations (discussed further in section 5.5).

5.4 Alternative Explanations for O₂ Release

The only SAM observation attributed to perchlorate that cannot be explained exclusively by the presence of chloride salts is a large release of O₂ between 200-500°C. Several chemical species (including perchlorate) could be responsible for this oxygen release. Rather than suggest ad hoc explanations for the observed low to moderate temperature O₂ release in each sample, we propose that a single chemical species is likely the major source of this O₂ in every sample. Here we attempt to present a comprehensive list of potential O₂ sources and discuss the viability of each as candidate sources of the SAM-observed O₂.

5.4.1 Hydrogen Peroxide/Superoxides

Superoxides (including hydrogen peroxide) were invoked to explain the release of O₂ and the lack of detected organics by the Viking mission (Oyama & Berdahl, 1977). Modeling and observation suggest that hydrogen peroxide exists in the Martian atmosphere and likely at the surface (Atreya et al., 2006; Atreya & Gu, 1994; Encrenaz et al., 2004). However, these species are temperature-stable only up to ~200°C (Yen et al., 2000; Zent et al., 2008). O₂ releases in SAM extend well above this temperature, so peroxides and superoxides can be ruled out.

5.4.2 Sulfates

Sulfates release O₂ upon heating (Gallagher et al., 1970; Holt & Engelkemeir, 1970), and are present in high abundance in veins permeating Gale crater (e.g., Nachon et al., 2014; Rampe et al., 2017). However, the release of O₂ from sulfate is always coincident with that of SO₂, which is not observed in the O₂ releases between 200 and 500°C attributed to perchlorate (Sutter et al., 2017). Such a correlation is observed in the higher temperature 500-700°C O₂ releases, which are thought to result from the breakdown of Fe- and/or Mg-sulfate (Sutter et al., 2017). Sulfates can therefore be eliminated as the source of the 200-500°C O₂ in SAM.

5.4.3 Nitrate

The release of NO in EGAs has been attributed to the breakdown of nitrate in SAM (Stern et al., 2015). The NO/O₂ molar ratio is consistent among EGA samples, which has been interpreted as evidence for a constant nitrate/perchlorate ratio and a related formation mechanism (Stern et al., 2017). Not only does NO correlate with O₂ by molar amount, but the NO release is correlated in time with the O₂ releases in nearly all samples, regardless of the absolute temperature of O₂ release (Figures 5-1 & 5-6). This double correlation raises the possibility that nitrate breakdown is the major source of O₂ in the samples. While nitrate breakdown does produce both NO and O₂ gases, the NO/O₂ ratio in EGA is ~1:20 (Stern et al., 2017), far lower than the expected 1:1 ratio for nitrate breakdown. We therefore rule out nitrate as a major contributor to the O₂ signal observed by SAM, as did Sutter et al. (2017).

5.4.4 Metal Oxides

Metal oxides and oxyhydroxides are also a candidate source of the SAM O₂ peak. When heated, these phases undergo reduction and release molecular oxygen. For example, under heating, hematite (Fe⁺³₂O₃) is converted to magnetite (Fe⁺²Fe⁺³₂O₄), and pyrolusite (Mn⁺⁴O₂) is converted to bixbyite (Mn⁺³₂O₃). Further heating releases additional O₂, e.g., in the conversion of bixbyite to hausmannite (Mn⁺²Mn⁺³₂O₄). CheMin has detected hematite, akaganeite, goethite, and magnetite in Gale crater rocks, while ChemCam analyses suggest the presence of manganese oxides (Blake et al., 2013; Lanza et al., 2014; Rampe et al., 2017). The high abundance of X-ray amorphous material detected by CheMin is thought to partly consist of very fine-grained mineral phases including

nanophase Fe-oxide (Dehouck et al., 2014). The two key questions are whether these phases yield oxygen at appropriate temperatures, and whether there is adequate metal oxide in Gale crater rocks to account for the amount of oxygen observed by SAM.

Metal oxide equilibrium phase diagrams provide a starting point for characterizing the temperature of oxygen release from metal oxides. At thermodynamic equilibrium, the partial pressure of oxygen over a system containing both reduced and oxidized forms of a single metal is fixed and is a sensitive function of temperature and the given metal (e.g., Hasegawa, 2014). For example, the partial pressure of O₂ in equilibrium with coarsely crystalline MnO₂ and Mn₂O₃ at 200°C is 10⁻⁸ bar, increasing to 1 bar at 450°C (Birkner & Navrotsky, 2012). Therefore, as a metal oxide is heated, the O₂ partial pressure increases and the fraction of metal oxide in the more oxidized form decreases. Of interest due to the amorphous fraction observed by CheMin (Blake et al., 2013; Rampe et al., 2017), nanophase Mn- and Fe-oxides are less thermodynamically stable at a given temperature compared to their coarsely crystalline counterparts. For example, the equilibrium partial pressure of O₂ over nanophase MnO₂ at 200°C is ~10⁻⁵ bar, 1000 times higher than over coarsely crystalline MnO₂ (Birkner & Navrotsky, 2012).

While thermodynamic considerations suggest oxygen release at SAM-relevant temperatures, an EGA run is not conducted at thermodynamic equilibrium. A He carrier gas is swept across the sample (Mahaffy et al., 2012), likely preventing the local oxygen partial pressure from ever achieving equilibrium with metal oxides present. Without kinetic limitations, continuous purging of evolved oxygen predicts O₂ generation at every temperature throughout an EGA until the metal oxides are fully consumed. However, kinetic limitations almost certainly effect the rate of oxide decomposition. The temporal pattern of O₂ release from any metal oxides in an EGA must therefore be viewed as an intricate interplay of thermodynamics and kinetics. An O₂ peak (as opposed to continuous release) in an EGA could be generated as follows. At the start of the run, temperatures are so low that kinetic inhibition precludes substantial O₂ release. Because reaction rates typically scale exponentially with temperature, as the temperature rises in the run the O₂ release rate will increase rapidly. This creates the rising edge of the O₂ peak. With increasing temperature and associated oxygen release rate from the metal oxide in the EGA, the oxidized form of the metal oxide will approach exhaustion, the release rate will decline, and the O₂ peak height will fall. The temperature of maximum O₂ release in this scenario is controlled by kinetics and the amount of metal

oxide present rather than directly by thermodynamics. We therefore consider the onset of O₂ release (a kinetic property of the metal oxide), rather than the peak of O₂ release (kinetics convolved with the amount present), to indicate the characteristic behavior of a metal oxide during EGA.

Previous work under SAM-like conditions indicates that MnO₂ releases O₂ at too high a temperature to be a candidate for the low temperature O₂ release observed from Gale crater rocks (Hogancamp et al., 2018b). We are not aware of any SAM-like experiments on hematite reduction in the literature.

To further inform the temperature of release of O₂ from iron and manganese oxides, especially nanophase materials (which favor lower temperature O₂ releases; Navrotsky et al., 2010), we undertook new EGA experiments under broadly SAM-like conditions. Experimental methods and detailed analytical results are provided in the appendix. We analyzed Fe₂O₃ (600 nm, 5 nm, and 20 nm rod-like morphology grain sizes), MnO₂ (100 nm, 50 nm), and Mn₂O₃ (100 nm, 30 nm). In all but two cases we analyzed a single pure metal oxide, with two runs of mixed phases to assess the possibility of back reaction of evolved O₂. Specifically, our goals were to assess the role of grain size on O₂ release temperature and establish whether these metal oxide phases evolve O₂ at temperatures compatible with the SAM releases attributed to perchlorate.

In the case of iron oxides, Figure 5-3 shows that the initiation of oxygen release from hematite occurs at >710°C for both 600 nm and 5 nm grain size. In contrast, the rod-shaped 20 nm hematite particles, specifically marketed as being “highly reactive”, initiated oxygen release around 475°C. Although grain size/morphology clearly affect the temperature of O₂ release from hematite, these temperatures are still higher than the initiation of most of the SAM O₂ releases. These data preclude hematite as a candidate for the source of the SAM O₂. Similarly, because goethite and presumably akaganeite devolatilize to make hematite at low temperature (i.e., prior to metal reduction and O₂ release), and because magnetite is expected to release O₂ at even higher temperatures as it is more reduced than hematite, the common iron oxides all seem unlikely candidates.

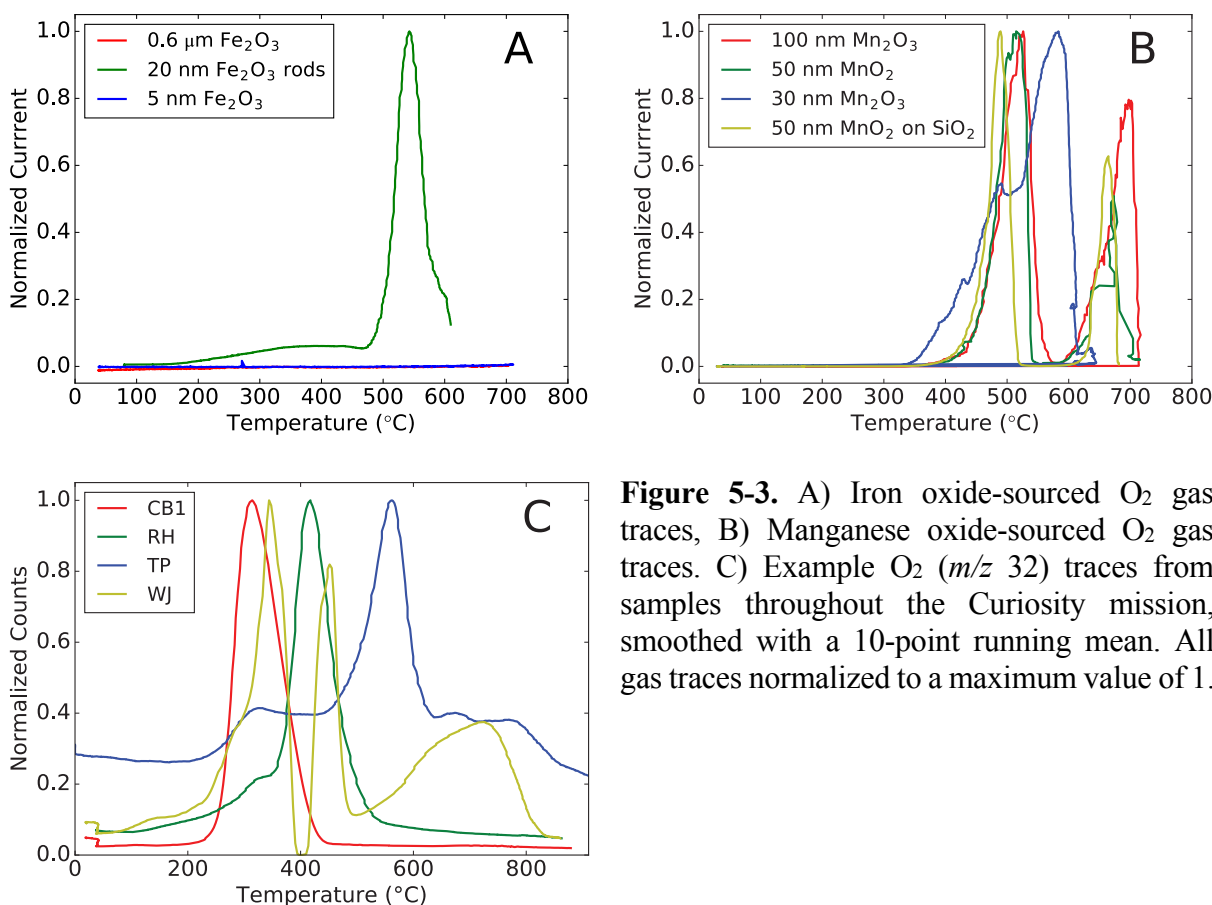


Figure 5-3. A) Iron oxide-sourced O₂ gas traces, B) Manganese oxide-sourced O₂ gas traces. C) Example O₂ (*m/z* 32) traces from samples throughout the Curiosity mission, smoothed with a 10-point running mean. All gas traces normalized to a maximum value of 1.

Our results on manganese oxides are shown in Figure 5-3b (see Table 5-3 in the appendix for detail). In the case of coarse (~ 100 μm) MnO₂, we found the initiation of O₂ release to occur at about 600°C, similar to the results obtained by Hogancamp et al. (2018b) on a MnO₂ sample of unspecified grain size. However, we detected the onset of O₂ release from nanophase manganese oxides at much lower temperatures. In particular, both 50 nm MnO₂ particles and 100 nm Mn₂O₃ particles began to release oxygen at 350°C, while 30 nm Mn₂O₃ particles did so at ~ 310 °C. That the less oxidized phase Mn₂O₃ began releasing oxygen at a temperature lower than the more oxidized MnO₂ is unexpected based on thermodynamics (Birkner & Navrotsky, 2012), suggesting that kinetics controlled by grain size is a major variable controlling the O₂ release temperature of Mn-oxides. The important role of grain size is reinforced by the slightly higher release temperature from 100 nm Mn₂O₃ compared to 30 nm Mn₂O₃.

Based solely on these analyses, nanophase Mn-oxides appear to be a feasible source of low temperature oxygen release, with variations in onset temperature of release potentially attributable to variations in grain size. However, there are two observations that argue against such a role for manganese oxides. First, the Mn-oxides heated in this experiment released a second O₂ peak, beginning at 600-650°C. The relative amounts of O₂ released suggest that the second release is associated with reduction of Mn₃O₄ to MnO. The absence of a similar high temperature O₂ release in the SAM data is evidence against Mn-oxides as the source of the O₂, unless that second release is back-reacted with the sample. For example, magnetite could plausibly be oxidized to hematite by the oxygen release associated with the conversion of Mn₃O₄ to MnO. To test this idea, two samples of MnO₂ were prepared: one intimately mixed with nanophase Fe₃O₄ as a weak reductant, and one intimately mixed with nanophase Fe⁰ as a strong reductant. No change in the O₂ release pattern was observed in the sample with admixed Fe₃O₄ compared to pure MnO₂. In contrast, the sample mixed with Fe⁰ released no oxygen at all, illustrating that solid-gas reactions which consume O₂ are possible under SAM-like conditions. Further experiments on oxides of different composition and grain size could be undertaken to further investigate these reactions, but in the absence of compelling information on the actual properties of the Martian samples, such experiments are unlikely to definitively confirm or rule out their role in the SAM observations.

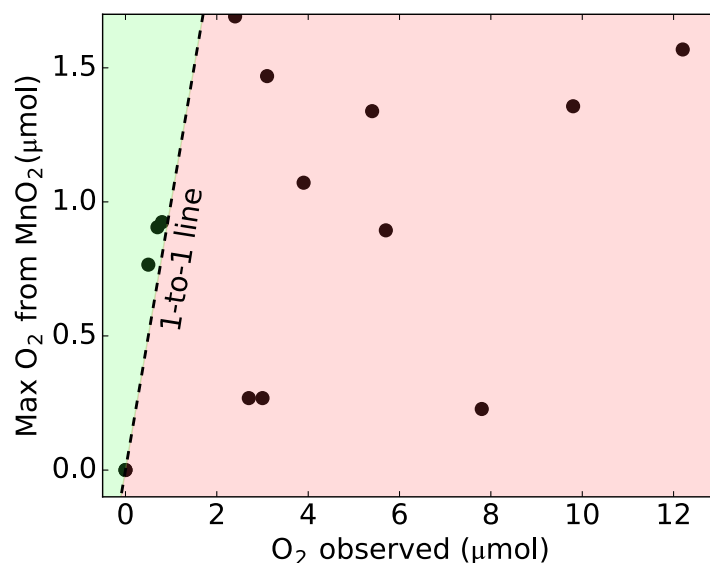


Figure 5-4. A comparison of the observed amount of O₂ released in each sample with the maximum amount possibly sourced from manganese, assuming all Mn is present as MnO₂ and is reduced to MnO upon heating. Green shading indicates O₂ can be accounted for assuming stoichiometric MnO₂; red shading indicates O₂ cannot be accounted for with manganese.

The second and stronger argument against nanophase Mn-oxides comes from mass balance. The presence of Mn-oxides in Gale crater rocks has been inferred by ChemCam via measurements of spatially discrete elevated Mn (Lanza et al., 2014, 2016), but it is not known whether all or any of the individual SAM samples include such elevated Mn. Here we develop the best-case assessment, in which all of the manganese in the APXS analyses of the SAM-analyzed samples is present in the form of manganese oxide. Manganese readily substitutes for iron in olivine, and since most of the olivine appears to have weathered away in Gale crater (Rampe et al., 2017), control of the manganese budget by Mn-oxides is a reasonable possibility. Which manganese oxidation state(s) are specifically present in Gale crater is not known, but a variety of poorly crystalline phases in an array of oxidation states tend to be intermingled in terrestrial occurrences of Mn-oxide (Post, 1999). Nevertheless, for present purposes we assume all manganese is present in its most oxidized form, MnO₂. As shown in Figure 5-4, APXS-derived manganese concentrations do not correlate with the amount of O₂ released during EGA. More importantly, in most samples, the amount of O₂ released during SAM analysis is higher than can be associated with the amount of detected manganese, even if it is all present as MnO₂ (Figure 5-4). Unless the APXS measurements are in error by far more than their estimated 13% uncertainty (Campbell et al., 2012), or the O₂ measurements are systematically much higher than actual, this observation precludes Mn-oxides as the source of O₂ release in the SAM samples.

5.4.5 Perchlorate

Perchlorate demonstrates O₂ release at the temperatures observed in SAM, with the varied release temperatures ascribed to differing cation compositions (e.g., Leshin et al., 2013; Ming et al., 2014; Sutter et al., 2017). Adequate chlorine is present for the O₂ release to be entirely explained by the presence of perchlorate salts, assuming that a substantial but variable proportion of the chlorine is contained in perchlorate. Perchlorate has also been clearly detected on Mars at the Phoenix landing site (Hecht et al., 2009) and can account for the wide range of $\delta^{37}\text{Cl}$ compositions observed by SAM (Farley et al., 2016). These lines of evidence and the lack of evidence *against* perchlorate suggest that the presence of perchlorate in SAM samples is the most likely scenario to explain the O₂ release.

5.5 Modern perchlorate

Though perchlorate offers the best explanation for oxygen release, indigenous ancient perchlorate is unlikely (section 5.3.1), indicating that any perchlorate observed in bedrock samples in Gale crater is probably young. An estimate of its maximum age can be obtained by extension of the radiolysis calculations presented for the Windjana sample in section 5.3.1.2. The perchlorate in this sample contains $14.4 \pm 4.3\%$ of the total chlorine. This proportion would be achieved after exposure to 38.0 ± 11.3 MGy of ionizing radiation assuming all chlorine was originally perchlorate. Based on Windjana's estimated radioelement content, this dose would be reached in 2.4 ± 0.7 Ga. This constraint provides a firm upper limit to how long the perchlorate may have been present in the rock. In short, the perchlorate can only be Amazonian in age.

The presence of such youthful material in these ancient rocks requires explanation. Deliquescent perchlorate salts could form thin films of briny liquid which percolate into the bedrock through cracks and fractures, depositing salts as they effloresce (Cull et al., 2010). As the Curiosity drill collects sample between 1.5 and 5 cm depth, the length scale of this percolation need only be on the order of a few centimeters. Such a process was inferred from the presence of a solubility-based gradient of sulfate salt coatings in the upper 15 cm of loose sediment exposed at the Troy site by the Spirit rover (Arvidson et al., 2010). Late-stage diagenetic vein-fill materials in Gale crater do not migrate outwards (Nachon et al., 2014), suggesting that these rocks are impermeable. However, small-scale fracturing of the Gale crater bedrock could permit percolation of salts if such cracks formed after the fracture-fills. Freeze-thaw cycles are known to generate cracks at fractal scales (Lu et al., 2016), implying that the decameter-scale cracks observed in Gale crater (Oehler et al., 2016) may be an indication that such small-scale fracturing exists. Impacts are another likely source of rock fracture.

In this model, the variability of perchlorate concentration across the stratigraphic section could be explained by differing permeability associated with fracture abundance and/or secondary mineral formation. This model is purely conceptual, and further work is needed to explain the detailed variability in concentration between samples (e.g., why the presumably more permeable Windjana sandstone has far less perchlorate than the Cumberland mudstone sample and why multiple samples have no detectable perchlorate; Archer et al., 2019) and the reportedly varying

cation chemistry of the perchlorate itself (Sutter et al., 2017). Potential mechanisms for modern perchlorate inclusion in ancient bedrock is an avenue of research that deserves further investigation.

5.6 Conclusions

The geologic history of Gale crater is not conducive to the deposition and preservation of indigenous perchlorate in the bedrock. The inferred abundance of perchlorate in several samples is too high for that perchlorate to have been present since deposition based on its rate of radiolytic destruction. Furthermore, the long-lived nature of the lacustrine succession and the lack of indicators of aridity such as bedded evaporites of less soluble salts, and associated sedimentary structures indicative of strongly evaporative processes, suggest that the deposition of highly soluble perchlorate salts as a native component of the Gale crater mudstones is unlikely.

The HCl and CH₃Cl in EGA initially thought to be related to perchlorate breakdown (Glavin et al., 2013; Ming et al., 2014) are shown here and elsewhere (Sutter et al., 2017) not to correlate with oxygen release. Therefore, there is no single direct line of evidence in SAM data that demands the presence of perchlorate in Gale crater. A large release of O₂ is the only observation attributed to perchlorate that cannot be explained via the presence of chloride salts. Regardless of the phase responsible, O₂ release upon heating is likely to destroy organic molecules by combustion (ten Kate, 2010; Lasne et al., 2016), making identification of the responsible chemical phase important in the search for biosignatures. We identify and assess five potential oxygen sources:

- 1) **Hydrogen peroxide/superoxides** are ruled out on the basis of the low temperatures (<200°C) at which they release oxygen.
- 2) **Sulfate salts** exhibit a generally high temperature (>500°C) oxygen release which consistently correlates with SO₂ (Sutter et al., 2017), eliminating this possibility.
- 3) **Nitrate** releases both NO and O₂ in EGA, but the NO/O₂ ratio is too low (~1:20 as opposed to ~1:1) for the main source of O₂ to be nitrate.
- 4) **Mn-oxides**, especially at nanophase grain size, release oxygen at a temperature range consistent with the SAM data. However, a double-peaked release pattern and manganese mass balance present

insurmountable challenges to this hypothesis. **Fe-oxides**, even at nanophase grain size, appear to release O₂ at too high a temperature.

5) **Perchlorate salts** have been shown to release oxygen at the temperatures observed by SAM (Sutter et al., 2017), and have been compellingly detected on Mars. Unusually ³⁷Cl-depleted and highly variable chlorine isotopes in Gale crater bedrock (Farley et al., 2016) support the presence of perchlorate on Mars by analogy to observed isotopes in the Atacama Desert on Earth.

Based on the radiolysis and geologic setting arguments, if perchlorate is indeed present, it is most likely geologically young (post mid-Amazonian). To date, the only Martian materials suggested to contain ancient perchlorate have been the drilled samples in Gale crater (Archer et al., 2016). If this proposed antiquity is conclusively eliminated, the only perchlorate observed on Mars would be geologically young. Without direct evidence for ancient perchlorate, Martian perchlorate may be exclusively an Amazonian phenomenon. We therefore suggest that interpretations of data invoking perchlorate in an ancient (pre-Amazonian) setting be evaluated for alternative explanations. We find geologically young perchlorate to be the most plausible explanation for the observation of O₂ release during EGA. A likely post-depositional source of perchlorate is percolation of thin films of briny liquid into rock pore space when sufficient humidity is present for deliquescence to occur. The exact mechanism of perchlorate inclusion deserves further detailed study.

5.7 Appendix

5.7.1 Radiolysis constant calculations

The radiolysis constants used in this work are taken from Prince and Johnson (1965), who report these values in units of molecules per 100 eV. This constant may be converted to Gy⁻¹ (equivalent to kgJ⁻¹) by Equation 5-1 below. These units are akin to the familiar yr⁻¹ decay constant units for radioactivity.

$$\frac{\text{molecules}}{100 \text{ eV}} \times \frac{6.242 \times 10^{18} \text{ eV}}{1 \text{ Joule}} \times \frac{\text{kg salt}}{\text{mol salt}} \times \frac{1 \text{ mol salt}}{6.022 \times 10^{23} \text{ molecules}} \quad (5-1)$$

5.7.2 Uncertainty calculations

Uncertainties are dominated by the uncertainty resulting from APXS measurement of K_2O (considered to be $\pm 12\%$ relative; Campbell et al., 2012) and from cosmic ray exposure ages (see Farley et al. (2014) for a detailed description). Based on work of (Taylor et al., 2007) we use a K/Th value of 5330 ± 220 . The uncertainty in the U/Th ratio is poorly constrained, so we take a conservative estimate of 20% relative uncertainty for these calculations. Uncertainties are not given in Prince & Johnson (1965), but the degradation curves presented are well-constrained, and it is unlikely the formal uncertainty associated with these experiments would have a significant impact on the final calculated uncertainty. We place an estimate on the uncertainty associated with the radiolysis constant derivation of 5% relative based on the goodness of fit to the data presented in (Prince & Johnson, 1965a). The uncertainty stemming from the GCR dose rate given in Pavlov et al. (2012) is not constrained; we place an uncertainty estimate of 20% relative on the GCR dose rate, as this number over long time spans is poorly constrained. As the majority of ionizing radiation reported here is sourced from radioactivity, the overall impact of GCR dose rate uncertainty is small.

5.7.3 Metal oxide reduction experiment

The motivation for metal oxide heating experiments is described in detail above. Briefly, metal oxides will thermodynamically favor O_2 release upon heating (Hasegawa, 2014); kinetics and grain size have the potential to significantly shift the release temperatures of these materials from their thermodynamically predicted temperatures (e.g., Birkner & Navrotsky, 2012; Navrotsky et al., 2010). To account for these potential changes, here we describe a set of measurements meant to probe the lowest temperatures of oxygen release plausibly occurring in SAM EGA. Section 5.7.3.3 expands on the main text; discussion relevant only to the minutiae of this experiment are contained here, while discussion relevant to the viability of metal oxides as an oxygen source in SAM are placed in the main body of the text.

5.7.3.1 Methods

Nanophase iron and manganese oxides were purchased from the commercial manufacturer US Research Nanomaterials, Inc and included various oxidation states, grain sizes, and in one case, grain shape (Table 5-2). Each sample was wrapped in a platinum foil pouch, suspended from a

thermocouple wire in a projector lamp cell (Farley et al., 1999), and evacuated to ultra-high vacuum at 80-100°C for about 12 hours to desorb loosely bound water. To provide SAM-like conditions, the sample was then heated at a programmed ramp rate identical to SAM experiments to ~720°C while high purity He swept any evolved gases through a Balzers Prisma quadrupole mass spectrometer and into a turbomolecular pump. The system was kept at 4.6×10^{-8} mbar He pressure at the beginning of each experiment. Because the system was always open to the turbomolecular pump, the He pressure may be considered a proxy for He flow rate.

Table 5-2. Metal oxide nanopowders purchased for oxygen release experiments. As indicated in the text, all chemicals were purchased from US Research Nanomaterials, Inc unless otherwise noted.

Identity	Grain size	Reported Purity
Fe ⁰ (American Elements)	60-80 nm	99%
Fe ₂ O ₃	5 nm	99.9%
Fe ₂ O ₃	20 x 120 nm rods	98%
Fe ₂ O ₃ (Caltech collection)	0.6 µm	Unknown
Fe ₃ O ₄	3 nm	99.9%
MnO ₂	50 nm	98%
MnO ₂ (Caltech collection)	~100 µm	Unknown
Mn ₂ O ₃	30 nm	99.2%
Mn ₂ O ₃	100 nm	98%
FeO(OH)	10 x 50 nm	98%

Many different experimental runs were performed under varied conditions or with different materials. The six key experiments consist of the analysis of samples of the smallest grainsize of the different oxides. To determine whether total mass of the sample impacted the results, the 50 nm MnO₂ and 30 nm Mn₂O₃ were each run with varied masses. Whether temperature ramp rate affected the experiment was determined by running a varied T schedule with holds at 250°C, and 370°C with reheats to 450°C, 575°C and 720°C. The effect of He flow rate was assessed by running the 30 nm Mn₂O₃ under an initial He pressure of 4.6×10^{-7} mbar. The 50 nm MnO₂ and 30 nm Mn₂O₃ were also mixed onto a substrate of amorphous SiO₂ to investigate whether spatial distribution of the particles (i.e., possible clumping of the pure phase) was an important factor in temperature of release. The impact of grainsize was tested by running larger grained synthetic MnO₂ and Fe₂O₃ from the Caltech collection. The MnO₂ was mixed with Fe₃O₄ and Fe⁰ to assess whether these more reduced substances would consume oxygen and reduce the amount of O₂ observed compared to the pure MnO₂ experiment. The FeO(OH) was heated in two additional experiments using a liquid nitrogen trap and a dry ice/alcohol slurry to assess the contribution of water to observed O₂. A blank was also

run, which resulted in no observable O₂, suggesting that the background levels of O₂ in these experiments is negligible. Each run is shown in Table 5-3 for reference.

5.7.3.2 Results

Table 5-3. Oxygen release experimental results. The letter in parentheses in the note column denotes the corresponding letter to Figure 5-5.

Sample	Mass (μg)	Initial O ₂ release (°C)	Peak O ₂ release (°C)	Notes
Blank	0	N/A	N/A	O ₂ background (A)
Fe ₂ O ₃ 5 nm	168	N/A	N/A	Smallest hematite grains (B)
Fe ₂ O ₃ 600 nm	418	N/A	N/A	Large-grained hematite (C)
Fe ₂ O ₃ 20x120 nm rods	1308	470	540	Grain shape (D)
MnO ₂ 100μm	258	575	650	Large-grained MnO ₂ (E)
MnO ₂ 50 nm	80	350	510	Portion size ^a (F)
MnO ₂ 50 nm	1255	310	510	Portion size ^a (G)
MnO ₂ 50 nm on Fe ⁰	5507	N/A	N/A	Strong reductant (H)
MnO ₂ 50 nm on Fe ₃ O ₄	388	350	510	Weak reductant ^a (I)
MnO ₂ 50 nm on SiO ₂	768	320	490	Substrate ^a (J)
Mn ₂ O ₃ 100 nm	727	310	520	Mid-size Mn ₂ O ₃ ^a (K)
Mn ₂ O ₃ 30 nm	188	310	540	Portion size/“standard” run (L)
Mn ₂ O ₃ 30 nm	1029	310	580	Portion size ^a (M)
Mn ₂ O ₃ 30 nm high P	89	325	510	Pressure ^a (N)
Mn ₂ O ₃ 30 nm on SiO ₂	294	360	600	Substrate ^a (O)
MnO ₂ 30 nm (T-hold)	1294	310	520	T-ramp rate ^b (P)
FeO(OH) 10 x 50 nm	484	450 ^c	500	“standard” run (Q)
FeO(OH) 10 x 50 nm	4414	N/A ^c	N/A	O ₂ from H ₂ O? LN2 trap (R)
FeO(OH) 10 x 50 nm	4703	N/A ^c	N/A	O ₂ from H ₂ O? dry ice trap (S)

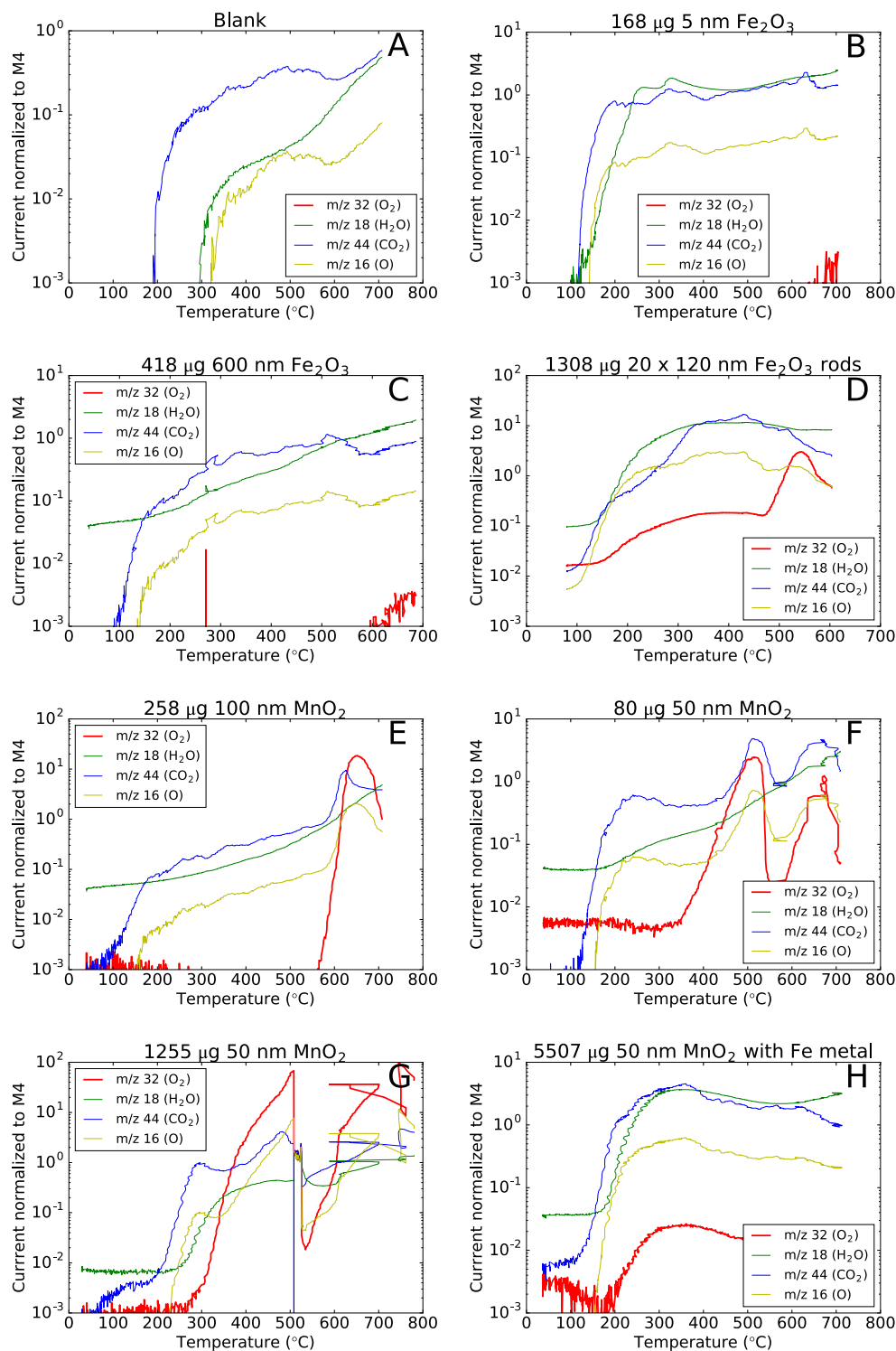
^aTwo O₂ peaks

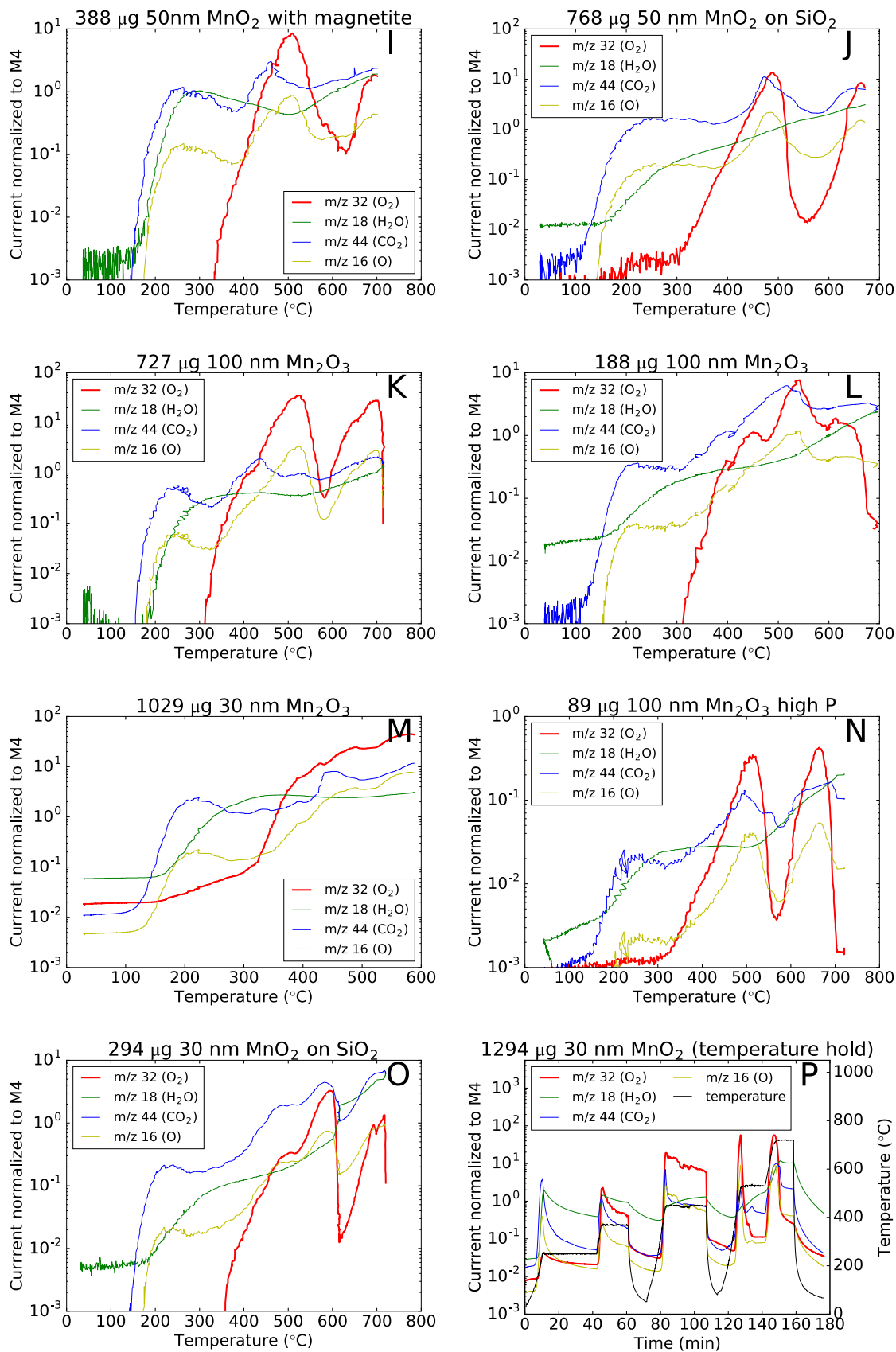
^bMultiple peaks

^cSee section 5.7.3.3 for discussion

Figure 5-5 shows the results from each heating experiment. No oxygen release was observed from the smallest and the largest grain sizes of hematite (5 and 600 nm) to a temperature as high as 710°C. An O₂ release beginning at ~475°C was observed from the rod-shaped hematite. Initial release of O₂ began at approximately 310°C in 30 nm Mn₂O₃ and 350°C in 50 nm MnO₂, while larger-grained 100 nm Mn₂O₃ began releasing O₂ at 350°C. In manganese oxide experiments, a second large release of oxygen began at 600-650°C. The temperature of this second release correlates with the temperature of the first oxygen release. The temperatures of release are highly replicable, varying by ≤10°C between runs of the same material (substance, grain size). These small variations

are most likely a result of uneven heating or other details unrelated to the chemistry of the metal oxides.





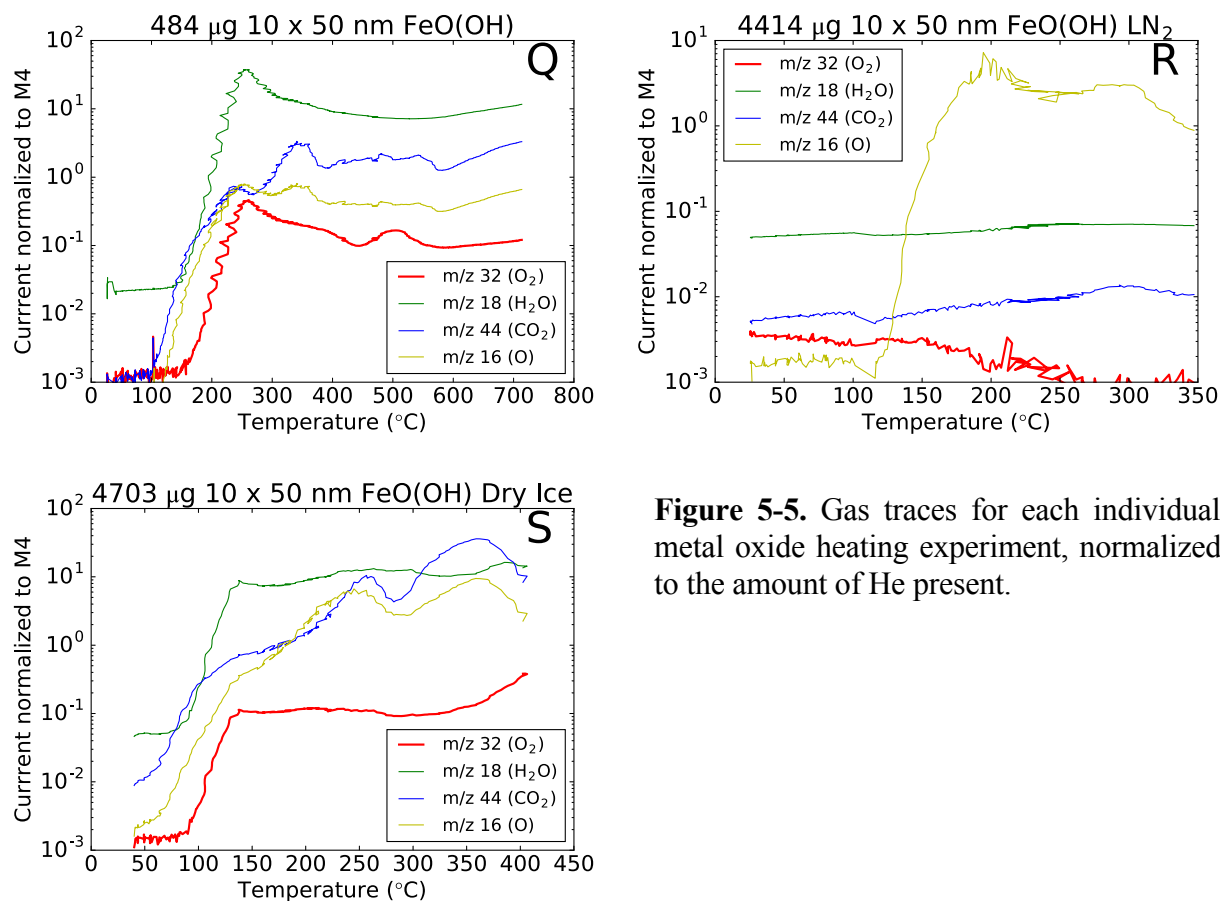


Figure 5-5. Gas traces for each individual metal oxide heating experiment, normalized to the amount of He present.

The numerous variations in methodology (He flow rate, temperature ramp schedule, mass of oxide, etc.) did not significantly impact the temperature of release. These experiments suggest that while grain size plays an important role in the temperature of oxygen release, neither the amount of material, the presence of a substrate, the He flow rate varying by over one order of magnitude, nor the presence of a weak reductant (Fe_2O_3) substantially affects this temperature or the absolute amount of oxygen released. The presence of a strong reductant (Fe^0) prevents measurement of O_2 , presumably via consumption of this gas as it is released from the Mn oxide. The FeO(OH) released a small amount of O_2 at a consistent ratio to H_2O during dehydration, and a small additional O_2 release was observed beginning around 450 °C. When this material was run with a liquid nitrogen trap, the consistent O_2/H_2O ratio during dehydration was unchanged. To eliminate the possibility of O_2 being drawn down on the vacuum line by liquid nitrogen, the experiment was repeated using a dry ice/alcohol slurry, which yielded the same consistent O_2/H_2O ratio.

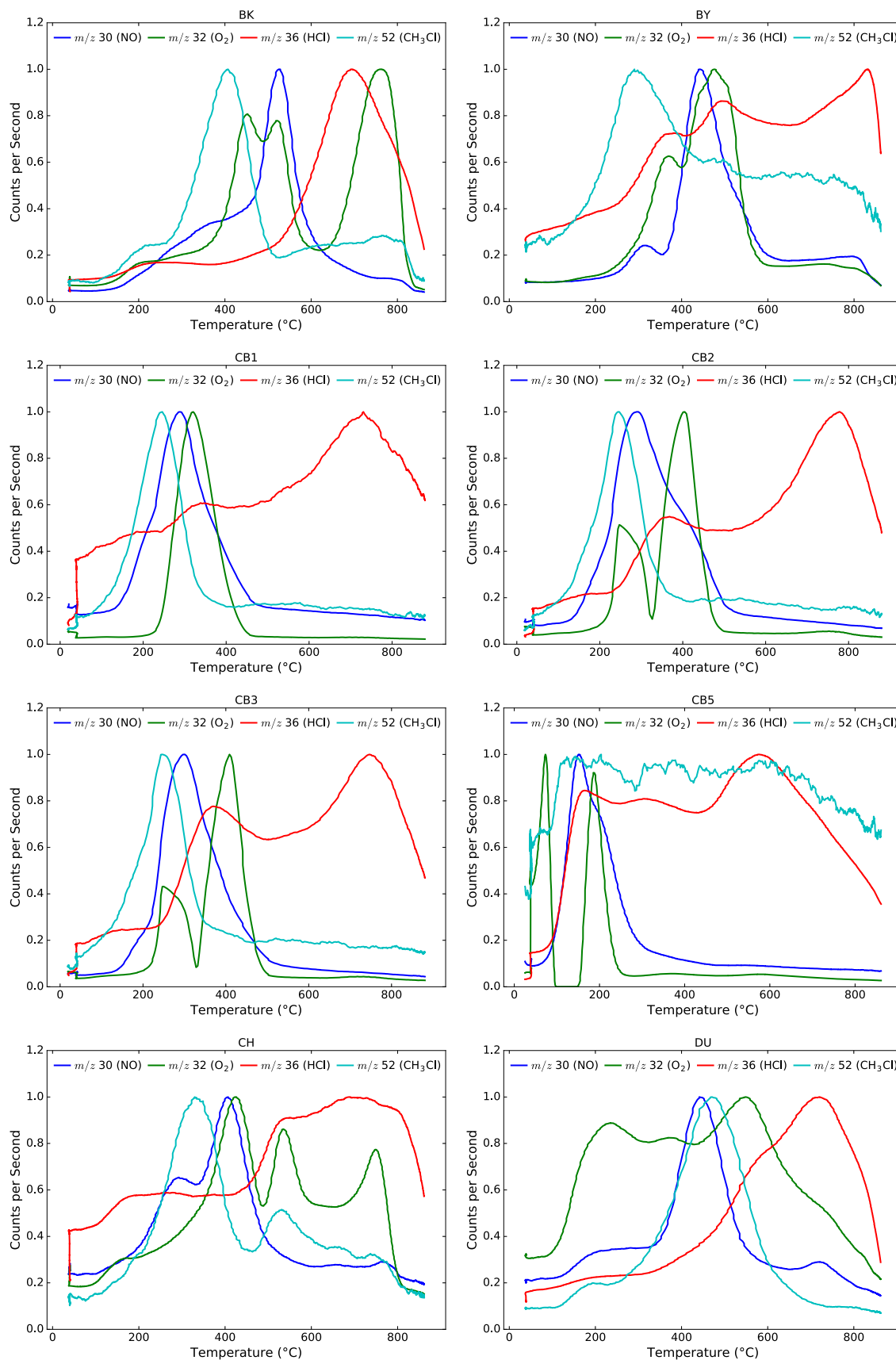
5.7.3.3 Discussion

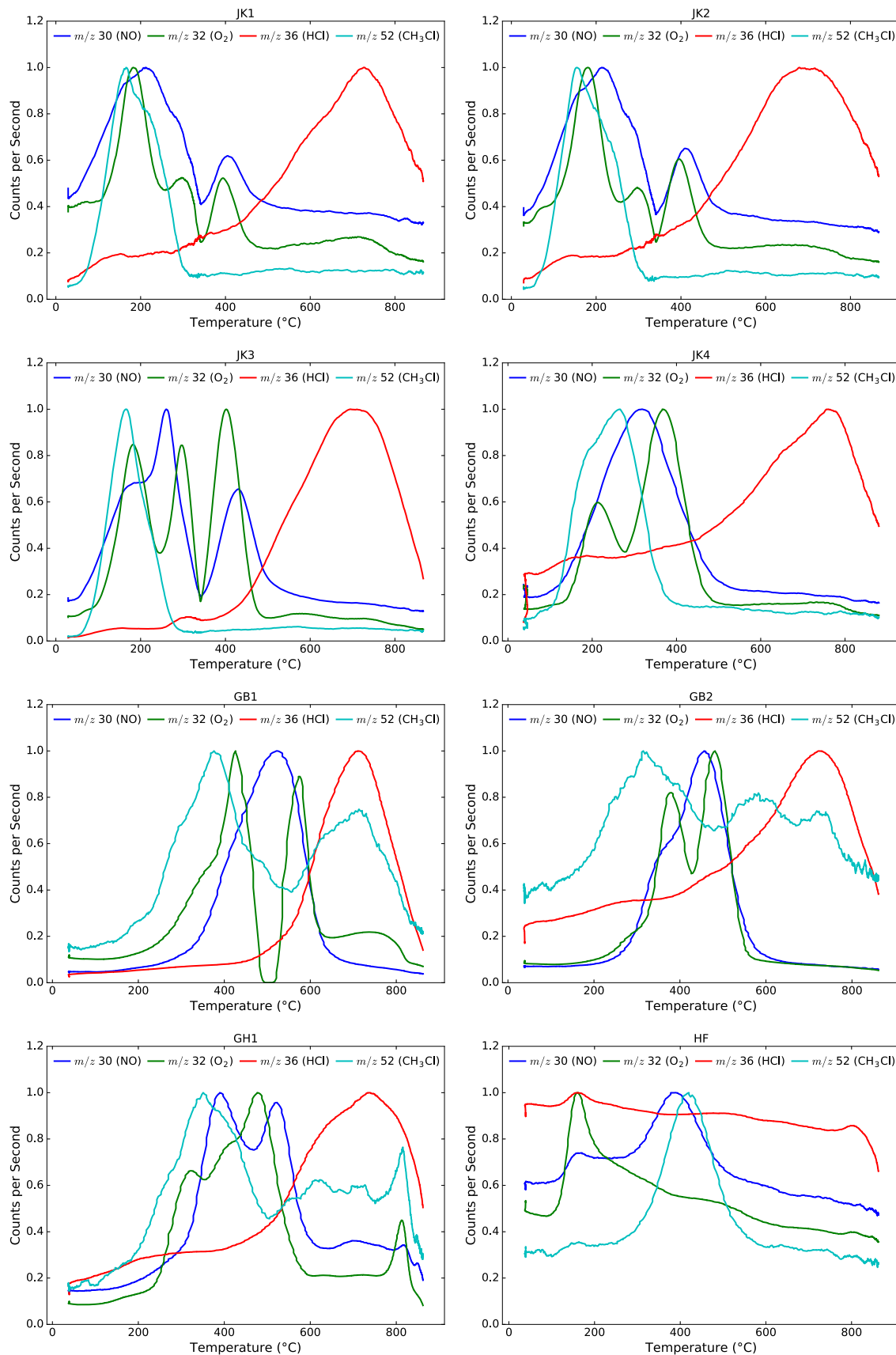
Despite the observation of oxygen released from rod-shaped hematite, the lack of observable O_2 from the other two hematite samples is an indication that iron oxides (hematite, magnetite) are probably not a source of O_2 in SAM EGAs. Grain size and/or morphology appear to play a role in oxygen release temperature. However, we did not demonstrate O_2 release in the temperature range observed by SAM. It is possible that the iron oxides in Gale crater are in some way different than those analyzed here, but there is no indication that they would be more reactive than the samples in this study. These conclusions likely extend to goethite and akaganeite, as both devolatilize and convert to hematite at low temperature.

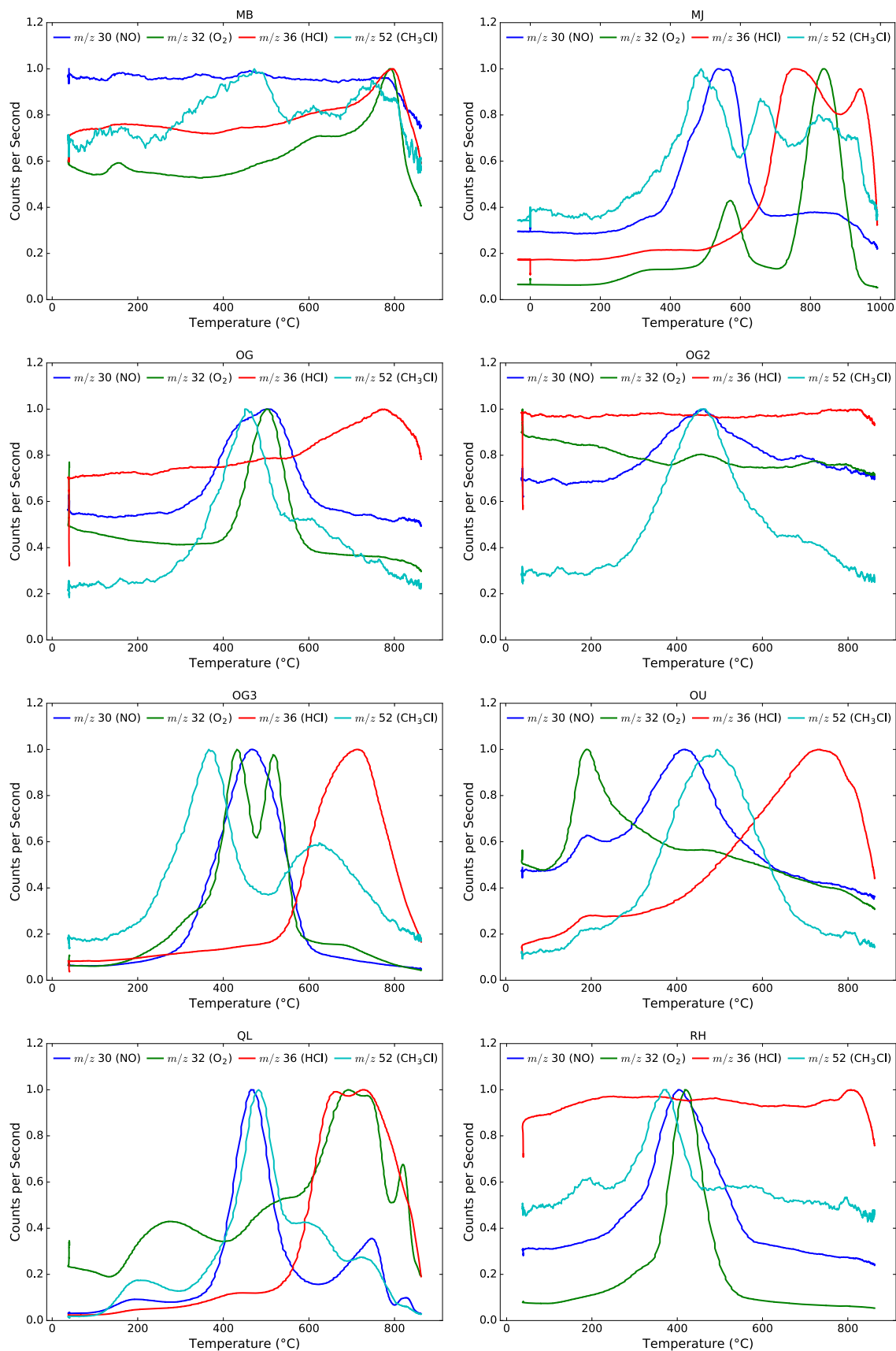
The similarity in the initial release temperatures of the MnO_2 and Mn_2O_3 can be explained in one of two ways: 1) the transitions $MnO_2 \rightarrow Mn_2O_3 \rightarrow Mn_3O_4$ happen in a single step or in such rapid succession that these steps are not resolvable in our system. 2) Chemical impurities of MnO_2 in the purchased Mn_2O_3 result in a release of oxygen from these impurities and the second release is in fact the transition $Mn_2O_3 \rightarrow Mn_3O_4$, implying that the breakdown to MnO is never achieved at these temperatures. Short of an extraordinary coincidence regarding the amount of MnO_2 impurity in the purchased Mn_2O_3 , the stoichiometry of the two peaks in MnO_2 (~2:1) compared to Mn_2O_3 (~1:2) suggests that the first release is $MnO_2 \rightarrow Mn_2O_3 \rightarrow Mn_3O_4$ or $Mn_2O_3 \rightarrow Mn_3O_4$, respectively, while the second peak is the transition $Mn_3O_4 \rightarrow MnO$ in both. We therefore prefer the first interpretation above: the reduction of both MnO_2 and Mn_2O_3 to Mn_3O_4 occurs within a brief temperature window and likely cannot be resolved by our system or by SAM. Work by Birkner and Navrotsky (2012) shows that the thermodynamically preferred O_2 release temperature of nanophase MnO_2 is lower than the release temperature we observe. It is therefore likely that a kinetic inhibition is preventing this release; if Mn_2O_3 lacks this inhibition, the production of Mn_3O_4 from MnO_2 likely proceeds instantaneously.

The release of O_2 from $FeO(OH)$ at a constant ratio with H_2O is consistent with the observation of minor goethite nanoparticle reduction during dehydration at $<300^\circ C$ (Till et al., 2015). The experiments of Till et al. (2015) were carried out under a CO/CO_2 atmosphere at atmospheric pressure; magnetite formation was not observed in air. To examine the possibility that this minor reduction occurs under He in vacuo, a liquid nitrogen trap was attached to draw down water during

heating. The heating experiment was repeated but separation of H_2O and O_2 was not observed: their ratio remained essentially constant throughout the run. The liquid nitrogen trap was replaced with a dry ice/alcohol slurry to avoid the possibility of O_2 being condensed in concert with water. However, the same consistent $\text{H}_2\text{O}/\text{O}_2$ ratio was observed in this case. We therefore conclude that we are not observing the reduction of goethite at low temperature and instead O_2 is formed from fragmenting H_2O at the electron impact ion source. While this is a plausible source of O_2 in SAM, the mass spectra used to trace H_2O evolution during EGA do not match the shape of O_2 peaks, suggesting that this is at most a minor contribution to O_2 in SAM EGA.







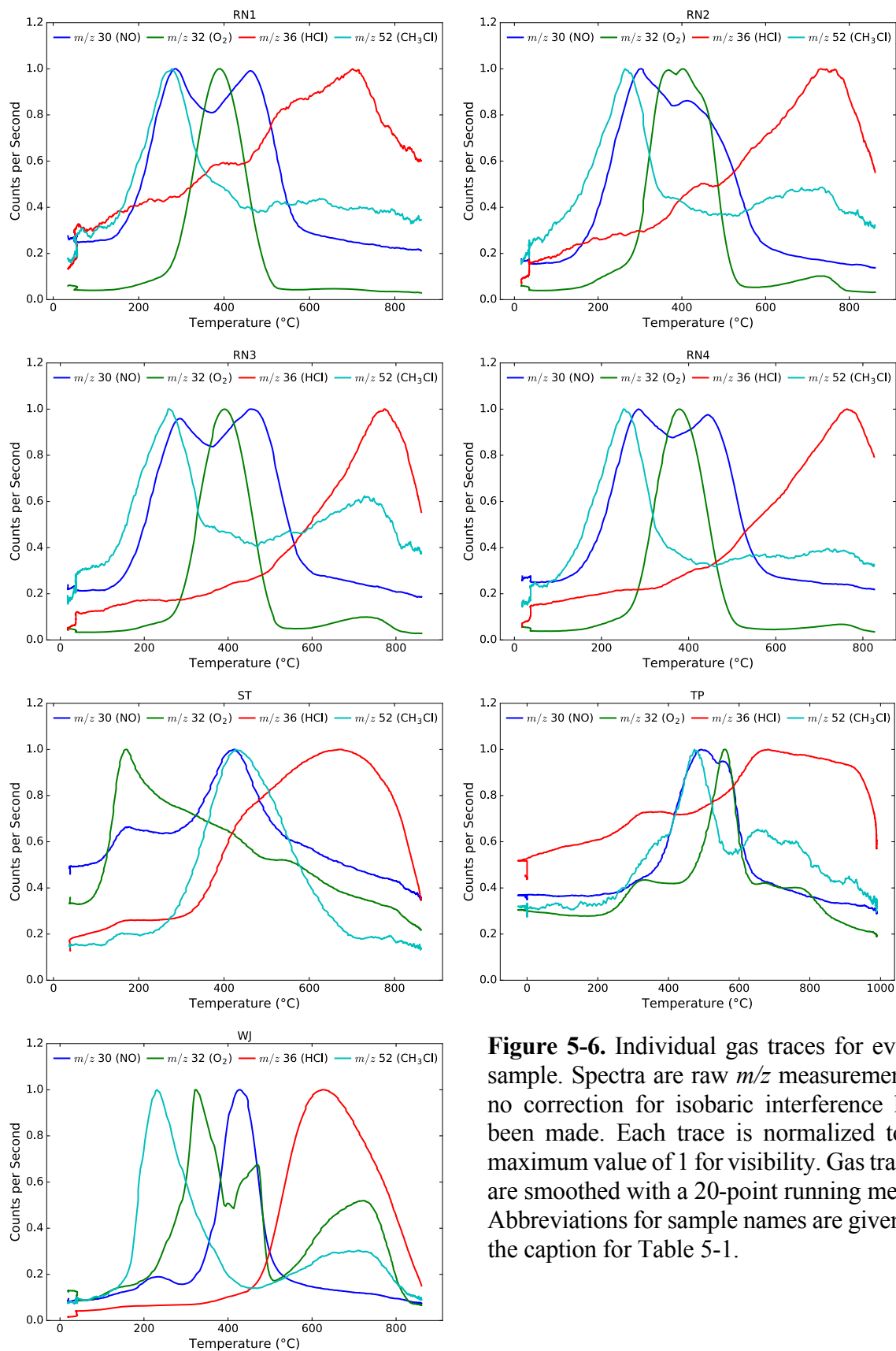


Figure 5-6. Individual gas traces for every sample. Spectra are raw m/z measurements; no correction for isobaric interference has been made. Each trace is normalized to a maximum value of 1 for visibility. Gas traces are smoothed with a 20-point running mean. Abbreviations for sample names are given in the caption for Table 5-1.

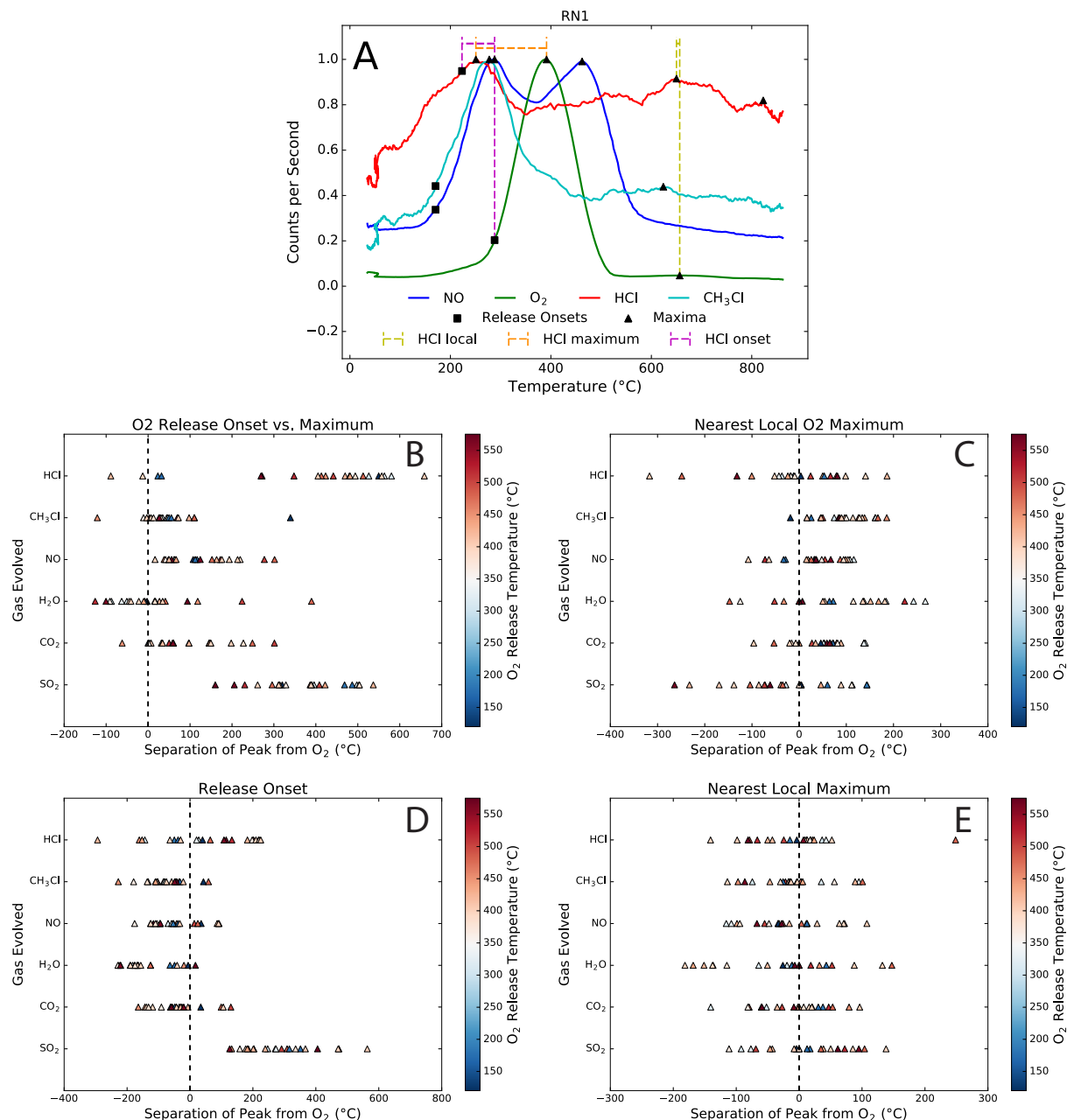


Figure 5-7. A) Parameters used to quantify gas release are shown as an example with the relevant chemical species observed at Rocknest, with a 20-data point running mean applied to smooth the data and all gas traces normalized to a maximum of 1. The separation between local peaks is shown in yellow dashed lines, where local peaks in HCl and O₂ are matched. The difference in global maximum between HCl and O₂ is shown in orange. The separation in onset of the main release of O₂ and HCl is in purple. B) The relative temperature difference between the onset of O₂ release and the global maximum for each gas. C) the nearest O₂ local maximum to the global maximum of each gas, D) the relative temperature difference between the onset of O₂ release and the onset of release of each gas, E) the relative temperature difference between the nearest O₂ local maximum and the local maximum for each gas.

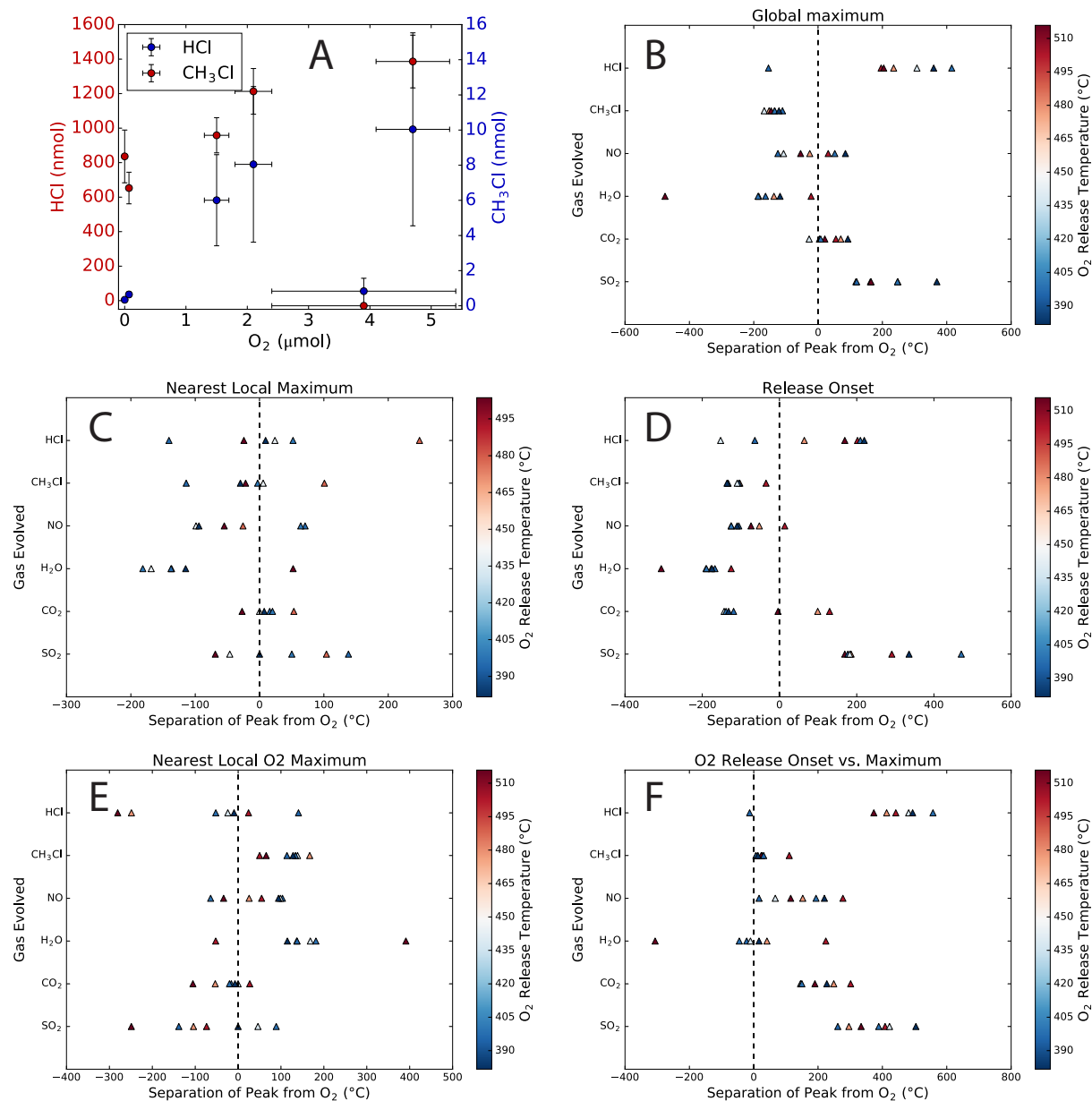


Figure 5-8. A) A comparison of molar gas release for each sediment sample. B-F) The same analyses performed in Figures 5-1 and 5-6b-e.

A NEW METHOD OF ISOTOPIC ANALYSIS OF PERCHLORATE USING ELECTROSPRAY-ORBITRAP MASS SPECTROMETRY

6.1 Abstract

Isotopic fingerprinting has been demonstrated as an effective means of tracing a source of perchlorate (ClO_4^-) contamination. These isotopic signatures may also be useful in tracking perchlorate remediation efforts, and in understanding the source of natural perchlorate on both Earth and Mars. Existing methods of perchlorate isotope analysis require significant sample preparation, multiple aliquots, and are unable to determine clumped isotope values. Here we report a new method of perchlorate isotope analysis using electrospray-Orbitrap mass spectrometry. This method involves the measurement of unfragmented perchlorate at a nominal mass resolution of 120,000, which permits simultaneous determination of $\delta^{37}\text{Cl}_{\text{SMOC}}$, $\delta^{18}\text{O}_{\text{VSMOW}}$, and $\Delta^{103}\text{ClO}_4$ (the clumped isotopologue $^{37}\text{Cl}^{18}\text{O}^{16}\text{O}_3$). In 35 minute analyses with minimal sample preparation, this technique yields $\delta^{37}\text{Cl}_{\text{SMOC}}$ precisions comparable to previous methods ($\pm 0.28\text{‰}$), while $\delta^{18}\text{O}_{\text{VSMOW}}$ precisions of $\pm 3.4\text{‰}$ and $\pm 15\text{‰}$ for $\Delta^{103}\text{ClO}_4$ are achieved. Improvement of these precisions by an order of magnitude and determination of $\delta^{17}\text{O}_{\text{VSMOW}}$ and $\Delta^{102}\text{ClO}_4$ are likely possible with continued development. We apply this method to the experimental reduction of perchlorate using Fe^0 nanoparticles. The associated fractionation factors are broadly temperature dependent, indicating that these fractionations are likely chemical kinetic in nature. Based on the isotopic range of common contaminant perchlorate and the magnitude of fractionation by perchlorate reduction, the precisions achieved here are well-suited to both perchlorate forensic analysis and tracing the extent of perchlorate remediation. Perchlorate reduction results in ^{37}Cl enrichment for residual perchlorate. The strongly depleted ^{37}Cl signature of perchlorate in the Atacama Desert, and in Gale crater on Mars, is therefore likely related to the formation mechanism of such perchlorate.

6.2 Introduction

Perchlorate is a well-documented groundwater, drinking water, and food contaminant (e.g., Gullick et al., 2001; Jackson et al., 2005; Kirk et al., 2003; Urbansky, 2002) with numerous sources including industrial and military use in rocketry, airbags and explosives (ATSDR, 2008), import of Chilean saltpeter fertilizers (Ericksen, 1981; Urbansky et al., 2001), and a natural background source that appears to be pervasive across the Earth (e.g., Kounaves et al., 2010; Parker et al., 2008; Rajagopalan et al., 2006). As concerns pertaining to perchlorate contamination have grown, so too have attempts to conclusively identify the source of the perchlorate, especially via isotopic fingerprinting by tracing the perchlorate's $\delta^{37}\text{Cl}$, $\delta^{18}\text{O}$, $\delta^{17}\text{O}$, and $\Delta^{17}\text{O}$ signatures (e.g., Bao & Gu, 2004; Böhlke et al., 2005, 2009; Jackson et al., 2010; Sturchio et al., 2011, 2014). The oxygen in perchlorate is not readily exchangeable (Hoering et al., 1958), making these studies effective in addressing the original source of a given perchlorate contamination even after long periods of time.

Remediation strategies for the problem of perchlorate contamination have made significant advances since the start of the 21st century. Removal via sequestration through nonselective resins, activated carbon, or other sorption media has proven to be largely inefficient and expensive (Coates & Jackson, 2008); selective ion exchange resins are effective and have become a major focus of perchlorate remediation (Gu et al., 2007). Remediation by destruction of the perchlorate ion via reduction to chloride is also possible. Electrochemical reduction of perchlorate is prohibitively inefficient (Brown, 1986). However, bioremediation, the use of microbial perchlorate metabolisms to degrade the perchlorate ion *in-situ*, is effective and has received a significant amount of attention (e.g., Coates & Achenbach, 2004). Methods of abiotic chemical reduction of perchlorate have been demonstrated (Cao et al., 2005), though the practical use of these methods is relatively unexplored compared to bioremediation efforts.

Isotopic studies may be used not only to trace the source of contaminant perchlorate, but in the case of perchlorate remediation by reduction, the extent of reduction (and by proxy, the effectiveness of the remediation method) may also be assessed by isotopic fingerprinting. While the isotopic effects of bioremediation have been studied (Ader et al., 2008; Hatzinger et al., 2009; Sturchio et al., 2007), the isotopic fractionations associated with abiotic means of perchlorate reduction have not been assessed.

In addition to the practical application of isotopic analysis to perchlorate contamination forensics and remediation, there is a growing body of literature focused on an academic understanding of the isotopic system of perchlorate, and especially the chlorine in perchlorate. The vast bulk of chlorine reservoirs on Earth appear to have little isotope variation, with most chlorine isotope signatures in groundwaters, seawater, evaporite deposits, and igneous and metamorphic rocks having chlorine isotope values that range within approximately $\pm 3\text{‰}$ $\delta^{37}\text{Cl}_{\text{SMOC}}$ (e.g., Bonifacie et al., 2008; Eastoe et al., 2007; Eggenkamp, 2014; Liu et al., 2013; Sharp et al., 2007). Chlorine redox reactions appear to be one of the few ways to cause large chlorine isotope fractionation. Atacama perchlorate has a negative $\delta^{37}\text{Cl}_{\text{SMOC}}$ value of approximately -10 to -15‰ (Böhlke et al., 2005; Jackson et al., 2010), while the theoretical fractionation factor for equilibrium perchlorate reduction results in chloride as isotopically light as -70‰ $\delta^{37}\text{Cl}_{\text{SMOC}}$ (Schauble et al., 2003), and microbial reduction of perchlorate produces chloride with an isotope signature as low as -15‰ $\delta^{37}\text{Cl}_{\text{SMOC}}$ (Ader et al., 2008). Chlorine isotope signatures measured by the Curiosity rover at the surface of Mars appear to be associated with the production and/or cycling of perchlorate, and have extremely negative signatures ranging between -51 ± 5 to $-1 \pm 25\text{‰}$ (Farley et al., 2016). A complete understanding of the perchlorate isotope system is dependent on understanding the isotopic effects of perchlorate formation and reduction.

Here we report a new method of measuring the isotopic fingerprint of unfragmented perchlorate ion (ClO_4^-) at high precision using electrospray orbitrap mass spectrometry (Eiler et al., 2017). This method allows the isotopes of perchlorate to be measured with minimal sample preparation and at high resolution, allowing assessment of the isotope signatures $\delta^{37}\text{Cl}$ and $\delta^{18}\text{O}$, and adding the ability to measure clumped $^{37}\text{Cl}^{18}\text{O}^{16}\text{O}_3$. With further work, the technique would also likely be amenable to $\delta^{17}\text{O}$, $\Delta^{17}\text{O}$, and clumped $^{37}\text{Cl}^{17}\text{O}^{16}\text{O}_3$ measurements. We apply this technique to the reduction of perchlorate by Fe^0 nanoparticles (Cao et al., 2005), and derive fractionation factors for this reaction, which has not previously been assessed with respect to its isotopic effects. Though we apply this method in a framework of tracing perchlorate remediation, it may also be applied to the analysis of unknown perchlorate contaminants for forensic analysis, and provides data relevant to the question of the mechanistic reasons for the observed isotopic signatures of perchlorate.

6.3 Methods

6.3.1 Perchlorate Reduction

Potassium perchlorate solutions of approximately 10 mM were prepared. Eight grams of iron nanoparticles provided by American Elements® were added to 100 mL of perchlorate solution in a roundbottom flask, and then placed in a hot water bath while being stirred at 600 rpm using a magnetic stir bar. A condenser was placed on the roundbottom flask and N₂ was bled over the reaction to ensure the iron was not oxidized by atmospheric oxygen. A thermocouple attached to a data logger was fed through the condenser to track the temperature of the reaction solution. A second thermocouple was placed in the water bath to monitor for any temperature differential between the reaction solution and the hot water bath. Temperatures of reaction were stable with no major fluctuations beyond ~2°C with the exception of instances of sampling. During sampling, the mass of the solution was taken to ensure minimal water loss, and Mili-Q water was added to replace any evaporation (generally <2 mL). Sample aliquots of 1 mL were pipetted out of the solution, a neodymium magnet was used to sequester residual iron, and the samples were decanted into fresh Eppendorf 1.5 mL centrifuge tubes. Samples were refrigerated prior to analysis to quench further reaction with any residual iron. This procedure was followed with water bath temperatures of 50, 75, and 90°C.

6.3.2 Perchlorate Quantification

High-precision perchlorate concentration measurements were made using a 5 microliter sample loop on a Dionex ICS-2000 ion chromatograph (IC) attached to a Dionex AS 40 autosampler. Anionic components in the sample were resolved using an AS-19 separator (2x250mm) column protected by an AG-19 guard (2x50mm). A hydroxide gradient was produced using a potassium hydroxide eluent generator cartridge and ultrapure water pumped at 0.25 mL per minute. The gradient began with a 10 mM hold for 10 minutes, increased linearly to 58 mM at 25 minutes, then held at 58 mM until the end of data acquisition at 32 minutes. Seven minutes were allowed between analyses to return the column to initial conditions. Anions were detected at neutral pH using a Thermo AERS-500 2 mm suppressor operated in eluent recycle mode with an applied current of 30 mA and conductivity detection cell maintained at 35°C.

A standard curve ranging between 10.1-100.6 μM with a calibration blank was generated and fit to a quadratic curve. Experimental samples were diluted as necessary to stay within the calibrated range and the ionic exchange capacity of the columns. This dilution was performed iteratively; if a sample was over- or under-concentrated in an initial run, a second dilution and measurement was performed.

6.3.3 Isotope Measurement

After perchlorate concentration was measured, each sample was diluted to 20 μM for isotopic measurement. A stock solution of 100:1 methanol:ammonium hydroxide was prepared, and each diluted sample aliquot was brought up in a 9:1 ratio with this stock solution, resulting in a 2 μM perchlorate concentration. Perchlorate isotope standards were also created using USGS potassium perchlorate standards 37 and 38 (United States Geologic Survey, 2018) at a concentration of 20 μM perchlorate, and prepared using the same methanol stock solution. These standards have known isotopic compositions of $+0.9 \pm 0.05\text{‰}$ $\delta^{37}\text{Cl}_{\text{SMOC}}$ and $-17.00 \pm 0.10\text{‰}$ $\delta^{18}\text{O}_{\text{VSMOW}}$ for USGS 37, and $-87.9 \pm 0.3\text{‰}$ $\delta^{37}\text{Cl}_{\text{SMOC}}$ and $+52.5 \pm 0.3\text{‰}$ $\delta^{18}\text{O}_{\text{VSMOW}}$ for USGS 38 (United States Geologic Survey, 2018).

Sample solutions were inlet at a rate of $3.0 \mu\text{L min}^{-1}$ to a Thermo Scientific Q Exactive mass spectrometer through an electrospray ionization source set to 3.0 kV spray voltage with no sheath gas flow. The instrument was placed in negative mode for perchlorate analysis and a nominal resolution of 120,000 was selected. The Automatic Gain Control (AGC) was set to target 200,000 ions (assuming single ionization for all) for admission to the orbitrap in each scan. Sample ions were routed via a bent flatpole to an Advanced Quadrupole Selector (AQSTM) which was tuned to permit ions 90-110 m/z . The analyte was then stored briefly in the “C trap” prior to being inlet to and analyzed by the Orbitrap mass spectrometer (Eiler et al., 2017).

Previous work utilized a fragmentation cell to address questions of site-specific isotopic enrichments (Eiler et al., 2017; Neubauer et al., 2018). Due to the high level of symmetry in the perchlorate molecule, this capability was not used as it would not yield any additional information. The mass window was intentionally selected to be wider than the nominal 99-103 m/z window required to observe all isotopologues of perchlorate to minimize second-order mass fractionating

instrumental effects (Eiler et al., 2017). In all cases, a 35 minute data recording time was utilized. Both perchlorate standards were analyzed prior to and immediately after experimental sample analysis to allow for correction of any secular drift in instrumental mass fractionation.

Raw data was processed through propriety software termed FT Statistic, which outputs the raw intensity of the signal. This raw intensity is converted to counts for a given resolved mass peak using an empirical calibration factor, according to the equation

$$C = A \times \sqrt{m} \times \frac{I}{PN} \quad (6-1)$$

where C is the number of counts, A is an empirically derived noise factor which depends on mass resolution, m is the number of microscans, I is the signal intensity, and PN is the peak noise (Eiler et al., 2017). For these measurements, A is 4.2416, m is 1, and both I and PN are read from the raw data file.

6.3.4 Isotope quantification

Table 6-1. Isotopologues of perchlorate. Abundance of the clumped isotopologue is calculated assuming a stochastic distribution.

Isotopologue	Nominal Mass (amu)	Standard abundance (%)
$^{35}\text{Cl}^{16}\text{O}_4$	98.948	75.065
$^{37}\text{Cl}^{16}\text{O}_4$	100.945	23.987
$^{35}\text{Cl}^{18}\text{O}^{16}\text{O}_3$	100.952	0.602
$^{37}\text{Cl}^{18}\text{O}^{16}\text{O}_3$	102.949	0.192

Raw counts were generated for the signals at the masses shown in Table 6-1. This data was restricted to the time interval with a stable signal as measured by the total ion count, which generally stabilized after 5 minutes of analysis (Figure 6-1). The resulting data was further trimmed by eliminating data points where the measured total ion count times the injection time was greater than 2 sigma outside the average, which generally indicates a temporary instability in the electrospray source.

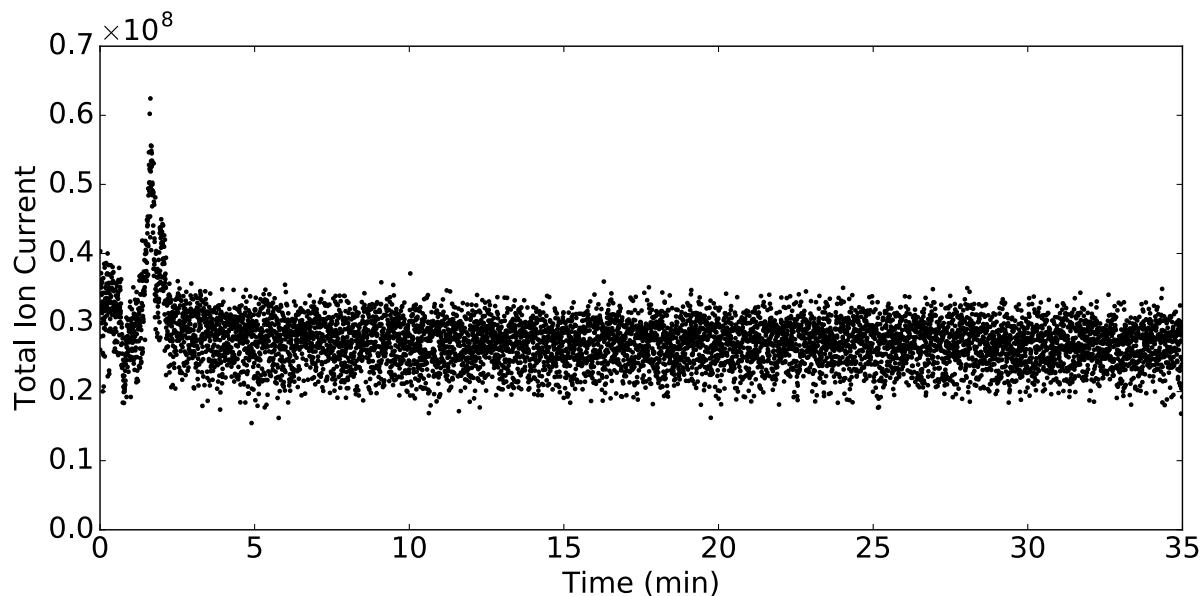


Figure 6-1. Example analysis showing total ion current over time, which is unstable for the first five minutes of analysis, but stabilizes after this time period.

After trimming, the raw ratio of each minor isotopologue for each scan was calculated, and the overall ratio for each sample run determined using a sum of these ratios, weighted by the total number of counts of the major isotopologue. For example,

$$^{37}R = \sum_{i=0}^n ^{37}R_i \times \frac{M99_i}{\sum_{i=0}^n M99_i} \quad (6-2)$$

where ^{37}R is the ratio of $^{37}\text{Cl}^{16}\text{O}_4/^{35}\text{Cl}^{16}\text{O}_4$, $^{37}R_i$ is the ratio for a given scan, $M99_i$ is the number of counts of 98.948 m/z for the same scan, and $M99$ is the total number of counts at 98.948 m/z . These raw ratios were then corrected for instrument mass fractionation and secular drift in this fractionation, as recorded by the measurement of the standards USGS 37 and USGS 38 using linear interpolation between the standard measurements, the time of measurement, and the raw ratio measured. These standards have known values of $\delta^{37}\text{Cl}_{\text{SMOC}}$ and $\delta^{18}\text{O}_{\text{VSMOW}}$, and therefore allow direct calculation of the true isotopic ratio for each experimental sample. We report these values relative to the values of standard mean ocean chlorine (SMOC; Wei et al., 2012), and Vienna standard mean ocean water (VSMOW; Gonfiantini, 1978). No standards are available for the clumped isotopologue. Instrumental mass fractionation is still correctable by tracing instrumental

drift in this isotopologue over time, providing a standard-based reference frame (as opposed to a more typical stochastic reference frame; Eiler et al., 2007).

The clumped isotope $^{37}\text{Cl}^{18}\text{O}^{16}\text{O}_3$ is reported here as $\Delta^{103}\text{ClO}_4$, calculated as

$$\Delta^{103}\text{ClO}_4 = \left(\frac{{}^{103}R}{{}^{103}R^*} - 1 \right) \times 1000 \quad (6-3)$$

where ${}^{103}R$ is the measured ratio of $^{37}\text{Cl}^{18}\text{O}^{16}\text{O}_3/^{35}\text{Cl}^{16}\text{O}_4$ and ${}^{103}R^*$ is the ratio which would occur naturally if ^{18}O and ^{37}Cl were distributed randomly (a stochastic distribution; Eiler, 2007). ${}^{130}R^*$ is calculated using the measured ${}^{18}R$ and ${}^{37}R$:

$${}^{103}R^* = 4 \times {}^{37}R \times {}^{18}R \quad (6-4)$$

We refer only to the isotopologue $^{37}\text{Cl}^{18}\text{O}^{16}\text{O}_3$. The other two possible isotopologues with a nominal mass of 103 ($^{35}\text{Cl}^{18}\text{O}_2^{16}\text{O}_2$ and $^{35}\text{Cl}^{17}\text{O}_4$) make up approximately 0.6% of the total perchlorate abundance at this mass; the low count rates of these isotopologues prevent their precise determination from the data presented here. Based on the nominal instrument resolution, the difference in mass defect between these isotopologues allows them to be fully resolved and removed from $\Delta^{103}\text{ClO}_4$ calculations.

6.3.5 Fractionation factor modeling

Given the thermodynamically favorable and unidirectional nature of perchlorate reduction, this reaction can be modeled using the Rayleigh equation

$$R = R_o \times F^{(\alpha-1)} \quad (6-5)$$

where R is the isotopic ratio of a species of interest, R_o is isotopic ratio of the starting material, F is the fraction remaining, and α is the fractionation factor. F is the ratio of the concentration of the reactant divided by the initial concentration (C/C_o). With both the concentration of perchlorate and the ratio measured in a series of time steps, python's `scipy curve_fit()` function was used to determine the fractionation factor. In addition to fitting for α , we also allow R_o and C_o to vary in the model

despite these values having been explicitly measured to avoid an overdependence on the sample measurement from t_0 in the regression for α . Because the Equation 6-5 can be rearranged to

$$R = \frac{R_o}{C_o^{(\alpha-1)}} \times C^{(\alpha-1)} \quad (6-6)$$

R_o and C_o are degenerate: if an explicit value for one of these parameters is asserted, the value of the other depends wholly on the asserted value. We allowed R_o to vary according to the measurement and uncertainty of C_o from the ion chromatograph data. The fit C_o parameter is therefore equal to the IC measurement in all cases, while the evaluation of R_o is a rigorous approximation of the true isotopic value of the starting material which takes into account all of the measured data.

6.3.6 Uncertainty calculations

There is uncertainty associated with the isotopic standards used in this study, the IC concentration measurements of perchlorate, the isotopic ratio measurements, and the derived fractionation factors. The uncertainties in the standards are given in a report by the United States Geological Survey (2018), described above. The uncertainty on measured isotope ratios is taken as the standard error of the mean of these measurements. The calibrated isotope ratios therefore encompass uncertainty in the true isotopic value of the standards, in the measured isotopic ratio of those standards, and in the measured isotopic ratio of the experimental samples; these uncertainties were propagated via a Monte Carlo model. The uncertainty in IC concentration measurements is $\pm 3.56\%$ relative (1 sigma), including both precision and accuracy. This value was empirically derived by running repeats of samples with known concentration to assess accuracy, and by running repeated dilutions of unknown samples to constrain precision. The uncertainty in the modeled fractionation factor results from the two-dimensional uncertainty in isotopic ratio and concentration measurement. This uncertainty was also propagated using a Monte Carlo model.

6.4 Results

6.4.1 Perchlorate reduction

All three experimental runs resulted in significant perchlorate reduction, as shown in Figure 6-2. The rate of perchlorate reduction was highly temperature-dependent, with reduction at 90°C progressing to approximately 80% completion in 58 hours, while reaction at 50°C resulted in reduction of only 36% of the initial perchlorate after 120 hours. Significant second order kinetics (evidenced by nonlinearity in Figure 6-2) are observed.

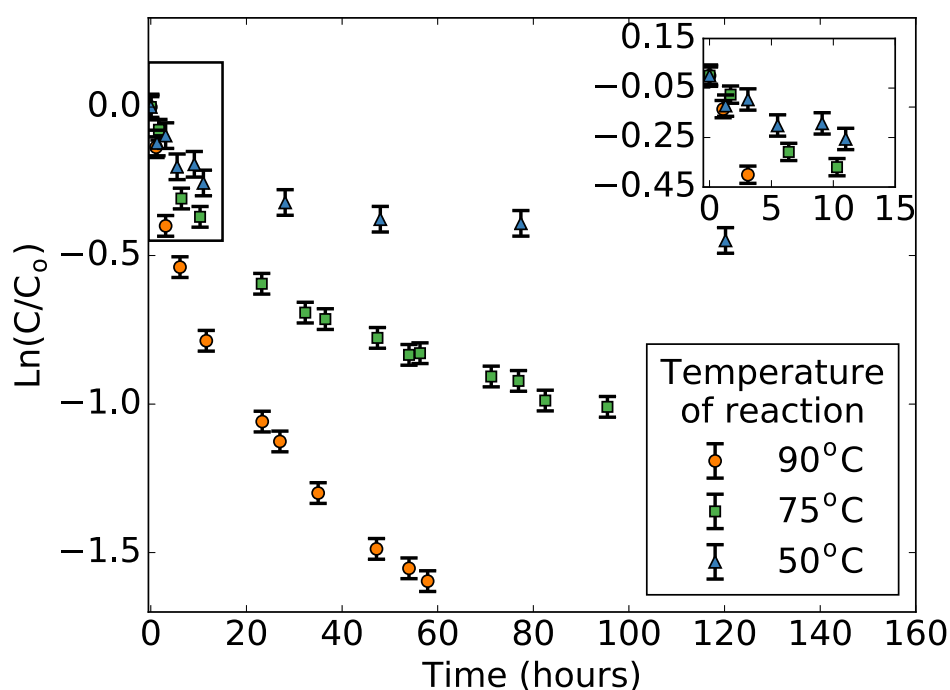


Figure 6-2. Perchlorate concentration over time, plotted as the natural log of the proportion remaining. These reactions show significant second-order behavior and suggest that iron was probably oxidized by atmospheric oxygen as well as perchlorate in solution.

The measurement of initial concentration for the reduction experiment at 75°C fell significantly below the concentration in the second sample (taken 1.7 hours after the initiation of the experiment). We interpret this unexpectedly low measurement as incomplete dissolution of the starting perchlorate salt prior to sampling. We therefore modeled the rate of perchlorate reduction assuming pseudo-first order kinetics for the first six hours of reduction to retrieve the likely initial concentration of perchlorate, which was found to be 11.310 ± 0.460 mM.

6.4.2 Perchlorate isotope results

The isotope ratios ^{37}R and ^{18}R were successfully measured and converted to $\delta^{37}\text{Cl}_{\text{SMOC}}$ and $\delta^{18}\text{O}_{\text{VSMOW}}$, respectively. Though the clumped isotopic ^{103}R measurement cannot be standardized, a distinct isotopic signature of each standard was observed. These observations are shown plotted against extent of perchlorate remaining in Figure 6-3. Data was collected at m/z 100 and 102 for analysis of $\delta^{17}\text{O}_{\text{VSMOW}}$ and $\Delta^{102}\text{ClO}_4$, but the signals from these analyses were of insufficient intensity to allow rigorous determination of these isotopic signatures.

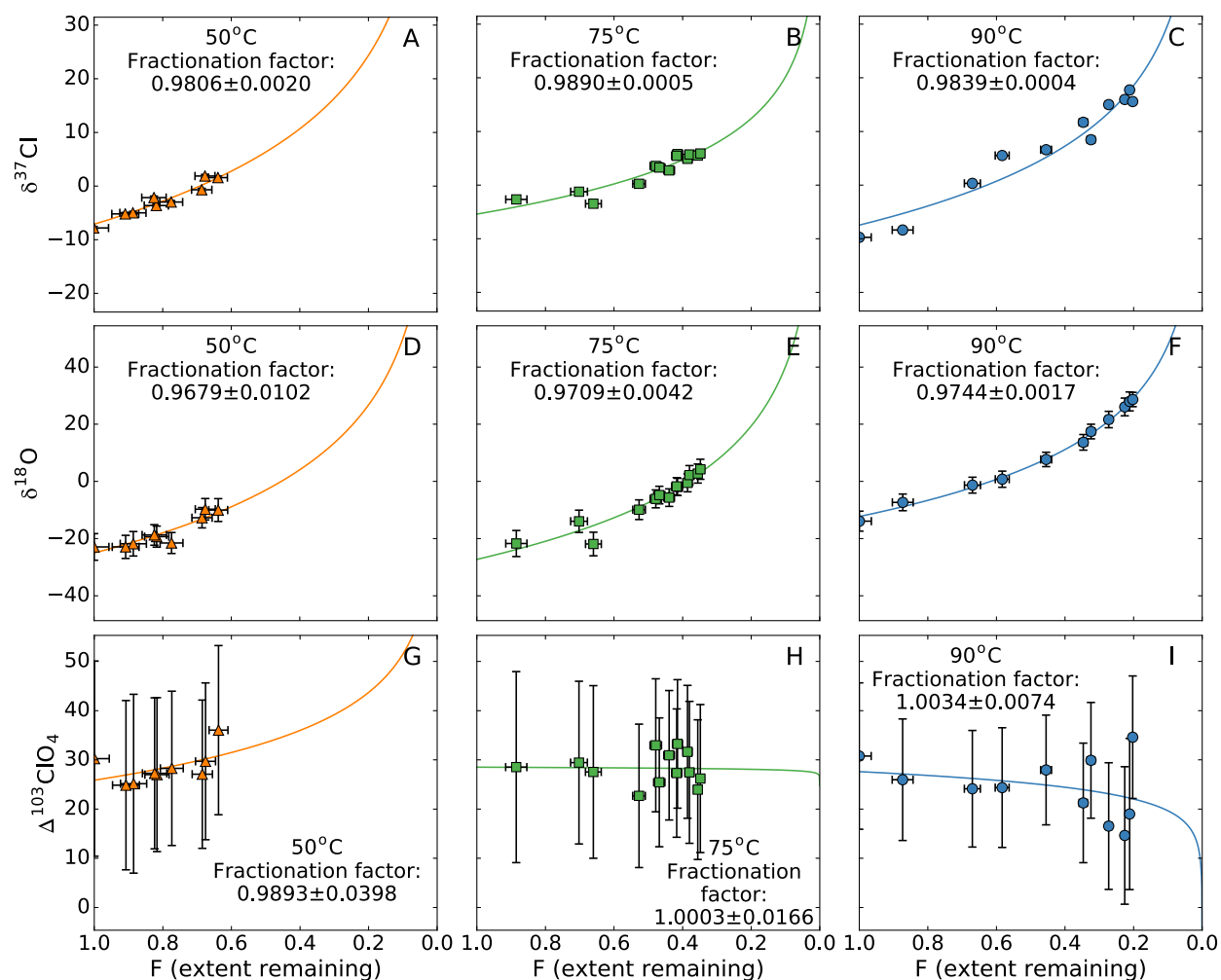


Figure 6-3. The measured isotopic values associated with each experimental reduction at 50, 75, and 90°C. The modeled fractionation factor for each reaction is also shown, along with the Rayleigh curve associated with each.

A wide range of isotopic values were measured. The observed range in $\delta^{37}\text{Cl}_{\text{SMOC}}$ values across all samples was $-9.8 \pm 0.3\text{‰}$ to $+17.7 \pm 0.3\text{‰}$, and $\delta^{18}\text{O}_{\text{VSMOW}}$ values ranged

between $-22.9 \pm 4.7\%$ and $+28.7 \pm 2.5\%$. As expected in Rayleigh distillation, these values correlate monotonically with extent of reaction: as perchlorate was reduced, the residual perchlorate became increasingly enriched in the heavier isotopes ^{37}Cl and ^{18}O at all three reaction temperatures (Figure 6-3). The fractionation factors associated with this observed trend varied with temperature. Clumped isotopic values of $+25 \pm 18\%$ to $+35 \pm 13\%$ $\Delta^{103}\text{ClO}_4$ were also measured. Unlike the traditional mass-dependent isotopic signals, the clumped isotopes do not clearly correlate with reaction progress. The resulting $^{103}\alpha$ values are therefore indistinguishable from unity within uncertainty.

Because the concentration of the data point at t_0 for the 75°C run was modeled rather than directly measured, this point is not included in the isotopic data above. Similarly, the measurement of the sample taken at 21.8 hours in the 50°C run returned anomalous isotopic results; $\delta^{37}\text{Cl}_{\text{SMOC}}$ and $\delta^{18}\text{O}_{\text{VSMOW}}$ fell more 3-sigma below the Rayleigh curve. This behavior suggests an error in the measurement as opposed to a true chemical signal, so this point was also discarded.

6.5 Discussion

6.5.1 Perchlorate reduction reaction

While the observation of temperature dependence in reaction rate is consistent with the results presented by Cao et al. (2005), the absolute rate of reduction was far lower in this experiment than predicted for each temperature by the earlier study. For example, (Cao et al., 2005) observed approximately 50% perchlorate reduction in 100 hours at 40°C . In this study, only 34% reduction was achieved in the same amount of time at the higher temperature of 50°C . In addition, the experiment by Cao et al. (2005) demonstrated pseudo-first order kinetic behavior throughout the experiment while Figure 6-2 shows clear second order kinetics for the perchlorate reduction in this study.

Presumably this second order behavior is a result of rate dependence on the availability of zero-valent iron for perchlorate reduction. We propose that the true rate law for this reaction is second-order, dependent on the perchlorate concentration and the effective concentration of Fe^0 available for reaction in the solution (which is likely a solid surface reaction; we term the activity of zero-valent iron for this surface reaction $e[\text{Fe}^0]$). The rate law would then be:

$$\frac{-d[\text{ClO}_4]}{dt} = k \times [\text{ClO}_4] \times e[\text{Fe}^0] \quad (6-7)$$

As the $e[\text{Fe}^0]$ was not measured in these experiments, the rate constant k cannot be determined from these data.

There are a number of potential reasons for the discrepancies from Cao et al. (2005). The slower reaction rate and second order chemical behavior are most likely attributable to the Fe^0/ClO_4 ratio in these experiments, which was an order of magnitude lower than those used by Cao et al. (2005). This lower ratio was likely exacerbated by several factors which further lowered $e[\text{Fe}^0]$ in solution. The use of a stir bar for agitation in this study, as opposed to a wrist-action shaker in Cao et al. (2005), could also have depressed the $e[\text{Fe}^0]$ as the stir bar may have been less effective in homogenizing the solution. The magnetic characteristic of the nanoparticles likely led to some amount of clumping on the stir bar, preventing interaction with perchlorate in solution. In addition, no anti-flocculation agent was added to the solutions and no imaging was performed to verify the dispersion of the nanoparticles. If significant clustering of the nanoparticles took place, $e[\text{Fe}^0]$ would be further reduced. The solution appeared black and iron nanoparticles were present in all sampled aliquots, indicating that iron was available for reaction in solution, but the exact amount of iron readily available for reduction is not known.

In addition to the effects discussed above, second-order kinetics could have been promoted by the consumption of iron over time by atmospheric oxygen. While N_2 was bled into the head space above the sample, the N_2 source was removed briefly for sampling, which likely led to Fe^0 oxidation. These second-order kinetics are likely to have an effect on the isotopic response of perchlorate to reduction; these will be discussed in the next section.

6.5.2 Isotopic effects of perchlorate reduction

The fractionation factors derived for $\delta^{37}\text{Cl}_{\text{SMOC}}$ and $\delta^{18}\text{O}_{\text{VSMOW}}$ have uncertainties that are dominated by the uncertainty in concentration measurement, due to the low slope of the distillation line in the regime covered by these experiments (Figure 6-3). Despite these relatively large uncertainties, these fractionation factors appear to demonstrate variability with temperature. For $\delta^{37}\text{Cl}_{\text{SMOC}}$, the fractionation factors do not have a monotonic temperature dependence, but clearly

vary with respect to T outside of uncertainty. In the case of $^{18}\alpha$, this variation is clearly monotonic, but the slope of the temperature dependence is within error of zero. We interpret $^{18}\alpha$ as temperature dependent despite the regression being within error of having a slope of zero by proxy with the $^{37}\alpha$ results.

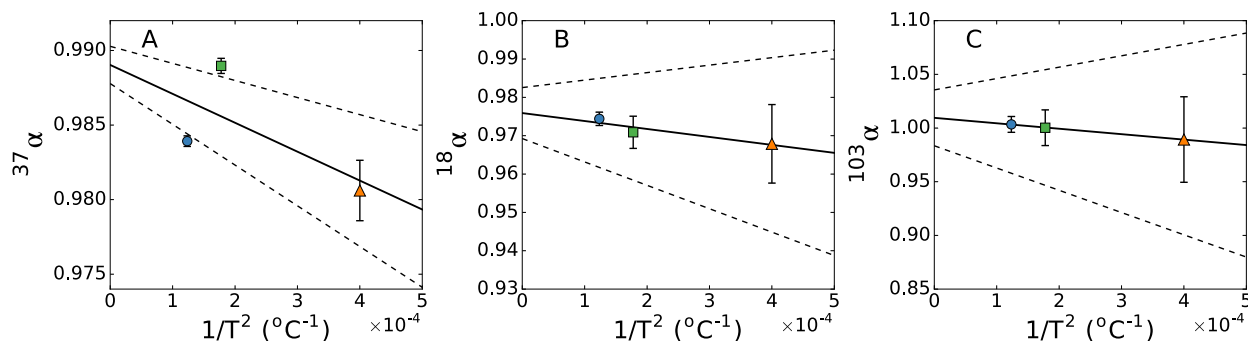


Figure 6-4. Alpha vs. $1/T^2$ for all three isotopic systems

As a unidirectional reaction, the fractionation factors reported here may either be a result of diffusion or chemical kinetic fractionations. The fact that both of these fractionation factors appear to have a dependence on temperature indicates that the isotopic effects of the Fe^0 perchlorate reduction observed here is dominated by chemical kinetics as opposed to diffusion. In a simple model of a diffusion-dominated regime, any interaction between perchlorate and an iron particle would cause perchlorate reduction. In this case, the slightly faster diffusion speed of the lighter isotopologues causes these lighter isotopologues to have a more rapid reaction rate; because the ratio of this reaction rate is dependent only on the ratio of the total mass of the molecule in question, no temperature dependence would be observed. The fractionation factor for such a mechanism may be predicted according to the mass difference of the isotopologues of interest (M_{101} and M_{99}) and the molecular mass of the fluid through which they are diffusing (in this case M_{18} , water):

$$\alpha = \frac{1}{\sqrt{\left(\frac{M_{101}}{M_{99}}\right) \times \left(\frac{M_{101} + M_{18}}{M_{99} + M_{18}}\right)}} \quad (6-8)$$

For this reaction, Equation 6-8 predicts a temperature (and isotopologue) independent fractionation factor of 0.997. That $^{37}\alpha$ and $^{18}\alpha$ are different from one another and that both indicate larger fractionations than this prediction further indicates a system dominated by chemical kinetic fractionations.

As a chemical kinetic effect occurring at temperatures well above absolute zero, these fractionations are fundamentally a result of differences in vibrational zero-point energies between the reactants and transition states for the reduction of the different isotopologues (Bigeleisen & Mayer, 1947; Urey, 1947). Without direct knowledge of the structure of the perchlorate reduction transition state, a complete predictive model of the temperature relationship with the chemical kinetic $^{37}\alpha$ and $^{18}\alpha$ fractionation factors described here is not possible. However, these data do provide some clues to understand the reasons behind the anomalous behavior of $^{37}\alpha$ and $^{18}\alpha$ as their non-monotonic and somewhat non-linear behavior (respectively) likely have the same root cause. The chemical kinetic isotopic fractionation is described by the ratio between the difference in zero-point energy of the partition functions for the transition state and the difference in zero-point energy of the reactants (Bigeleisen & Mayer, 1947). This difference in zero-point energy is dominated by the vibrational term in the partition function for each isotopologue, calculated as

$$\alpha \approx \frac{\left(\frac{Q_{vib}}{Q'_{vib}}\right)^{\ddagger}}{\left(\frac{Q_{vib}}{Q'_{vib}}\right)_r} = \frac{v'_{im}{}^{\ddagger}}{v_{im}^{\ddagger}} \times \frac{\left[\prod \frac{v'_i e^{-u_i/2}}{v_i e^{-u'_i/2}} \times \frac{1 - e^{-u_i}}{1 - e^{-u'_i}}\right]^{\ddagger}}{\left[\prod \frac{v'_i e^{-u_i/2}}{v_i e^{-u'_i/2}} \times \frac{1 - e^{-u_i}}{1 - e^{-u'_i}}\right]_r} \quad (6-9)$$

$$u_i = \frac{h\nu_i}{K_B T} \quad (6-10)$$

for each vibrational mode i where \ddagger denotes a transition state, the subscript r refers to the reactant, a subscript of im indicates the imaginary frequency of the transition state across the saddle point, a prime refers to the isotopologue of interest, h is the plank constant, K_B is the Boltzmann constant, T is temperature, and ν_i is the vibration frequency, which depends on the “spring constant” of the bond and the reduced mass of the atoms participating. It can therefore be seen that the overall fractionation resulting from perchlorate reduction is the weighted product of the various vibrational modes of the transition state. These modes will have varying, and non-linear, overall contributions to the fractionation of an isotopologue during reduction at a given temperature. The non-linear and even non-monotonic relationships between T and α can therefore be explained by the weighted dependence of varying vibrational modes and their associated fractionation with T . In addition, the second-order kinetics of reaction may influence the relative contribution of chemical kinetic vs. diffusion-associated isotope fractionation. Such a scenario implies that a single fractionation factor

may not adequately describe the isotopic effects observed in these experiments, and may explain the apparent underestimation of uncertainty in $\delta^{37}\text{Cl}_{\text{SMOC}}$ (discussed in section 6.5.3).

The fractionation factors for $\Delta^{103}\text{ClO}_4$ also appear to be weakly related to temperature. As the regression of this fractionation approaches infinite temperature, the predicted fractionation factor approaches unity, as would be expected in a clumped isotope system. We note that the regressed fractionation line from these data climbs above one at infinite temperature, essentially indicating an opposite sign in $\Delta^{103}\text{ClO}_4$. This behavior is likely a result of the lack of standardization—with a proper standard, we anticipate a regression which goes to one at infinite temperature. The large uncertainties associated with $\Delta^{103}\text{ClO}_4$ measurements preclude further in-depth discussion of the possible T- α correlation, as the slope of the linear regression is indistinguishable from zero within uncertainty.

6.5.3 Methodological considerations

Previously reported methods of perchlorate isotope analysis for $\delta^{37}\text{Cl}_{\text{SMOC}}$ require quantitative perchlorate reduction, achieved by evaporation to dryness and heating at 550-600°C to cause breakdown of the perchlorate molecule (Ader et al., 2001; Sturchio et al., 2003). Once chloride is obtained, conversion to CH_3Cl using CH_3I is required for measurement using a traditional isotope-ratio mass spectrometer (Sturchio et al., 2003). These techniques generally result in precisions of $\pm 0.3\text{‰}$ (Böhlke et al., 2005; Sturchio et al., 2003) and can achieve precisions of $\pm 0.05\text{‰}$ (Ader et al., 2001). Analysis of perchlorate-associated $\delta^{18}\text{O}_{\text{VSMOW}}$ requires a separate aliquot of perchlorate, and involves reaction with carbon to produce CO , which is also measured on a traditional isotope-ratio mass spectrometer and allows precisions of approximately $\pm 0.2\text{‰}$ (Böhlke et al., 2005). No previous methods for clumped perchlorate isotope analysis have been reported.

With analyses 35 minutes in length, average precisions of $\pm 0.28\text{‰}$ in $\delta^{37}\text{Cl}_{\text{SMOC}}$, $\pm 3.4\text{‰}$ in $\delta^{18}\text{O}_{\text{VSMOW}}$, and $\pm 15\text{‰}$ $\Delta^{103}\text{ClO}_4$ were obtained in this study. These precisions are consistent with the shot noise limits for each analysis based purely on the number of counts observed for the rare isotope. The precision in $\delta^{37}\text{Cl}_{\text{SMOC}}$ is comparable to previously available analytical techniques; the naturally low abundance of ^{18}O results in precision around an order of magnitude lower than readily achieved using these earlier techniques. Neither $^{35}\text{Cl}^{17}\text{O}^{16}\text{O}_3$ nor $^{37}\text{Cl}^{17}\text{O}^{16}\text{O}_3$ could be quantified in

these analyses due to low abundance of these isotopologues. At sufficiently low signal, the Orbitrap utilizes a different algorithm for determining signal strength, which causes a dramatic and uncharacterized shift in the converted number of counts based on the intensity data. Much of the $^{35}\text{Cl}^{17}\text{O}^{16}\text{O}_3$ scan and nearly all of the $^{37}\text{Cl}^{17}\text{O}^{16}\text{O}_3$ involved this different algorithm (Figure 6-5), and this algorithm has not been calibrated for conversion to counts. These signals therefore cannot be reliably ratioed to the major isotopologue, precluding their further use in this study.

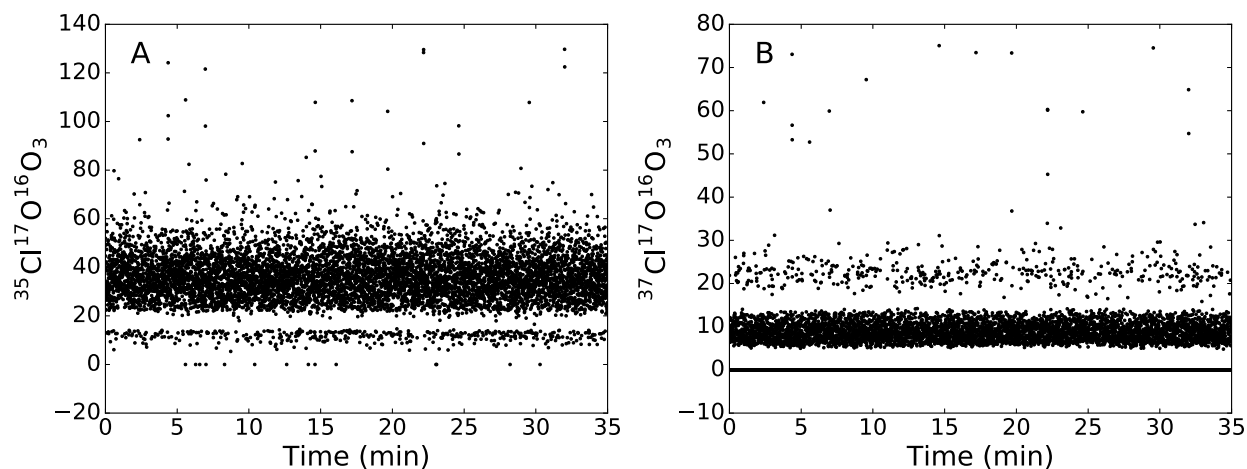


Figure 6-5. Time plots of m/z 99 and 102 demonstrating jumping behavior in the low abundance isotopes.

The major advantages of this technique are the minimal sample preparation required, the single aliquot necessary for measurement, and the ability to measure clumped isotopes. In addition, the total amount of perchlorate necessary to conduct an analysis is small. A 35 minute injection of 2 μM perchlorate at 3 uL min^{-1} equates to 2.1×10^{10} perchlorate molecules, or 20.9 ng of perchlorate. Of course, in practical terms, more perchlorate than this is needed to prepare for analysis, but the dilute nature of the analyte in this technique permits analysis of small absolute amounts of perchlorate.

Key to the analysis of unfragmented perchlorate ion is the mass resolving power of the Orbitrap mass spectrometer, which allows completely resolved signals of the nominally isobaric $^{37}\text{Cl}^{16}\text{O}_4$ and $^{35}\text{Cl}^{18}\text{O}^{16}\text{O}_4$ (Figure 6-6). As a result of counting statistics, when measuring these isotopologues simultaneously $\delta^{37}\text{Cl}_{\text{SMOC}}$ will always have a formal precision around an order of magnitude better than $\delta^{18}\text{O}_{\text{VSMOW}}$. However, as can be seen in Figure 6-3, the values and standard error of the $\delta^{37}\text{Cl}_{\text{SMOC}}$ measurements lie beyond 1-sigma off of the Rayleigh curve. We interpret this

behavior as a sign that the true uncertainty in $\delta^{37}\text{Cl}_{\text{SMOC}}$ is underestimated by the standard error of the mean. An additional error term was added to the Monte Carlo model used to determine the fractionation factors and was used to retrieve the amount of additional uncertainty necessary for all measured points to lie on the Rayleigh curve within a 1-sigma distribution. For all measurements other than $\delta^{37}\text{Cl}_{\text{SMOC}}$, no additional error was required. For $\delta^{37}\text{Cl}_{\text{SMOC}}$ however, approximately 70% additional uncertainty was indicated, resulting in an average uncertainty for $\delta^{37}\text{Cl}_{\text{SMOC}}$ measurements of $\pm 1.4\%$. With this error term included, the $\delta^{37}\text{Cl}_{\text{SMOC}}$ measurements are fully consistent with the Rayleigh curve (Figure 6-7), while the major results discussed above remain unchanged. The measurements of $\delta^{37}\text{Cl}_{\text{SMOC}}$ at t_0 (a direct measurement of R_0) for the three temperature runs also function as an independent measure of inter-sample reproducibility; the inclusion of this additional uncertainty brings all three measured R_0 values within 1-sigma uncertainty of one another. These measurements also closely match the regressed values of R_0 , shown in Figure 6-7d. We therefore postulate that this added uncertainty fully captures the true accuracy of the $\delta^{37}\text{Cl}_{\text{SMOC}}$ measurement.

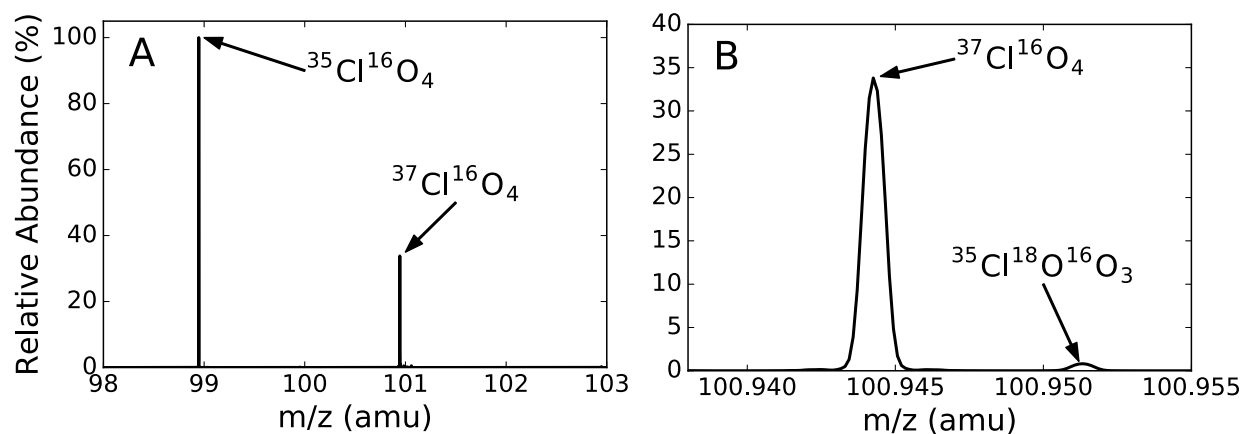


Figure 6-6. A) An example mass spectrum within the mass range of interest for perchlorate. B) A zoomed mass spectrum, showing the full resolution of the $^{37}\text{Cl}^{16}\text{O}_4$ and $^{35}\text{Cl}^{18}\text{O}^{16}\text{O}_3$ peaks.

The source of this additional error is currently not known, but we postulate that it is a result of a known phenomenon of discrimination against large ion populations in Orbitrap mass spectrometers, likely due to space charge effects in the C trap (Eiler et al., 2017). This effect can be seen in the raw measured ratio of $^{37}\text{Cl}^{16}\text{O}_4/^{35}\text{Cl}^{16}\text{O}_4$ and $^{35}\text{Cl}^{18}\text{O}^{16}\text{O}_3/^{35}\text{Cl}^{16}\text{O}_4$, which were generally 1.05 and 4 times their corrected values, respectively. Because the $^{37}\text{Cl}^{16}\text{O}_4$ signal is comparatively large ($\sim 30\%$ of the total signal), any deleterious effects on abundant ion beams will impact the

measurement of this signal as well as the major isotopologue. Another possible source of error is the lack of perchlorate standards isotopically enriched in ^{37}Cl . Without such standards, we are forced to correct signals as enriched as $+17.7 \pm 0.3\text{‰}$ $\delta^{37}\text{Cl}_{\text{SMOC}}$ despite the fact that the standards span -87.9‰ to 0.9‰ $\delta^{37}\text{Cl}_{\text{SMOC}}$, which could introduce additional error.

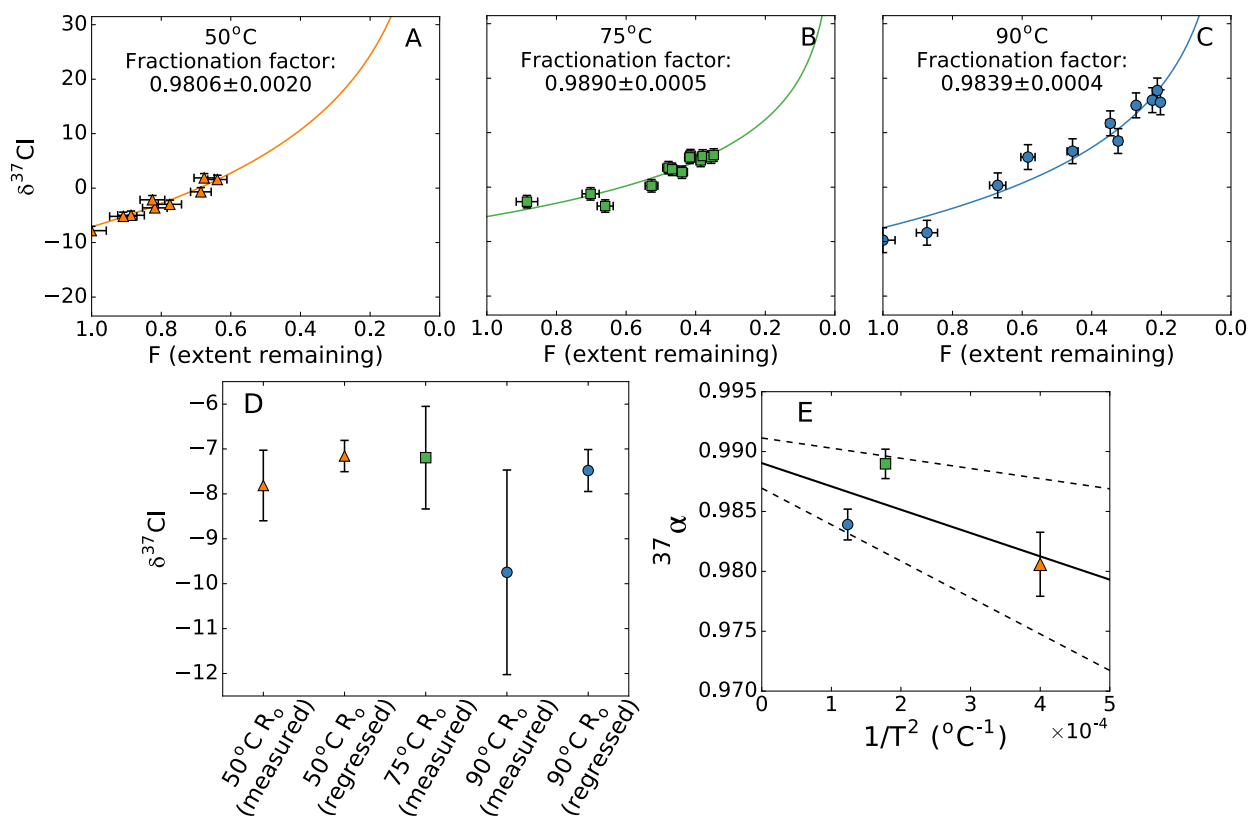


Figure 6-7. A-C) Regression for $^{37}\alpha$ with an additional error term implemented. D) Measured and regressed values of R_0 , which are all within uncertainty of one another with the additional error term. The regressed R_0 for the 75°C run is not included due to the associated C_0 being modeled. E) $^{37}\alpha$ vs. $1/T^2$ with the additional error.

6.5.3.1 Instrumental mass fractionation

We correct for instrumental mass fractionation and secular drift using linear interpolation of the standards measured at the beginning and end of each day of measurement. For mass fractionation, this is known to be valid, at least within the isotopic range defined by the standards, because the contrast in the traditional isotopic ratios (i.e., non-clumped ^{37}R and ^{18}R) of the USGS standards were recovered to better than 1-sigma uncertainty in each instrumental run, as shown in Figure 6-8a&b. Secular drift in the instrumental mass fractionation was also apparent, and was unidirectional, with uncorrected isotopic ratios falling over the course of a day measurements. A linear interpolation is

not necessarily valid for such secular drift. To address this possible issue, a standard was measured at the midpoint between the typical standard measurements at the beginning and end of a day. This analysis indicates that the secular drift is roughly linear, shown in Figure 6-8c above. The nonlinearity in this regression is sufficiently small that any second-order effects on the final corrected isotope values will be well within uncertainty.

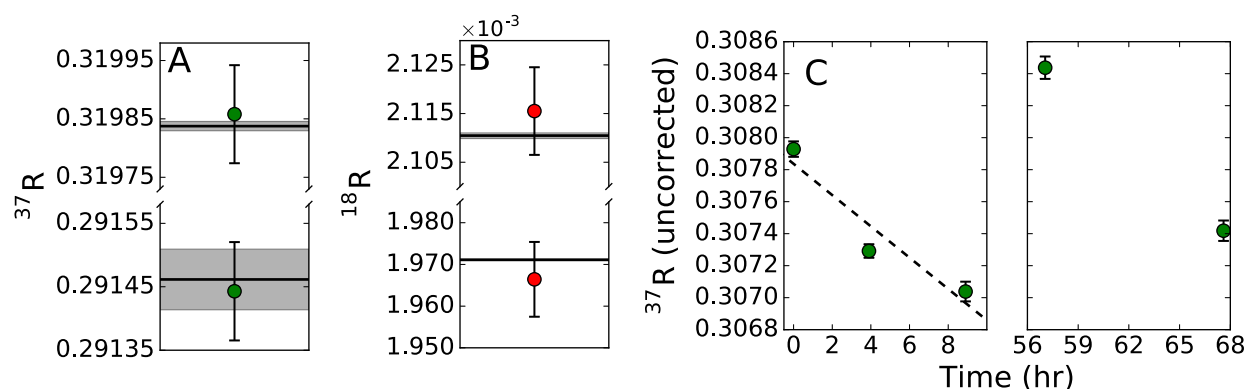


Figure 6-8. A & B) Example measured isotope ratio of each standard, corrected to be centered on the known isotopic ratios of ^{37}R and ^{18}R for the USGS37 and USGS38 standards. The true value for each standard is shown as a black bar with uncertainty in gray. C) Time vs. raw (uncorrected) measured ratio of standards, showing secular drift in instrumental fractionation.

6.5.3.2 Future development

A number of significant improvements on the technique described here are possible with additional work. The precision reported for these analyses was achieved using relatively short 35 minute integration times. Based on the count rates observed in these data, and assuming that longer integrations are also shot-noise limited, the best precisions reported in the literature for perchlorate-associated $\delta^{37}\text{Cl}_{\text{SMOC}}$ ($\pm 0.05\%$; Ader et al., 2001) and $\delta^{18}\text{O}_{\text{VSMOW}}$ ($\pm 0.2\%$; Böhlke et al., 2005) will approximately be matched with integration for 3.5 hours, which would yield $\pm 0.051\%$ $\delta^{37}\text{Cl}_{\text{SMOC}}$ and $\pm 0.33\%$ $\delta^{18}\text{O}_{\text{VSMOW}}$. This increase in precision is likely possible while also reducing the total amount of perchlorate necessary for measurement. No effort was made to minimize the concentration of perchlorate in analyte solutions for this study and the injection time for each scan averaged all data collected here was 0.576 msec. These injection times are short compared to those in a pilot study of Orbitrap isotope ratio mass spectrometry (Eiler et al., 2017), which is a direct indication that more dilute analyte solutions are likely feasible. In addition to allowing an even

smaller total amount of perchlorate to achieve the same precision, more dilute solutions may in fact raise the sensitivity of the measurement (Eiler et al., 2017).

Both $\delta^{17}\text{O}_{\text{VSMOW}}$ and $\Delta^{102}\text{ClO}_4$ are likely amenable to quantification with minor alterations to the method presented in this study. For reliable observation of these isotopologues, the number of counts per scan must be increased by approximately twofold in the case of $^{35}\text{Cl}^{17}\text{O}^{16}\text{O}_3$ and tenfold in the case of $^{37}\text{Cl}^{17}\text{O}^{16}\text{O}_3$. There are two potential strategies to achieve these increases: 1) increasing the AGC target, or 2) utilizing dual scans with independent AQS settings. Increasing the AGC target simply increases the number of ions inlet to the Orbitrap, thereby increasing the count rate. This potential method has the advantage that it is simple to implement and directly addresses the base issue of an insufficient number of counts at m/z 100 and 102. As count rates increase, the amount of time required to reach a given level of precision will also fall correspondingly. For measurement of $^{35}\text{Cl}^{17}\text{O}^{16}\text{O}_3$, this simple change is likely to be effective, as an increase in AGC target from the current setting of 200,000 to 400,000 ions is unlikely to have significant effects on the overall behavior of the instrument. However, with the increase to 2,000,000 ions likely necessary for measurement of $^{37}\text{Cl}^{17}\text{O}^{16}\text{O}_3$, non-negligible space charge effects are likely to occur in the ion trap, causing changes in instrumental mass fractionation (Eiler et al., 2017). As we believe these space charge effects to be the root cause of inaccuracy in the measurement of $\delta^{37}\text{Cl}_{\text{SMOC}}$, large increases in the AGC target may have a prohibitively adverse effect on the mass spectrum. Evaluating this option would also provide a check of whether space charge effects are indeed the root issue behind the $\delta^{37}\text{Cl}_{\text{SMOC}}$ measurement inaccuracies. If $\delta^{37}\text{Cl}_{\text{SMOC}}$ inaccuracy increases with increased AGC settings, it is likely that even 200,000 is too high of a setting for accurate $\delta^{37}\text{Cl}_{\text{SMOC}}$ measurement.

The alternative measurement mode to retrieve $\delta^{17}\text{O}_{\text{VSMOW}}$ and $\Delta^{102}\text{ClO}_4$ is a dual measurement mode, where the mass window of the AQS is changed to exclude the primary ion beam at m/z 99. While changing the relative position of each beam within the mass window will have second-order effects on total ion counts via instrumental mass fractionation, these changes are known to be stable over time and are correctable (Eiler et al., 2017). This measurement mode would therefore involve integrating for the standard 35 minutes with the mass window at the nominal m/z 90-100 range, and then repeating the measurement, with the mass window trimmed to m/z 99.5-103.5, effectively tripling the counts per scan for each of the minor isotopologues. Using the $^{37}\text{Cl}^{16}\text{O}_4$ beam to back out the number of counts of the main isotopologue, $\delta^{17}\text{O}_{\text{VSMOW}}$ and $\Delta^{102}\text{ClO}_4$ may then

be calculated. Though this mode requires two measurements, it has the advantage that the total ion current in a single scan is unchanged, meaning that space charge effects will not become a complicating factor. Another advantage is that the tripling of counts for all minor isotopologues will improve precision for $\delta^{18}\text{O}_{\text{VSMOW}}$ measurement. These two measurements are also made on the same analyte solution, meaning that they may be made back-to-back without changing or cleaning the syringe. As this measurement mode will inherently increase the number of counts threefold, it will be sufficient for quantification of $\delta^{17}\text{O}_{\text{VSMOW}}$, and insufficient on its own for observation of $\Delta^{102}\text{ClO}_4$.

On the whole, both of the above modifications are likely to be required in tandem for $\Delta^{102}\text{ClO}_4$ measurement—the double scan method offers a threefold increase, and a further threefold increase is possible by raising the AGC target to 600,000. This higher AGC target is far less likely to exhibit deleterious space charge effects than a simple tenfold increase in the AGC target for $\Delta^{102}\text{ClO}_4$ observation.

Accurate calculation of both $\Delta^{103}\text{ClO}_4$ and $\Delta^{102}\text{ClO}_4$ requires that a standard be prepared which is known to have a stochastic distribution of the relevant minor isotopes. Preparation of such a standard would involve equilibrating perchlorate at thermodynamic equilibrium and high temperature (Eiler & Schauble, 2004; Stolper et al., 2014). As perchlorate does not readily exchange oxygen (Hoering et al., 1958) and perchlorate decomposition is thermodynamically favorable (Urbansky, 2002), significant effort may be involved in producing such a standard.

There are two other small areas for continued study. 1) The secular drift observed in this study has not been reported previously. While this drift is empirically correctable, developing a mechanistic understanding of its source may allow mitigation of the drift, or allow it to be eliminated entirely. 2) The methodology presented here is likely amenable to the study of other oxychlorine species. No values for the isotopic composition of chlorate (ClO_3^-) have been reported despite the fact that it frequently coexists with perchlorate in nature (Rao et al., 2010), and therefore has the potential to augment our understanding of the formation processes of perchlorate.

6.5.4 Environmental perchlorate remediation

With accuracy of $\pm 1.4\text{‰}$ in $\delta^{37}\text{Cl}_{\text{SMOC}}$, $\pm 3.4\text{‰}$ in $\delta^{18}\text{O}_{\text{VSMOW}}$ and the potential for more accurate and precise analyses, this technique shows great promise for utility in rapidly assessing the

source of an unknown perchlorate contaminant. As the $\delta^{37}\text{Cl}_{\text{VSMOW}}$ of perchlorate varies by $\sim 17\text{‰}$ between natural Atacama perchlorate and synthetic perchlorate, and $\delta^{18}\text{O}_{\text{VSMOW}}$ varies by $\sim 28\text{‰}$ (Böhlke et al., 2005), determination of perchlorate source should be readily obtained given an unknown perchlorate specimen for identification. Standardization of $\Delta^{103}\text{ClO}_4$ will yield an additional dimension for comparison, and is likely to contain information on the formation process of a sample of perchlorate, assisting in forensic perchlorate analyses. Additionally, as naturally occurring perchlorate is known to have a strong mass-independent oxygen isotope signal even without an unusual $\delta^{37}\text{Cl}_{\text{SMOC}}$ signature (Böhlke et al., 2005; Jackson et al., 2010), further development for measurement of ^{17}O has the potential to aid in uniquely identifying any given perchlorate source.

The second-order behavior of perchlorate reduction using Fe^0 observed in this study indicates that this technique is likely poorly suited to large-scale perchlorate remediation. A strictly anoxic reactor would need to be maintained for effective perchlorate reduction, and the reactor would have to be held at high temperature for efficient kinetics of reduction. A constant supply of fresh Fe^0 would also be needed, and a mechanism to keep iron nanoparticles from escaping would be required to prevent these particles from posing an environmental hazard of their own.

Regardless of the utility of the reaction investigated here for perchlorate remediation, this new perchlorate isotope analysis technique may be efficiently applied to assess the extent and efficiency of perchlorate remediation via reduction. As the ultimate goal of remediation is to achieve near 100% perchlorate reduction (i.e., $F \sim 0$), very strong isotopic fractionation should be observed. The per mille-level precisions achieved in this study are well-suited to assess the extent of reduction in a system where at 5% perchlorate remaining, $+52\text{‰}$ $\delta^{37}\text{Cl}_{\text{SMOC}}$ and $+71\text{‰}$ $\delta^{18}\text{O}_{\text{VSMOW}}$ are predicted, using the fractionation factors derived in this study and the isotopic composition of the starting material (other perchlorate reduction fractionation factors in the literature are similar; Ader et al., 2008; Schauble et al., 2003). At 1% perchlorate remaining, these signatures are $+85\text{‰}$ $\delta^{37}\text{Cl}_{\text{SMOC}}$ and $+127\text{‰}$ $\delta^{18}\text{O}_{\text{VSMOW}}$. Utilizing this technique to trace the extent of perchlorate reduction for remediation requires only that the initial isotopic ratios are known or measured and the fractionation factor associated with the remediation technique has been derived or is known independently.

6.5.5 Implications for naturally occurring perchlorate

This study reports the first experimentally determined fractionation factors for the chemical reduction of perchlorate. At a range of temperatures and in both traditional isotopic systems investigated, the residual perchlorate is enriched in the heavy isotope (i.e., $\alpha < 1.0$). Fractionation associated with perchlorate reduction at thermodynamic equilibrium and through biological processes also leaves residual perchlorate isotopically enriched in ^{37}Cl , both with single-step fractionation factors of ~ 0.985 (Ader et al., 2008; Schauble et al., 2003). No physical mechanism has therefore been identified which would deplete perchlorate with respect to ^{37}Cl . As the global chlorine isotope reservoirs rarely vary outside of $\pm 3\text{‰}$ $\delta^{37}\text{Cl}_{\text{SMOC}}$ (e.g., Bonifacie et al., 2008; Eastoe et al., 2007; Eggenkamp, 2014; Liu et al., 2013; Sharp et al., 2007), the identification of strongly ^{37}Cl -depleted perchlorate in the Atacama and elsewhere (Böhlke et al., 2005; Jackson et al., 2010) indicates that any chlorine isotope signature in perchlorate with a negative $\delta^{37}\text{Cl}_{\text{SMOC}}$ is likely primary and related to the mechanism of perchlorate formation. The mechanistic causes of this isotopic effect have yet to be identified or studied.

This conclusion also sheds light on the detection of ^{37}Cl -depleted signals observed in HCl evolved from Martian rocks measured in-situ by the Curiosity rover (Farley et al., 2016). Two possible sources of the observed -51 ± 5 to $-1 \pm 25\text{‰}$ $\delta^{37}\text{Cl}_{\text{SMOC}}$ range were proposed: either direct measurement of particularly ^{37}Cl depleted primary perchlorate, or chloride which had been reduced stepwise through the various oxychlorine phases (e.g., ClO_3^- , ClO_2^- , and ClO^-) at thermodynamic equilibrium and removed from the system at the chloride step (Farley et al., 2016). The observation here that kinetic reduction of perchlorate causes ^{37}Cl enrichment in the residual perchlorate reinforces that one of these two mechanisms must be responsible for the Martian $\delta^{37}\text{Cl}_{\text{SMOC}}$ as all fractionation factors associated with perchlorate reduction result in ^{37}Cl -enriched perchlorate. Additionally, the magnitude of fractionation based on kinetic reduction of perchlorate is insufficient to explain the isotopically extreme chlorine observed on Mars as chloride produced by this process. The most negative chloride possible (from a starting point of 0‰) based on single-step kinetic reduction is roughly -20‰ , while the bulk Martian chlorine isotope composition is thought to be approximately -3 to -4‰ $\delta^{37}\text{Cl}_{\text{SMOC}}$ (Sharp et al., 2016; Williams et al., 2016). Given the highly thermodynamically favorable but kinetically inhibited nature of perchlorate reduction (e.g., Urbansky, 2002), reduction of perchlorate at thermodynamic equilibrium is not probable and direct

measurement of primary perchlorate is likely the best interpretation of the Martian data by analogy to the highly ^{37}Cl -depleted signals observed in some terrestrial perchlorate (Böhlke et al., 2005; Farley et al., 2016). However, as the mechanism of fractionation in Atacama perchlorate has not been identified, an understanding of the cause of this isotopic depletion in natural perchlorate must be developed for a full understanding of the Martian chlorine isotope system and budget to emerge.

6.6 Conclusions

We demonstrate a new method of perchlorate isotope analysis which allows the determination of $\delta^{37}\text{Cl}_{\text{SMOC}}$, $\delta^{18}\text{O}_{\text{VSMOW}}$, and $\Delta^{103}\text{ClO}_4$. Existing perchlorate isotope measurement modes require the quantitative reduction of perchlorate to chloride, followed by conversion to CH_3Cl for isotope measurement; sample preparation in this study simply involves bringing up a perchlorate salt in a solution of water and methanol. Current methods are also unable to assess the clumped isotope signature of perchlorate, and multiple aliquots of sample must be prepared to evaluate the range of isotopic dimensions in perchlorate (i.e., $\delta^{37}\text{Cl}_{\text{SMOC}}$, $\delta^{18}\text{O}_{\text{VSMOW}}$, and $\delta^{17}\text{O}_{\text{VSMOW}}$). In this new method, the relevant isotopologues are measured simultaneously on unfragmented perchlorate using an electrospray-Orbitrap mass spectrometer. With the analysis of ~ 21 ng of perchlorate, precisions of $\pm 0.28\text{‰}$ $\delta^{37}\text{Cl}_{\text{SMOC}}$, $\pm 3.4\text{‰}$ $\delta^{18}\text{O}_{\text{VSMOW}}$ and $\pm 15\text{‰}$ $\Delta^{103}\text{ClO}_4$ are possible. With continued development, improved precision is likely achievable while also requiring a smaller total amount of perchlorate. In addition, future development may permit the determination of $\delta^{17}\text{O}_{\text{VSMOW}}$, and $\Delta^{102}\text{ClO}_4$.

The reduction of perchlorate using Fe^0 nanoparticles in a simulated real-world application of this technique demonstrates that this new method is capable of tracking perchlorate isotopic changes in $\delta^{37}\text{Cl}_{\text{SMOC}}$, $\delta^{18}\text{O}_{\text{VSMOW}}$, and $\Delta^{103}\text{ClO}_4$. The fractionation factors associated with this reduction are temperature dependent, though they exhibit non-linear and non-monotonic variations that suggest this temperature dependence is a function of the weighted product of the vibrational modes of the transition state at a given temperature. As the structure of the transition state of this reaction is unknown, a predictive framework for fractionation factor at a given temperature cannot currently be established.

The results from the perchlorate reduction by Fe^0 also indicate that the range of isotopic signatures likely to be observed during perchlorate remediation can easily be detected in multiple isotopic dimensions using this new method. The range of perchlorate isotope signatures in common contaminant perchlorate is also readily observable using this technique; the use of multiple isotopic dimensions in this case permits unique identification of a perchlorate source. Natural perchlorate often has a strong depletion in ^{37}Cl , the only example of strongly fractionated chlorine in nature. As perchlorate reduction via thermodynamic, biogenic, and abiotic processes results in ^{37}Cl enrichment in the residual perchlorate, this chlorine isotope signature is most likely primary and related to the mechanism of perchlorate formation. These results also suggest that the highly ^{37}Cl -depleted HCl observed on Mars using the SAM instrument is sourced from primary perchlorate rather than reduced chloride as the single-step fractionation of chloride reduction is of insufficient magnitude to produce the SAM observations.

BIBLIOGRAPHY

Chapter 1

- Arvidson, R., Guinness, E., & Lee, S. (1979). Differential aeolian redistribution rates on Mars. *Nature*, 278(5704), 533–535. <https://doi.org/10.1038/278533a0>
- Bibring, J.-P., Langevin, Y., Mustard, J. F., Poulet, F., Arvidson, R., Gendrin, A., et al. (2006). Global mineralogical and aqueous Mars history derived from OMEGA/Mars Express data. *Science*, 312(5772), 400–404.
- Carr, M. H., & Head, J. W. (2010). Geologic history of Mars. *Earth and Planetary Science Letters*, 294(3), 185–203. <https://doi.org/10.1016/j.epsl.2009.06.042>
- Chevrier, V., Poulet, F., & Bibring, J.-P. (2007). Early geochemical environment of Mars as determined from thermodynamics of phyllosilicates. *Nature*, 448(7149), 60–63. <https://doi.org/10.1038/nature05961>
- Day, M., & Kocurek, G. (2016). Observations of an aeolian landscape: From surface to orbit in Gale Crater. *Icarus*, 280, 37–71. <https://doi.org/10.1016/j.icarus.2015.09.042>
- Ehlmann, B. L., & Edwards, C. S. (2014). Mineralogy of the Martian Surface. *Annual Review of Earth and Planetary Sciences*, 42(1), 291–315. <https://doi.org/10.1146/annurev-earth-060313-055024>
- Ehlmann, B. L., Mustard, J. F., Murchie, S. L., Bibring, J.-P., Meunier, A., Fraeman, A. A., & Langevin, Y. (2011). Subsurface water and clay mineral formation during the early history of Mars. *Nature*, 479(7371), 53–60.
- Farley, K., Martin, P., Archer, P., Atreya, S., Conrad, P., Eigenbrode, J., et al. (2016). Light and variable 37 Cl/35 Cl ratios in rocks from Gale Crater, Mars: Possible signature of perchlorate. *Earth and Planetary Science Letters*, 438, 14–24.
- Fassett, C. I., & Head, J. W. (2008). The timing of martian valley network activity: Constraints from buffered crater counting. *Icarus*, 195(1), 61–89.
- Golombek, M. P., Warner, N. H., Ganti, V., Lamb, M. P., Parker, T. J., Fergason, R. L., & Sullivan, R. (2014). Small crater modification on Meridiani Planum and implications for erosion rates and climate change on Mars. *Journal of Geophysical Research: Planets*, 119(12), 2522–2547. <https://doi.org/10.1002/2014JE004658>
- Hartmann, W. K., & Neukum, G. (2001). Cratering chronology and the evolution of Mars. *Space Science Reviews*, 96(1), 165–194.
- Mahaffy, P. R., Webster, C. R., Cabane, M., Conrad, P. G., Coll, P., Atreya, S. K., et al. (2012). The sample analysis at Mars investigation and instrument suite. *Space Science Reviews*, 170(1–4), 401–478.
- Malin, M. C., & Edgett, K. S. (2003). Evidence for Persistent Flow and Aqueous Sedimentation on Early Mars. *Science*, 302(5652), 1931–1934. <https://doi.org/10.1126/science.1090544>
- Mangold, N., Quantin, C., Ansan, V., Delacourt, C., & Allemand, P. (2004). Evidence for Precipitation on Mars from Dendritic Valleys in the Valles Marineris Area. *Science*, 305(5680), 78–81. <https://doi.org/10.1126/science.1097549>
- Nimmo, F., & Tanaka, K. (2005). Early crustal evolution of Mars 1. *Annu. Rev. Earth Planet. Sci.*, 33, 133–161.

- Poulet, F., Bibring, J.-P., Mustard, J. F., Gendrin, A., Mangold, N., Langevin, Y., et al. (2005). Phyllosilicates on Mars and implications for early martian climate. *Nature*, 438(7068), 623–627. <https://doi.org/10.1038/nature04274>
- Squyres, S. W. (1984). The History of Water on Mars. *Annual Review of Earth and Planetary Sciences*, 12(1), 83–106. <https://doi.org/10.1146/annurev.ea.12.050184.000503>
- Squyres, S. W., Grotzinger, J. P., Arvidson, R. E., Bell, J. F., Calvin, W., Christensen, P. R., et al. (2004). In Situ Evidence for an Ancient Aqueous Environment at Meridiani Planum, Mars. *Science*, 306(5702), 1709–1714. <https://doi.org/10.1126/science.1104559>
- Tanaka, K. L., Skinner, J. A., Dohm, J. M., Irwin III, R. P., Kolb, E. J., Fortezzo, C. M., et al. (2014). *Geologic map of Mars* (USGS Numbered Series No. 3292) (p. 48). Reston, VA: U.S. Geological Survey. Retrieved from <http://pubs.er.usgs.gov/publication/sim3292>

Chapter 2

- Abbey, W. J., Bhartia, R., Beegle, L. W., DeFlores, L., Paez, V., Sijapati, K., et al. (2017). Deep UV Raman spectroscopy for planetary exploration: The search for in situ organics. *Icarus*, 290, 201–214. <https://doi.org/10.1016/j.icarus.2017.01.039>
- Allwood, A. C., Clark, B., Flannery, D., Hurowitz, J., Wade, L., Elam, T., et al. (2015). Texture-specific elemental analysis of rocks and soils with PIXL: The Planetary Instrument for X-ray Lithochemistry on Mars 2020. In *2015 IEEE Aerospace Conference* (pp. 1–13). <https://doi.org/10.1109/AERO.2015.7119099>
- Allwood, A. C., Wade, L. A., & Hurowitz, J. A. (2016). PIXL Investigation on the Mars 2020 Rover (Vol. 4138). Presented at the 3rd International Workshop on Instrumentation for Planetary Mission. Retrieved from <http://adsabs.harvard.edu/abs/2016LPICo1980.4138A>
- Anderson, R.B., Finch, N., Clegg, S., Gaff, T., Morris, R. V., & Laura, J. (2017). Python Spectral Analysis Tool (PySAT) For Preprocessing, Multivariate Analysis, And Machine Learning With Point Spectra. Abstract #1986 Presented at the 3rd Planetary Data Workshop, Lunar and Planetary Institute.
- Anderson, Ryan B., Morris, R. V., Clegg, S. M., Bell, J. F., Wiens, R. C., Humphries, S. D., et al. (2011). The influence of multivariate analysis methods and target grain size on the accuracy of remote quantitative chemical analysis of rocks using laser induced breakdown spectroscopy. *Icarus*, 215(2), 608–627. <https://doi.org/10.1016/j.icarus.2011.07.034>
- Arvidson, R. E., Bell, J. F., Bellutta, P., Cabrol, N. A., Catalano, J. G., Cohen, J., et al. (2010). Spirit Mars Rover Mission: Overview and selected results from the northern Home Plate Winter Haven to the side of Scamander crater. *Journal of Geophysical Research: Planets*, 115(E7). <https://doi.org/10.1029/2010JE003633>
- Beegle, L., Bhartia, R., White, M., DeFlores, L., Abbey, W., Wu, Y.-H., et al. (2015). SHERLOC: Scanning habitable environments with Raman amp; luminescence for organics amp; chemicals. In *2015 IEEE Aerospace Conference* (pp. 1–11). <https://doi.org/10.1109/AERO.2015.7119105>
- Beegle, L. W., Bhartia, R., DeFlores, L., Miller, E., Pollack, R., Abbey, W., & Carrier, B. (2016). SHERLOC: On the Road to Mars. Abstract #4117. Presented at the 3rd International Workshop on Instrumentation for Planetary Mission. Retrieved from <http://adsabs.harvard.edu/abs/2016LPICo1980.4117B>

- Beegle, L. W., Bhartia, R., Carrier, B., DeFlores, L., Abbey, W., Asher, S., et al. (2017). The SHERLOC Investigation. Abstract #2839. Presented at the 48th Lunar and Planetary Science Conference. Retrieved from <http://adsabs.harvard.edu/abs/2017LPI....48.2839B>
- Bell, J. F., Squyres, S. W., Herkenhoff, K. E., Maki, J. N., Arneson, H. M., Brown, D., et al. (2003). Mars Exploration Rover Athena Panoramic Camera (Pancam) investigation. *Journal of Geophysical Research: Planets*, 108(E12). <https://doi.org/10.1029/2003JE002070>
- Bell, J. F., Maki, J. N., Mehall, G. L., Ravine, M. A., & Caplinger, M. A. (2014). Mastcam-Z: A Geologic, Stereoscopic, and Multispectral Investigation on the NASA Mars-2020 Rover. Abstract #1151. Presented at the 2nd International Workshop on Instrumentation for Planetary Missions.
- Bell, J. F., Maki, J. N., Mehall, G. L., Ravine, M. A., Caplinger, M. A., & Mastcam-Z Team. (2016). Mastcam-Z: Designing a Geologic, Stereoscopic, and Multispectral Pair of Zoom Cameras for the NASA Mars 2020 Rover (Vol. 1980, p. 4126). Presented at the 3rd International Workshop on Instrumentation for Planetary Mission. Retrieved from <http://adsabs.harvard.edu/abs/2016LPICo1980.4126B>
- Berlman, I. B. (1971). Handbook of fluorescence spectra of aromatic compounds. *Acad. Press, New York*, 342.
- Beyssac, O., Bollinger, L., Avouac, J.-P., & Goffé, B. (2004). Thermal metamorphism in the lesser Himalaya of Nepal determined from Raman spectroscopy of carbonaceous material. *Earth and Planetary Science Letters*, 225(1), 233–241. <https://doi.org/10.1016/j.epsl.2004.05.023>
- Bibring, J.-P., Langevin, Y., Mustard, J. F., Poulet, F., Arvidson, R., Gendrin, A., et al. (2006). Global mineralogical and aqueous Mars history derived from OMEGA/Mars Express data. *Science*, 312(5772), 400–404.
- Buz, J., Ehlmann, B. L., Kinch, K., Madsen, M. B., Johnson, J. R., Rice, M. S., et al. (2019). Photometric characterization of Lucideon and Avian Technologies color standards including application for calibration of the Mastcam-Z instrument on the Mars 2020 rover. *Optical Engineering*, 58(2), 027108. <https://doi.org/10.1117/1.OE.58.2.027108>
- Clark, R. N., King, T. V. V., Klejwa, M., Swayze, G. A., & Vergo, N. (1990). High spectral resolution reflectance spectroscopy of minerals. *Journal of Geophysical Research: Solid Earth*, 95(B8), 12653–12680. <https://doi.org/10.1029/JB095iB08p12653>
- Clegg, S. M., Wiens, R. C., Anderson, R., Forni, O., Frydenvang, J., Lasue, J., et al. (2017). Recalibration of the Mars Science Laboratory ChemCam instrument with an expanded geochemical database. *Spectrochimica Acta Part B: Atomic Spectroscopy*, 129, 64–85. <https://doi.org/10.1016/j.sab.2016.12.003>
- Edgett, K. S., Ravine, M. A., Caplinger, M. A., Ghaemi, F. T., Schaffner, J. A., Malin, M. C., et al. (2009). The Mars Science Laboratory (MSL) Mars Hand Lens Imager (MAHLI) Flight Instrument. Abstract #1197. Presented at the 40th Lunar and Planetary Science Conference. Retrieved from <http://adsabs.harvard.edu/abs/2009LPI....40.1197E>
- Ehlmann, B. L., & Edwards, C. S. (2014). Mineralogy of the Martian Surface. *Annual Review of Earth and Planetary Sciences*, 42(1), 291–315. <https://doi.org/10.1146/annurev-earth-060313-055024>
- Ehlmann, B. L., Mustard, J. F., Murchie, S. L., Poulet, F., Bishop, J. L., Brown, A. J., et al. (2008). Orbital Identification of Carbonate-Bearing Rocks on Mars. *Science*, 322(5909), 1828–1832. <https://doi.org/10.1126/science.1164759>

- Farley, K. A. (2017). *Mars 2020 Mission*. Presented at the Mars Exploration Program Analysis Group Meeting.
- Farmer, J. D., & Des Marais, D. J. (1999). Exploring for a record of ancient Martian life. *Journal of Geophysical Research: Planets*, 104(E11), 26977–26995. <https://doi.org/10.1029/1998JE000540>
- Farrand, W. H., Bell, J. F., Johnson, J. R., Squyres, S. W., Soderblom, J., & Ming, D. W. (2006). Spectral variability among rocks in visible and near-infrared multispectral Pancam data collected at Gusev crater: Examinations using spectral mixture analysis and related techniques. *Journal of Geophysical Research: Planets*, 111(E2), E02S15. <https://doi.org/10.1029/2005JE002495>
- Fassett, C. I., & Head, J. W. (2005). Fluvial sedimentary deposits on Mars: Ancient deltas in a crater lake in the Nili Fossae region. *Geophysical Research Letters*, 32(14), L14201. <https://doi.org/10.1029/2005GL023456>
- Fouchet, T., Montmessin, F., Forni, O., Maurice, S., Wiens, R. C., Johnson, J. R., et al. (2015). The Infrared Investigation on the SuperCam Instrument for the Mars2020 Rover. Abstract #1736. Presented at the 46th Lunar and Planetary Science Conference. Retrieved from <http://adsabs.harvard.edu/abs/2015LPI....46.1736F>
- Frost, R. L., & Shurvell, H. F. (1997). Raman microprobe spectroscopy of halloysite. *Clays and Clay Minerals*, 45(1), 68–72.
- Gandin, A., & Capezzuoli, E. (2014). Travertine: Distinctive depositional fabrics of carbonates from thermal spring systems. *Sedimentology*, 61(1), 264–290. <https://doi.org/10.1111/sed.12087>
- Gasda, P. J., Haldeman, E. B., Wiens, R. C., Rapin, W., Bristow, T. F., Bridges, J. C., et al. (2017). In situ detection of boron by ChemCam on Mars. *Geophysical Research Letters*, 44(17), 8739–8748. <https://doi.org/10.1002/2017GL074480>
- Gasnault, O., Maurice, S., Wiens, R. C., Le Mouélic, S., Fischer, W. W., Caïs, P., et al. (2015). SuperCam Remote Micro-Imager on Mars 2020. Abstract #2990. Presented at the 46th Lunar and Planetary Science Conference. Retrieved from <http://adsabs.harvard.edu/abs/2015LPI....46.2990G>
- Gellert, R., Berger, J. A., Boyd, N., Brunet, C., Campbell, J. L., Curry, M., et al. (2013). Initial MSL APXS Activities and Observations at Gale Crater, Mars. Abstract#1432. Presented at the 44th Lunar and Planetary Science Conference. Retrieved from <http://adsabs.harvard.edu/abs/2013LPI....44.1432G>
- Golombek, M. P. (1997). The Mars Pathfinder Mission. *Journal of Geophysical Research: Planets*, 102(E2), 3953–3965. <https://doi.org/10.1029/96JE02805>
- Goudge, T. A., Mustard, J. F., Head, J. W., Fassett, C. I., & Wiseman, S. M. (2015). Assessing the mineralogy of the watershed and fan deposits of the Jezero crater paleolake system, Mars. *Journal of Geophysical Research: Planets*, 120(4), 2014JE004782. <https://doi.org/10.1002/2014JE004782>
- Grove, C. I. H. (1992, February 15). *Laboratory Reflectance Spectra of 160 Minerals, 0.4 to 2.5 Micrometers*. Retrieved from <https://ntrs.nasa.gov/search.jsp?R=20070030855>
- Hillhouse, J. W. (1987). *Late Tertiary and Quaternary Geology of the Tecopa Basin, Southeastern California* (No. USGS/Map/I--1728). Geological Survey, Reston, VA (United States). <https://doi.org/10.2172/60181>
- Hillier, S. (2016). Accurate quantitative analysis of clay and other minerals in sandstones by XRD: comparison of a Rietveld and a reference intensity ratio (RIR) method and the

- importance of sample preparation. *Clay Minerals*, 35(1), 291–302.
<https://doi.org/10.1180/000985500546666>
- Horgan, B. H. N., Cloutis, E. A., Mann, P., & Bell, J. F. (2014). Near-infrared spectra of ferrous mineral mixtures and methods for their identification in planetary surface spectra. *Icarus*, 234, 132–154. <https://doi.org/10.1016/j.icarus.2014.02.031>
- Hu, R., Kass, D. M., Ehlmann, B. L., & Yung, Y. L. (2015). Tracing the fate of carbon and the atmospheric evolution of Mars. *Nature Communications*, 6.
<https://doi.org/10.1038/ncomms10003>
- Hunt, G. R., & Salisbury, J. W. (1971). Visible and near infrared spectra of minerals and rocks. II. Carbonates. *Modern Geology*, 2, 23–30.
- Hunt, G. R., Salisbury, J. W., & Lenhoff, C. J. (1971). Visible and near infrared spectra of minerals and rocks. IV. sulphides and sulphates. *Modern Geology*, 3, 1–14.
- Jennings, C. W., Burnett, J. L., & Troxel, B. W. (1962). Geologic map of California : Trona sheet. Geologic, California Division of Mines and Geology.
- Johnson, J. R., Ruff, S. W., Moersch, J., Roush, T., Horton, K., Bishop, J., et al. (2001). Geological characterization of remote field sites using visible and infrared spectroscopy: Results from the 1999 Marsokhod field test. *Journal of Geophysical Research: Planets*, 7683–7711. <https://doi.org/10.1029/1999JE001149>@10.1002/(ISSN)2169-9100.MARSOK1
- Kennedy, M. J., Pevear, D. R., & Hill, R. J. (2002). Mineral Surface Control of Organic Carbon in Black Shale. *Science*, 295(5555), 657–660. <https://doi.org/10.1126/science.1066611>
- Klima, R. L., Dyar, D. M., & Pieters, C. M. (2011). Near-infrared spectra of clinopyroxenes: Effects of calcium content and crystal structure. *Meteoritics & Planetary Science*, 46(3), 379–395. <https://doi.org/10.1111/j.1945-5100.2010.01158.x>
- Lanza, N. L., Fischer, W. W., Wiens, R. C., Grotzinger, J., Ollila, A. M., Cousin, A., et al. (2014). High manganese concentrations in rocks at Gale crater, Mars. *Geophysical Research Letters*, 41(16), 5755–5763. <https://doi.org/10.1002/2014GL060329>
- Maki, J. N., McKinney, C. M., Sellar, R. G., Copley-Woods, D. S., Gruel, D. C., Nuding, D. L., et al. (2016). Enhanced Engineering Cameras (EECAMs) for the Mars 2020 Rover. Abstract#4132. Presented at the 3rd International Workshop on Instrumentation for Planetary Mission. Retrieved from <http://adsabs.harvard.edu/abs/2016LPICo1980.4132M>
- Malin, M. C., Ravine, M. A., Caplinger, M. A., Ghaemi, F. T., Schaffner, J. A., Maki, J. N., et al. (2017). The Mars Science Laboratory (MSL) Mast cameras and Descent imager: Investigation and instrument descriptions. *Earth and Space Science*, 4(8), 506–539.
<https://doi.org/10.1002/2016EA000252>
- Mason, J. F. (1948). Geology of the Tecopa Area, Southeastern California. *GSA Bulletin*, 59(4), 333–352. [https://doi.org/10.1130/0016-7606\(1948\)59\[333:GOTTAS\]2.0.CO;2](https://doi.org/10.1130/0016-7606(1948)59[333:GOTTAS]2.0.CO;2)
- Maurice, S., Wiens, R. C., Saccoccio, M., Barraclough, B., Gasnault, O., Forni, O., et al. (2012). The ChemCam Instrument Suite on the Mars Science Laboratory (MSL) Rover: Science Objectives and Mast Unit Description. *Space Science Reviews*, 170(1), 95–166.
<https://doi.org/10.1007/s11214-012-9912-2>
- Morris, R. V., Lauer, H. V., Lawson, C. A., Gibson, E. K., Nace, G. A., & Stewart, C. (1985). Spectral and other physicochemical properties of submicron powders of hematite (α -Fe₂O₃), maghemite (γ -Fe₂O₃), magnetite (Fe₃O₄), goethite (α -FeOOH), and lepidocrocite (γ -FeOOH). *Journal of Geophysical Research: Solid Earth*, 90(B4), 3126–3144. <https://doi.org/10.1029/JB090iB04p03126>

- Mustard, J. F., Adler, M., Allwood, A. C., Bass, D. S., Beaty, D. W., Bell, J. F., et al. (2013). Report of the Mars 2020 Science Definition Team. *Mars Exploration Program Analysis Group*, 154.
- Nakamoto, K. (2008). *Infrared and Raman Spectra of Inorganic and Coordination Compounds, Part A: Theory and Applications in Inorganic Chemistry*. John Wiley & Sons.
- Pavlov, A. A., Vasilyev, G., Ostryakov, V. M., Pavlov, A. K., & Mahaffy, P. (2012). Degradation of the organic molecules in the shallow subsurface of Mars due to irradiation by cosmic rays. *Geophysical Research Letters*, 39(13).
<https://doi.org/10.1029/2012GL052166>
- Payré, V., Fabre, C., Cousin, A., Sautter, V., Wiens, R. C., Forni, O., et al. (2017). Alkali trace elements in Gale crater, Mars, with ChemCam: Calibration update and geological implications. *Journal of Geophysical Research: Planets*, 122(3), 650–679.
<https://doi.org/10.1002/2016JE005201>
- Rapin, W., Meslin, P.-Y., Maurice, S., Wiens, R. C., Laporte, D., Chauviré, B., et al. (2017). Quantification of water content by laser induced breakdown spectroscopy on Mars. *Spectrochimica Acta Part B: Atomic Spectroscopy*, 130, 82–100.
<https://doi.org/10.1016/j.sab.2017.02.007>
- Rice, M. S., Bell, J. F., Cloutis, E. A., Wang, A., Ruff, S. W., Craig, M. A., et al. (2010). Silica-rich deposits and hydrated minerals at Gusev Crater, Mars: Vis-NIR spectral characterization and regional mapping. *Icarus*, 205(2), 375–395.
<https://doi.org/10.1016/j.icarus.2009.03.035>
- Rieder, R., Gellert, R., Brückner, J., Klingelhöfer, G., Dreibus, G., Yen, A., & Squyres, S. W. (2003). The new Athena alpha particle X-ray spectrometer for the Mars Exploration Rovers. *Journal of Geophysical Research: Planets*, 108(E12), 8066.
<https://doi.org/10.1029/2003JE002150>
- Rivera-Hernández, F., Sumner, D. Y., Mangold, N., Stack, K. M., Forni, O., Newsom, H., et al. (2018). Using ChemCam LIBS data to constrain grain size in rocks on Mars: Proof of concept and application to rocks at Yellowknife Bay and Pahrump Hills, Gale crater. *Icarus*, 321, 82–98. <https://doi.org/10.1016/j.icarus.2018.10.023>
- Schofield, R. E., Hurowitz, J. A., Parise, J. B., Zhong, H., Allwood, A., Flannery, D., & Hodyss, R. (2017). Using Diffraction Peaks in X-Ray Fluorescence Spectra from the Mars 2020 PIXL Instrument for Mineral Phase Identification. Abstract # 2955. Presented at the 48th Lunar and Planetary Science Conference. Retrieved from <http://adsabs.harvard.edu/abs/2017LPI....48.2955S>
- Schopf, J. W., Farmer, J. D., Foster, I. S., Kudryavtsev, A. B., Gallardo, V. A., & Espinoza, C. (2012). Gypsum-Permineralized Microfossils and Their Relevance to the Search for Life on Mars. *Astrobiology*, 12(7), 619–633. <https://doi.org/10.1089/ast.2012.0827>
- Smith, P. H., Tomasko, M. G., Britt, D., Crowe, D. G., Reid, R., Keller, H. U., et al. (1997). The imager for Mars Pathfinder experiment. *Journal of Geophysical Research: Planets*, 102(E2), 4003–4025. <https://doi.org/10.1029/96JE03568>
- Socrates, G. (2004). *Infrared and Raman Characteristic Group Frequencies: Tables and Charts*. John Wiley & Sons.
- Summons, R. E., Albrecht, P., McDonald, G., & Moldowan, J. M. (2008). Molecular Biosignatures. *Space Science Reviews*, 135(1–4), 133–159.
<https://doi.org/10.1007/s11214-007-9256-5>

- Thomas, N. H., Ehlmann, B. L., Anderson, D. E., Clegg, S. M., Forni, O., Schröder, S., et al. (2018). Characterization of Hydrogen in Basaltic Materials With Laser-Induced Breakdown Spectroscopy (LIBS) for Application to MSL ChemCam Data. *Journal of Geophysical Research: Planets*, *In Press*. <https://doi.org/10.1029/2017JE005467>
- Thomas, N. H., Ehlmann, B. L., Meslin, P.-Y., Rabin, W., Anderson, D. E., Rivera-Hernández, F., et al. (2019). Mars Science Laboratory Observations of Chloride Salts in Gale Crater, Mars. *Geophysical Research Letters*, *0*(in press). <https://doi.org/10.1029/2019GL082764>
- Van Gorp, B., Mouroulis, P., Blaney, D., Green, R. O., Ehlmann, B. L., & Rodriguez, J. I. (2014). Ultra-compact imaging spectrometer for remote, in situ, and microscopic planetary mineralogy. *Journal of Applied Remote Sensing*, *8*(1), Art. No. 084988.
- Wang, A., Freeman, J. J., & Jolliff, B. L. (2015). Understanding the Raman spectral features of phyllosilicates. *Journal of Raman Spectroscopy*, *46*(10), 829–845. <https://doi.org/10.1002/jrs.4680>
- Wiens, R.C., Maurice, S., & Perez, F. R. (2017). The SuperCam Remote Sensing Instrument Suite for the Mars 2020 Rover: A Preview. *Spectroscopy Online*, *32*(5), 50–55.
- Wiens, Roger C., Maurice, S., Barraclough, B., Saccoccio, M., Barkley, W. C., Bell, J. F., et al. (2012). The ChemCam Instrument Suite on the Mars Science Laboratory (MSL) Rover: Body Unit and Combined System Tests. *Space Science Reviews*, *170*(1), 167–227. <https://doi.org/10.1007/s11214-012-9902-4>
- Williford, K. H., Farley, K. A., Stack, K. M., Allwood, A. C., Beaty, D., Beegle, L. W., et al. (2018). Chapter 11 - The NASA Mars 2020 Rover Mission and the Search for Extraterrestrial Life. In N. A. Cabrol & E. A. Grin (Eds.), *From Habitability to Life on Mars* (pp. 275–308). Elsevier. <https://doi.org/10.1016/B978-0-12-809935-3.00010-4>

Chapter 3

- Amirkhanoff, K. I., S. Brandt, and E. Bartnitsky (1961), Radiogenic argon in minerals and its migration, *Annals of the New York Academy of Sciences*, *91*(1), 235–275.
- Anderson, R. C., L. Jandura, A. Okon, D. Sunshine, C. Roumeliotis, L. Beegle, J. Hurowitz, B. Kennedy, D. Limonadi, and S. McCloskey (2012), Collecting samples in Gale Crater, Mars; an overview of the Mars Science Laboratory sample acquisition, sample processing and handling system, *Space Science Reviews*, *170*(1-4), 57-75.
- Bibring, J.-P., Y. Langevin, J. F. Mustard, F. Poulet, R. Arvidson, A. Gendrin, B. Gondet, N. Mangold, P. Pinet, and F. Forget (2006), Global mineralogical and aqueous Mars history derived from OMEGA/Mars Express data, *Science*, *312*(5772), 400-404.
- Bischoff, J. L. (1972), A ferroan nontronite from the Red Sea geothermal system, *Clays and Clay Minerals*, *20*(4), 217-223.
- Bish, D. L., D. Blake, D. Vaniman, S. Chipera, R. Morris, D. Ming, A. Treiman, P. Sarrazin, S. Morrison, and R. T. Downs (2013), X-ray diffraction results from Mars Science Laboratory: Mineralogy of Rocknest at Gale crater, *Science*, *341*(6153), 1238932.
- Blake, D. F., R. V. Morris, G. Kocurek, S. Morrison, R. T. Downs, D. Bish, D. Ming, K. Edgett, D. Rubin, and W. Goetz (2013), Curiosity at Gale crater, Mars: Characterization and analysis of the Rocknest sand shadow, *Science*, *341*(6153), 1239505.

- Bogard, D., L. Husain, and L. Nyquist (1979), 40Ar-39Ar age of the Shergotty achondrite and implications for its post-shock thermal history, *Geochimica et Cosmochimica Acta*, 43(7), 1047-1055.
- Bridges, J. C., S. Schwenzer, R. Leveille, F. Westall, R. Wiens, N. Mangold, T. Bristow, P. Edwards, and G. Berger (2015), Diagenesis and clay mineral formation at Gale Crater, Mars, *Journal of Geophysical Research: Planets*, 120(1), 1-19.
- Bristow, T. F., D. L. Bish, D. T. Vaniman, R. V. Morris, D. F. Blake, J. P. Grotzinger, E. B. Rampe, J. A. Crisp, C. N. Achilles, and D. W. Ming (2015), The origin and implications of clay minerals from Yellowknife Bay, Gale crater, Mars, *American Mineralogist*, 100(4), 824-836.
- Brophy, G. P., and M. F. Sheridan (1965), Sulfate Studies IV: The Jarosite-Natrojarosite-Hydronium Jarosite Solid Solution Series, *American Mineralogist*, 50, 1595-1607.
- Cannon, K. M., and J. F. Mustard (2015), Preserved glass-rich impactites on Mars, *Geology*, 43(7), 635-638.
- Cassata, W. S., P. R. Renne, and D. L. Shuster (2009), Argon diffusion in plagioclase and implications for thermochronometry: a case study from the Bushveld Complex, South Africa, *Geochimica et Cosmochimica Acta*, 73(21), 6600-6612.
- Cassata, W. S., P. R. Renne, and D. L. Shuster (2011), Argon diffusion in pyroxenes: implications for thermochronometry and mantle degassing, *Earth and Planetary Science Letters*, 304(3), 407-416.
- Changela, H., and J. Bridges (2010), Alteration assemblages in the nakhlites: Variation with depth on Mars, *Meteoritics & Planetary Science*, 45(12), 1847-1867.
- Deer, W. A., R. A. Howie, and J. Zussman (1997), Rock-Forming Minerals: Single-Chain Silicates, Volume 2A, Geological Society of London.
- Dehouck, E., S. M. McLennan, P. Y. Meslin, and A. Cousin (2014), Constraints on abundance, composition, and nature of X-ray amorphous components of soils and rocks at Gale crater, Mars, *Journal of Geophysical Research: Planets*, 119(12), 2640-2657.
- Dekov, V. M., G. D. Kamenov, J. Stummeyer, M. Thiry, C. Savelli, W. C. Shanks, D. Fortin, E. Kuzmann, and A. Vértés (2007), Hydrothermal nontronite formation at Eolo seamount (Aeolian volcanic arc, Tyrrhenian Sea), *Chemical Geology*, 245(1), 103-119.
- Dutrizac, J. (1983), Factors affecting alkali jarosite precipitation, *Metallurgical Transactions B*, 14(4), 531-539.
- Dutrizac, J. (2008), Factors affecting the precipitation of potassium jarosite in sulfate and chloride media, *Metallurgical and Materials Transactions B*, 39(6), 771-783.
- Ehlmann, B. L., and J. Buz (2015), Mineralogy and fluvial history of the watersheds of Gale, Knobel, and Sharp craters: A regional context for the Mars Science Laboratory Curiosity's exploration, *Geophysical Research Letters*, 42(2), 264-273.
- Ehlmann, B. L., J. F. Mustard, S. L. Murchie, J.-P. Bibring, A. Meunier, A. A. Fraeman, and Y. Langevin (2011), Subsurface water and clay mineral formation during the early history of Mars, *Nature*, 479(7371), 53-60.
- Evernden, J. F., G. H. Curtis, R. Kistler, and J. Obradovich (1960), Argon diffusion in glauconite, microcline, sanidine, leucite and phlogopite, *American Journal of Science*, 258(8), 583-604.
- Farley, K., C. Malespin, P. Mahaffy, J. Grotzinger, P. Vasconcelos, R. Milliken, M. Malin, K. Edgett, A. Pavlov, and J. Hurowitz (2014), In situ radiometric and exposure age dating of the Martian surface, *Science*, 343(6169), 1247166.

- Fassett, C. I., and J. W. Head (2008), The timing of martian valley network activity: Constraints from buffered crater counting, *Icarus*, 195(1), 61-89.
- Freissinet, C., D. Glavin, P. R. Mahaffy, K. Miller, J. Eigenbrode, R. Summons, A. Brunner, A. Buch, C. Szopa, and P. Archer (2015), Organic molecules in the sheepbed mudstone, Gale crater, mars, *Journal of Geophysical Research: Planets*, 120(3), 495-514.
- Gellert, R., J. Berger, N. Boyd, J. Campbell, E. Desouza, B. Elliott, M. Fisk, B. Pavri, G. Perrett, M. Schmidt, L. Thompson, S. VanBommel, and A. Yen. (2015), Chemical evidence for an aqueous history at pahrump, Gale Crater, Mars, as seen by the APXS, *Lunar and Planetary Science Conference*, Abstract #1855.
- Glavin, D. P., C. Freissinet, K. E. Miller, J. L. Eigenbrode, A. E. Brunner, A. Buch, B. Sutter, P. D. Archer, S. K. Atreya, and W. B. Brinckerhoff (2013), Evidence for perchlorates and the origin of chlorinated hydrocarbons detected by SAM at the Rocknest aeolian deposit in Gale Crater, *Journal of Geophysical Research: Planets*, 118(10), 1955-1973.
- Gombosi, D. J., S. L. Baldwin, E. B. Watson, T. D. Swindle, J. W. Delano, and W. G. Roberge (2015), Argon diffusion in Apollo 16 impact glass spherules: Implications for 40 Ar/39 Ar dating of lunar impact events, *Geochimica et Cosmochimica Acta*, 148, 251-268.
- Grant, J. A., S. A. Wilson, N. Mangold, F. Calef, and J. P. Grotzinger (2014), The timing of alluvial activity in Gale crater, Mars, *Geophysical Research Letters*, 41(4), 1142-1149.
- Grotzinger, J., S. Gupta, M. Malin, D. Rubin, J. Schieber, K. Siebach, D. Sumner, K. Stack, A. Vasavada, and R. Arvidson (2015), Deposition, exhumation, and paleoclimate of an ancient lake deposit, Gale crater, Mars, *Science*, 350(6257), aac7575.
- Grotzinger, J. P., D. Y. Sumner, L. Kah, K. Stack, S. Gupta, L. Edgar, D. Rubin, K. Lewis, J. Schieber, and N. Mangold (2014), A habitable fluvio-lacustrine environment at Yellowknife Bay, Gale Crater, Mars, *Science*, 343(6169), 1242777.
- Halliday, A. (1978), ⁴⁰Ar-³⁹Ar stepheating studies of clay concentrates from Irish orebodies, *Geochimica et Cosmochimica Acta*, 42(12), 1851-1858.
- Hamilton, P., S. Kelley, and A. E. Fallick (1989), K-Ar dating of illite in hydrocarbon reservoirs, *Clay Minerals*, 24(2), 215-231.
- Hartmann, W., and I. Daubar (2017), Martian cratering 11. Utilizing decameter scale crater populations to study Martian history, *Meteoritics & Planetary Science*, 52(3), 493-510.
- Hartmann, W. K. (2005), Martian cratering 8: Isochron refinement and the chronology of Mars, *Icarus*, 174(2), 294-320.
- Hartmann, W. K., and G. Neukum (2001), Cratering chronology and the evolution of Mars, *Space Science Reviews*, 96(1), 165-194.
- Hassanipak, A., and J. Wampler (1996), Radiogenic argon released by stepwise heating of glauconite and illite: The influence of composition and particle size, *Clays and Clay Minerals*, 44(6), 717-726.
- Hicks, L. J., J. C. Bridges, and S. Gurman (2014), Ferric saponite and serpentine in the nakhlite martian meteorites, *Geochimica et Cosmochimica Acta*, 136, 194-210.
- Humayun, M., A. Nemchin, B. Zanda, R. Hewins, M. Grange, A. Kennedy, J. Lorand, C. Göpel, C. Fieni, and S. Pont (2013), Origin and age of the earliest Martian crust from meteorite NWA7533, *Nature*, 503(7477), 513-516.
- Kula, J., and S. L. Baldwin (2011), Jarosite, argon diffusion, and dating aqueous mineralization on Earth and Mars, *Earth and Planetary Science Letters*, 310(3), 314-318.

- Le Deit, L., E. Hauber, F. Fueten, N. Mangold, M. Pondrelli, A. Rossi, and R. Jaumann (2012), Model Age of Gale Crater and Origin of its Layered Deposits, *LPI Contributions*, 1680, 7045.
- Lee, M. R., and E. Chatzitheodoridis (2016), Replacement of glass in the Nakhla meteorite by berthierine: Implications for understanding the origins of aluminum-rich phyllosilicates on Mars, *Meteoritics & Planetary Science*, 51(9), 1643-1653.
- Leitner, C., F. Neubauer, J. Genser, S. Borojević-Šoštarić, and G. Rantitsch (2014), $^{40}\text{Ar}/^{39}\text{Ar}$ ages of crystallization and recrystallization of rock-forming polyhalite in Alpine rocksalt deposits, *Geological Society, London, Special Publications*, 378(1), 207-224.
- Lofgren, G. (1970), Experimental devitrification rate of rhyolite glass, *Geological Society of America Bulletin*, 81(2), 553-560.
- Madden, M. E., R. Bodnar, and J. Rimstidt (2004), Jarosite as an indicator of water-limited chemical weathering on Mars, *Nature*, 431(7010), 821-823.
- Mahaffy, P. R., C. R. Webster, M. Cabane, P. G. Conrad, P. Coll, S. K. Atreya, R. Arvey, M. Barciniak, M. Benna, and L. Bleacher (2012), The sample analysis at Mars investigation and instrument suite, *Space Science Reviews*, 170(1-4), 401-478.
- Martín-Torres, F. J., M.-P. Zorzano, P. Valentín-Serrano, A.-M. Harri, M. Genser, O. Kemppinen, E. G. Rivera-Valentin, I. Jun, J. Wray, and M. B. Madsen (2015), Transient liquid water and water activity at Gale crater on Mars, *Nature Geoscience*, 8(5), 357-361.
- Morrison, S. M., R. T. Downs, D. F. Blake, D. T. Vaniman, D. W. Ming, R. M. Hazen, A. H. Treiman, C. N. Achilles, A. S. Yen, R. V. Morris, E. B. Rampe, T. F. Bristow, S. J. Chipera, P. C. Sarrazin, R. Gellert, K. V. Fendrich, J. M. Morookian, J. D. Farmer, D. J. Des Marais, and P. I. Craig (2017), Crystal chemistry of martian minerals from Bradbury Landing through Naukluft Plateau, Gale crater, Mars, *American Mineralogist*, 10.2138/am-2018-6123.
- McAdam, A., B. Sutter, H. Franz, J. Hogancamp, C. Knudson, S. Andrejkovicova, P. Archer, J. Eigenbrode, D. Ming, and P. Mahaffy (2017), Constraints on the Mineralogy of Gale Crater Mudstones from MSL SAM Evolved Water, *Lunar and Planetary Sciences Conference*, Abstract # 1853.
- McBride, M., M. Manitti, K. Stack, R. Yingst, K. Edgett, W. Goetz, K. Herkenhoff, E. Heydari, L. Kah, S. Rowland, J. Schieber, D. Harker, M. R. Kennedy, G. M. Krezoski, L. Lipkamin, B. Nixon, and J. Van Beek (2015), Mars Hand Lens Imager (MAHLI) Observations at the Pahrump Hills Field Site, Gale Crater, *Lunar and Planetary Science Conference*, Abstract # 2855.
- McEwen, A. S., C. M. Dundas, S. S. Mattson, A. D. Toigo, L. Ojha, J. J. Wray, M. Chojnacki, S. Byrne, S. L. Murchie, and N. Thomas (2014), Recurring slope lineae in equatorial regions of Mars, *Nature Geoscience*, 7(1), 53-58.
- McEwen, A. S., L. Ojha, C. M. Dundas, S. S. Mattson, S. Byrne, J. J. Wray, S. C. Cull, S. L. Murchie, N. Thomas, and V. C. Gulick (2011), Seasonal flows on warm Martian slopes, *Science*, 333(6043), 740-743.
- McEwen, A. S., B. S. Preblich, E. P. Turtle, N. A. Artemieva, M. P. Golombek, M. Hurst, R. L. Kirk, D. M. Burr, and P. R. Christensen (2005), The rayed crater Zunil and interpretations of small impact craters on Mars, *Icarus*, 176(2), 351-381.
- McSween, H. Y., and A. H. Treiman (1998), Martian meteorites, *Reviews in Mineralogy and Geochemistry*, 36(1), 6.1-6.53.

- Mees, F., C. Casteñeda, J. Herrero, and E. Van Ranst (2012), The nature and significance of variations in gypsum crystal morphology in dry lake basins, *Journal of Sedimentary Research*, 82(1), 41-56.
- Ming, D., P. Archer, D. Glavin, J. Eigenbrode, H. Franz, B. Sutter, A. Brunner, J. Stern, C. Freissinet, and A. McAdam (2014), Volatile and organic compositions of sedimentary rocks in Yellowknife Bay, Gale Crater, Mars, *Science*, 343(6169), 1245267.
- Minitti, M., L. Kah, R. Yingst, K. Edgett, R. Anderson, L. Beegle, J. Carsten, R. Deen, W. Goetz, and C. Hardgrove (2013), MAHLI at the Rocknest sand shadow: Science and science-enabling activities, *Journal of Geophysical Research: Planets*, 118(11), 2338-2360.
- Morris, R., E. Rampe, T. Graff, P. Archer Jr, L. Le, D. Ming, and B. Sutter (2015), Transmission X-ray diffraction (XRD) patterns relevant to the MSL CheMin amorphous component: Sulfates and silicates, *Lunar and Planetart Sciences Conference*, Abstract # 2434.
- Morris, R. V., D. Golden, J. F. Bell, T. D. Shelfer, A. C. Scheinost, N. W. Hinman, G. Furniss, S. A. Mertzman, J. L. Bishop, and D. W. Ming (2000), Mineralogy, composition, and alteration of Mars Pathfinder rocks and soils: Evidence from multispectral, elemental, and magnetic data on terrestrial analogue, SNC meteorite, and Pathfinder samples, *Journal of Geophysical Research: Planets*, 105(E1), 1757-1817.
- Nachon, M., S. Clegg, N. Mangold, S. Schröder, L. Kah, G. Dromart, A. Ollila, J. Johnson, D. Oehler, and J. Bridges (2014), Calcium sulfate veins characterized by ChemCam/Curiosity at Gale crater, Mars, *Journal of Geophysical Research: Planets*, 119(9), 1991-2016.
- Nachon, M., N. Mangold, O. Forni, L. C. Kah, A. Cousin, R. C. Wiens, R. Anderson, D. Blaney, J. G. Blank, and F. Calef (2017), Chemistry of diagenetic features analyzed by ChemCam at Pahrump Hills, Gale crater, Mars, *Icarus*, 281, 121-136.
- Nimmo, F., and K. Tanaka (2005), Early crustal evolution of Mars 1, *Annual Review of Earth and Planetary Sciences*, 33, 133-161.
- Nyquist, L., D. Bogard, C.-Y. Shih, A. Greshake, D. Stöffler, and O. Eugster (2001), Ages and geologic histories of Martian meteorites, *Space Science Reviews* 96, 105–164.
- Ojha, L., A. McEwen, C. Dundas, S. Byrne, S. Mattson, J. Wray, M. Masse, and E. Schaefer (2014), HiRISE observations of recurring slope lineae (RSL) during southern summer on Mars, *Icarus*, 231, 365-376.
- Ojha, L., M. B. Wilhelm, S. L. Murchie, A. S. McEwen, J. J. Wray, J. Hanley, M. Massé, and M. Chojnacki (2015), Spectral evidence for hydrated salts in recurring slope lineae on Mars, *Nature Geoscience*, 8(11), 829-832.
- Papike, J., J. Karner, C. Shearer, and P. Burger (2009), Silicate mineralogy of martian meteorites, *Geochimica et Cosmochimica Acta*, 73(24), 7443-7485.
- Rampe, E., D. Ming, D. Blake, T. Bristow, S. Chipera, J. Grotzinger, R. Morris, S. Morrison, D. Vaniman, A. Yen, C. Ach (2017), Mineralogy of an ancient lacustrine mudstone succession from the Murray formation, Gale crater, Mars, *Earth and Planetary Science Letters*, 471, 172–185.
- Renne, P. R., R. Mundil, G. Balco, K. Min, and K. R. Ludwig (2010), Joint determination of 40 K decay constants and $^{40}\text{Ar}^*/^{40}\text{K}$ for the Fish Canyon sanidine standard, and improved accuracy for $^{40}\text{Ar}/^{39}\text{Ar}$ geochronology, *Geochimica et Cosmochimica Acta*, 74(18), 5349-5367.

- Renne, P. R., W. D. Sharp, I. P. Montañez, T. A. Becker, and R. A. Zierenberg (2001), $^{40}\text{Ar}/^{39}\text{Ar}$ dating of Late Permian evaporites, southeastern New Mexico, USA, *Earth and Planetary Science Letters*, 193(3), 539-547.
- Robbins, S. J., I. Antonenko, M. R. Kirchoff, C. R. Chapman, C. I. Fassett, R. R. Herrick, K. Singer, M. Zanetti, C. Lehan, and D. Huang (2014), The variability of crater identification among expert and community crater analysts, *Icarus*, 234, 109-131.
- Schieber, J., D. Sumner, D. Bish, K. Stack, M. Minitti, A. Yingst, K. Edgett, M. Malin, and J. Grotzinger (2015), The Pahrump Succession in Gale Crater—A Potential Evaporite Bearing Lacustrine Mudstone with Resemblance to Earth Analogs, *Lunar and Planetary Science Conference*, Abstract # 2153.
- Schwenzer, S., O. Abramov, C. Allen, S. Clifford, C. Cockell, J. Filiberto, D. Kring, J. Lasue, P. McGovern, and H. Newsom (2012), Puncturing Mars: How impact craters interact with the Martian cryosphere, *Earth and Planetary Science Letters*, 335, 9-17.
- Siebach, K., M. Baker, J. Grotzinger, S. McLennan, R. Gellert, L. Thompson, and J. Hurowitz (2017), Sorting out compositional trends in sedimentary rocks of the Bradbury group (Aeolis Palus), Gale crater, Mars, *Journal of Geophysical Research: Planets*, 122(2), 295-328.
- Singer, R. B. (1985), Spectroscopic observation of Mars, *Advances in Space Research*, 5(8), 59-68.
- Smits, F., and W. Gentner (1950), Argonbestimmungen an kalium-mineralien I. Bestimmungen an tertiären kalisalzzen, *Geochimica et Cosmochimica Acta*, 1(1), 22-27.
- Stack, K., J. Grotzinger, L. Kah, M. Schmidt, N. Mangold, K. Edgett, D. Sumner, K. Siebach, M. Nachon, and R. Lee (2014), Diagenetic origin of nodules in the Sheepbed member, Yellowknife Bay formation, Gale crater, Mars, *Journal of Geophysical Research: Planets*, 119(7), 1637-1664.
- Sunshine, D. (2010), Mars science laboratory CHIMRA: a device for processing powdered Martian samples, *Technical Report for NASA*.
- Sutter, B., A. McAdam, P. Mahaffy, D. Ming, K. Edgett, E. Rampe, J. Eigenbrode, H. Franz, C. Freissinet, and J. Grotzinger (2017), Evolved Gas Analyses of Sedimentary Rocks and Eolian Sediment in Gale Crater, Mars: Results of the Curiosity Rover's Sample Analysis at Mars (SAM) Instrument from Yellowknife Bay to the Namib Dune, *Journal of Geophysical Research: Planets*, 10.1002/2016JE005225.
- Swindle, T., A. Treiman, D. Lindstrom, M. Burkland, B. Cohen, J. Grier, B. Li, and E. Olson (2000), Noble gases in iddingsite from the Lafayette meteorite: Evidence for liquid water on Mars in the last few hundred million years, *Meteoritics & Planetary Science*, 35(1), 107-115.
- Thomson, B., N. Bridges, R. Milliken, A. Baldrige, S. Hook, J. Crowley, G. Marion, C. de Souza Filho, A. Brown, and C. Weitz (2011), Constraints on the origin and evolution of the layered mound in Gale Crater, Mars using Mars Reconnaissance Orbiter data, *Icarus*, 214(2), 413-432.
- Treiman, A. H. (2005), The nakhlite meteorites: Augite-rich igneous rocks from Mars, *Chemie der Erde-Geochemistry*, 65(3), 203-270.
- Treiman, A. H., D. L. Bish, D. T. Vaniman, S. J. Chipera, D. F. Blake, D. W. Ming, R. V. Morris, T. F. Bristow, S. M. Morrison, and M. B. Baker (2016), Mineralogy, provenance, and diagenesis of a potassic basaltic sandstone on Mars: CheMin X-ray diffraction of the

- Windjana sample (Kimberley area, Gale Crater), *Journal of Geophysical Research: Planets*, 121(1), 75-106.
- Treiman, A. H., and J. Filiberto (2015), Geochemical diversity of shergottite basalts: Mixing and fractionation, and their relation to Mars surface basalts, *Meteoritics & Planetary Science*, 50(4), 632-648.
- Vaniman, D., D. Bish, D. Ming, T. Bristow, R. Morris, D. Blake, S. Chipera, S. Morrison, A. Treiman, and E. Rampe (2014), Mineralogy of a mudstone at Yellowknife Bay, Gale crater, Mars, *Science*, 343(6169), 1243480.
- Vasconcelos, P., K. Farley, C. Malespin, P. Mahaffy, D. Ming, S. McLennan, J. Hurowitz, and M. S. Rice (2016), Discordant K-Ar and young exposure dates for the Windjana sandstone, Kimberley, Gale Crater, Mars, *Journal of Geophysical Research: Planets*, 121(10), 2176-2192.
- Vasconcelos, P. M., G. H. Brimhall, T. A. Becker, and P. R. Renne (1994), 40Ar39Ar analysis of supergene jarosite and alunite: Implications to the paleoweathering history of the western USA and West Africa, *Geochimica et Cosmochimica Acta*, 58(1), 401-420.
- Wolff-Boenisch, D., S. R. Gislason, E. H. Oelkers, and C. V. Putnis (2004), The dissolution rates of natural glasses as a function of their composition at pH 4 and 10.6, and temperatures from 25 to 74 C, *Geochimica et Cosmochimica Acta*, 68(23), 4843-4858.

Chapter 4

- Armstrong, J. C., & Leovy, C. B. (2005). Long term wind erosion on Mars. *Icarus*, 176(1), 57–74. <https://doi.org/10.1016/j.icarus.2005.01.005>
- Arvidson, R., Guinness, E., & Lee, S. (1979). Differential aeolian redistribution rates on Mars. *Nature*, 278(5704), 533–535. <https://doi.org/10.1038/278533a0>
- Arvidson, R. E., Bell, J. F., Bellutta, P., Cabrol, N. A., Catalano, J. G., Cohen, J., et al. (2010). Spirit Mars Rover Mission: Overview and selected results from the northern Home Plate Winter Haven to the side of Scamander crater. *Journal of Geophysical Research: Planets*, 115(E7). <https://doi.org/10.1029/2010JE003633>
- Banham, S. G., Gupta, S., Rubin, D. M., Watkins, J. A., Sumner, D. Y., Edgett, K. S., et al. (2018). Ancient Martian aeolian processes and palaeomorphology reconstructed from the Stimson formation on the lower slope of Aeolis Mons, Gale crater, Mars. *Sedimentology*, 65(4), 993–1042. <https://doi.org/10.1111/sed.12469>
- Bridges, N. T., Greeley, R., Haldemann, A. F. C., Herkenhoff, K. E., Kraft, M., Parker, T. J., & Ward, A. W. (1999). Ventifacts at the Pathfinder landing site. *Journal of Geophysical Research: Planets*, 104(E4), 8595–8615. <https://doi.org/10.1029/98JE02550>
- Bridges, N. T., Calef, F. J., Hallet, B., Herkenhoff, K. E., Lanza, N. L., Mouélic, S. L., et al. (2014). The rock abrasion record at Gale Crater: Mars Science Laboratory results from Bradbury Landing to Rocknest. *Journal of Geophysical Research: Planets*, 119(6), 1374–1389. <https://doi.org/10.1002/2013JE004579>
- Bristow, T. F., Rampe, E. B., Achilles, C. N., Blake, D. F., Chipera, S. J., Craig, P., et al. (2018). Clay mineral diversity and abundance in sedimentary rocks of Gale crater, Mars. *Science Advances*, 4(6), eaar3330. <https://doi.org/10.1126/sciadv.aar3330>
- Carr, M. H., & Head, J. W. (2010). Geologic history of Mars. *Earth and Planetary Science Letters*, 294(3), 185–203. <https://doi.org/10.1016/j.epsl.2009.06.042>

- Caswell, T. E., & Milliken, R. E. (2017). Evidence for hydraulic fracturing at Gale crater, Mars: Implications for burial depth of the Yellowknife Bay formation. *Earth and Planetary Science Letters*, 468, 72–84. <https://doi.org/10.1016/j.epsl.2017.03.033>
- Cull, S. C., Arvidson, R. E., Catalano, J. G., Ming, D. W., Morris, R. V., Mellon, M. T., & Lemmon, M. (2010). Concentrated perchlorate at the Mars Phoenix landing site: Evidence for thin film liquid water on Mars. *Geophysical Research Letters*, 37(22). <https://doi.org/10.1029/2010GL045269>
- Dartnell, L. R., Desorgher, L., Ward, J. M., & Coates, A. J. (2007). Modelling the surface and subsurface Martian radiation environment: Implications for astrobiology. *Geophysical Research Letters*, 34(2). <https://doi.org/10.1029/2006GL027494>
- Day, M., & Kocurek, G. (2016). Observations of an aeolian landscape: From surface to orbit in Gale Crater. *Icarus*, 280, 37–71. <https://doi.org/10.1016/j.icarus.2015.09.042>
- Eugster, O., Herzog, G. F., Marti, K., & Caffee, M. W. (2006). Irradiation Records, Cosmic-Ray Exposure Ages, and Transfer Times of Meteorites. In *Meteorites and the Early Solar System II* (pp. 829–851). University of Arizona Press.
- Farley, K., Malespin, C., Mahaffy, P., Grotzinger, J., Vasconcelos, P., Milliken, R., et al. (2014). In situ radiometric and exposure age dating of the Martian surface. *Science*, 343(6169), 1247166.
- Farley, K., Martin, P., Archer, P., Atreya, S., Conrad, P., Eigenbrode, J., et al. (2016). Light and variable 37 Cl/35 Cl ratios in rocks from Gale Crater, Mars: Possible signature of perchlorate. *Earth and Planetary Science Letters*, 438, 14–24.
- Fraeman, A. A., Ehlmann, B. L., Arvidson, R. E., Edwards, C. S., Grotzinger, J. P., Milliken, R. E., et al. (2016). The stratigraphy and evolution of lower Mount Sharp from spectral, morphological, and thermophysical orbital data sets. *Journal of Geophysical Research: Planets*, 121(9), 1713–1736. <https://doi.org/10.1002/2016JE005095>
- Golombek, M. P., & Bridges, N. T. (2000). Erosion rates on Mars and implications for climate change: Constraints from the Pathfinder landing site. *Journal of Geophysical Research: Planets*, 105(E1), 1841–1853. <https://doi.org/10.1029/1999JE001043>
- Golombek, M. P., Grant, J. A., Crumpler, L. S., Greeley, R., Arvidson, R. E., Bell, J. F., et al. (2006). Erosion rates at the Mars Exploration Rover landing sites and long-term climate change on Mars. *Journal of Geophysical Research: Planets*, 111(E12). <https://doi.org/10.1029/2006JE002754>
- Golombek, M. P., Warner, N. H., Ganti, V., Lamb, M. P., Parker, T. J., Ferguson, R. L., & Sullivan, R. (2014). Small crater modification on Meridiani Planum and implications for erosion rates and climate change on Mars. *Journal of Geophysical Research: Planets*, 119(12), 2522–2547. <https://doi.org/10.1002/2014JE004658>
- Grant, J. A., Wilson, S. A., Mangold, N., Calef, F., & Grotzinger, J. P. (2014). The timing of alluvial activity in Gale crater, Mars. *Geophysical Research Letters*, 41(4), 1142–1149.
- Greeley, R., Arvidson, R. E., Barlett, P. W., Blaney, D., Cabrol, N. A., Christensen, P. R., et al. (2006). Gusev crater: Wind-related features and processes observed by the Mars Exploration Rover Spirit. *Journal of Geophysical Research: Planets*, 111(E2). <https://doi.org/10.1029/2005JE002491>
- Grindrod, P. M., & Warner, N. H. (2014). Erosion rate and previous extent of interior layered deposits on Mars revealed by obstructed landslides. *Geology*, 42(9), 795–798. <https://doi.org/10.1130/G35790.1>

- Grotzinger, J., Gupta, S., Malin, M., Rubin, D., Schieber, J., Siebach, K., et al. (2015). Deposition, exhumation, and paleoclimate of an ancient lake deposit, Gale crater, Mars. *Science*, 350(6257), aac7575.
- Hartmann, W. K., & Neukum, G. (2001). Cratering chronology and the evolution of Mars. *Space Science Reviews*, 96(1), 165–194.
- Jakosky, B. M., Pepin, R. O., Johnson, R. E., & Fox, J. L. (1994). Mars Atmospheric Loss and Isotopic Fractionation by Solar-Wind-Induced Sputtering and Photochemical Escape. *Icarus*, 111(2), 271–288. <https://doi.org/10.1006/icar.1994.1145>
- Kite, E. S., & Mayer, D. P. (2017). Mars sedimentary rock erosion rates constrained using crater counts, with applications to organic-matter preservation and to the global dust cycle. *Icarus*, 286, 212–222. <https://doi.org/10.1016/j.icarus.2016.10.010>
- Knoll, A. H., Jolliff, B. L., Farrand, W. H., Bell III, J. F., Clark, B. C., Gellert, R., et al. (2008). Veneers, rinds, and fracture fills: Relatively late alteration of sedimentary rocks at Meridiani Planum, Mars. *Journal of Geophysical Research*, 113(E6), E06S16. <https://doi.org/10.1029/2007JE002949>
- Lal, D. (1988). In Situ-Produced Cosmogenic Isotopes in Terrestrial Rocks. *Annual Review of Earth and Planetary Sciences*, 16(1), 355–388. <https://doi.org/10.1146/annurev.earth.16.050188.002035>
- Lal, D. (1991). Cosmic ray labeling of erosion surfaces: in situ nuclide production rates and erosion models. *Earth and Planetary Science Letters*, 104(2), 424–439. [https://doi.org/10.1016/0012-821X\(91\)90220-C](https://doi.org/10.1016/0012-821X(91)90220-C)
- Le Deit, L., Hauber, E., Fueten, F., Mangold, N., Pondrelli, M., Rossi, A., & Jaumann, R. (2012). Model Age of Gale Crater and Origin of its Layered Deposits. *LPI Contributions*, 1680, 7045.
- Malin, M. C., Edgett, K. S., Posiolova, L. V., McColley, S. M., & Dobra, E. Z. N. (2006). Present-Day Impact Cratering Rate and Contemporary Gully Activity on Mars. *Science*, 314(5805), 1573–1577. <https://doi.org/10.1126/science.1135156>
- Martin, P. E., Farley, K. A., Baker, M. B., Malespin, C. A., Schwenzer, S. P., Cohen, B. A., et al. (2017). A Two-Step K-Ar Experiment on Mars: Dating the Diagenetic Formation of Jarosite from Amazonian Groundwaters. *Journal of Geophysical Research: Planets*, 122(12), 2017JE005445. <https://doi.org/10.1002/2017JE005445>
- Meslin, P.-Y., Johnson, J. R., Forni, O., Beck, P., Cousin, A., Bridges, J., et al. (2017). Egg Rock Encounter: Analysis of an Iron-Nickel Meteorite Found in Gale Crater by Curiosity (Vol. 48, p. 2258). Presented at the Lunar and Planetary Science Conference. Retrieved from <http://adsabs.harvard.edu/abs/2017LPI...48.2258M>
- Milliken, R., Grotzinger, J., & Thomson, B. (2010). Paleoclimate of Mars as captured by the stratigraphic record in Gale Crater. *Geophysical Research Letters*, 37(4).
- Oró, J., & Holzer, G. (1979). The photolytic degradation and oxidation of organic compounds under simulated Martian conditions. *Journal of Molecular Evolution*, 14(1–3), 153–160. <https://doi.org/10.1007/BF01732374>
- Ozima, M., Takayanagi, M., Zashu, S., & Amari, S. (1984). High $^3\text{He}/^4\text{He}$ ratio in ocean sediments. *Nature*, 311(5985), 448–450. <https://doi.org/10.1038/311448a0>
- Palucis, M. C., Dietrich, W. E., Hayes, A. G., Williams, R. M. E., Gupta, S., Mangold, N., et al. (2014). The origin and evolution of the Peace Vallis fan system that drains to the Curiosity landing area, Gale Crater, Mars. *Journal of Geophysical Research: Planets*, 119(4), 705–728. <https://doi.org/10.1002/2013JE004583>

- Pavlov, A. A., Vasilyev, G., Ostryakov, V. M., Pavlov, A. K., & Mahaffy, P. (2012). Degradation of the organic molecules in the shallow subsurface of Mars due to irradiation by cosmic rays. *Geophysical Research Letters*, 39(13). <https://doi.org/10.1029/2012GL052166>
- Pepin, R. O., Palma, R. L., & Schlutter, D. J. (2000). Noble gases in interplanetary dust particles, I: The excess helium-3 problem and estimates of the relative fluxes of solar wind and solar energetic particles in interplanetary space. *Meteoritics & Planetary Science*, 35(3), 495–504. <https://doi.org/10.1111/j.1945-5100.2000.tb01431.x>
- Rampe, E. B., Ming, D. W., Blake, D. F., Bristow, T. F., Chipera, S. J., Grotzinger, J. P., et al. (2017). Mineralogy of an ancient lacustrine mudstone succession from the Murray formation, Gale crater, Mars. *Earth and Planetary Science Letters*, 471, 172–185. <https://doi.org/10.1016/j.epsl.2017.04.021>
- Stack, K. M., Edwards, C. S., Grotzinger, J. P., Gupta, S., Sumner, D. Y., Calef, F. J., et al. (2016). Comparing orbiter and rover image-based mapping of an ancient sedimentary environment, Aeolis Palus, Gale crater, Mars. *Icarus*, 280, 3–21. <https://doi.org/10.1016/j.icarus.2016.02.024>
- Sutter, B., McAdam, A. C., Mahaffy, P. R., Ming, D. W., Edgett, K. S., Rampe, E. B., et al. (2017). Evolved gas analyses of sedimentary rocks and eolian sediment in Gale Crater, Mars: Results of the Curiosity rover's sample analysis at Mars instrument from Yellowknife Bay to the Namib Dune. *Journal of Geophysical Research: Planets*, 122(12), 2574–2609. <https://doi.org/10.1002/2016JE005225>
- Thomas, N. H., Ehlmann, B. L., Meslin, P.-Y., Rapin, W., Anderson, D. E., Rivera-Hernández, F., et al. (2019). Mars Science Laboratory Observations of Chloride Salts in Gale Crater, Mars. *Geophysical Research Letters*, (in press). <https://doi.org/10.1029/2019GL082764>
- Thomson, B. J., Bridges, N. T., Milliken, R., Baldridge, A., Hook, S. J., Crowley, J. K., et al. (2011). Constraints on the origin and evolution of the layered mound in Gale Crater, Mars using Mars Reconnaissance Orbiter data. *Icarus*, 214(2), 413–432. <https://doi.org/10.1016/j.icarus.2011.05.002>
- VanBommel, S. J., Gellert, R., Clark, B. C., & Ming, D. W. (2018). Seasonal Atmospheric Argon Variability Measured in the Equatorial Region of Mars by the Mars Exploration Rover Alpha Particle X-Ray Spectrometers: Evidence for an Annual Argon-Enriched Front. *Journal of Geophysical Research: Planets*, 123(2), 544–558. <https://doi.org/10.1002/2017JE005454>
- Vasconcelos, P., Farley, K., Malespin, C., Mahaffy, P., Ming, D., McLennan, S., et al. (2016). Discordant K-Ar and young exposure dates for the Windjana sandstone, Kimberley, Gale Crater, Mars. *Journal of Geophysical Research: Planets*, 121(10), 2176–2192.
- Ward, A. W. (1979). Yardangs on Mars: Evidence of recent wind erosion. *Journal of Geophysical Research: Solid Earth*, 84(B14), 8147–8166. <https://doi.org/10.1029/JB084iB14p08147>
- Watkins, J. A., Grotzinger, J. P., Stein, N., Banham, S. G., Gupta, S., Rubin, D., et al. (2016). Paleotopography of Erosional Unconformity, Base of Stimson Formation, Gale Crater, Mars. Abstract #2939. Presented at the Lunar and Planetary Sciences Conference.
- Wieler, R. (2002). Cosmic-Ray-Produced Noble Gases in Meteorites. *Reviews in Mineralogy and Geochemistry*, 47(1), 125–170. <https://doi.org/10.2138/rmg.2002.47.5>

- Wieler, R., Beer, J., & Leya, I. (2013). The Galactic Cosmic Ray Intensity over the Past 106–109 Years as Recorded by Cosmogenic Nuclides in Meteorites and Terrestrial Samples. *Space Science Reviews*, 176(1), 351–363. <https://doi.org/10.1007/s11214-011-9769-9>
- Williams, J., Day, M., Chojnacki, M., & Rice, M. (2020). Scarp orientation in regions of active aeolian erosion on Mars. *Icarus*, 335, 113384. <https://doi.org/10.1016/j.icarus.2019.07.018>

Chapter 5

- Anderson, R. C., Jandura, L., Okon, A., Sunshine, D., Roumeliotis, C., Beegle, L., et al. (2012). Collecting samples in Gale Crater, Mars; an overview of the Mars Science Laboratory sample acquisition, sample processing and handling system. *Space Science Reviews*, 170(1–4), 57–75.
- Archer, P. D., Ming, D. W., Sutter, B., Morris, R. V., Clark, B. C., Mahaffy, P. H., et al. (2016). Oxychlorine Species on Mars: Implications from Gale Crater Samples. (Vol. 47, p. 2947). Presented at the Lunar and Planetary Sciences Conference.
- Archer, P. D., Ming, D. W., Sutter, B., Hogancamp, J. V., Morris, R., Clark, B. C., et al. (2019). Oxychlorine Detection in Gale Crater, Mars and Implications for Past Environmental Conditions, (2132), 2.
- Archer, Paul Douglas, Franz, H. B., Sutter, B., Arevalo, R. D., Coll, P., Eigenbrode, J. L., et al. (2014). Abundances and implications of volatile-bearing species from evolved gas analysis of the Rocknest aeolian deposit, Gale Crater, Mars. *Journal of Geophysical Research: Planets*, 119(1), 237–254. <https://doi.org/10.1002/2013JE004493>
- Arvidson, R. E., Bell, J. F., Bellutta, P., Cabrol, N. A., Catalano, J. G., Cohen, J., et al. (2010). Spirit Mars Rover Mission: Overview and selected results from the northern Home Plate Winter Haven to the side of Scamander crater. *Journal of Geophysical Research: Planets*, 115(E7). <https://doi.org/10.1029/2010JE003633>
- Atreya, S. K., & Gu, Z. G. (1994). Stability of the Martian atmosphere: Is heterogeneous catalysis essential? *Journal of Geophysical Research: Planets*, 99(E6), 13133–13145. <https://doi.org/10.1029/94JE01085>
- Atreya, S. K., Wong, A.-S., Renno, N. O., Farrell, W. M., Delory, G. T., Sentman, D. D., et al. (2006). Oxidant Enhancement in Martian Dust Devils and Storms: Implications for Life and Habitability. *Astrobiology*, 6(3), 439–450. <https://doi.org/10.1089/ast.2006.6.439>
- Biemann, K., & Bada, J. L. (2011). Comment on “Reanalysis of the Viking results suggests perchlorate and organics at midlatitudes on Mars” by Rafael Navarro-González et al. *Journal of Geophysical Research*, 116(E12). <https://doi.org/10.1029/2011JE003869>
- Birkner, N., & Navrotsky, A. (2012). Thermodynamics of manganese oxides: Effects of particle size and hydration on oxidation-reduction equilibria among hausmannite, bixbyite, and pyrolusite. *American Mineralogist*, 97(8–9), 1291–1298. <https://doi.org/10.2138/am.2012.3982>
- Blake, D. F., Morris, R. V., Kocurek, G., Morrison, S., Downs, R. T., Bish, D., et al. (2013). Curiosity at Gale crater, Mars: Characterization and analysis of the Rocknest sand shadow. *Science*, 341(6153), 1239505.

- Böhlke, J. K., Sturchio, N. C., Gu, B., Horita, J., Brown, G. M., Jackson, W. A., et al. (2005). Perchlorate Isotope Forensics. *Analytical Chemistry*, 77(23), 7838–7842. <https://doi.org/10.1021/ac051360d>
- Brennecka, G. A., Borg, L. E., & Wadhwa, M. (2014). Insights into the Martian mantle: The age and isotopics of the meteorite fall Tissint. *Meteoritics & Planetary Science*, 49(3), 412–418. <https://doi.org/10.1111/maps.12258>
- Bristow, T. F., Rampe, E. B., Achilles, C. N., Blake, D. F., Chipera, S. J., Craig, P., et al. (2018). Clay mineral diversity and abundance in sedimentary rocks of Gale crater, Mars. *Science Advances*, 4(6), eaar3330. <https://doi.org/10.1126/sciadv.aar3330>
- Brown, G. M. (1986). The reduction of chlorate and perchlorate ions at an active titanium electrode. *Journal of Electroanalytical Chemistry and Interfacial Electrochemistry*, 198(2), 319–330. [https://doi.org/10.1016/0022-0728\(86\)90008-2](https://doi.org/10.1016/0022-0728(86)90008-2)
- Brown, G. M., & Gu, B. (2006). The Chemistry of Perchlorate in the Environment. In B. Gu & J. D. Coates (Eds.), *Perchlorate: Environmental Occurrence, Interactions and Treatment* (pp. 17–47). Boston, MA: Springer US. https://doi.org/10.1007/0-387-31113-0_2
- Campbell, J. L., Perrett, G. M., Gellert, R., Andrushenko, S. M., Boyd, N. I., Maxwell, J. A., et al. (2012). Calibration of the Mars Science Laboratory Alpha Particle X-ray Spectrometer. *Space Science Reviews*, 170(1), 319–340. <https://doi.org/10.1007/s11214-012-9873-5>
- Cao, J., Elliott, D., & Zhang, W. (2005). Perchlorate Reduction by Nanoscale Iron Particles. *Journal of Nanoparticle Research*, 7(4–5), 499–506. <https://doi.org/10.1007/s11051-005-4412-x>
- Carrier, B. L., & Kounaves, S. P. (2015). The origins of perchlorate in the Martian soil. *Geophysical Research Letters*, 42(10), 3739–3745. <https://doi.org/10.1002/2015GL064290>
- Caswell, T. E., & Milliken, R. E. (2017). Evidence for hydraulic fracturing at Gale crater, Mars: Implications for burial depth of the Yellowknife Bay formation. *Earth and Planetary Science Letters*, 468, 72–84. <https://doi.org/10.1016/j.epsl.2017.03.033>
- Catling, D. C., Claire, M. W., Zahnle, K. J., Quinn, R. C., Clark, B. C., Hecht, M. H., & Kounaves, S. (2010). Atmospheric origins of perchlorate on Mars and in the Atacama. *Journal of Geophysical Research: Planets*, 115(E1). <https://doi.org/10.1029/2009JE003425>
- Chevrier, V. F., & Rivera-Valentin, E. G. (2012). Formation of recurring slope lineae by liquid brines on present-day Mars. *Geophysical Research Letters*, 39(21). <https://doi.org/10.1029/2012GL054119>
- Coates, J. D., & Achenbach, L. A. (2004). Microbial perchlorate reduction: rocket-fuelled metabolism. *Nature Reviews Microbiology*, 2(7), 569–580. <https://doi.org/10.1038/nrmicro926>
- Cull, S. C., Arvidson, R. E., Catalano, J. G., Ming, D. W., Morris, R. V., Mellon, M. T., & Lemmon, M. (2010). Concentrated perchlorate at the Mars Phoenix landing site: Evidence for thin film liquid water on Mars. *Geophysical Research Letters*, 37(22). <https://doi.org/10.1029/2010GL045269>
- Dehouck, E., McLennan, S. M., Meslin, P., & Cousin, A. (2014). Constraints on abundance, composition, and nature of X-ray amorphous components of soils and rocks at Gale crater, Mars. *Journal of Geophysical Research: Planets*, 119(12), 2640–2657.

- Eggenkamp, H. (2014). Natural Variations of Stable Chlorine and Bromine Isotopes on Earth. In *The Geochemistry of Stable Chlorine and Bromine Isotopes* (pp. 115–144). Springer, Berlin, Heidelberg. https://doi.org/10.1007/978-3-642-28506-6_10
- Eigenbrode, J. L., Summons, R. E., Steele, A., Freissinet, C., Millan, M., Navarro-González, R., et al. (2018). Organic matter preserved in 3-billion-year-old mudstones at Gale crater, Mars. *Science*, 360(6393), 1096–1101. <https://doi.org/10.1126/science.aas9185>
- Encrenaz, T., Bézard, B., Greathouse, T. K., Richter, M. J., Lacy, J. H., Atreya, S. K., et al. (2004). Hydrogen peroxide on Mars: evidence for spatial and seasonal variations. *Icarus*, 170(2), 424–429. <https://doi.org/10.1016/j.icarus.2004.05.008>
- Ericksen, G. E. (1981). *Geology and origin of the Chilean nitrate deposits* (USGS Numbered Series No. 1188). U.S. G.P.O. : for sale by the Supt. of Docs., GPO,. Retrieved from <http://pubs.er.usgs.gov/publication/pp1188>
- Farley, K., Malespin, C., Mahaffy, P., Grotzinger, J., Vasconcelos, P., Milliken, R., et al. (2014). In situ radiometric and exposure age dating of the Martian surface. *Science*, 343(6169), 1247166.
- Farley, K., Martin, P., Archer, P., Atreya, S., Conrad, P., Eigenbrode, J., et al. (2016). Light and variable 37 Cl/35 Cl ratios in rocks from Gale Crater, Mars: Possible signature of perchlorate. *Earth and Planetary Science Letters*, 438, 14–24.
- Farley, K. A., Reiners, P. W., & Nenow, V. (1999). An Apparatus for High-Precision Helium Diffusion Measurements from Minerals. *Analytical Chemistry*, 71(10), 2059–2061. <https://doi.org/10.1021/ac9813078>
- Gallagher, P. K., Johnson, D. W., & Schrey, F. (1970). Thermal Decomposition of Iron(II) Sulfates. *Journal of the American Ceramic Society*, 53(12), 666–670. <https://doi.org/10.1111/j.1151-2916.1970.tb12038.x>
- Gasnault, O., Mazoyer, J., Cousin, A., Meslin, P.-Y., Lasue, J., Lacour, J.-L., et al. (2012). Deciphering Sample and Atmospheric Oxygen Contents with ChemCam on Mars (Vol. 43, p. 2888). Presented at the Lunar and Planetary Science Conference. Retrieved from <http://adsabs.harvard.edu/abs/2012LPI....43.2888G>
- Glavin, D. P., Freissinet, C., Miller, K. E., Eigenbrode, J. L., Brunner, A. E., Buch, A., et al. (2013). Evidence for perchlorates and the origin of chlorinated hydrocarbons detected by SAM at the Rocknest aeolian deposit in Gale Crater. *Journal of Geophysical Research: Planets*, 118(10), 1955–1973.
- Gough, R. V., Chevrier, V. F., & Tolbert, M. A. (2014). Formation of aqueous solutions on Mars via deliquescence of chloride–perchlorate binary mixtures. *Earth and Planetary Science Letters*, 393, 73–82. <https://doi.org/10.1016/j.epsl.2014.02.002>
- Grotzinger, J., Gupta, S., Malin, M., Rubin, D., Schieber, J., Siebach, K., et al. (2015). Deposition, exhumation, and paleoclimate of an ancient lake deposit, Gale crater, Mars. *Science*, 350(6257), aac7575.
- Grotzinger, J. P., Sumner, D. Y., Kah, L., Stack, K., Gupta, S., Edgar, L., et al. (2014). A habitable fluvio-lacustrine environment at Yellowknife Bay, Gale Crater, Mars. *Science*, 343(6169), 1242777.
- Gu, B., Dong, W., Brown, G. M., & Cole, D. R. (2003). Complete Degradation of Perchlorate in Ferric Chloride and Hydrochloric Acid under Controlled Temperature and Pressure. *Environmental Science & Technology*, 37(10), 2291–2295. <https://doi.org/10.1021/es0262378>
- Hardie, L., Smoot, J., & Eugster, O. (1978). *Lake Sediments*. John Wiley & Sons.

- Hasegawa, M. (2014). Chapter 3.3 - Ellingham Diagram. In S. Seetharaman (Ed.), *Treatise on Process Metallurgy* (pp. 507–516). Boston: Elsevier. <https://doi.org/10.1016/B978-0-08-096986-2.00032-1>
- Hecht, M. H., Kounaves, S. P., Quinn, R. C., West, S. J., Young, S. M. M., Ming, D. W., et al. (2009). Detection of Perchlorate and the Soluble Chemistry of Martian Soil at the Phoenix Lander Site. *Science*, 325(5936), 64–67. <https://doi.org/10.1126/science.1172466>
- Hogancamp, J. V., Sutter, B., Archer, D., Jr., Ming, D. W., & Mahaffy, P. R. (2017). Oxychlorine and Chloride/Ferrian Saponite Mixtures as a Possible Source of Hydrochloric Acid Detected by the Sample Analysis at Mars (SAM) Instrument in Gale Crater, Mars. *AGU Fall Meeting Abstracts*, 51. Retrieved from <http://adsabs.harvard.edu/abs/2017AGUFM.P51H..09H>
- Hogancamp, J. V., Sutter, B., Morris, R. V., Archer, P. D., Ming, D. W., Rampe, E. B., et al. (2018). Chlorate/Fe-Bearing Phase Mixtures as a Possible Source of Oxygen and Chlorine Detected by the Sample Analysis at Mars (SAM) Instrument in Gale Crater, Mars. *Journal of Geophysical Research: Planets*, 123(11), 2920–2938. <https://doi.org/10.1029/2018JE005691>
- Hogancamp, J. V., Archer, P. D., Morris, R. V., Tu, V., Lanza, N., Sutter, B., et al. (2018). Detectability of Manganese-Bearing Phases by the Sample Analysis at Mars (SAM) Instrument On Board the Curiosity Rover in Gale Crater, Mars. Abstract #2482. Presented at the 49th Lunar and Planetary Science Conference. Retrieved from <http://adsabs.harvard.edu/abs/2018LPI....49.2482H>
- Holt, B. D., & Engelkemeir, A. G. (1970). Thermal decomposition of barium sulfate to sulfur dioxide for mass spectrometric analysis. *Analytical Chemistry*, 42(12), 1451–1453. <https://doi.org/10.1021/ac60294a032>
- Jackson, W. A., Böhlke, J. K., Andraski, B. J., Fahlquist, L., Bexfield, L., Eckardt, F. D., et al. (2015). Global patterns and environmental controls of perchlorate and nitrate co-occurrence in arid and semi-arid environments. *Geochimica et Cosmochimica Acta*, 164, 502–522. <https://doi.org/10.1016/j.gca.2015.05.016>
- Jaramillo, E. A., Royle, S. H., Claire, M. W., Kounaves, S. P., & Sephton, M. A. (2019). Indigenous Organic-Oxidized Fluid Interactions in the Tissint Mars Meteorite. *Geophysical Research Letters*, 46(6), 3090–3098. <https://doi.org/10.1029/2018GL081335>
- ten Kate, I. L. (2010). Organics on Mars? *Astrobiology*, 10(6), 589–603. <https://doi.org/10.1089/ast.2010.0498>
- Keppler, F., Harper, D. B., Greule, M., Ott, U., Sattler, T., Schöler, H. F., & Hamilton, J. T. G. (2014). Chloromethane release from carbonaceous meteorite affords new insight into Mars lander findings. *Scientific Reports*, 4. <https://doi.org/10.1038/srep07010>
- Kounaves, S. P., Stroble, S. T., Anderson, R. M., Moore, Q., Catling, D. C., Douglas, S., et al. (2010). Discovery of Natural Perchlorate in the Antarctic Dry Valleys and Its Global Implications. *Environmental Science & Technology*, 44(7), 2360–2364. <https://doi.org/10.1021/es9033606>
- Kounaves, S. P., Carrier, B. L., O’Neil, G. D., Stroble, S. T., & Claire, M. W. (2014). Evidence of martian perchlorate, chlorate, and nitrate in Mars meteorite EETA79001: Implications for oxidants and organics. *Icarus*, 229, 206–213. <https://doi.org/10.1016/j.icarus.2013.11.012>

- Kronyak, R. E., Kah, L. C., Edgett, K. S., VanBommel, S. J., Thompson, L. M., Wiens, R. C., et al. (2019). Mineral-Filled Fractures as Indicators of Multigenerational Fluid Flow in the Pahrump Hills Member of the Murray Formation, Gale Crater, Mars. *Earth and Space Science*, 6(2), 238–265. <https://doi.org/10.1029/2018EA000482>
- Lanza, N. L., Fischer, W. W., Wiens, R. C., Grotzinger, J., Ollila, A. M., Cousin, A., et al. (2014). High manganese concentrations in rocks at Gale crater, Mars. *Geophysical Research Letters*, 41(16), 5755–5763. <https://doi.org/10.1002/2014GL060329>
- Lanza, N. L., Wiens, R. C., Arvidson, R. E., Clark, B. C., Fischer, W. W., Gellert, R., et al. (2016). Oxidation of manganese in an ancient aquifer, Kimberley formation, Gale crater, Mars. *Geophysical Research Letters*, 43(14), 7398–7407. <https://doi.org/10.1002/2016GL069109>
- Lasne, J., Noblet, A., Szopa, C., Navarro-González, R., Cabane, M., Poch, O., et al. (2016). Oxidants at the Surface of Mars: A Review in Light of Recent Exploration Results. *Astrobiology*, 16(12), 977–996. <https://doi.org/10.1089/ast.2016.1502>
- Le Deit, L., Hauber, E., Fueten, F., Mangold, N., Pondrelli, M., Rossi, A., & Jaumann, R. (2012). Model Age of Gale Crater and Origin of its Layered Deposits. *LPI Contributions*, 1680, 7045.
- Leask, E. K., Ehlmann, B. L., Dundar, M., Murchie, S. L., & Seelos, F. P. (2018). Challenges in the Search for Perchlorate and Other Hydrated Minerals with 2.1- μm Absorptions on Mars. *Geophysical Research Letters*, 45(22), 12180–12189. <https://doi.org/10.1029/2018GL080077>
- Leshin, L. A., Mahaffy, P. R., Webster, C. R., Cabane, M., Coll, P., Conrad, P. G., et al. (2013). Volatile, Isotope, and Organic Analysis of Martian Fines with the Mars Curiosity Rover. *Science*, 341(6153), 1238937. <https://doi.org/10.1126/science.1238937>
- Lu, Y., Liu, S., Weng, L., Wang, L., Li, Z., & Xu, L. (2016). Fractal analysis of cracking in a clayey soil under freeze–thaw cycles. *Engineering Geology*, 208, 93–99. <https://doi.org/10.1016/j.enggeo.2016.04.023>
- Mahaffy, P. R., Webster, C. R., Cabane, M., Conrad, P. G., Coll, P., Atreya, S. K., et al. (2012). The sample analysis at Mars investigation and instrument suite. *Space Science Reviews*, 170(1–4), 401–478.
- Marion, G. M., Catling, D. C., Zahnle, K. J., & Claire, M. W. (2010). Modeling aqueous perchlorate chemistries with applications to Mars. *Icarus*, 207(2), 675–685. <https://doi.org/10.1016/j.icarus.2009.12.003>
- Martin, P. E., Farley, K. A., Baker, M. B., Malespin, C. A., Schwenzer, S. P., Cohen, B. A., et al. (2017a). A Two-Step K-Ar Experiment on Mars: Dating the Diagenetic Formation of Jarosite from Amazonian Groundwaters. *Journal of Geophysical Research: Planets*, 122(12), 2017JE005445. <https://doi.org/10.1002/2017JE005445>
- Martin, P., Farley, K. A., Mahaffy, P. R., Malespin, C., & Vasconcelos, P. M. (2017b). Landscape Evolution Mechanisms in Gale Crater from In-Situ Measurement of Cosmogenic Noble Gas Isotopes. *AGU Fall Meeting Abstracts*, 52. Retrieved from <http://adsabs.harvard.edu/abs/2017AGUFM.P52C..01M>
- McEwen, A. S., Ojha, L., Dundas, C. M., Mattson, S. S., Byrne, S., Wray, J. J., et al. (2011). Seasonal flows on warm Martian slopes. *Science*, 333(6043), 740–743.
- McKay, C. P., Stoker, C. R., Glass, B. J., Davé, A. I., Davila, A. F., Heldmann, J. L., et al. (2013). The Icebreaker Life Mission to Mars: A Search for Biomolecular Evidence for Life. *Astrobiology*, 13(4), 334–353. <https://doi.org/10.1089/ast.2012.0878>

- Ming, D., Archer, P., Glavin, D., Eigenbrode, J., Franz, H., Sutter, B., et al. (2014). Volatile and organic compositions of sedimentary rocks in Yellowknife Bay, Gale Crater, Mars. *Science*, 343(6169), 1245-1267.
- Mitra, K., & Catalano, J. G. (in press). Chlorate as a Potential Oxidant on Mars: Rates and Products of Dissolved Fe(II) Oxidation. *Journal of Geophysical Research: Planets*. <https://doi.org/10.1029/2019JE006133>
- Morrison, S. M., Downs, R. T., Blake, D. F., Vaniman, D. T., Ming, D. W., Hazen, R. M., et al. (2018). Crystal chemistry of martian minerals from Bradbury Landing through Naukluft Plateau, Gale crater, Mars. *American Mineralogist*, 103(6), 857–871. <https://doi.org/10.2138/am-2018-6124>
- Nachon, M., Clegg, S., Mangold, N., Schröder, S., Kah, L., Dromart, G., et al. (2014). Calcium sulfate veins characterized by ChemCam/Curiosity at Gale crater, Mars. *Journal of Geophysical Research: Planets*, 119(9), 1991–2016.
- Navarro-González, R., Vargas, E., de la Rosa, J., Raga, A. C., & McKay, C. P. (2010). Reanalysis of the Viking results suggests perchlorate and organics at midlatitudes on Mars. *Journal of Geophysical Research*, 115(E12). <https://doi.org/10.1029/2010JE003599>
- Navrotsky, A., Ma, C., Lillova, K., & Birkner, N. (2010). Nanophase Transition Metal Oxides Show Large Thermodynamically Driven Shifts in Oxidation-Reduction Equilibria. *Science*, 330(6001), 199–201. <https://doi.org/10.1126/science.1195875>
- Nyquist, L., Bogard, D., Shih, C.-Y., Greshake, A., Stöffler, D., & Eugster, O. (2001). Ages and geologic histories of Martian meteorites. In *Chronology and evolution of Mars* (pp. 105–164). Springer.
- Oehler, D. Z., Mangold, N., Hallet, B., Fairén, A. G., Deit, L. L., Williams, A. J., et al. (2016). Origin and significance of decameter-scale polygons in the lower Peace Vallis fan of Gale crater, Mars. *Icarus*, 277, 56–72. <https://doi.org/10.1016/j.icarus.2016.04.038>
- Ojha, L., Wilhelm, M. B., Murchie, S. L., McEwen, A. S., Wray, J. J., Hanley, J., et al. (2015). Spectral evidence for hydrated salts in recurring slope lineae on Mars. *Nature Geoscience*, 8(11), 829–832.
- Oren, A., Elevi Bardavid, R., & Mana, L. (2014). Perchlorate and halophilic prokaryotes: implications for possible halophilic life on Mars. *Extremophiles*, 18(1), 75–80. <https://doi.org/10.1007/s00792-013-0594-9>
- Orosei, R., Lauro, S. E., Pettinelli, E., Cicchetti, A., Coradini, M., Cosciotti, B., et al. (2018). Radar evidence of subglacial liquid water on Mars. *Science*, 361(6401), 490–493. <https://doi.org/10.1126/science.aar7268>
- Oyama, V. I., & Berdahl, B. J. (1977). The Viking Gas Exchange Experiment results from Chryse and Utopia surface samples. *Journal of Geophysical Research*, 82(28), 4669–4676. <https://doi.org/10.1029/JS082i028p04669>
- Pavlov, A. A., Vasilyev, G., Ostryakov, V. M., Pavlov, A. K., & Mahaffy, P. (2012). Degradation of the organic molecules in the shallow subsurface of Mars due to irradiation by cosmic rays. *Geophysical Research Letters*, 39(13). <https://doi.org/10.1029/2012GL052166>
- Post, J. E. (1999). Manganese oxide minerals: Crystal structures and economic and environmental significance. *Proceedings of the National Academy of Sciences*, 96(7), 3447–3454. <https://doi.org/10.1073/pnas.96.7.3447>

- Prince, L. A., & Johnson, E. R. (1965a). The Radiation—Induced Decomposition of the Alkali and Alkaline Earth Perchlorates. I. Product Yields and Stoichiometry ^{1a}. *The Journal of Physical Chemistry*, 69(2), 359–377. <https://doi.org/10.1021/j100886a002>
- Prince, L. A., & Johnson, E. R. (1965b). The Radiation—Induced Decomposition of the Alkali and Alkaline Earth Perchlorates. II. Mechanism of the Decomposition ^{1a}. *The Journal of Physical Chemistry*, 69(2), 377–384. <https://doi.org/10.1021/j100886a003>
- Quinn, R. C., Martucci, H. F. H., Miller, S. R., Bryson, C. E., Grunthaner, F. J., & Grunthaner, P. J. (2013). Perchlorate Radiolysis on Mars and the Origin of Martian Soil Reactivity. *Astrobiology*, 13(6), 515–520. <https://doi.org/10.1089/ast.2013.0999>
- Rampe, E., Ming, D., Blake, D., Bristow, T., Chipera, S., Grotzinger, J., et al. (2017). Mineralogy of an ancient lacustrine mudstone succession from the Murray formation, Gale crater, Mars. *Earth and Planetary Science Letters*.
- Rapin, W., Ehlmann, B. L., Dromart, G., Schieber, J., Thomas, N. H., Fischer, W. W., et al. (2019). An interval of high salinity in ancient Gale crater lake on Mars. *Nature Geoscience*, 12(11), 889–895. <https://doi.org/10.1038/s41561-019-0458-8>
- Smith, M. L., Claire, M. W., Catling, D. C., & Zahnle, K. J. (2014). The formation of sulfate, nitrate and perchlorate salts in the martian atmosphere. *Icarus*, 231, 51–64. <https://doi.org/10.1016/j.icarus.2013.11.031>
- Srinivasan, R., Sorial, G., & Sahle-Demessie, E. (2009). Removal of Perchlorate and Chlorate in Aquatic Systems Using Integrated Technologies. *Environmental Engineering Science*, 26(11), 1661–1671. <https://doi.org/10.1089/ees.2009.0153>
- Stack, K. M., Grotzinger, J. P., Lamb, M. P., Gupta, S., Rubin, D. M., Kah, L. C., et al. (2018). Evidence for plunging river plume deposits in the Pahrump Hills member of the Murray formation, Gale crater, Mars. *Sedimentology*, 66(5), 1768–1802. <https://doi.org/10.1111/sed.12558>
- Steele, A., Benning, L. G., Wirth, R., Siljeström, S., Fries, M. D., Hauri, E., et al. (2018). Organic synthesis on Mars by electrochemical reduction of CO₂. *Science Advances*, 4(10), eaat5118. <https://doi.org/10.1126/sciadv.aat5118>
- Stein, N., Grotzinger, J. P., Schieber, J., Mangold, N., Hallet, B., Newsom, H., et al. (2018). Desiccation cracks provide evidence of lake drying on Mars, Sutton Island member, Murray formation, Gale Crater. *Geology*, 46(6), 515–518. <https://doi.org/10.1130/G40005.1>
- Stern, J. C., Sutter, B., Freissinet, C., Navarro-González, R., McKay, C. P., Archer, P. D., et al. (2015). Evidence for indigenous nitrogen in sedimentary and aeolian deposits from the Curiosity rover investigations at Gale crater, Mars. *Proceedings of the National Academy of Sciences*, 201420932. <https://doi.org/10.1073/pnas.1420932112>
- Stern, J. C., Sutter, B., Jackson, W. A., Navarro-González, R., McKay, C. P., Ming, D. W., et al. (2017). The nitrate/(per)chlorate relationship on Mars. *Geophysical Research Letters*, 44(6), 2643–2651. <https://doi.org/10.1002/2016GL072199>
- Sutter, B., McAdam, A. C., Mahaffy, P. R., Ming, D. W., Edgett, K. S., Rampe, E. B., Eigenbrode, J. L., Franz, H. B., Freissinet, C., Grotzinger, J. P., et al. (2017). Evolved gas analyses of sedimentary rocks and eolian sediment in Gale Crater, Mars: Results of the Curiosity rover's sample analysis at Mars instrument from Yellowknife Bay to the Namib Dune. *Journal of Geophysical Research: Planets*, 122(12), 2574–2609. <https://doi.org/10.1002/2016JE005225>

- Taylor, G. J. (2013). The bulk composition of Mars. *Geochemistry*, 73(4), 401–420.
<https://doi.org/10.1016/j.chemer.2013.09.006>
- Taylor, G. J., Stopar, J. D., Boynton, W. V., Karunatillake, S., Keller, J. M., Brückner, J., et al. (2007). Variations in K/Th on Mars. *Journal of Geophysical Research*, 112(E3), E03S06.
<https://doi.org/10.1029/2006JE002676>
- Taylor, S. R., & McLennan, S. (2009). *Planetary Crusts: Their Composition, Origin and Evolution*. Cambridge University Press.
- Thomas, N. H., Ehlmann, B. L., Meslin, P.-Y., Cousin, A., Forni, O., Rapin, W., et al. (2018). MSL ChemCam Observations of Chloride Salts in Gale Crater, Mars. Abstract #2876. Presented at the 49th Lunar and Planetary Science Conference. Retrieved from <http://adsabs.harvard.edu/abs/2018LPI...49.2876T>
- Till, J. L., Guyodo, Y., Lagroix, F., Morin, G., & Ona-Nguema, G. (2015). Goethite as a potential source of magnetic nanoparticles in sediments. *Geology*, 43(1), 75–78.
<https://doi.org/10.1130/G36186.1>
- Toner, J. D., Catling, D. C., & Light, B. (2014). The formation of supercooled brines, viscous liquids, and low-temperature perchlorate glasses in aqueous solutions relevant to Mars. *Icarus*, 233, 36–47. <https://doi.org/10.1016/j.icarus.2014.01.018>
- Toner, J. D., Catling, D. C., & Light, B. (2015). A revised Pitzer model for low-temperature soluble salt assemblages at the Phoenix site, Mars. *Geochimica et Cosmochimica Acta*, 166, 327–343. <https://doi.org/10.1016/j.gca.2015.06.011>
- Tosca, N. J., McLennan, S. M., Clark, B. C., Grotzinger, J. P., Hurowitz, J. A., Knoll, A. H., et al. (2005). Geochemical modeling of evaporation processes on Mars: Insight from the sedimentary record at Meridiani Planum. *Earth and Planetary Science Letters*, 240(1), 122–148. <https://doi.org/10.1016/j.epsl.2005.09.042>
- Turner, A. M., Abplanalp, M. J., & Kaiser, R. I. (2016). Mechanistic Studies on the Radiolytic Decomposition of Perchlorates on the Martian Surface. *The Astrophysical Journal*, 820(2), 127. <https://doi.org/10.3847/0004-637X/820/2/127>
- Urbansky, E. T. (2002). Perchlorate as an environmental contaminant. *Environmental Science and Pollution Research*, 9(3), 187–192. <https://doi.org/10.1007/BF02987487>
- Van Schmus, W. R. (1995). Natural Radioactivity of the Crust and Mantle. In *Global Earth Physics* (pp. 283–291). American Geophysical Union (AGU).
<https://doi.org/10.1029/RF001p0283>
- Vaniman, D., Bish, D., Ming, D., Bristow, T., Morris, R., Blake, D., et al. (2014). Mineralogy of a mudstone at Yellowknife Bay, Gale crater, Mars. *Science*, 343(6169), 1243480.
- Vaniman, D. T., Martínez, G. M., Rampe, E. B., Bristow, T. F., Blake, D. F., Yen, A. S., et al. (2018). Gypsum, bassanite, and anhydrite at Gale crater, Mars. *American Mineralogist*, 103(7), 1011–1020. <https://doi.org/10.2138/am-2018-6346>
- Vasconcelos, P., Farley, K., Malespin, C., Mahaffy, P., Ming, D., McLennan, S., et al. (2016). Discordant K-Ar and young exposure dates for the Windjana sandstone, Kimberley, Gale Crater, Mars. *Journal of Geophysical Research: Planets*, 121(10), 2176–2192.
- Vincendon, M., Pilorget, C., Carter, J., & Stcherbinine, A. (2019). Observational evidence for a dry dust-wind origin of Mars seasonal dark flows. *Icarus*, 325, 115–127.
<https://doi.org/10.1016/j.icarus.2019.02.024>
- Wänke H., Dreibus G., Wright I. P., Cowley Stanley William Herbert, Runcorn Stanley Keith, & Southwood D. J. (1994). Chemistry and accretion history of Mars. *Philosophical*

- Transactions of the Royal Society of London. Series A: Physical and Engineering Sciences*, 349(1690), 285–293. <https://doi.org/10.1098/rsta.1994.0132>
- Wilson, E. H., Atreya, S. K., Kaiser, R. I., & Mahaffy, P. R. (2016). Perchlorate formation on Mars through surface radiolysis-initiated atmospheric chemistry: A potential mechanism. *Journal of Geophysical Research: Planets*, 121(8), 1472–1487. <https://doi.org/10.1002/2016JE005078>
- Yen, A. S., Kim, S. S., Hecht, M. H., Frant, M. S., & Murray, B. (2000). Evidence That the Reactivity of the Martian Soil Is Due to Superoxide Ions. *Science*, 289(5486), 1909–1912. <https://doi.org/10.1126/science.289.5486.1909>
- Zent, A. P., Ichimura, A. S., Quinn, R. C., & Harding, H. K. (2008). The formation and stability of the superoxide radical (O_2^-) on rock-forming minerals: Band gaps, hydroxylation state, and implications for Mars oxidant chemistry. *Journal of Geophysical Research*, 113(E9). <https://doi.org/10.1029/2007JE003001>
- Zhao, Y.-Y. S., McLennan, S. M., Jackson, W. A., & Karunatillake, S. (2018). Photochemical controls on chlorine and bromine geochemistry at the Martian surface. *Earth and Planetary Science Letters*, 497, 102–112. <https://doi.org/10.1016/j.epsl.2018.06.015>

Chapter 6

- Ader, M., Coleman, M. L., Doyle, S. P., Stroud, M., & Wakelin, D. (2001). Methods for the Stable Isotopic Analysis of Chlorine in Chlorate and Perchlorate Compounds. *Analytical Chemistry*, 73(20), 4946–4950. <https://doi.org/10.1021/ac010489u>
- Ader, M., Chaudhuri, S., Coates, J. D., & Coleman, M. (2008). Microbial perchlorate reduction: A precise laboratory determination of the chlorine isotope fractionation and its possible biochemical basis. *Earth and Planetary Science Letters*, 269(3), 605–613. <https://doi.org/10.1016/j.epsl.2008.03.023>
- ATSDR. (2008). *TOXICOLOGICAL PROFILE FOR PERCHLORATES*. U.S. Department of Health and Human Services Agency for Toxic Substances and Disease Registry.
- Bao, H., & Gu, B. (2004). Natural Perchlorate Has a Unique Oxygen Isotope Signature. *Environmental Science & Technology*, 38(19), 5073–5077. <https://doi.org/10.1021/es049516z>
- Bigeleisen, J., & Mayer, M. G. (1947). Calculation of Equilibrium Constants for Isotopic Exchange Reactions. *The Journal of Chemical Physics*, 15(5), 261–267. <https://doi.org/10.1063/1.1746492>
- Böhlke, J. K., Sturchio, N. C., Gu, B., Horita, J., Brown, G. M., Jackson, W. A., et al. (2005). Perchlorate Isotope Forensics. *Analytical Chemistry*, 77(23), 7838–7842. <https://doi.org/10.1021/ac051360d>
- Böhlke, J. K., Hatzinger, P. B., Sturchio, N. C., Gu, B., Abbene, I., & Mroczkowski, S. J. (2009). Atacama Perchlorate as an Agricultural Contaminant in Groundwater: Isotopic and Chronologic Evidence from Long Island, New York. *Environmental Science & Technology*, 43(15), 5619–5625. <https://doi.org/10.1021/es9006433>
- Bonifacie, M., Busigny, V., Mével, C., Philippot, P., Agrinier, P., Jendrzewski, N., et al. (2008). Chlorine isotopic composition in seafloor serpentinites and high-pressure metaperidotites. Insights into oceanic serpentinization and subduction processes.

- Geochimica et Cosmochimica Acta*, 72(1), 126–139.
<https://doi.org/10.1016/j.gca.2007.10.010>
- Brown, G. M. (1986). The reduction of chlorate and perchlorate ions at an active titanium electrode. *Journal of Electroanalytical Chemistry and Interfacial Electrochemistry*, 198(2), 319–330. [https://doi.org/10.1016/0022-0728\(86\)90008-2](https://doi.org/10.1016/0022-0728(86)90008-2)
- Cao, J., Elliott, D., & Zhang, W. (2005). Perchlorate Reduction by Nanoscale Iron Particles. *Journal of Nanoparticle Research*, 7(4–5), 499–506. <https://doi.org/10.1007/s11051-005-4412-x>
- Coates, J. D., & Achenbach, L. A. (2004). Microbial perchlorate reduction: rocket-fuelled metabolism. *Nature Reviews Microbiology*, 2(7), 569–580.
<https://doi.org/10.1038/nrmicro926>
- Coates, J. D., & Jackson, W. A. (2008). Principles of Perchlorate Treatment. In *In Situ Bioremediation of Perchlorate in Groundwater* (pp. 29–53). Springer, New York, NY.
https://doi.org/10.1007/978-0-387-84921-8_3
- Eastoe, C. J., Peryt, T. M., Petrychenko, O. Y., & Geisler-Cussey, D. (2007). Stable chlorine isotopes in Phanerozoic evaporites. *Applied Geochemistry*, 22(3), 575–588.
<https://doi.org/10.1016/j.apgeochem.2006.12.012>
- Eggenkamp, H. (2014). Natural Variations of Stable Chlorine and Bromine Isotopes on Earth. In *The Geochemistry of Stable Chlorine and Bromine Isotopes* (pp. 115–144). Springer, Berlin, Heidelberg. https://doi.org/10.1007/978-3-642-28506-6_10
- Eiler, J., Cesar, J., Chimiak, L., Dallas, B., Grice, K., Griep-Raming, J., et al. (2017). Analysis of molecular isotopic structures at high precision and accuracy by Orbitrap mass spectrometry. *International Journal of Mass Spectrometry*, 422, 126–142.
<https://doi.org/10.1016/j.ijms.2017.10.002>
- Eiler, J. M. (2007). “Clumped-isotope” geochemistry—The study of naturally-occurring, multiply-substituted isotopologues. *Earth and Planetary Science Letters*, 262(3), 309–327. <https://doi.org/10.1016/j.epsl.2007.08.020>
- Eiler, J. M., & Schauble, E. (2004). $^{18}\text{O}^{13}\text{C}^{16}\text{O}$ in Earth’s atmosphere. *Geochimica et Cosmochimica Acta*, 68(23), 4767–4777. <https://doi.org/10.1016/j.gca.2004.05.035>
- Ericksen, G. E. (1981). *Geology and origin of the Chilean nitrate deposits* (USGS Numbered Series No. 1188). U.S. G.P.O. : for sale by the Supt. of Docs., GPO,. Retrieved from <http://pubs.er.usgs.gov/publication/pp1188>
- Farley, K., Martin, P., Archer, P., Atreya, S., Conrad, P., Eigenbrode, J., et al. (2016). Light and variable $^{37}\text{Cl}/^{35}\text{Cl}$ ratios in rocks from Gale Crater, Mars: Possible signature of perchlorate. *Earth and Planetary Science Letters*, 438, 14–24.
- Gonfiantini, R. (1978). Standards for stable isotope measurements in natural compounds. *Nature*, 271(5645), 534–536. <https://doi.org/10.1038/271534a0>
- Gu, B., Brown, G. M., & Chiang, C.-C. (2007). Treatment of Perchlorate-Contaminated Groundwater Using Highly Selective, Regenerable Ion-Exchange Technologies. *Environmental Science & Technology*, 41(17), 6277–6282.
<https://doi.org/10.1021/es0706910>
- Gullick, R. W., Lechevallier, M. W., & Barhorst, T. S. (2001). Occurrence of perchlorate in drinking water sources. *American Water Works Association. Journal; Denver*, 93(1), 66.
- Hatzinger, P. B., Böhlke, J. K., Sturchio, N. C., Gu, B., Heraty, L. J., & Borden, R. C. (2009). Fractionation of stable isotopes in perchlorate and nitrate during in situ biodegradation in a sandy aquifer. *Environmental Chemistry*, 6(1), 44–52. <https://doi.org/10.1071/EN09008>

- Hoering, T. C., Ishimori, F. T., & McDonald, H. O. (1958). The Oxygen Exchange Between Oxy-anions and Water. II. Chlorite, Chlorate and Perchlorate Ions. *Journal of the American Chemical Society*, 80(15), 3876–3879. <https://doi.org/10.1021/ja01548a020>
- Jackson, W. A., Joseph, P., Laxman, P., Tan, K., Smith, P. N., Yu, L., & Anderson, T. A. (2005). Perchlorate Accumulation in Forage and Edible Vegetation. *Journal of Agricultural and Food Chemistry*, 53(2), 369–373. <https://doi.org/10.1021/jf0493021>
- Jackson, W. A., Böhlke, J. K., Gu, B., Hatzinger, P. B., & Sturchio, N. C. (2010). Isotopic Composition and Origin of Indigenous Natural Perchlorate and Co-Occurring Nitrate in the Southwestern United States. *Environmental Science & Technology*, 44(13), 4869–4876. <https://doi.org/10.1021/es903802j>
- Kirk, A. B., Smith, E. E., Tian, K., Anderson, T. A., & Dasgupta, P. K. (2003). Perchlorate in Milk. *Environmental Science & Technology*, 37(21), 4979–4981. <https://doi.org/10.1021/es034735q>
- Kounaves, S. P., Stroble, S. T., Anderson, R. M., Moore, Q., Catling, D. C., Douglas, S., et al. (2010). Discovery of Natural Perchlorate in the Antarctic Dry Valleys and Its Global Implications. *Environmental Science & Technology*, 44(7), 2360–2364. <https://doi.org/10.1021/es9033606>
- Liu, Y., Zhou, A., Gan, Y., Liu, C., Yu, T., & Li, X. (2013). An online method to determine chlorine stable isotope composition by continuous flow isotope ratio mass spectrometry (CF-IRMS) coupled with a Gasbench II. *Journal of Central South University*, 20(1), 193–198. <https://doi.org/10.1007/s11771-013-1476-0>
- Neubauer, C., Sweredoski, M. J., Moradian, A., Newman, D. K., Robins, R. J., & Eiler, J. M. (2018). Scanning the isotopic structure of molecules by tandem mass spectrometry. *International Journal of Mass Spectrometry*, 434, 276–286. <https://doi.org/10.1016/j.ijms.2018.08.001>
- Parker, D. R., Seyfferth, A. L., & Reese, B. K. (2008). Perchlorate in Groundwater: A Synoptic Survey of “Pristine” Sites in the Coterminous United States. *Environmental Science & Technology*, 42(5), 1465–1471. <https://doi.org/10.1021/es7021957>
- Rajagopalan, S., Anderson, T. A., Fahlquist, L., Rainwater, K. A., Ridley, M., & Jackson, W. A. (2006). Widespread Presence of Naturally Occurring Perchlorate in High Plains of Texas and New Mexico. *Environmental Science & Technology*, 40(10), 3156–3162. <https://doi.org/10.1021/es052155i>
- Rao, B., Hatzinger, P. B., Böhlke, J. K., Sturchio, N. C., Andraski, B. J., Eckardt, F. D., & Jackson, W. A. (2010). Natural Chlorate in the Environment: Application of a New IC-ESI/MS/MS Method with a Cl18O3- Internal Standard. *Environmental Science & Technology*, 44(22), 8429–8434. <https://doi.org/10.1021/es1024228>
- Schauble, E. A., Rossman, G. R., & Taylor, H. P. (2003). Theoretical estimates of equilibrium chlorine-isotope fractionations. *Geochimica et Cosmochimica Acta*, 67(17), 3267–3281. [https://doi.org/10.1016/S0016-7037\(02\)01375-3](https://doi.org/10.1016/S0016-7037(02)01375-3)
- Sharp, Z., Williams, J., Shearer, C., Agee, C., & McKeegan, K. (2016). The chlorine isotope composition of Martian meteorites 2. Implications for the early solar system and the formation of Mars. *Meteoritics & Planetary Science*, 51(11), 2111–2126. <https://doi.org/10.1111/maps.12591>
- Sharp, Z. D., Barnes, J. D., Brearley, A. J., Chaussidon, M., Fischer, T. P., & Kamenetsky, V. S. (2007). Chlorine isotope homogeneity of the mantle, crust and carbonaceous chondrites. *Nature*, 446(7139), 1062–1065. <https://doi.org/10.1038/nature05748>

- Stolper, D. A., Sessions, A. L., Ferreira, A. A., Santos Neto, E. V., Schimmelmann, A., Shusta, S. S., et al. (2014). Combined ^{13}C -D and D-D clumping in methane: Methods and preliminary results. *Geochimica et Cosmochimica Acta*, 126, 169–191. <https://doi.org/10.1016/j.gca.2013.10.045>
- Sturchio, N. C., Hatzinger, P. B., Arkins, M. D., Suh, C., & Heraty, L. J. (2003). Chlorine Isotope Fractionation during Microbial Reduction of Perchlorate. *Environmental Science & Technology*, 37(17), 3859–3863. <https://doi.org/10.1021/es034066g>
- Sturchio, N. C., Böhlke, J. K., Beloso, Abelardo D., Streger, S. H., Heraty, L. J., & Hatzinger, P. B. (2007). Oxygen and Chlorine Isotopic Fractionation during Perchlorate Biodegradation: Laboratory Results and Implications for Forensics and Natural Attenuation Studies. *Environmental Science & Technology*, 41(8), 2796–2802. <https://doi.org/10.1021/es0621849>
- Sturchio, N. C., Hoaglund, J. R., Marroquin, R. J., Beloso, A. D., Heraty, L. J., Bortz, S. E., & Patterson, T. L. (2011). Isotopic Mapping of Groundwater Perchlorate Plumes. *Groundwater*, 50(1), 94–102. <https://doi.org/10.1111/j.1745-6584.2011.00802.x>
- Sturchio, N. C., Beloso, A., Heraty, L. J., Wheatcraft, S., & Schumer, R. (2014). Isotopic tracing of perchlorate sources in groundwater from Pomona, California. *Applied Geochemistry*, 43, 80–87. <https://doi.org/10.1016/j.apgeochem.2014.01.012>
- United States Geologic Survey. (2018). *Reference Materials USGS37, USGS38, and USGS39* (Report of Stable Isotopic Composition). Reston, VA.
- Urbansky, E. T. (2002). Perchlorate as an environmental contaminant. *Environmental Science and Pollution Research*, 9(3), 187–192. <https://doi.org/10.1007/BF02987487>
- Urbansky, E. T., Brown, S. K., Magnuson, M. L., & Keltz, C. A. (2001). Perchlorate levels in samples of sodium nitrate fertilizer derived from Chilean caliche. *Environmental Pollution*, 112(3), 299–302. [https://doi.org/10.1016/S0269-7491\(00\)00132-9](https://doi.org/10.1016/S0269-7491(00)00132-9)
- Urey, H. C. (1947). The thermodynamic properties of isotopic substances. *Journal of the Chemical Society (Resumed)*, (0), 562–581. <https://doi.org/10.1039/JR9470000562>
- Wei, H.-Z., Jiang, S.-Y., Xiao, Y.-K., Wang, J., Lu, H., Wu, B., et al. (2012). Precise Determination of the Absolute Isotopic Abundance Ratio and the Atomic Weight of Chlorine in Three International Reference Materials by the Positive Thermal Ionization Mass Spectrometer- Cs_2Cl^+ -Graphite Method. *Analytical Chemistry*, 84(23), 10350–10358. <https://doi.org/10.1021/ac302498q>
- Williams, J. T., Shearer, C. K., Sharp, Z. D., Burger, P. V., McCubbin, F. M., Santos, A. R., et al. (2016). The chlorine isotopic composition of Martian meteorites 1: Chlorine isotope composition of Martian mantle and crustal reservoirs and their interactions. *Meteoritics & Planetary Science*, 51(11), 2092–2110. <https://doi.org/10.1111/maps.12647>